

Doctoral Dissertation

博士論文

**Physical mechanism of volcanic tsunami earthquakes repeating at  
submarine volcanoes**

(海底火山体で繰り返す火山性津波地震の物理メカニズム)

A Dissertation Submitted for the Degree of Doctor of Science

December 2019

令和元年12月博士（理学）申請

Department of Earth and Planetary Science, Graduate School of Science,

The University of Tokyo

東京大学大学院理学系研究科地球惑星科学専攻

**Osamu Sandanbata**

三反畑 修



# *Abstract*

Anomalous tsunami earthquakes have repeatedly occurred at submarine volcanoes near Torishima Island in Japan and Curtis Island in New Zealand. All centroid moment tensor solutions obtained for these earthquakes were non-double-couple types dominated by vertical compensated-linear-vector-dipole (vertical-CLVD) components, indicating an atypical source mechanism of volcanic origin. Despite their intermediate-class seismic magnitudes of  $M_w$  5-6, large amplitude tsunamis with peak amplitudes of tens of centimeters were observed at tide gauges across wide regions after the earthquakes. Considering their volcanic origins and the efficiency of tsunami excitation, these can be regarded as “volcanic tsunami earthquakes.” Previous studies have proposed several possible models for the physical mechanism of such earthquakes based on seismic analysis. However, their shallow source depths and remote locations (far from developed seismic networks) have made it difficult to determine the physical mechanism reliably via seismic data. Although tsunami records have also been used to explore the mechanism, limitations of past tsunami analyses (such as lack of good records and lower computational accuracy) have prevented detailed source modeling. Therefore, the physical mechanism of volcanic tsunami earthquakes has yet to be determined. In this study, I aimed to determine the physical mechanism by constructing kinematic source models of volcanic tsunami earthquakes through an interdisciplinary approach based on tsunami analysis, as well as modeling of long-period seismic waves and crustal deformation.

I first estimated an approximate tsunami source, or initial sea-surface displacement, caused by a volcanic tsunami earthquake near Torishima Island in 2015 (the 2015 Torishima earthquake) with high-quality tsunami records at an array of stations equipped with ocean-bottom pressure gauges. The peak location of the initial sea-surface uplift was constrained over a submarine caldera by comparing tsunami ray-tracing simulations with dispersion properties observed at the array. In order to obtain the profile of the tsunami source, I assumed an axially symmetric profile over the caldera to compute tsunami waveforms at the array. By comparing the synthetic and observed waveforms, I modeled a central uplift  $> 1$  m with a smaller peripheral subsidence surrounding the caldera structure. Synthetic tsunami waveforms showed good agreement to observations at both the array and a tide-gauge station. The estimated tsunami model implied a possible source mechanism related to characteristic structures below the submarine caldera, such as a vertical opening of a shallow horizontal crack that would generate tsunamis efficiently with little release of long-period seismic energy.

Next, I explored a kinematic source model of the 2015 Torishima earthquake that explained observed tsunami and long-period seismic waves. To constrain candidates for fault geometries capable of causing the earthquake, I estimated its detailed initial sea-surface displacement by comparing more accurate synthetic tsunami waveforms with tsunami records from different observation networks (the Dense Oceanfloor Network system for Earthquakes and Tsunamis (DONET) and the Deep Sea Floor

Observatory (DSFO) off southwestern Japan and the Deep-ocean Assessment and Reporting of Tsunamis (DART) in the offshore deep ocean), as well as the array. This confirmed that the earthquake generated large uplift concentrated just above the caldera floor and clear outside subsidence along the rim structure. Therefore, I hypothesized a composite fault model consisting of a ring-fault structure and a horizontal fault as a possible source model. Next, I developed an efficient inversion method using tsunami waveforms to estimate fault slips and applied it to multiple assumed fault models with different fault parameters, such as the dip angle and ruptured portion of the ring fault as well as the depth of the horizontal fault. From the slip distributions of the multiple fault models obtained by the inversion of tsunami waveforms, I constructed a point seismic moment tensor source to synthesize long-period seismic waves at regional stations of the Japanese broadband seismic network (F-net) and Global Seismograph Network (GSN). Finally, I obtained a composite source model composed of thrust slip along an inwardly down-dipping ring fault extending along three-quarters of the caldera rim structure along with the instantaneous vertical opening and closing of a horizontal fault at approximately 2 km depth. This slip model sufficiently explained both the tsunami and long-period seismic wave records, confirming its plausibility as a kinematic source model of the 2015 Torishima earthquake.

A similar approach was also applied to another volcanic tsunami earthquake near Curtis Island in 2017 (the 2017 Curtis earthquake). After estimating an approximate tsunami source location from tide-gauge records on the North Island and remote islands of New Zealand, the initial sea-surface displacement was estimated by the inversion of tsunami waveforms. This revealed similar characteristics to the 2015 Torishima earthquake, i.e., large uplift over a caldera-like structure with a clear boundary of the uplifted area along the rim structure. I next inverted tsunami waveforms to estimate slip distributions on different assumed fault geometries, then examined the validities of the slip models by comparing synthetic long-period seismic waveforms with the records at regional stations at New Zealand, Australia, and islands along the Tonga-Kermadec Ridge and in Melanesia. Finally, I obtained a kinematic source model composed of a ring-fault slip on the southwestern part and a horizontal crack opening at  $< 5$  km depth.

These modeling studies revealed that composite slip models of ring-fault and horizontal-crack structures in submarine calderas quantitatively explained both the tsunami and long-period seismic records for the two events. Previous analyses of volcanic tsunami earthquakes have common characteristics to attribute them to thrust slips on a ring fault induced by magmatic pressure inside a horizontal crack at shallow depth below submarine calderas. The mechanism is quite similar to the “trap-door faulting” observed at the Sierra Negra caldera in the Galápagos. The ability of these intermediate-class seismic magnitudes to create large tsunamis can be theoretically and synthetically explained by the atypical mechanism at shallow depth in the crust. Although some elements of the moment tensor of the complex fractures in shallow crust cannot be constrained seismologically, observable elements sensitively reflect ring-fault geometries. These properties enable us to obtain source information from moment tensor analysis using long-period seismic waveforms. Most of the repeating earthquakes showed similarities in these observable elements, implying that their ruptures occurred at almost identical ring-fault structures in the

submarine calderas. Through this study, the physical mechanism of volcanic tsunami earthquakes was successfully determined with kinematic source models validated quantitatively by both tsunami and seismic records. The results provide new and specific pictures of peculiar tsunami earthquakes repeatedly occurring in active submarine calderas.



# Contents

<i>Abstract</i> .....	3
<i>Contents</i> .....	7
<i>Figures</i> .....	11
<i>Tables</i> 15	
<b>Chapter 1 Introduction</b> .....	<b>17</b>
1.1 Volcanic tsunami earthquakes.....	17
1.2 Previous studies .....	23
1.3 Purpose and strategy .....	25
<b>Chapter 2 Tsunami source modeling of the 2015 Torishima earthquake using array of stations equipped with ocean-bottom pressure gauges</b> .....	<b>27</b>
2.1 Tsunami data at array of stations equipped with ocean-bottom pressure gauges..	28
2.1.1 Phase analysis .....	30
2.1.2 Zero-cross time and weak downswing motion preceding major upswing.....	30
2.2 Estimation of tsunami source location using ray-tracing method for dispersive tsunamis .....	31
2.2.1 Methods .....	31
2.2.2 Results.....	33
2.3 Tsunami source modeling with axially symmetric shape .....	35
2.3.1 Methods .....	35
2.3.2 Results.....	38
2.4 Discussion.....	39
2.4.1 Reasonability of assumptions for the peak location estimation.....	39
2.4.2 Implications for the physical mechanism of the 2015 Torishima earthquake .....	40
<b>Chapter 3 Kinematic source modeling for the 2015 Torishima volcanic tsunami earthquake</b> .....	<b>43</b>

<b>3.1</b>	<b>Inversion of tsunami waveforms for the initial sea-surface displacement.....</b>	<b>43</b>
3.1.1	Questions remaining from Chapter 2.....	43
3.1.2	Data and Methods .....	44
3.1.3	Inversion of tsunami waveforms for initial sea-surface displacement .....	45
3.1.4	Physical mechanism inferred from the inverted tsunami source model .....	50
<b>3.2</b>	<b>Inversion of tsunami waveforms for fault slips .....</b>	<b>55</b>
3.2.1	Seafloor deformation modeling .....	57
3.2.2	Methods .....	58
3.2.3	Results.....	61
<b>3.3</b>	<b>Forward modeling of long-period seismic waves .....</b>	<b>69</b>
3.3.1	Methods and Data .....	69
3.3.2	Results.....	71
<b>3.4</b>	<b>Summary of Chapters 2 and 3 .....</b>	<b>84</b>
<b><i>Chapter 4 Kinematic source modeling for the 2017 Curtis volcanic tsunami earthquake.....</i></b>		<b>87</b>
<b>4.1</b>	<b>Data and tsunami simulations.....</b>	<b>87</b>
4.1.1	Tsunami data.....	87
4.1.2	Tsunami simulation.....	87
<b>4.2</b>	<b>Estimation of tsunami source area .....</b>	<b>88</b>
4.2.1	Methods .....	88
4.2.2	Results.....	89
<b>4.3</b>	<b>Inversion of tsunami waveforms for initial sea-surface displacement.....</b>	<b>90</b>
4.3.1	Methods .....	90
4.3.2	Results.....	92
4.3.3	Physical mechanism inferred from the inverted tsunami model.....	94
<b>4.4</b>	<b>Kinematic source modeling .....</b>	<b>95</b>

4.4.1	Methods .....	95
4.4.2	Results.....	98
4.4.3	Discussion.....	114
<b>4.5</b>	<b>Summary of Chapter 4 .....</b>	<b>114</b>
<b><i>Chapter 5 General discussion.....</i></b>		<b><i>117</i></b>
<b>5.1</b>	<b>Physical mechanism of volcanic tsunami earthquakes.....</b>	<b>117</b>
<b>5.2</b>	<b>Long-period seismic waves excited by volcanic tsunami earthquakes.....</b>	<b>120</b>
5.2.1	Observable moment tensor elements .....	120
5.2.2	Moment tensor inversion using W-phase of seismic waves .....	125
5.2.3	Relationship of long-period seismic waves to ring-fault slips.....	128
5.2.4	Usefulness of observable moment-tensor elements for the kinematic source modeling of volcanic tsunami earthquakes .....	135
<b>5.3</b>	<b>Recurrent volcanic tsunami earthquakes .....</b>	<b>139</b>
<b>5.4</b>	<b>Causes of tsunami earthquake characteristics .....</b>	<b>142</b>
<b>5.5</b>	<b>Future studies .....</b>	<b>145</b>
5.5.1	Dynamics of volcanic tsunami earthquakes.....	145
5.5.2	Submarine caldera volcanology .....	145
5.5.3	Tsunami risk evaluations .....	146
5.5.4	Application of the kinematic source modeling approach .....	146
<b><i>Chapter 6 Major findings and conclusions.....</i></b>		<b><i>149</i></b>
<b><i>Acknowledgements.....</i></b>		<b><i>153</i></b>
<b><i>References .....</i></b>		<b><i>155</i></b>
<b><i>Data resources.....</i></b>		<b><i>164</i></b>
<b><i>Appendix 1. Phase correction method for short-period tsunamis.....</i></b>		<b><i>165</i></b>
<b><i>Appendix 2. Moment tensor inversion using W-phases of seismic waves .....</i></b>		<b><i>181</i></b>



# Figures

Fig. 1.1 Map of the Torishima volcanic tsunami earthquakes.....	19
Fig. 1.2 Tsunami records of the Torishima volcanic tsunami earthquakes at tide-gauge stations .....	20
Fig. 1.3 Map of the Curtis volcanic tsunami earthquakes .....	21
Fig. 1.4 Tsunami records of the Curtis volcanic tsunami earthquakes at tide-gauge stations.....	22
Fig. 1.5 Amplitude-distance diagrams of the 2015 Torishima and the 2017 Curtis volcanic tsunami earthquakes .....	23
Fig. 2.1 Tsunami observations at the array of Aogashima Island .....	29
Fig. 2.2 Frequency dependency of travel times and slowness directions.....	31
Fig. 2.3 Average trace of 10 tsunami records mutually time-shifted to a common zero-cross time [ <i>Fukao et al.</i> , 2018].....	32
Fig. 2.4 Estimate of tsunami source location.....	34
Fig. 2.5 Search for the best initial sea-surface displacement.....	36
Fig. 2.6 Best initial sea-surface displacement model and waveform comparison at the array.....	37
Fig. 2.7 Bathymetry for waveform simulation at Yaene Port on Hachijojima Island.....	38
Fig. 2.8 Schematic illustration of phase-peak origins.....	39
Fig. 3.1 Map of the tsunami observation networks .....	46
Fig. 3.2 Distributions of unit sources of initial sea-surface displacement around Smith Caldera.....	47
Fig. 3.3 Selection of a damping parameter .....	49
Fig. 3.4 Inversion results using all the stations.....	51
Fig. 3.5 Inversion results using different datasets .....	52
Fig. 3.6 Inversion result assuming uplifted sea-surface displacement .....	53
Fig. 3.7 Hypothesized subsurface structures of Smith Caldera.....	54
Fig. 3.8 Model setting of the composite fault system discretized by triangular meshes .....	55
Fig. 3.9 Variable fault parameters and assumed fault models.....	56
Fig. 3.10 Procedures to compute tsunami Green's functions .....	59

Fig. 3.11 Slip distributions of the 18 fault models .....	63
Fig. 3.12 Slip inversion results of Model 4 (2 km/TR/75°).....	64
Fig. 3.13 Slip inversion results of Model 9 (2 km/FR/75°).....	65
Fig. 3.14 Slip inversion results of Model 14 (2 km/HR/75°) .....	66
Fig. 3.15 Slip models with different block thickness .....	67
Fig. 3.16 Singular value decomposition .....	68
Fig. 3.17 Computation of moment tensor from a slip model and 1-D velocity structure.....	70
Fig. 3.18 Long-period seismic waves of the best TR model (TR/75°/2 km) .....	73
Fig. 3.19 Seismic waves of slip models with different ring-fault dip angles .....	75
Fig. 3.20 Grid-search for the best dip angle and best TR/FR/HR and heterogeneous-TR models .....	76
Fig. 3.21 Long-period seismic waves of the best FR model (FR/76°/2 km).....	78
Fig. 3.22 Long-period seismic waves of the best HR model (HR/72°/2 km).....	80
Fig. 3.23 Long-period seismic waves of the heterogeneous-dip TR model (TR/73-77°/2 km).....	82
Fig. 4.1 Nested bathymetry data and tide-gauge stations used for tsunami simulations .....	88
Fig. 4.2 Estimation of the tsunami source region .....	89
Fig. 4.3 Waveforms of the Gaussian-shaped uplift models.....	90
Fig. 4.4 Unit sources distributed around Curtis and Cheeseman Islands .....	92
Fig. 4.5 Grid-search results of travel time delays at LOTT and GBIT stations .....	92
Fig. 4.6 Results of inversions for the initial sea-surface displacement .....	93
Fig. 4.7 Caldera-like structure around the tsunami source region.....	94
Fig. 4.8 Reference and modified fault models.....	96
Fig. 4.9 Selection of a proper value of damping parameter for the slip inversion .....	97
Fig. 4.10 Inversion results with the reference fault model .....	100
Fig. 4.11 Moment tensor and long-period seismic waves of slip distributions of the reference fault model .....	101
Fig. 4.12 Modified fault models .....	103

Fig. 4.13 Inversion results with the modified-dip fault model .....	104
Fig. 4.14 Moment tensor and long-period seismic waves of slip distributions of the modified-dip fault model .....	105
Fig. 4.15 Inversion results with the modified-thickness fault model .....	107
Fig. 4.16 Moment tensor and long-period seismic waves of slip distributions of the modified-thickness fault model.....	108
Fig. 4.17 Half-ring fault model.....	110
Fig. 4.18 Inversion results with the half-ring fault model .....	111
Fig. 4.19 Moment tensor and long-period seismic waves of slip distributions of the half-ring fault model .....	112
Fig. 5.1 Interpretation of the physical mechanism with a rupture scenario of volcanic tsunami earthquake .....	119
Fig. 5.2 Moment tensor of the Torishima source model.....	122
Fig. 5.3 Long-period seismic waves excited by fractures of the horizontal fault of the Torishima source model .....	123
Fig. 5.4 Decomposition of moment tensor .....	124
Fig. 5.5 Decomposition of the moment tensor from the ring fault of the Torishima source model.....	125
Fig. 5.6 Long-period seismic waves excited by the <i>Dip-DC</i> element of the Torishima source model....	126
Fig. 5.7 MT inversion using W-phases of seismic waves for the 2015 Torishima volcanic tsunami earthquake.....	127
Fig. 5.8 MT inversion using W-phases of seismic waves for the 2017 Curtis volcanic tsunami earthquake .....	127
Fig. 5.9 Modeling of the ring-fault slip .....	128
Fig. 5.10 Seismic radiation properties of ring-fault slips .....	130
Fig. 5.11 Moment tensors of the ring-fault slip with different geometries.....	131
Fig. 5.12 Waveforms of the ISO and CLVD elements at source depth 2.0 km .....	134
Fig. 5.13 Observable moment-tensor elements of slip models of the 2015 Torishima volcanic tsunami earthquakes .....	136

Fig. 5.14 Observable moment-tensor elements of slip models of the 2017 Curtis volcanic tsunami earthquakes .....	138
Fig. 5.15 Moment tensor of a trapdoor faulting event on 22 October 2005 and intra-caldera fault of Sierra Negra .....	139
Fig. 5.16 Moment tensors of recurrent volcanic tsunami earthquakes at Smith Caldera .....	140
Fig. 5.17 Estimated geometries of the ring fault ruptured by recurrent Torishima volcanic tsunami earthquakes at Smith Caldera .....	141
Fig. 5.18 Moment tensors of recurrent volcanic tsunami earthquakes at Curtis Caldera .....	142
Fig. 5.19 Comparison of volcanic tsunami earthquakes with a scaling law of global earthquakes. ....	144

## *Tables*

Table 1.1 Earthquake information of volcanic tsunami earthquakes .....	18
Table 2.1 Information of stations of the array off Aogashima Island .....	28
Table 2.2 Array analysis of phase and onset arrivals [ <i>Fukao et al.</i> , 2018] .....	30
Table 3.1 Results of the inversion of tsunami waveforms.....	61
Table 3.2 Results of the forward modeling of long-period seismic waves .....	72
Table 4.1 Results of the inversion of tsunami waveforms and their tsunami and seismic NRMS errors ..	99



# Chapter 1 Introduction

## 1.1 Volcanic tsunami earthquakes

*Tsunamis* are long-wavelength water waves which are often generated by sea-floor deformation accompanying large earthquakes with seismic magnitudes over  $M_w$  7–8. Recent mega-earthquakes such as the 2011 Tohoku-Oki earthquake ( $M_w$  9.0) and the 2004 Sumatra-Andaman earthquake ( $M_w$  9.1) resulted in  $> 10$  m tsunamis and caused catastrophic damage to coastal cities. These types of earthquakes are called *tsunamigenic earthquakes* [e.g. Satake, 2015]. In comparison, *tsunami earthquakes* can excite larger tsunamis than empirically expected from their seismic waves, which can be attributed to relatively weak seismic excitation, efficiency in tsunami generation, or both. Several physical mechanisms have been proposed for tsunami earthquakes. The most typical is a slow rupture on interplate boundaries near the trench of subduction zones [e.g. Kanamori *et al.*, 1972]. Tsunamis can also be amplified by high-angle secondary faulting in the accretionary wedge [e.g. Fukao, 1979] or submarine landslides triggered by resultant ground motions [e.g. Tappin *et al.*, 1999]. Low rigidity in the shallow crust can result in weaker seismic radiation and efficient tsunami generation [Okal, 1988]. Exploration for physical mechanisms of tsunami earthquakes is one of the most important problems in geoscience, since the gap between tsunami and seismic magnitudes may reflect their abnormal physical mechanisms and makes it difficult to predict tsunamis from seismic information.

In contrast to the well-known types of tsunami earthquakes mentioned above, anomalous tsunami earthquakes have been observed repeatedly at submarine volcanoes. These earthquakes have consistently had intermediate seismic magnitudes ( $M_w$  5–6), while larger tsunamis with peak amplitudes of tens of centimeters were recorded at tide gauge stations. Their peculiar source mechanisms were characterized by non-double-couple focal mechanisms with dominant compensated-linear-vector-dipole (CLVD) components [e.g. Knopoff and Randall, 1970] and by shallow source depth at submarine volcanic edifices. These characteristics indicated that an anomalous mechanism with volcanic origins [e.g. Kanamori *et al.*, 1993; Ekström, 1994]. Observations of T-phase waves lacking high-frequency energy originating from submarine volcanoes before or after some of these events also implied their associations with volcanic processes [Sugioka *et al.*, 2000; *Global Volcanism Program*, 2009]. Therefore, I named these

**Table 1.1 Earthquake information of volcanic tsunami earthquakes**

Earthquake parameters of GCMT catalog for (a) the Torishima volcanic tsunami earthquakes. (b) the Curtis volcanic tsunami earthquakes. All the data is provided from GCMT catalog. It is noted that shallow source depth cannot be determined accurately with long-period seismic data used for the standard GCMT analysis [Shuler *et al.*, 2013a].

**(a) Torishima volcanic tsunami earthquakes**

Event	Date (Y/M/D)	Time (h:m:s)	Longitude	Latitudes	Depth [km]	$M_w$	$M_s$
1	1984/6/13	29:28.5	139.93°	31.39°	15.2	5.6	5.4
2	1996/9/4	16:07.2	140.06°	31.48°	24.4	5.7	5.1
3	2006/1/1	12:07.4	140.07°	31.51°	12	5.6	5.0
4	2015/5/2	50:49.7	139.94°	31.47°	12	5.7	5.7
5	2018/5/6	04:06.2	139.98°	31.51°	12	5.4	5.4

**(b) Curtis volcanic tsunami earthquakes**

Event	Date (Y/M/D)	Time (h:m:s)	Longitude	Latitudes	Depth [km]	$M_w$	$M_s$
1	2009/2/17	30:58.6	-178.54°	-30.56°	12.1	5.8	6.0
2	2017/12/8	10:02.7	-178.56°	-30.49°	13.4	5.8	6.2

*volcanic tsunami earthquakes*. It is also noteworthy that such volcanic tsunami earthquakes reoccurred at each volcano quasi-regularly with intervals of  $\sim 10$  years in most cases.

The source locations of volcanic tsunami earthquakes recognized in the past are limited to two undersea volcanic areas. The most well-known is Smith Caldera (also known as Sumisu Caldera), a submarine volcano with a well-formed caldera structure  $\sim 6\text{--}8$  km in diameter, near Torishima Island along Izu-Bonin Ridge, south of Japan (Fig. 1.1) [e.g. Tani *et al.*, 2008; *Global Volcanism Program*, 2013]. Since 1984, when the first volcanic tsunami earthquake was recognized, five similar earthquakes were observed around Smith Caldera on July 13, 1984, September 4, 1996, January 1, 2006, May 2, 2015, and May 6, 2018 (based on UTC), until December 2019 (Table 1.1a, Fig. 1.1c). All the focal mechanisms reported by the Global Centroid Moment Tensor (GCMT) catalogue showed non-double-couple types with dominant vertical-CLVD components in tension-axis (T-axis). The reported moment magnitudes ( $M_w$ ) for the 1984, 1996, 2006, 2015, and 2018 earthquakes were 5.6, 5.7, 5.6, 5.7, and 5.4, respectively. Despite these intermediate magnitudes, many tide gauges in the wider region recorded clear tsunami signals with amplitudes of tens of centimeters following the earthquakes (Fig. 1.2). The recorded tsunamis from the five events were remarkably similar in their arrival times and waveforms at each tide-gauge station, although the amplitudes of the 2018 event were smaller relative to its smaller seismic magnitude. These similarities in focal mechanism, seismic magnitude, and tsunami waveform indicated that the recurrent events had a common physical mechanism at the same location. Since the epicenter location of the 1984 earthquake was reported as “near Torishima Island” by the Japan Meteorological Agency (JMA), this series of earthquakes has been historically called the “Torishima earthquakes” [e.g. Satake and Kanamori, 1991;

Kanamori *et al.*, 1993] or “Torishima-Kinkai (oceanic area near Torishima Island) earthquakes” [Hatori, 1985]. In this thesis, the events near Smith Caldera are referred as the “Torishima earthquakes,” following previous studies. Note that the source locations are closer to Smith Caldera than the volcanic rise containing Torishima Island.

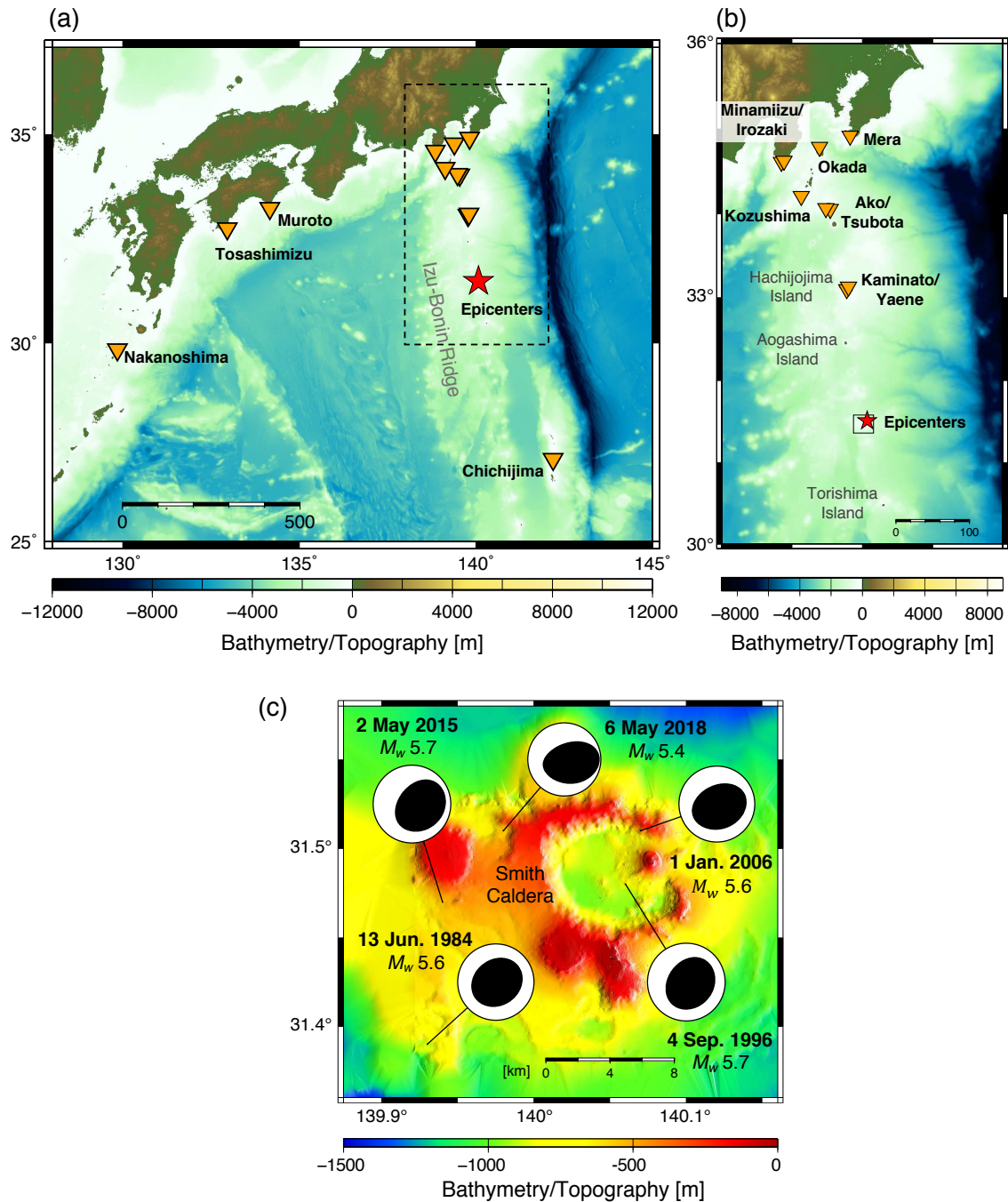


**Fig. 1.1 Map of the Torishima volcanic tsunami earthquakes**

(a-b) Centroid locations of the Torishima volcanic tsunami earthquake (red star) and tide-gauge stations (orange triangle). Dashed rectangle in (a) and solid rectangle in (b) represents the area shown in (b) and (c), respectively. (c) Centroid locations and focal mechanisms of the Torishima volcanic tsunami earthquakes around Smith Caldera. The earthquake information is from GCMT catalog (see Table 1.1).

The other area where volcanic tsunami earthquakes have been observed is a submarine volcanic edifice below Curtis Island and Cheeseman Island, on the Tonga-Kermadec Ridge, about 900 km northeast of New Zealand’s North Island (Fig. 1.3). These two small islands (< 1 km in diameter) are emergent portions of a submarine volcano containing a crater with fumarolic emission [Doyle *et al.*, 1997; Smith *et al.*, 1988; *Global Volcanism Program*, 2009]. Two volcanic tsunami earthquakes occurred at shallow depth near these islands on February 17, 2009 ( $M_w$  5.8,  $M_s$  6.0) and December 8, 2017 ( $M_w$  5.8,  $M_s$  6.2) (by UTC), hereafter referred to as the “Curtis earthquakes.” Non-double-couple focal mechanisms were reported for these earthquakes, similar to the Torishima earthquakes. The 2017 event was first recognized as a volcanic tsunami earthquake when clear tsunami signals were recorded at tide gauges on remote islands and the North Island (Fig. 1.4). After the recognition of the 2017 event, I checked tide-gauge records following a

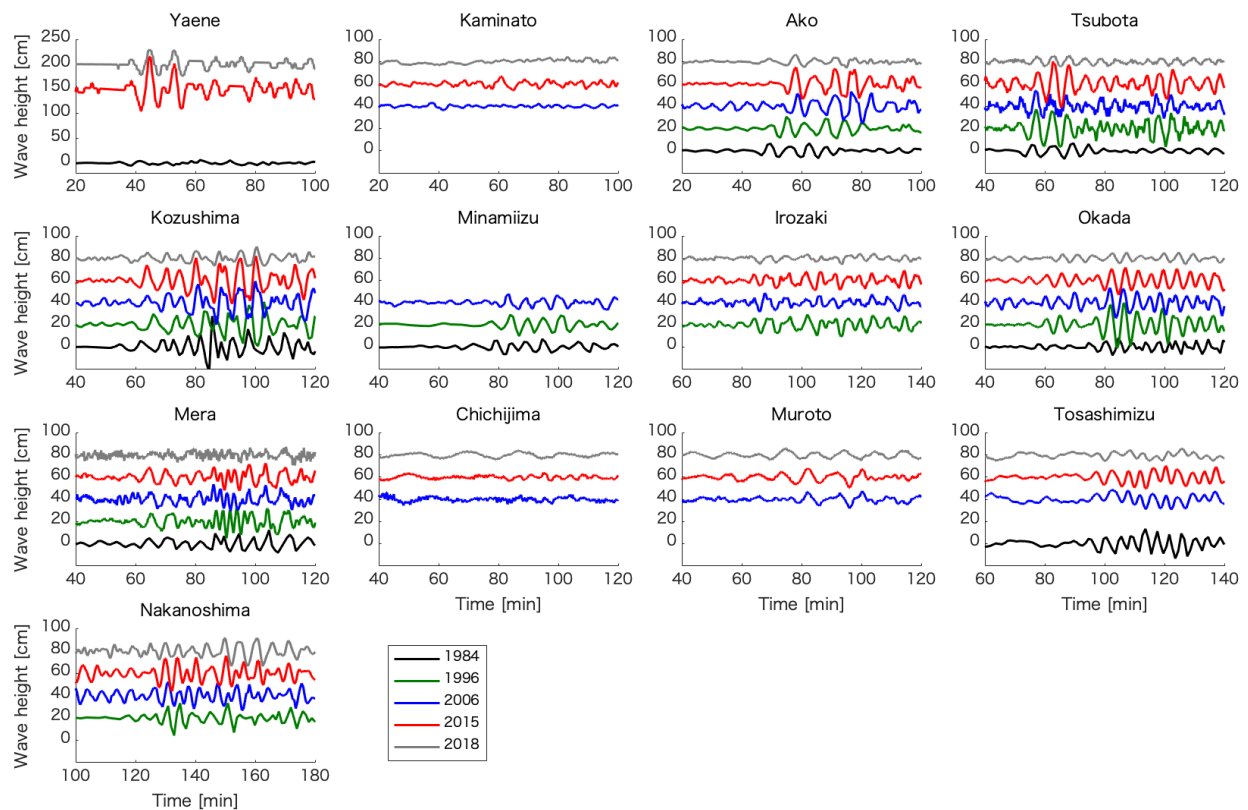


**Fig. 1.2 Tsunami records of the Torishima volcanic tsunami earthquakes at tide-gauge stations**

Names of tide-gauge stations are shown above each plate (see Fig.1.1a-b). Black, red, blue, green, and gray lines represent tsunami records of the Torishima earthquakes in 1984, 1996, 2006, 2015, and 2018, respectively. Base lines for different events are shifted by multiples of 20 cm or 50 cm in the y-axis direction. Horizontal axis represents time from earthquake origin times. Tsunami signals are extracted from the raw data by removing tidal signals with the polynomial fitting. Note that the location of Yaene station changed between the 1984 and 2015 events. The records were provided by JMA and Hydrographic and Oceanographic Department, Japan Coast Guard. Some of the data in 1984 and 1996 tsunamis were digitized from analogue data by Aditya Gusman.

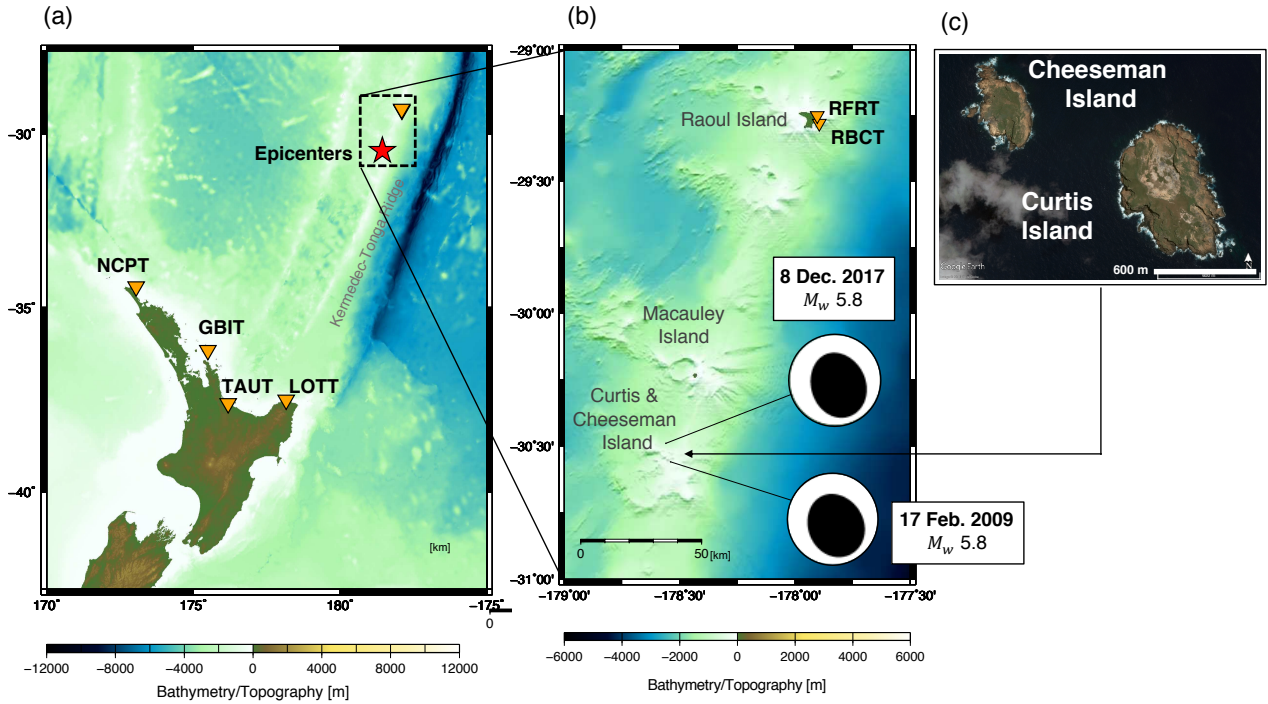


**Fig. 1.3 Map of the Curtis volcanic tsunami earthquakes**

(a-b) Centroid locations of the Curtis volcanic tsunami earthquakes (red star) and tide-gauge stations (orange triangle). The earthquake information is from GCMT catalog (see Table 1.1).

similar non-double-couple earthquake in 2009 listed in the earthquake catalog by *Shuler et al.* [2013a] to find tsunami signals as well. Although some stations were deployed after the 2009 event, other stations obtained surprisingly similar tsunami records for the 2009 and 2017 earthquakes. These similarities of the Curtis earthquakes to the Torishima earthquakes strongly indicate the same physical mechanism for the two series of recurrent volcanic tsunami earthquakes.

The tsunami magnitude scale,  $M_t$ , was defined by *Abe* [1981] to quantitatively distinguish tsunami earthquakes from tsunamigenic ones. For tsunamis propagating in a regional ocean ( $100 \text{ km} < \Delta < 3500 \text{ km}$ ), the  $M_t$  is calculated as:

$$M_t = \log H + \log \Delta + 5.55, \quad \text{Eq. 1.1}$$

where  $H$  and  $\Delta$  are the maximum peak-to-peak tsunami amplitude of tide gauge records (in m) and epicentral distances (in km), respectively. The constant value of 5.55 was calibrated using the  $M_w$  values from tide-gauge tsunami data for three interplate earthquakes along Japan and the Kuril Trench by *Abe* [1981], who defined earthquakes with  $M_t$  greater than  $M_s$  by 0.5 as “tsunami earthquakes”. Here, tsunami magnitudes for the 2015 Torishima earthquake and the 2017 Curtis earthquake were calculated using Eq. 1.1 with tide-gauge records (Fig. 1.5). Tsunami magnitudes  $M_t$  were 7.5 for the 2015 Torishima earthquake ( $M_s$  5.7) and 7.8 for the 2017 Curtis earthquake ( $M_s$  6.2), far greater than their moment

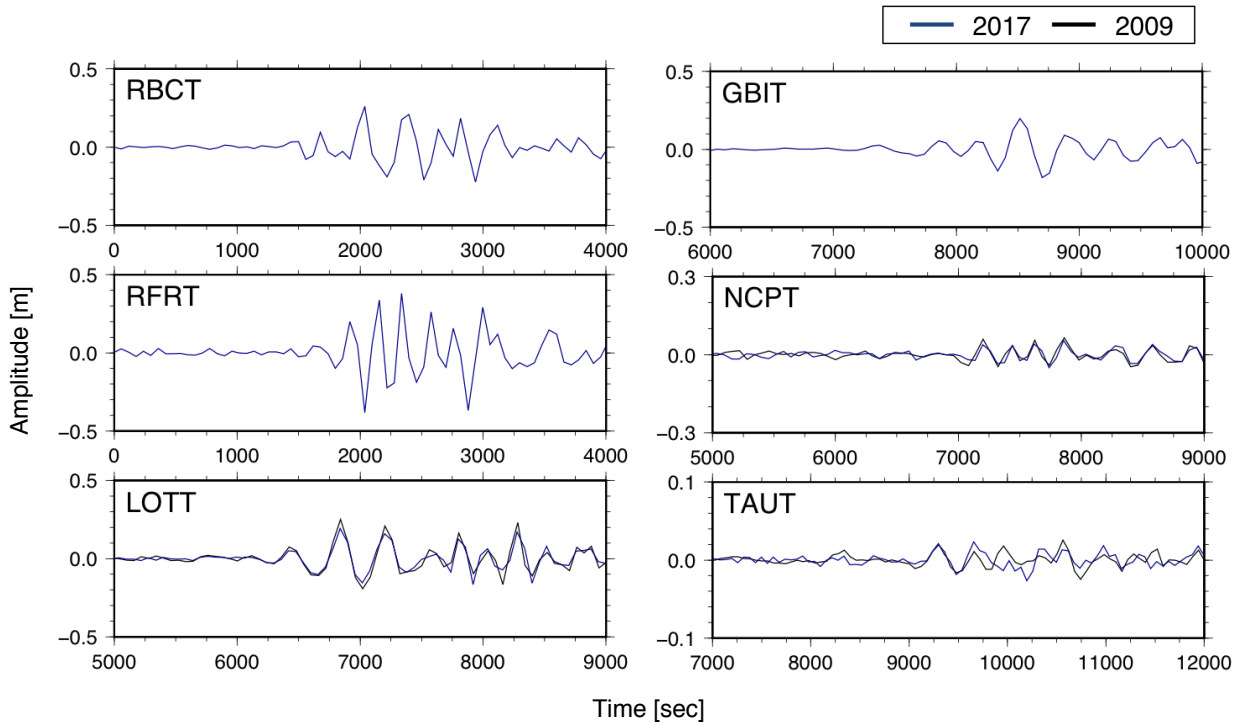


**Fig. 1.4 Tsunami records of the Curtis volcanic tsunami earthquakes at tide-gauge stations**

Blue and black line represent tsunami waveforms of the 2009 and 2017 Curtis earthquakes, respectively. Note that RBCT, RFRT and GBIT stations, which were deployed between the 2009 and 2017 events, did not record the tsunami from the 2009 event.

magnitudes by 1.8 and 1.6, respectively. Therefore, these earthquakes can be categorized as tsunami earthquakes, reflecting their abnormal source mechanism with high efficiency of tsunami excitation despite lower seismic wave energy radiation.

The gap between seismic and tsunami magnitudes makes it challenging to evaluate tsunami risks promptly on the basis of real-time seismological information. For example, following the 2015 Torishima earthquake, a tsunami advisory was announced by JMA about 49 min after the earthquake origin time, no earlier than the largest tsunami peak (60 cm) reached Yaene Port on Hachijojima Island, ~180 km away from the epicenter [*Japan Meteorological Agency, 2015 (report in Japanese)*]. For the Curtis earthquakes, no tsunami alert was issued. Fortunately, no damage to residents or property has been reported following these events, but such mispredictions of disproportional tsunamis shows the importance of evaluating their potential to cause tsunami disasters, and of making preparations for similar future events with a real-time forecasting system.

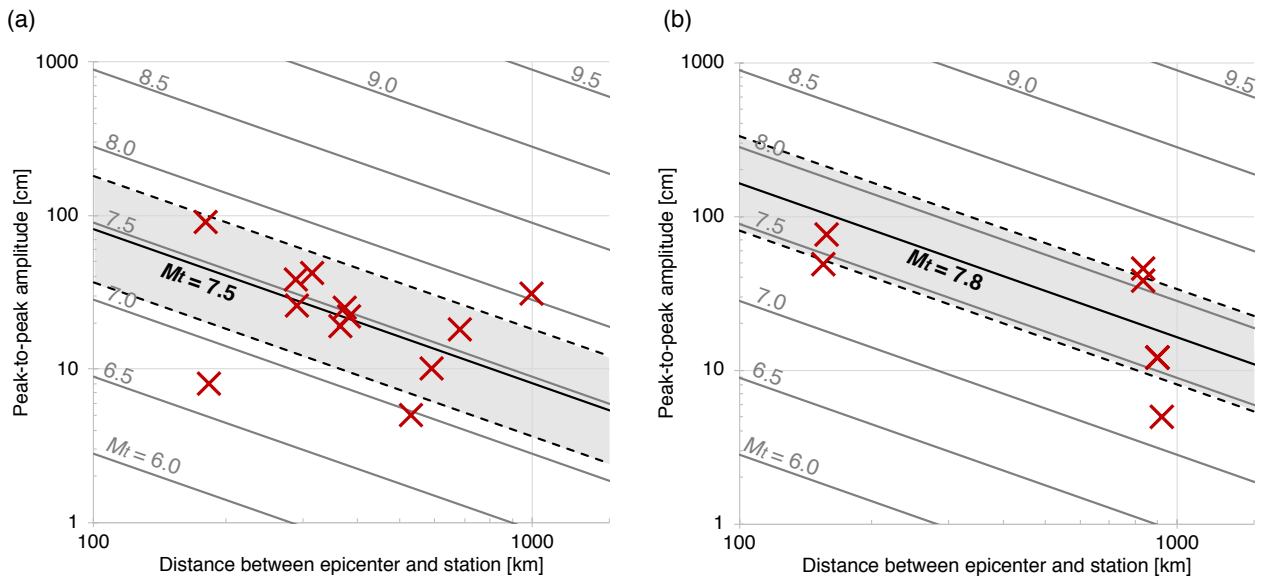


**Fig. 1.5 Amplitude-distance diagrams of the 2015 Torishima and the 2017 Curtis volcanic tsunami earthquakes**

Amplitude-distance diagram of tide-gauge tsunami records of (a) the 2015 Torishima earthquake and (b) the 2017 Curtis earthquake. Red crosses represent relations of maximum peak-to-peak tsunami amplitudes and epicentral distances of tide gauges. Gray lines represent the relations defined by Eq. 1.1 with tsunami magnitude values written on the left or top in the figures. Black line and gray area represent tsunami magnitude values  $M_t$  and standard deviations, respectively.

## 1.2 Previous studies

Since the 1984 Torishima earthquake was recognized as the first example of volcanic tsunami earthquakes, several seismological studies pursued the physical mechanism. *Kanamori et al.* [1993] pointed out that the Torishima earthquake had an azimuthally symmetrical radiation pattern of Rayleigh waves and absence of Love waves, which cannot be explained by a shear rupture model on planar faults. The authors suggested a physical mechanism of horizontal magma injection involving magma-water interaction driving hydrofracturing. On the other hand, *Ekström* [1994] suggested a different mechanism of slip on volcanic ring-fault structures, which explained the dominant vertical-CLVD mechanisms [*Frohlich*, 1989, 1990, 1994, 1995; *Julian et al.*, 1998] and partial cancellation of long-period seismic moment reducing seismic magnitudes [*Ekström*, 1994].

Seismologically, volcanic tsunami earthquakes are categorized as “vertical-CLVD earthquakes,” following the definition by *Shuler et al.* [2013a,b]. In their first paper [*Shuler et al.*, 2013a], they detected 101 vertical-CLVD earthquakes globally with magnitudes  $4.3 \leq M_w \leq 5.8$  at shallow depth around volcanic or geothermal regions from the GCMT catalog (1976–2009) and the Surface Wave catalog (1991–2009) [*Ekström*, 2006], including events found by *Nettles and Ekström* [1998] and *Shuler and Ekström*

[2009]. All the volcanic tsunami earthquakes during their target period of 1976–2009 (i.e., the Torishima earthquakes in 1984, 1996, and 2006, and the Curtis earthquake in 2009) were listed as vertical-CLVD earthquakes in the papers. Most of these detected earthquakes were associated with volcanoes having caldera structures and temporally linked to their volcanic unrest. In their companion paper [Shuler *et al.*, 2013b], they analyzed teleseismic body waves to demonstrate that source durations of vertical-CLVD earthquakes were longer than those of typical tectonic earthquakes with similar magnitudes, implying the peculiarity of their source mechanisms.

However, seismological consensus has not been reached for the physical mechanism of vertical-CLVD earthquakes. This is mainly because of the difficulties in moment tensor analysis for shallow earthquakes ( $< 10$  km). One difficulty comes from the well-known trade-off for long-period seismic displacement between the isotropic components and vertical-CLVD components of moment tensors [e.g. Kawakatsu *et al.*, 1996]. This makes it impossible to determine seismic contribution by source mechanism involving the volumetric changes often observed at active volcanoes [e.g. Kawakatsu and Yamamoto, 2007]. Other poorly-constrained factors in moment tensors for shallow earthquakes are the  $M_{xz}$  and  $M_{yz}$  elements, which are equivalent to pure-dip slip on a vertical or horizontal fault, since these elements at shallow depth do not excite long-period seismic waves [e.g. Kanamori and Given, 1981]. Moreover, the physical mechanism of earthquakes including dominant vertical-CLVD components seismologically allow wide varieties of interpretations [Shuler *et al.*, 2013b, and references therein], such as slip on ring faults [e.g. Ekström, 1994; Contreras-Arratia and Neuberg, 2019], volume exchange between two reservoirs [e.g. Chouet, 1996; Tkalcic *et al.*, 2009], the opening and closing of tensile cracks [e.g. Kanamori *et al.*, 1993; Konstantinou *et al.*, 2003; Riel *et al.*, 2015], and other types of volumetric changes. In addition to this disadvantage, due to their intermediate magnitudes ( $M_w < 6$ ) and source locations far from major seismic networks, most studies described the earthquake sources as a point source without a finite-sized geometry. This, along with the lack of information on the spatial source extension, has made it difficult to constrain the physical mechanism, including a specific scenario for a concrete geometry of vertical-CLVD earthquakes, which has been the same for volcanic tsunami earthquakes.

In order to compensate for these defects in seismic analysis, tsunami records can be utilized to investigate the mechanism of volcanic tsunami earthquakes with shallow source geometries, because tsunamis convey spatial and temporal information related to seafloor deformation that sensitively reflects earthquake kinematics at shallow depth [e.g., Satake *et al.* 2013, Ho *et al.* 2017]. Several previous studies analyzed tsunami records to examine the source for the 1984 Torishima earthquake [Satake and Kanamori, 1991; Hatori, 1985], and roughly estimated that the tsunami originated near Smith Caldera. However, it was technically difficult to obtain detailed distributions of seafloor deformation from tsunami records at that time for the following reasons: (1) tsunamis were recorded only at tide-gauge stations that were affected strongly by nearshore effects, (2) tsunami models based on the long-wave theory without the dispersion were used, and (3) only rough bathymetry/topography data were available for numerical simulations. Recently, however, clear progress have been made in the tsunami research field by the

widespread deployment of tsunami observation networks in deep oceans (e.g., DONET, DART), the development of tsunami simulation codes using dispersive tsunami models [e.g. *Saito et al.*, 2010; *Watada et al.*, 2014], and finer bathymetry/topography data collected in oceanic and coastal regions. With these advancements, tsunami analysis has become a more powerful tool to examine the physical mechanism of volcanic tsunami earthquakes.

### 1.3 Purpose and strategy

The unknown mechanism of volcanic tsunami earthquakes presents several geoscientific issues: (1) How and why do  $M_w$  5–6 earthquakes repeat at submarine volcanoes with moment tensors significantly different from those of typical tectonic earthquakes? (2) How are large tsunamis generated by intermediate-magnitude earthquakes and propagated over broad oceanic regions? (3) What kind of volcanic activities repeat at submarine volcanoes? Determining the physical mechanism of volcanic tsunami earthquakes will provide new insights in geoscience fields including seismology, oceanography, and volcanology. In addition, understanding this mechanism is important for developing a forecasting technique for such abnormal tsunamis.

To address the above questions, I set the goal of this study as determining the physical mechanism of volcanic tsunami earthquakes. To understand the mechanism with specific source geometries, I used a kinematic source modeling approach to explain both tsunami and long-period seismic wave records in a quantitative manner. I first estimated the spatial distribution of seafloor deformation excited by volcanic tsunami earthquakes from tsunami records, providing context for their source geometry and kinematics. Second, I assumed possible source geometries to invert tsunami records for slip distributions, or kinematic source models, from tsunami records. Third, I synthesized long-period seismic waves of the source models to evaluate their validity with respect to the seismic records. Finally, I obtained kinematic source models of volcanic tsunami earthquakes quantitatively explaining both tsunami and long-period seismic wave records. These models allowed further discussion of the physical mechanism of volcanic tsunami earthquakes.

In this thesis, I focused on two recent volcanic tsunami earthquake events in different regions, the 2015 Torishima and 2017 Curtis earthquakes. In Chapter 2, a tsunami source model of the 2015 Torishima earthquake with an axially symmetric shape is constructed by analyzing tsunami records at the array of stations equipped with ocean-bottom pressure (OBP) gauges near the epicenter; this includes collaborative work with a research group led by Dr. Y. Fukao. In Chapter 3, a kinematic source of the 2015 Torishima earthquake is modeled using abundant tsunami and seismic records. In Chapter 4, I apply a similar approach to the 2017 Curtis earthquake. In Chapter 5, I propose a physical mechanism for volcanic tsunami earthquakes based on the kinematic source models and discuss their characteristics in terms of seismic excitation. The similarity and diversity of recurrent volcanic tsunami earthquakes are also

discussed through moment tensor analyses. After stating future directions for related studies, I present concluding remarks with a summary of major findings.

# ***Chapter 2 Tsunami source modeling of the 2015 Torishima earthquake using array of stations equipped with ocean-bottom pressure gauges***

*Contents in this chapter consist, in part, of collaborative work with Y. Fukao, H. Sugioka, A. Ito, H. Shiobara, S. Watada, and K. Satake, which was published as:*

- *Fukao, Y., Sandanbata, O., Sugioka, H., Ito, A., Shiobara, H., Watada, S., and Satake, K. (2018). Mechanism of the 2015 volcanic tsunami earthquake near Torishima, Japan. Science Advances,4(4), eaao0219.*

*Here, I describe my contribution to this work as part of my thesis, while the paper above is referred to as Fukao et al. [2018] when I mention work mainly done by collaborators.*

In this chapter, I estimate the initial sea-surface displacement, or the tsunami source, of the 2015 Torishima volcanic tsunami earthquake with high-quality tsunami records at array stations of ocean-bottom-pressure (OBP) gauges. In Chapter 2.1, I first summarize waveform analysis results from *Fukao et al. [2018]*, which were used for the analyses in the following sections. In Chapters 2.2–2.3, the tsunami source is investigated using a ray-tracing method for dispersive tsunamis and numerical simulations of tsunami waveforms. In Chapter 2.4, I suggest associations between volcanic tsunami earthquakes and sub-caldera structures such as horizontal cracks and ring faults.

## 2.1 Tsunami data at array of stations equipped with ocean-bottom pressure gauges

Tsunamis from the 2015 Torishima volcanic tsunami earthquake were recorded by a temporary array of ten stations equipped with OBP gauges. These stations were deployed on the seafloor at depths of 1470–2240 m east of Aogashima Island, ~100 km from the epicenter of the 2015 event (Fig. 2.1, Table 2.1) [Fukao *et al.*, 2018]. The ten OBP stations formed equilateral triangles with station intervals of 10 km and recorded clear tsunami signals reaching a maximum amplitude of ~2 cm with a high sampling frequency of 4 Hz (Fig. 2.1c).

The tsunami records gathered by the OBP stations were appropriate for tsunami source explorations. The observational conditions in the deep ocean, relatively near the epicenter, enabled us to acquire direct information from the tsunami source without nearshore effects or much interference by reflected waves. The densely distributed stations also made it possible to investigate detailed characteristics of tsunami sources by measuring propagation directions through the array and extracting unclear features by stacking the waveforms. In this section, I summarize the waveform analysis done by Fukao *et al.* [2018].

**Table 2.1 Information of stations of the array off Aogashima Island**

The column indicates, from left to right, station code, station location in latitude and longitude, water depth, location in the (X, Y) coordinates (eastward and northward from the A05 location, respectively).

	Lat.	Lon.	Depth	X	Y
	32N	140E			
	min				
A01	14.9603	21.0968	1756.7	0.300390	-17.203705
A02	19.5473	17.9161	1776.8	-5.064311	-8.717755
A03	19.5666	24.1255	2183.5	5.408723	-8.682050
A04	24.2925	14.7472	1687.0	-10.409111	0.060865
A05	24.2596	20.9187	1761.9	0	0
A06	24.2789	27.3866	1981.1	10.909031	0.035705
A07	29.0177	11.4314	1470.8	-16.001678	8.802485
A08	29.0138	17.8974	1800.9	-5.095851	8.795270
A09	29.1479	24.1770	1969.1	5.495585	9.043355
A10	29.0288	30.5480	2214.1	16.241181	8.823020

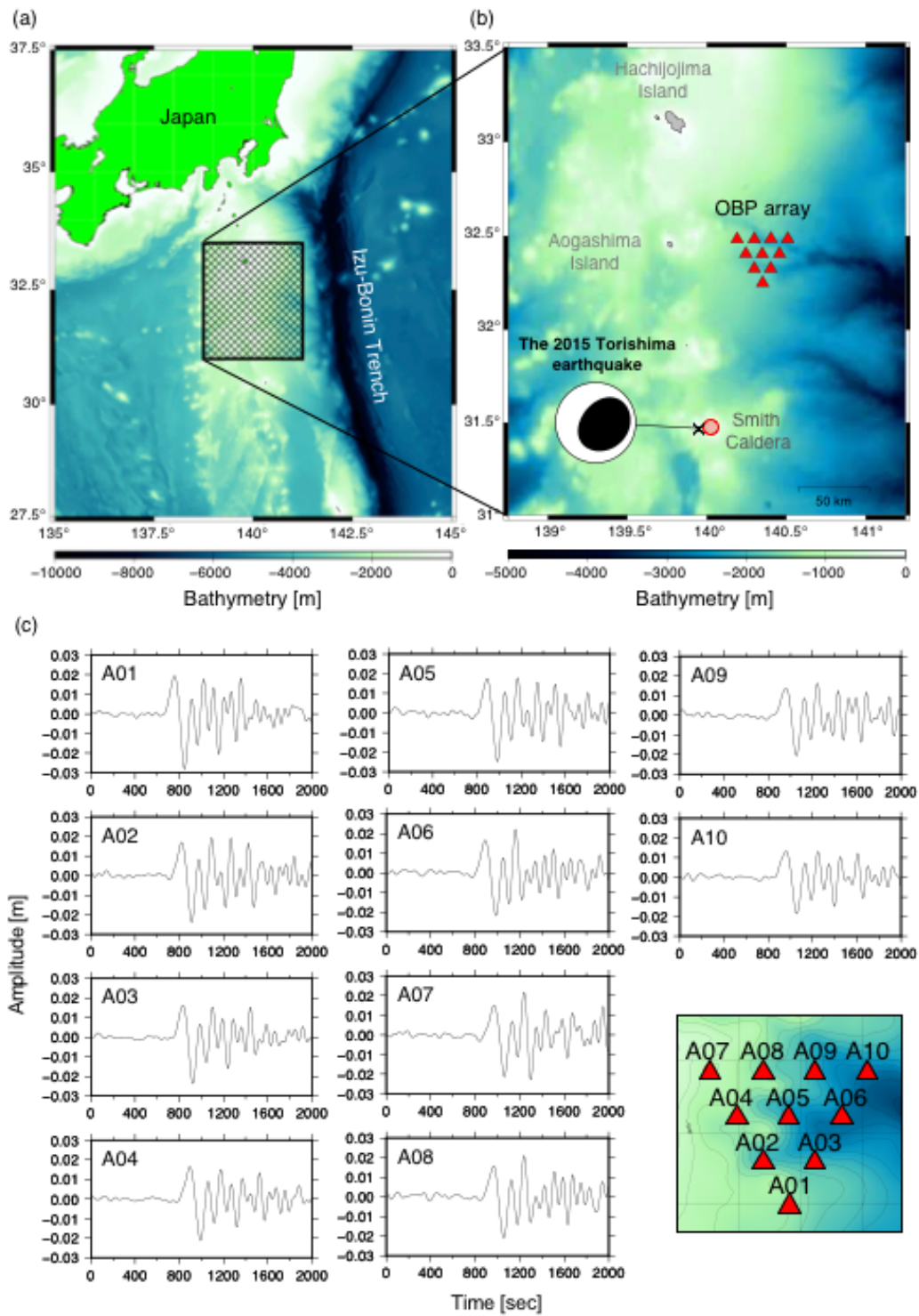


**Fig. 2.1** Tsunami observations at the array of Aogashima Island

(a-b) Red triangles represent station locations of the array off Aogashima Island. The centroid location of the 2015 Torishima earthquake reported by GCMT is indicated by black cross with the focal mechanism. Red circle represents an approximate location of Smith Caldera. (c) Observed tsunami records at the array distributed as the right-bottom figure shows.

## 2.1.1 Phase analysis

*Fukao et al.* [2018] conducted phase analysis to obtain the frequency dependency of tsunami propagations at the array. First, after applying narrow band-pass-filters with different central frequencies, they read a peak travel time of an upswing crest on each narrowly band-pass-filtered wave trains. They then used the phase travel time data from the 10 stations to determine phase slowness vectors at each frequency of tsunami propagation through the array under the plane-wave approximation.

The phase analysis revealed that the tsunamis propagated differently for each frequency. Figure 2.2 shows the frequency dependency of the travel time at station A05 and the slowness direction. The travel time was clearly delayed at higher frequencies due to the dispersive property of tsunami waves (Fig. 2.2a). On the other hand, the slowness direction deviated more from the direction of the great circle connecting the epicenter and station A05 ( $\sim 80^\circ$  measured counter-clockwise from east) at lower frequencies (Fig. 2.2b). These variations in slowness directions were attributed to the stronger dispersion effect in deeper water regions close to the Izu–Bonin trench by *Sandanbata et al.* [2018], who applied a ray-tracing method to consider such dispersive effects.

## 2.1.2 Zero-cross time and weak downswing motion preceding major upswing

*Fukao et al.* [2018] also measured a zero-cross time preceding the maximum upswing peak at each OBP station, which can be considered to have originated from the approximate edge of the uplifted sea-surface area. At each station, a major upswing motion was confirmed to transition from a weak downswing at the zero-cross time, regardless of the use of causal or acausal filters. They shifted tsunami traces from the 10 stations along the time axis so that their major upswings started at a common zero-cross

**Table 2.2 Array analysis of phase and onset arrivals [*Fukao et al.*, 2018]**

Sx, Sy: x- and y-components of slowness vector,  $T_0$ : Travel time to reference station, S: Absolute slowness value,  $\psi$ : Propagation direction measured counterclockwise from the x-axis. Quantities preceded by “d” refer to uncertainties associated with measurements. Onset is equivalent to the zero-cross signal (see the text).

		Phase									Onset
		01–03 mHz	02–04 mHz	03–05 mHz	04–06 mHz	05–07 mHz	06–08 mHz	07–09 mHz	08–10 mHz	09–11 mHz	
Sx	s/km	-0.316	-0.222	-0.184	-0.266	-0.115	-0.016	-0.016	0.010	0.077	-0.193
dSx	s/km	0.170	0.132	0.160	0.166	0.185	0.159	0.107	0.126	0.195	0.312
Sy	s/km	8.034	7.732	7.824	7.974	7.929	8.021	8.295	8.456	8.628	7.463
dSy	s/km	0.181	0.140	0.170	0.176	0.197	0.168	0.113	0.134	0.207	0.331
To	s	840.1	858.1	874.2	879.6	883.7	896.2	913.3	930.1	951.1	801.5
dTo	s	5.0	3.9	4.7	4.9	5.4	4.6	3.1	3.7	5.7	9.1
S	s/km	8.046	7.735	7.827	7.978	7.930	8.021	8.295	8.456	8.629	7.465
dS	s/km	0.187	0.143	0.173	0.181	0.199	0.169	0.113	0.134	0.209	0.339
$\psi$	degree	92.25	91.64	91.35	91.91	90.83	90.11	90.11	89.93	89.49	91.48
d $\psi$	degree	1.26	1.00	1.20	1.23	1.36	1.13	0.74	0.86	1.31	2.46

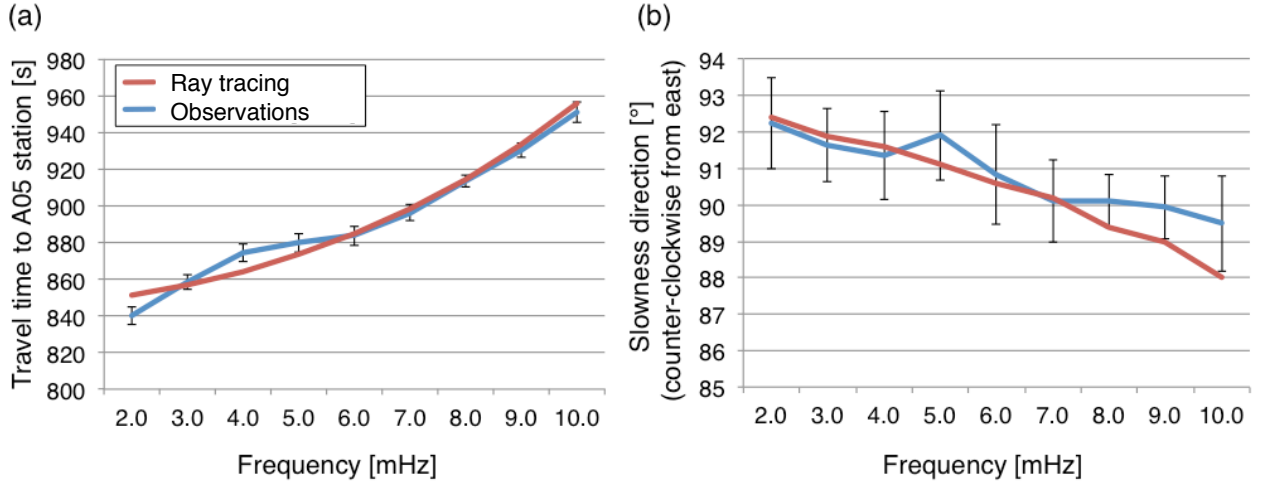


**Fig. 2.2 Frequency dependency of travel times and slowness directions**

Comparison of (a) travel times at A05 station and (b) slowness directions between the phase analysis of observed tsunami records by *Fukao et al.* [2018] (blue) and the ray tracing method by *Sandanbata et al.* [2018] (red). A05 station of the array is located in the great circle direction of around  $80^\circ$  measured counter-clockwise from the east.

time, then calculated the averaged trace of waveforms with their standard deviations, confirming the presence of weak precursory downswing signals (Fig. 2.3). Such a precursory first motion with reversed polarity is often observed for trans-oceanic tsunamis due to dispersion of tsunamis gravitationally and elastically coupled with the Earth at long periods [e.g. *Watada et al.*, 2014]. However, the travel distance to the array was too short to cause such dispersion. Therefore, this small precursory downswing signal was attributed to the tsunami source, suggesting that it contained smaller peripheral subsidence around a larger uplifted area. The slowness directions of the zero-cross signals was also measured in the same way as the phase analysis, assuming the long-wave speed (Table 2.2).

## 2.2 Estimation of tsunami source location using ray-tracing method for dispersive tsunamis

### 2.2.1 Methods

I first estimated an approximate peak location of the tsunami source of the 2015 Torishima earthquake, by comparing theoretical travel times and slowness direction at the array with the measured values by *Fukao et al.* [2018]. Assuming that the picked phase peaks at every frequency originated instantaneously from the peak point of uplifted sea surface, I searched the optimal point source explaining the measured travel times and slowness direction.

Theoretical travel times and slowness directions at the array were predicted by the ray-tracing method for dispersive tsunamis [*Sandanbata et al.*, 2018]. First, phase speeds of tsunamis at different

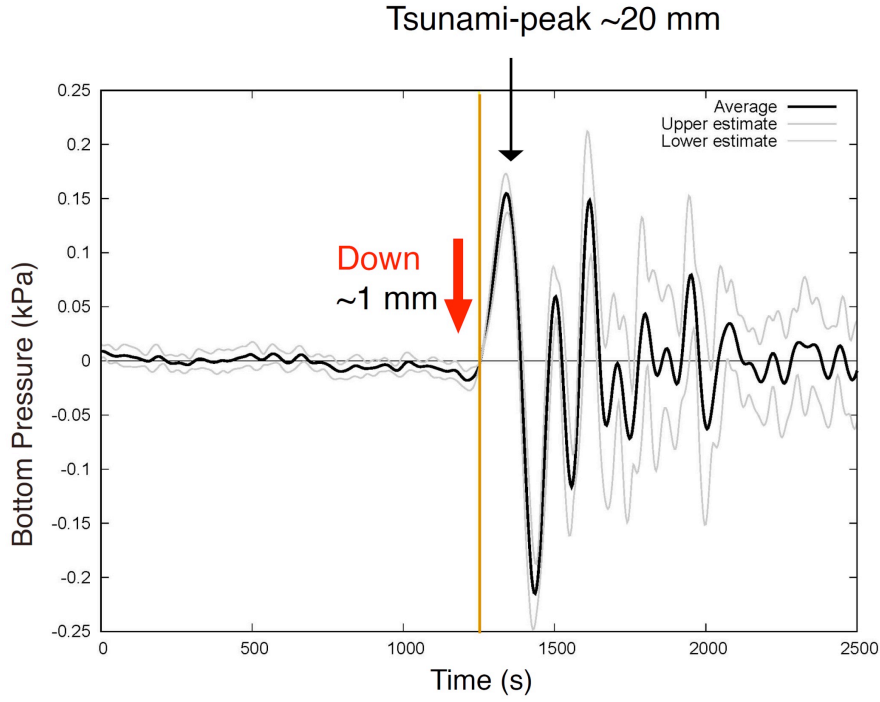


**Fig. 2.3 Average trace of 10 tsunami records mutually time-shifted to a common zero-cross time [Fukao et al., 2018]**

The dotted lines indicate the standard deviation of these time-shifted records. This figure emphasizes the weak downswing prior to the major upswing of the tsunami motion. Orange line represents a common zero-cross time.

frequencies are transformed from water depth data in the computation region by an iterative algorithm using the dispersion relation of tsunami as follows;

$$C = \frac{\omega}{k} = \frac{2\pi f}{k} = \sqrt{\frac{g}{k} \tanh kD} = \sqrt{\frac{g\lambda}{2\pi} \tanh \frac{2\pi D}{\lambda}}, \quad \text{Eq. 2.1}$$

where  $\omega$ ,  $f$ , and  $D$  represent the angular frequency, frequency, and water depth, respectively, and  $k$ ,  $\lambda$ , and  $g$  are the wavenumber, wavelength, and gravitational acceleration, respectively [e.g. Lamb, 1932; Dingemans, 1997]. Then, ray paths at each frequency were computed from an assumed point source by solving the ray equations:

$$\frac{d\theta}{ds} = \frac{1}{R} \cos \zeta, \quad \text{Eq. 2.2}$$

$$\frac{d\phi}{ds} = \frac{1 \sin \zeta}{R \sin \theta} \quad \text{Eq. 2.3}$$

where  $\theta$  and  $\phi$  are the colatitude and longitude of the ray at each time step, respectively,  $R$  is the radius of the Earth (6,371 km),  $\zeta$  is the ray direction measured counter-clockwise from south, and  $ds$  represents

the line element of the ray, calculated by  $ds = C \cdot dt$  where  $dt$  is set as 1.0 s. From an assumed point source, multiple ray paths were traced toward the array with an azimuthal interval of  $0.1^\circ$ , and travel times were recorded for the closest points on the ray paths at each station. To determine the slowness direction at the array, I followed the plane-wave approximation method employed by *Fukao et al.* [2018]. Finally, I obtained theoretical travel times at station A05 and slowness directions at each frequency from the assumed point source.

In order to examine the optimal source location explaining the values measured by *Fukao et al.* [2018] (Table 2.2), a point source location was shifted on grids around Smith Caldera. The misfit function was defined at each grid point of the tsunami source as:

$$M = \sum_{n=2}^{10} \left[ \left( \frac{T_{ray}^{(n)} - T_o^{(n)}}{dT_o^{(n)}} \right)^2 + \left( \frac{\psi_{ray}^{(n)} - \psi_o^{(n)}}{d\psi_o^{(n)}} \right)^2 \right], \quad \text{Eq. 2.4}$$

where  $T_{ray}$  and  $\psi_{ray}$  are the phase travel time and the slowness direction estimated by the ray-tracing analysis, respectively,  $T_o$  and  $\psi_o$  are the values measured by the phase analysis, with their standard deviations of  $dT_o$  and  $d\psi_o$ , respectively, and  $n$  indicates the frequency in mHz at which the values were measured ( $n = 1, 2, \dots, 10$ ). Grid intervals were  $0.005^\circ$ .

I also investigated an approximate edge of the uplifted source area by back-projecting the zero-cross signals from station A05 with its measured travel time and slowness direction (Table 2.2). The speed of the zero-cross signal was assumed as the long-wave speed, or  $C = \sqrt{gD}$ .

## 2.2.2 Results

The spatial distribution of the misfit function around Smith Caldera is shown in Fig. 2.4b, which marks small values within the topographic depression of the caldera. The optimal point-source location minimizing the misfit value (indicated by ‘‘C’’ in Fig. 2.4a-b) explained the travel times and slowness directions measured from the tsunami records at the array at the analyzed frequency range (Fig. 2.4c-d). If the point source is shifted by  $\sim 5$  km in any direction, either the theoretical travel time or slowness direction deviated from the measured values beyond their error bars (Fig. 2.4c-d), supporting the conclusion that the source location was within the caldera structure. Moreover, earthquake locations reported by the USGS, GCMT, and JMA were more broadly scattered than the shifted tsunami sources, indicating that the tsunami-record analysis constrained the source location more accurately than the earthquake location technique using seismic records from regional or far-field stations. It may be challenging to constrain a source location within a small area when only using limited observations from one azimuthal direction. However, travel times that sensitively change with the distance from source to station were constrained along a NNE-SSW direction, while slowness directions sensitive to their azimuth yielded a constraint along the NW-SE direction. In this analysis, these two parameters along different directions yielded a good constraint for controlling the source location.

The back-projected zero-cross signal, which approximately corresponded to the edge of the uplifted sea-surface area, was located on the northern structural boundary of the caldera rim (Fig. 2.4b). This implied that the earthquake caused large uplift that was focused within the caldera structure, rather than deformation of the entire volcanic rise containing the caldera at its crest. However, the assumption that the zero-cross signal traveled at the long-wave speed may contain some uncertainty, because the

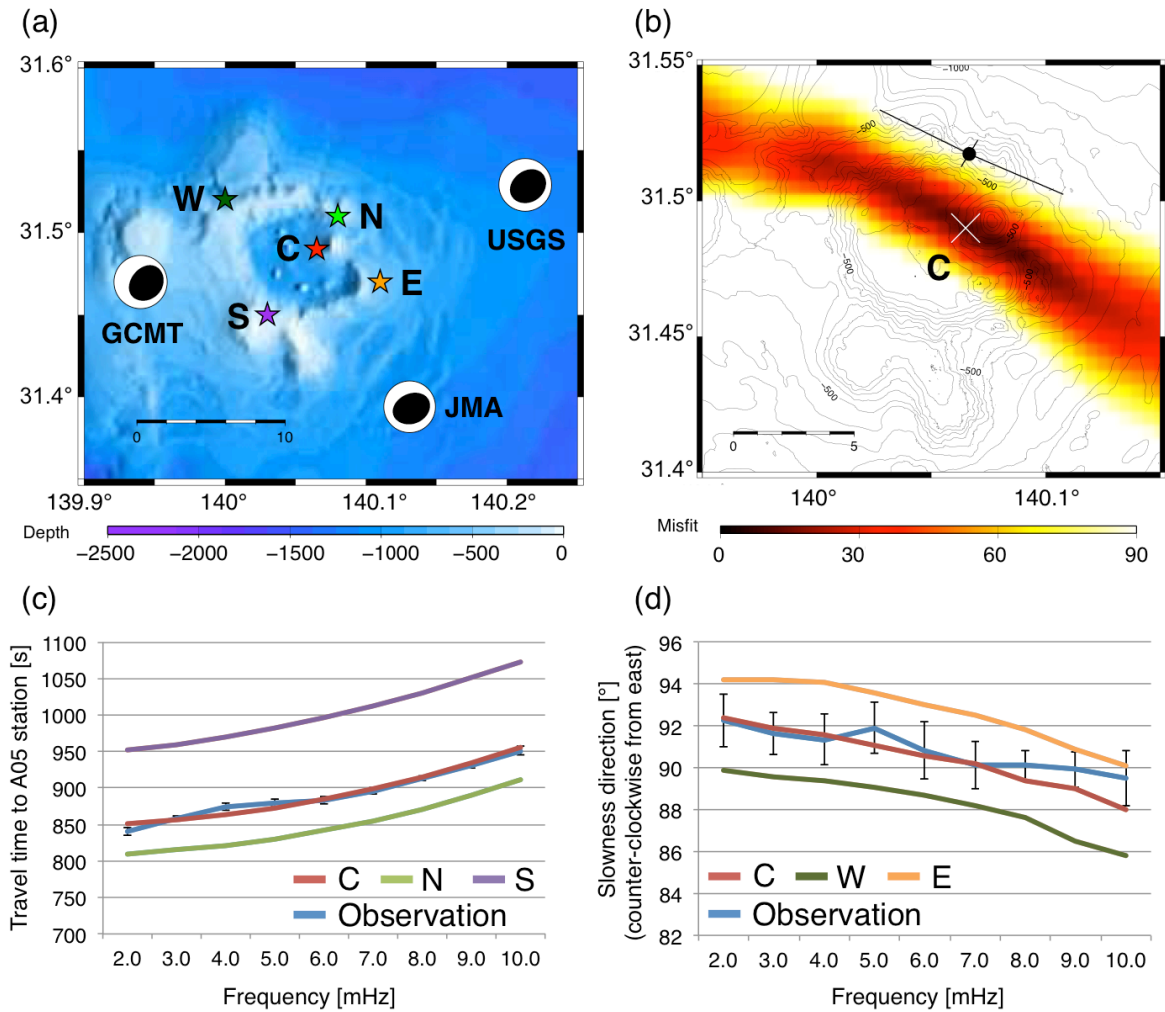


**Fig. 2.4 Estimate of tsunami source location**

(a) Five test tsunami source locations. One is within the caldera and four along the rim. The CMT diagrams obtained by GCMT, USGS, and JMA are shown at their source locations estimated seismologically. (b) Spatial distribution of the misfit of the calculated phase travel time and propagating direction to the observed values as a function of the assigned source location. The minimum misfit shown by a white cross is located within the caldera. The small circle with a cross indicates the estimated location of back-projected zero-cross signals with its uncertainty. (c) Test result showing the sensitivity of tsunami travel time at A05 station to the shift of source location from N to S through C. Blue line with error bars shows the observed travel times. (d) Test result showing the sensitivity of tsunami propagating direction to the shift of source location from E to W through C. Black line with error bars shows the observed propagating directions.

dispersion effect also changes its speed and waveform. For more robust estimations, tsunami waveform simulations including the dispersion effect will be presented in the following section.

## 2.3 Tsunami source modeling with axially symmetric shape

### 2.3.1 Methods

To obtain a tsunami source model, I next conducted numerical simulations of dispersive tsunamis and compared them with the observed waveforms at the array. Because of the limited station coverage (only NNE from the epicenter, Fig. 2.1b), I simply considered an axially symmetric source shape. On the basis of the uplifted source located by the ray-tracing analysis (Fig. 2.4) and the weak downswing motion preceding major upswing observed at the array (Fig. 2.3), I assumed a tsunami source composed of a main central uplift surrounded by a small peripheral subsidence with a symmetric axis pointing at the center of Smith Caldera, expressed as:

$$\eta(r) = A \left[ \exp \left\{ - \left( \frac{2r/R}{1.27} \right)^2 \right\} - 0.113 \exp \left\{ - \left( \frac{2(r - 1.27)/R}{1.0} \right)^2 \right\} \right], \quad \text{Eq. 2.5}$$

where  $r$  is the distance in kilometers from the center of the caldera (Fig. 2.5a). This model has a main central uplift of  $A$  (m) surrounded by a minor depression of  $A/10$  (m), the radius of the uplift being  $R$  (km). I varied  $A$  in a range from 0.5–5.5 m at 0.1 m intervals and  $R$  in a range from 0.5–5.5 km at 0.1 km intervals. I computed tsunami propagations from different source models with a combination of the two variable parameters using the JAGURS code [Baba *et al.*, 2015] by solving the standard Boussinesq equations [e.g. Peregrine, 1972] in the following linear formulations:

$$\frac{\partial M}{\partial t} = - \frac{gD}{R_E \sin \theta} \frac{\partial \eta}{\partial \phi} + \frac{D^2}{3R \sin \theta} \frac{\partial}{\partial \phi} \left[ \frac{1}{R \sin \theta} \left( \frac{\partial^2 M}{\partial \phi \partial t} + \frac{\partial^2 (N \sin \theta)}{\partial \theta \partial t} \right) \right], \quad \text{Eq. 2.6}$$

$$\frac{\partial N}{\partial t} = - \frac{gD}{R_E \sin \theta} \frac{\partial \eta}{\partial \theta} + \frac{D^2}{3R \partial \theta} \left[ \frac{1}{R \sin \theta} \left( \frac{\partial^2 M}{\partial \phi \partial t} + \frac{\partial^2 (N \sin \theta)}{\partial \theta \partial t} \right) \right], \quad \text{Eq. 2.7}$$

$$\frac{\partial \eta}{\partial t} = - \frac{1}{R_E \sin \theta} \left( \frac{\partial M}{\partial \phi} + \frac{\partial (N \sin \theta)}{\partial \theta} \right), \quad \text{Eq. 2.8}$$

where  $\eta$  is the wave height,  $D$  is the water depth,  $R_E$  is the radius of the Earth, and  $M$  and  $N$  are the depth-integrated flow along colatitude  $\theta$  and longitude  $\phi$ , respectively. The computational time-step interval is 0.25 s to satisfy the CFL condition. The tsunami source was assumed to be uplifted or subsided instantaneously. The complex bathymetry near Smith Caldera was incorporated by preparing bathymetry data with a grid size of 10 arcsec ( $\sim 250$  m) near Smith Caldera using the M7000 series, while bathymetry data with a 30 arcsec grid ( $\sim 750$  m) from JTOPO30 were used in the other region. Both of the original datasets were provided by the Marine Information Research Center (MIRC), Japan Hydrographic Association (JHA).

To determine the optimum parameter set of  $A$  and  $R$  that minimized the misfit function between the observed and synthetic waveforms at the array, I defined the normalized root-mean-square misfit for the  $k$ th station as:

$$\eta NRMS_k = \frac{\sqrt{\sum_{i=1}^N (obs_i - sim_i)^2}}{\sqrt{\sum_{i=1}^N (obs_i - \overline{obs_i})^2}} \quad \text{Eq. 2.9}$$

where  $i$  refers to the sampling time step,  $N$  is the sampling number at each station,  $obs_i$  and  $sim_i$  are the observed and synthetic waveform data, respectively, and  $\overline{obs_i}$  is the average of the observed record over

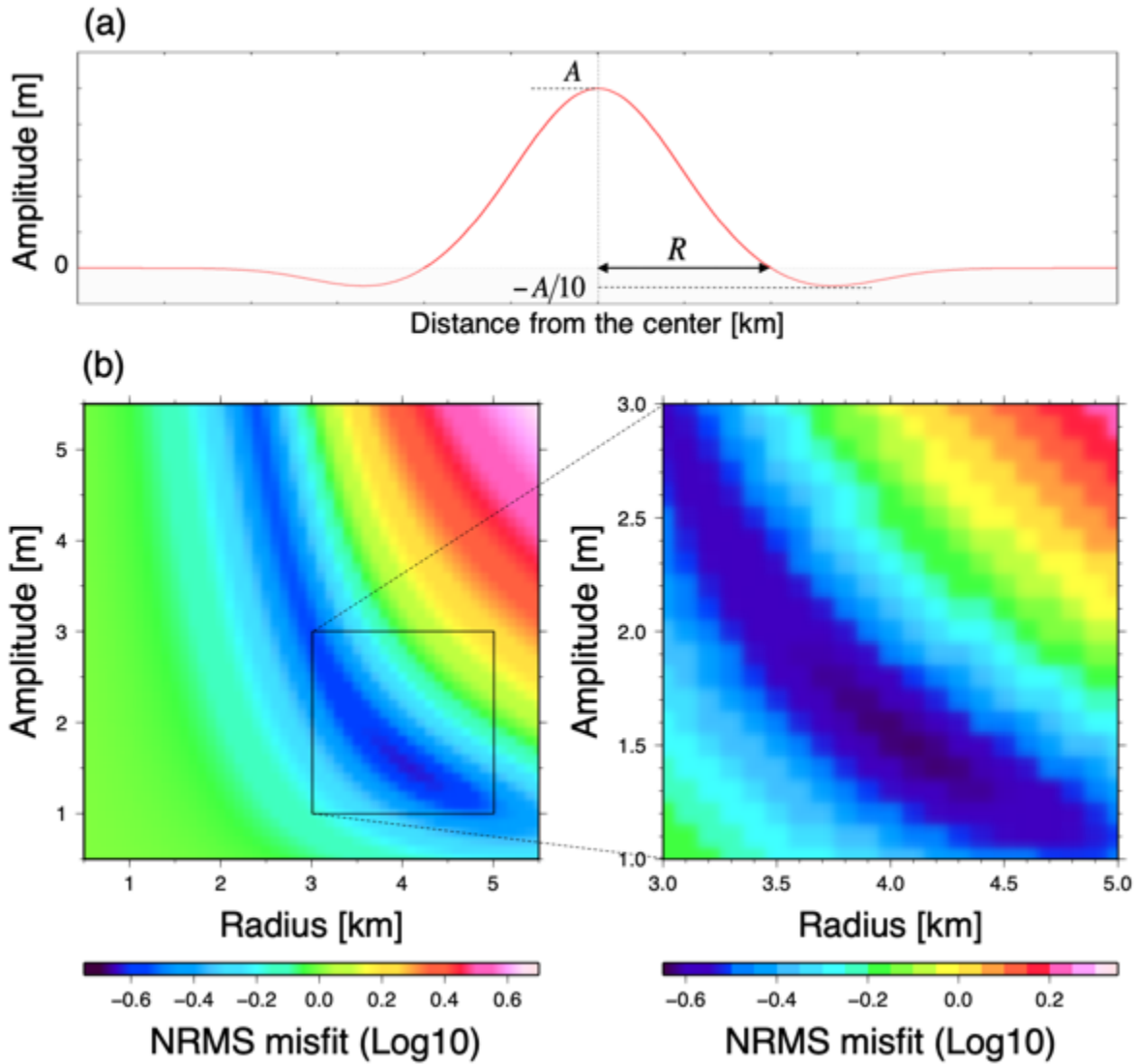


**Fig. 2.5 Search for the best initial sea-surface displacement**

(a) Profile of the axially symmetric initial sea-surface displacement. Amplitude  $A$  and radius  $R$  are the parameters for which the grid search is made. (b) Distribution of the NRMS misfit values in the  $A$ - $R$  domain.

the time window at each station. The final NRMS misfit value was an average of the misfits over the stations:

$$NRMS\ misfit = \frac{\sum_{k=1}^M NRMS_k}{M}, \quad \text{Eq. 2.10}$$

where  $M$  is the number of stations (10). I set time windows including the precursory downswing signal and the first and second major crests and troughs (blue line in Fig. 2.6a).

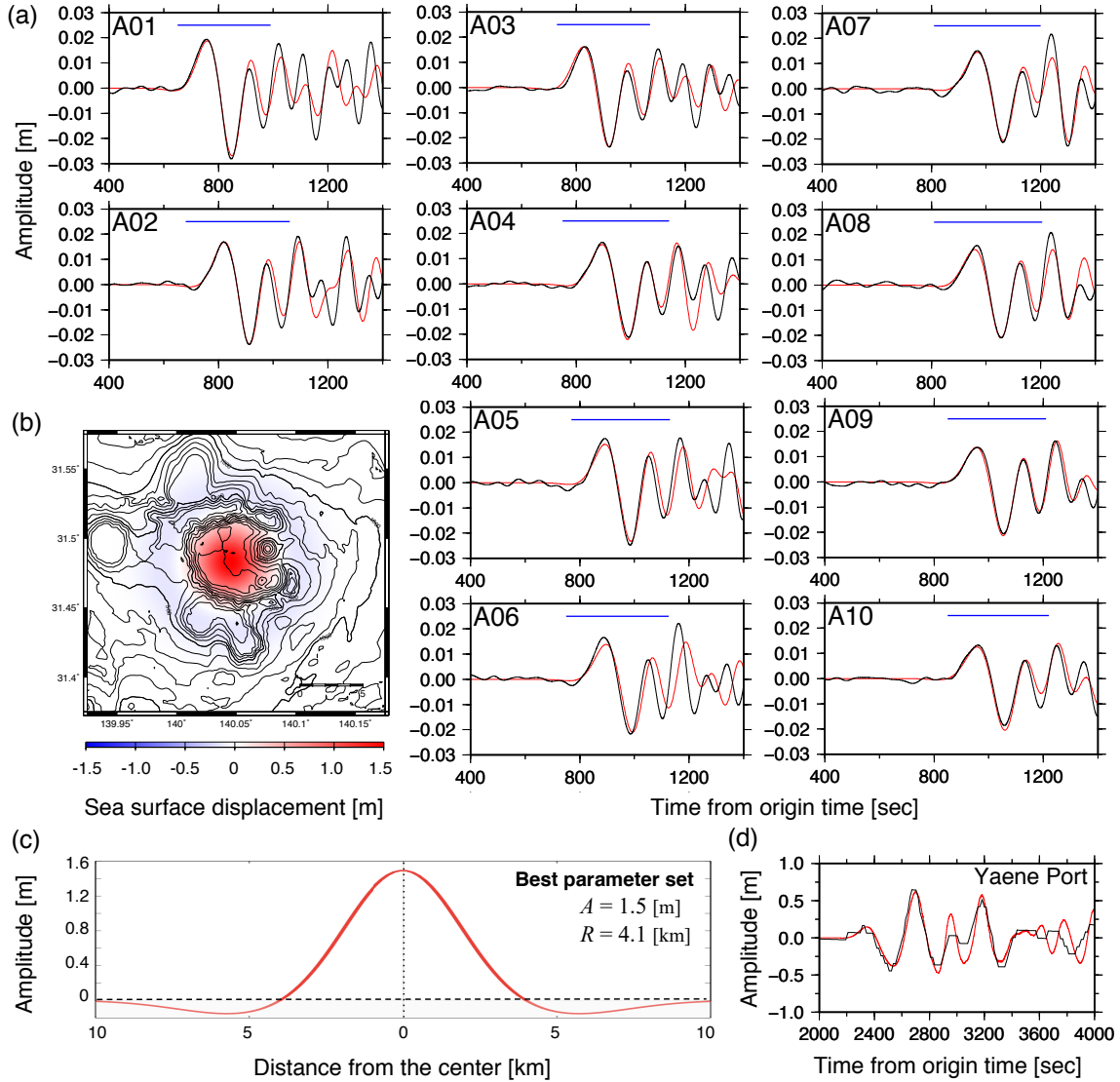


**Fig. 2.6 Best initial sea-surface displacement model and waveform comparison at the array**

(a) Observed (black) and simulated (red) waveforms at the array (see Fig. 2.1b-c for locations). The blue horizontal line represents the time window to calculate the normalized root mean square (NRMS) misfit at each station. (b) The sea-surface displacement for a model of  $A = 1.5$  m and  $R = 4.1$  km. Contour lines represent the bathymetry near Smith Caldera. (c) The cross-sectional profile of the initial sea-surface displacement. (d) Observed (black) and synthetic (red) waveforms at Yaene Port on Hachijojima Island (see Fig. 2.7).

## 2.3.2 Results

The calculated NRMS misfit value is plotted as a function of  $A$  and  $R$  in Fig. 2.5b. The misfit was small when the amplitude  $A$  was 1.3–1.8 m and the radius  $R$  was 3.7–4.3 km with the minimum value at  $A=1.5$  m and  $R=4.1$  km, corresponding to the source model shown in Fig. 2.6b-c. The uplifted area was comparable to the topographic structure of Smith Caldera with a diameter of  $\sim 8$  km (Fig. 2.6b) and the peripheral subsidence extended almost all the way along the circular rim. The estimated axially symmetric source with the optimal parameter set reasonably explained the tsunami waves, including later phases at all the OBP stations, despite the simple assumptions used here (Fig. 2.6a).

Based on the estimated source, I computed synthetic waveforms at a tide-gauge station inside Yaene Port on Hachijojima Island, where the maximum tsunami height of 60 cm was recorded (Yaene in Fig. 1.2). This height was in marked contrast to the tsunami height of  $\sim 2$  cm observed at the OBP stations  $\sim 100$  km NNE of the epicenter. If the estimated tsunami source model derived from the open-sea OBP observations is reasonable, it should be able explain the observation in the port as well. To calculate the waveform at the tide-gauge station in the bay, I prepared nested bathymetry grid data to accurately include the effect of the port shape (Fig. 2.7), and set the finest grid near the port at 0.2 arcsec, or  $\sim 5$  m, as digitized from an physical chart of Yaene Port. Because the nonlinear effects on tsunami waves are non-negligible in shallow-water coastal regions, nonlinear terms were incorporated for computations near the port (bathy04 and 05 in Fig. 2.7b). The simulated waveform also accurately reproduced the tide-gauge record

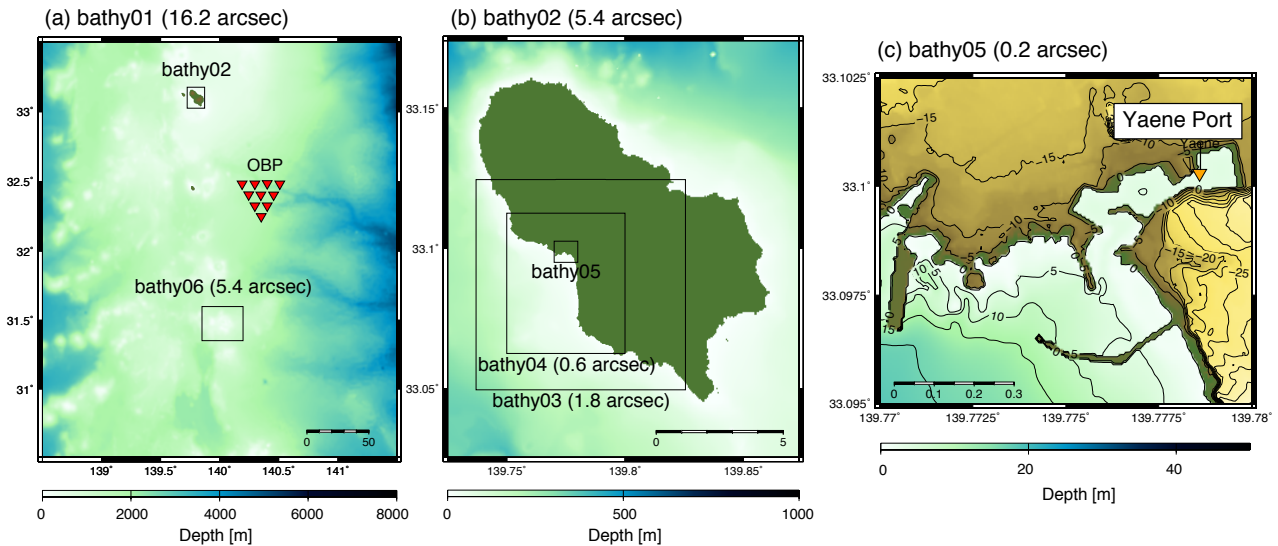


**Fig. 2.7 Bathymetry for waveform simulation at Yaene Port on Hachijojima Island**

(a) Bathymetry map showing Smith Caldera (bathy06), OBP stations (red triangles) and Hachijojima Island (bathy02). (b) The bathymetry near Hachijojima Island. (c) Topography and bathymetry near Yaene Port at Hachijojima Island. Yellow triangle represents the location of a tide gauge station. Observed and synthetic waveforms at the port are shown in Fig. 2.6d.



I estimated the peak location of the ray-tracing analysis without considering the effects of the initial phase of cylindrically spreading waves and finite source duration (Fig. 2.4), but here discuss these effects. In the tsunami simulation for the source model (Fig. 2.6b), it took 43 s for the peak of disturbance to propagate from the source to the edge at a radius of 4.0 km. On the contrary, the long wave with a speed of 89 m/s traveled only 3.8 km within this time duration, assuming a water depth of 800 m inside Smith Caldera. The higher speed of the peak propagation in the tsunami simulation was caused by the initial phase effect of cylindrically spreading waves [e.g. *Aki and Richards*, 1980]. If this effect is taken into account, the source location as estimated in Fig. 2.4 shifts SSW by  $\sim 0.2$  km. However, the post-shift source is still located inside the caldera.

An instantaneous seafloor deformation was assumed at the earthquake origin time in the phase analysis. According to the GCMT catalog, the centroid time from the hypocenter time of the 2015 event was 6.7 s. The source durations expected from an empirical scaling with scalar moment for vertical-CLVD earthquakes are, similarly, 7–8 s [*Shuler et al.*, 2013b]. Because the tsunami phase peaks were projected backward to the source up to the earthquake origin time, I made a correction for the source location using the reported centroid time shift. This correction shifted the source location NNE by  $\sim 0.6$  km. Thus, the phase shift due to the initial phase of cylindrically spreading waves and the phase delay due to a finite source duration acted in opposite directions, such that their effects on source location partially canceled each other.

## 2.4.2 Implications for the physical mechanism of the 2015 Torishima earthquake

The tsunami source modeling study using tsunami simulation techniques together with the OBP records revealed that the 2015 Torishima volcanic tsunami earthquake caused seafloor uplift up to 1 m, surrounded by smaller peripheral subsidence, which was distributed consistently within the surface structure of Smith Caldera (Fig. 2.6b). Because the model was estimated under simple assumptions (i.e., an axially symmetric shape composed of central uplift and surrounding subsidence, and a symmetric axis at the center of the source shape), it may not be a unique solution and may lack detailed features or heterogeneity. However, good agreements between the predictions and the observations seen in the ray-tracing analyses (Fig. 2.4c,d) and numerical waveform simulations (Fig. 2.6a,d) suggest that the model's overall characteristics (large uplift surrounded by peripheral subsidence) are reasonable based on the dataset used in this study.

The characteristics of seafloor deformation accompanying the earthquake as estimated from the tsunami analysis were very different from those for typical tectonic earthquakes on a planar fault structure. It is surprising that the intermediate-class earthquake with  $M_w$  5.7 generated seafloor deformation  $> 1$  m. The circular uplifted deformation focused within a small area (diameter of  $< \sim 10$  km) was also unpredictable from a typical planar fault rupture mechanism at source depth ( $\sim 10$  km) when estimated seismologically. For example, *Satake and Gusman* [2015] assumed a slip model on a planar fault with the

equivalent seismic magnitude  $M_w$  5.7 (fault size = 16 km  $\times$  8 km; slip amount = 0.2 m; strike = 215°; dip = 55°; rake = 86°) at depth of 10 km below Smith Caldera. However, they predicted uplift no larger than 5 cm and deformation broadened around 20 km along the fault orientation. Therefore, the large and focused seafloor deformation implies an atypical physical mechanism or very shallow source depth for the 2015 Torishima earthquake.

The tsunami source geometry was consistent with the topographic structure of Smith Caldera (Fig. 2.6c), strongly suggesting that the 2015 Torishima earthquake was closely associated with volcanic activity at the caldera. The large uplift concentrated over and within the rim structure could therefore have been caused by a volcanic phenomenon involving an upward motion of the caldera floor. It is known that a caldera floor sometimes moves upward in an aseismic manner due to the magma stress below, which is called “resurgence” [e.g. *Acocella and Funicello*, 1999; *Acocella et al.*, 2000]. In this analogy, the uplift focused on the caldera floor, as estimated for this earthquake, may imply the existence of highly pressurized magma below. On the other hand, a peripheral subsidence with a clear amplitude along the NNE part of the rim structure was also confirmed based on the numerical tests and observations. This downward motion on the outside may be caused by a reaction of the upward motion of the caldera floor on the inside, due to a fault rupture on an intra-caldera ring-fault system, which could be expected to cause seismic radiation with a vertical-CLVD focal mechanism [e.g. *Ekström*, 1994].

*Fukao et al.* [2018] suggested a “vertical opening of shallow horizontal crack” model as a source mechanism for the 2015 Torishima earthquake, demonstrating that such an opening at very shallow depth (0.2) km had the potential to generate large seafloor uplift but excite little long-period seismic energy. Thus, this model may explain the tsunami earthquake’s characteristics as well as the large uplift over the caldera that accompanied the 2015 Torishima earthquake.

Although the proposed model partially explained the observations (i.e., large caldera uplift and inefficient seismic energy release), other questions remained to be answered. First, the model explained the uplift deformation on the seafloor but not the peripheral subsidence that was estimated from the tsunami analysis. In addition, despite its predicted weak excitation rate of long-period seismic waves, the volcanic tsunami earthquakes actually had detectable seismic magnitudes of  $M_w$  5–6. These issues implied that the physical mechanism of volcanic tsunami earthquakes could not be fully explained using only the model proposed by *Fukao et al.* [2018]. Therefore, further investigations were required to fully determine the physical mechanism by quantitative analysis of both tsunami and seismic records.



# ***Chapter 3 Kinematic source modeling for the 2015 Torishima volcanic tsunami earthquake***

In Chapter 3, I further explore a kinematic source model of the 2015 Torishima volcanic tsunami earthquake through an interdisciplinary approach based on modeling studies of tsunamis, seafloor deformation, and long-period seismic waves. This chapter is composed of three parts: (1) the inversion of tsunami waveforms for investigating the initial sea-surface displacement, (2) the inversion of tsunami waveforms for estimating slip distributions on assumed faults, and (3) forward modeling of long-period seismic waves. I then use the results to propose a kinematic source model for the 2015 Torishima earthquake that explains both the observed tsunami and long-period seismic wave records.

## **3.1 Inversion of tsunami waveforms for the initial sea-surface displacement**

### **3.1.1 Questions remaining from Chapter 2**

In Chapter 2, I examined the initial sea-surface displacement of the 2015 Torishima earthquake to reveal its resultant large seafloor uplift at Smith Caldera. However, that modeling study contained several limitations and assumptions: (1) the shape of the assumed model was assumed as axially symmetric, (2) the source location was fixed as the axis points at the center of the caldera, (3) the amplitude ratio of the central uplift and the peripheral subsidence was fixed, and (4) the azimuthal coverage of the stations was limited to a NNE direction from the epicenter. These issues prevented the development of a tsunami source model with spatial heterogeneity and robustness. Therefore, before exploring subsurface structures associated with the earthquake, I further examined the initial sea-surface displacement, including more details in the inversion analysis using more tsunami data and more accurate tsunami simulation methods.

## 3.1.2 Data and Methods

### 3.1.2.1 Tsunami data

I obtained tsunami waveform data from records at 24 stations from the array off Aogashima Island (10 stations) [Fukao *et al.*, 2018], DONET (11 stations) [Kawaguchi *et al.*, 2015; Kaneda *et al.*, 2015; National Research Institute for Earth Science and Disaster Resilience (NIED), 2019a], the DSFO off Muroto Cape (two stations) [Momma *et al.*, 1997], and the DART system (one station) [Bernard and Meinig, 2011] (Fig. 3.1). To extract tsunami signals from the raw data, I processed them as follows. First, data quality (i.e., data gaps, spikes, or repeating values) near the arrival times of tsunami signals was checked manually. Second, I removed tidal signals by fitting polynomial functions. Third, I extracted tsunami signals by applying the 2-pass and 2nd-order Butterworth low-pass filter. The cut-off frequencies were set to 0.0125, 0.0083, 0.0083, and 0.00667 Hz at stations from the array, DONET, DSFO, and DART, respectively. The cut-off frequencies were determined according to approximate maximum water depth along ray paths between the source and stations, because the equations employed for tsunami simulations cause larger computational errors at short-period ranges in deeper water (see Appendix 1). Therefore, I used tsunami energy alone, only in the valid period range for waveform comparisons, by removing short-period energy.

### 3.1.2.2 Tsunami simulation

Synthetic tsunami waveforms for the array, DONET, and DSFO (but not DART) were computed using the phase correction method for short-period tsunamis (see Appendix. 1). I first computed tsunami propagations with the JAGURS code [Baba *et al.*, 2015] by solving the linear formulations of the standard Boussinesq equations (Eq. 2.6–2.8). The computational time-step interval was set to 0.25 s to satisfy the CFL condition in the finite-difference numerical scheme, and spatial wavefields in the entire computation region were output every 5.0 s. For the bathymetry data, I used a nested-grid system. Around Smith Caldera and Aogashima Island, high-resolution grid data (10 arcsec spacing) processed from the M7000 series were used to incorporate the effects of complicated bathymetry, while the broad region was modeled by JTOPO30 (30 arcsec grid spacing).

To compare the synthetic waveforms with actual records from OBP gauges, the pressure attenuation effect at depth needed to be incorporated [Chikasada., 2019]. In linear potential theory, when water waves with amplitude  $\eta$  propagate on the sea surface, the pressure change  $\Delta p$  at ocean bottom with water depth  $D$  is expressed as:

$$\Delta p(t) = \int \frac{\rho g}{\cosh(kD)} \bar{\eta}(k, t) dk_x dk_y, \quad \text{Eq. 3.1}$$

where

$$k = \sqrt{k_x^2 + k_y^2}, \quad \text{Eq. 3.2}$$

where  $\bar{\eta}(k_x, k_y, t)$  is the Fourier transform of  $\eta(x, y, t)$  over space and  $\rho$  and  $g$  are the water density and the gravitational acceleration, respectively. Following the method proposed by *Chikasada* [2019], I performed the Kajiura's filter ( $1/\cosh kD$ ) [*Kajiura*, 1963] on the output wavefields around stations to incorporate the pressure attenuation factor at the ocean bottom, and obtained synthetic pressure changes at ocean bottom depth, which were comparable to the observed pressure records.

I then performed phase correction on the synthetic waveforms to incorporate the sPREM effect (i.e., the elasticity of the Earth, compressibility of sea water, gravity potential change, and ocean density stratification) [e.g. *Watada et al.*, 2014; *Ho et al.*, 2017], and to reduce computational errors in short-period energy due to the approximation of the dispersion terms (see Appendix. 1). The phase-corrected waveforms were filtered in the same manner as for the observed records.

On the other hand, waveforms at the DART station( located over 1,400 km from the epicenter) were computed in a different manner, because computations over such a wide region using standard Boussinesq equations are time-consuming (around 22 hr for a computation of 10,000 s propagation with an eight-core parallel-computation system using the EIC Supercomputer at the Earthquake Research Institute, University of Tokyo). Instead, I first solved the nondispersive linear long-wave equations using the JAGURS code. After performing the Kaiura's filter, I applied *Ho et al.*'s [2017] phase correction method to incorporate the dispersion effects and the sPREM effects. This alternative method reduced the computational time to < 30 min. Although this approach generally has problems related to miscalculations of ray paths for shorter-period energy (see Appendix. 1), its feasibility for the DART station was confirmed by the fact that the synthetic waveforms computed by the two methods were similar to each other in earlier phases used for the inversion analysis. This may be because short-period energy, which was not used for the inversion, arrives much later than the phases due to strong dispersion effects during long-distance propagation.

### 3.1.3 Inversion of tsunami waveforms for initial sea-surface displacement

#### 3.1.3.1 Methods

I estimated a tsunami model, or initial sea-surface displacement, by the tsunami inversion using the OBP records from different tsunami observation networks. Based on the preliminary tsunami source model (Chapter 1), I set a source area 32 km x 32 km square and distributed 113 unit sources of initial sea-surface displacement with 2 km intervals (Fig. 3.2). Each unit source on sea surface had a cosine-tapered shape that was expressed as [*Hossen et al.*, 2015]:

$$\eta_i(x, y) = 0.25 \times \left[ 1.0 + \cos \frac{\pi(x - x_i)}{L} \right] \times \left[ 1.0 + \cos \frac{\pi(y - y_i)}{L} \right], \quad \text{Eq. 3.3}$$

$$(|x - x_i|, |y - y_i| \leq L),$$

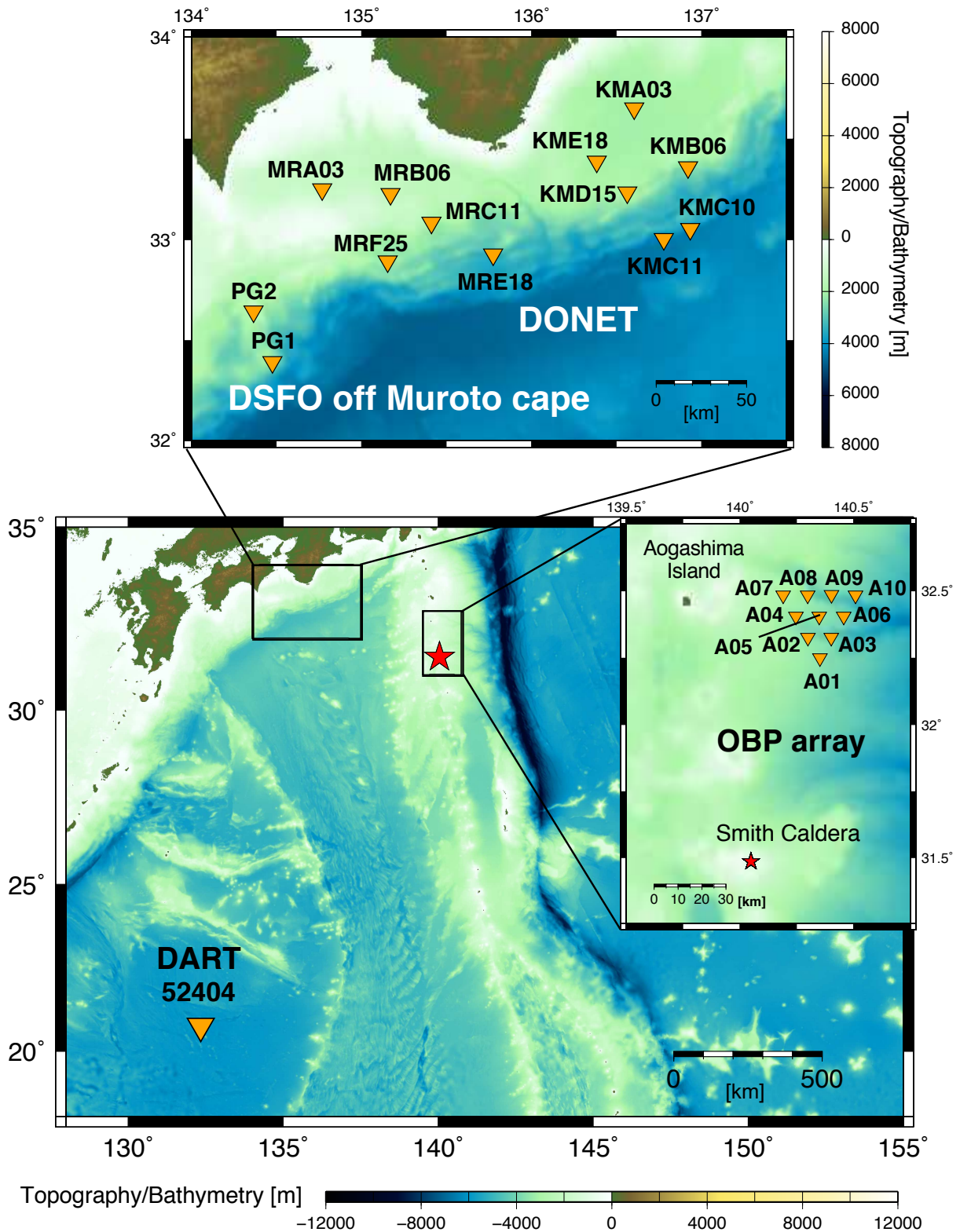


**Fig. 3.1** Map of the tsunami observation networks

Orange triangles represent the tsunami observation networks using ocean bottom pressure gauges. Red star represents the location of Smith Caldera.

where  $\eta_i$  is the initial distribution of vertical displacement on the sea surface of the  $i$ th unit source with the central location at  $(x_i, y_i)$  in kilometer ( $i = 1, 2, \dots, N$ ) and a source size of  $2L$  (4.0 km, here). I computed synthetic waveforms from the  $i$ th unit source at the  $j$ th station ( $j = 1, 2, \dots, M$ ) to obtain tsunami Green's functions  $\mathbf{g} = g_{ij}(t)$ . The rise time for each unit source was set as 10 s, considering the W-phase moment tensor inversion results indicating a source duration of  $\sim 10$  s (Chapter 5.2).

Since amplitudes of tsunami records differ from station to station, I normalized both the observed and synthetic waveforms by the inverse RMS value of observed records:

$$\frac{1}{w_i} = \sqrt{\frac{\sum_0^{\gamma_j} b_j(t) dt}{\gamma}}, \quad \text{Eq. 3.4}$$

where  $b_j(t)$  is the observed records at the  $j$ th station and  $\gamma_j$  is the data length used for the inversion [e.g. *Ho et al., 2017*].

To construct a tsunami source model, I solved the following observational equation with the damped least-squares method [e.g. *Aki and Richards, 1980*]:

$$\begin{bmatrix} \mathbf{b} \\ \mathbf{0} \end{bmatrix} = \begin{bmatrix} \mathbf{g} \\ \alpha \mathbf{I} \end{bmatrix} \mathbf{m}^T, \quad \text{Eq. 3.5}$$

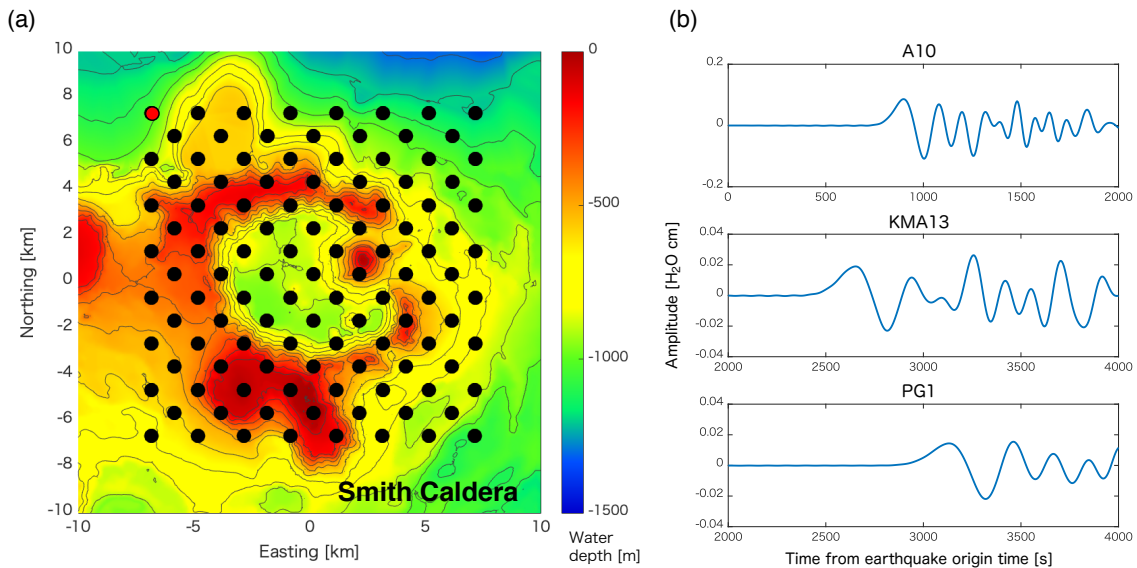


**Fig. 3.2 Distributions of unit sources of initial sea-surface displacement around Smith Caldera**  
 (a) Black and red dots represent central locations of unit sources of initial sea-surface displacement. Each unit source has a cosine-tapered shape with a horizontal source size of 4 x 4 km. Contour lines of the water depth are painted every 100 m. (b) Examples of tsunami Green's functions from a unit source with a central location represented by a red dot in (a).

where  $\mathbf{b}$  ( $= w_j b_j$ ) is the column vector of the observed waveforms  $b_j$  weighted by  $w_j$  at the  $j$ th station,  $\mathbf{g}$  ( $= w_j g_{ij}$ ) is the matrix of the tsunami Green's functions  $g_{ij}$  weighted by  $w_j$ ,  $\mathbf{m}$  ( $= m_i$ ) is unknown raw vector of the weighting factors of the  $i$ -th unit source,  $\mathbf{I}$  is the identity matrix, and  $\alpha$  is the damping parameter used to obtain a smooth source model. I set inversion time windows that included several wave crests and troughs.

In order to find a natural and stable solution, it is important to select a proper value of the damping parameter. In general, the smaller the damping parameter, the better the waveform fitness. However, this does not mean that the solution is more natural, because it can be significantly affected by small perturbations (due to data noises or imperfections of Green's functions). For example, when  $\alpha$  is 0.2, the solution contains complex patterns with a short wavelength (Fig. 3.3a, top), and the waveform fitness is quite good within the inversion time window (blue line in Fig. 3.3a, bottom). However, the solution can be excluded for a natural solution, because amplitudes of later phases dominant in shorter-period energy are significantly overestimated, which can be attributed to unrealistic short-wavelength patterns that are possibly sensitive to data noise or imperfections of Green's functions.

Therefore, I selected a damping parameter that suppressed such unstable short-wavelength patterns by considering the waveform fitness in later phases as well, following *Saito et al.* [2010]. I conducted inversion tests with different damping parameters from 0.25–10.0 at intervals of 0.25, and quantified the fitness between the inverted and observed waveforms with the normalized root-mean-square (NRMS) misfit:

$$NRMS \text{ misfit} = \frac{\sum_{j=1}^M NRMS_j}{M}, \quad \text{Eq. 3.6}$$

where  $NRMS_j$  is the NRMS error for  $j$ -th station:

$$NRMS_j = \frac{\sqrt{\sum_0^{\gamma_j} (obs_j(t) - inv_j(t))^2 dt}}{\sqrt{\sum_0^{\gamma_j} (obs_j(t) - \overline{obs_j})^2 dt}}, \quad \text{Eq. 3.7}$$

where  $obs_j(t)$  and  $inv_j(t)$  are the observed and inverted waveforms, respectively,  $\gamma_j$  is the data length, and  $\overline{obs_j}$  is the average of the observed record. The NRMS misfit was computed with different data lengths (i.e., the inversion time window) and the inversion time plus additional later phases (500 s) (Fig. 3.3a-c).

Figure 3.3d shows the NRMS misfits as functions of the damping parameter. The misfit of the inversion time alone was naturally smaller when  $\alpha$  was close to zero, and increased for larger  $\alpha$  (blue line in Fig. 3.3d). On the other hand, the NRMS misfit including later phases was quite large when  $\alpha$  was close to zero, and reached its minimum value when  $\alpha$  was around 2.0 (orange line in Fig. 3.3d). When  $\alpha$  was 2.0, the solution contained only longer-wavelength patterns (Fig. 3.3b, top), different from the solution

when  $\alpha$  was 0.2 (Fig. 3.3a). Although the fitness kept a sufficient waveform fitness during the inversion time window, in later phases it was significantly improved (Fig. 3.3b, bottom), based on which I considered it as a more reasonable solution. When  $\alpha$  was even larger, the waveform fitness became worse overall, as seen when  $\alpha$  was 6.0 (Fig. 3.3c, bottom). Therefore, I decided to use a damping parameter of 2.0, based on the minimum value of the NRMS misfit including later phases.

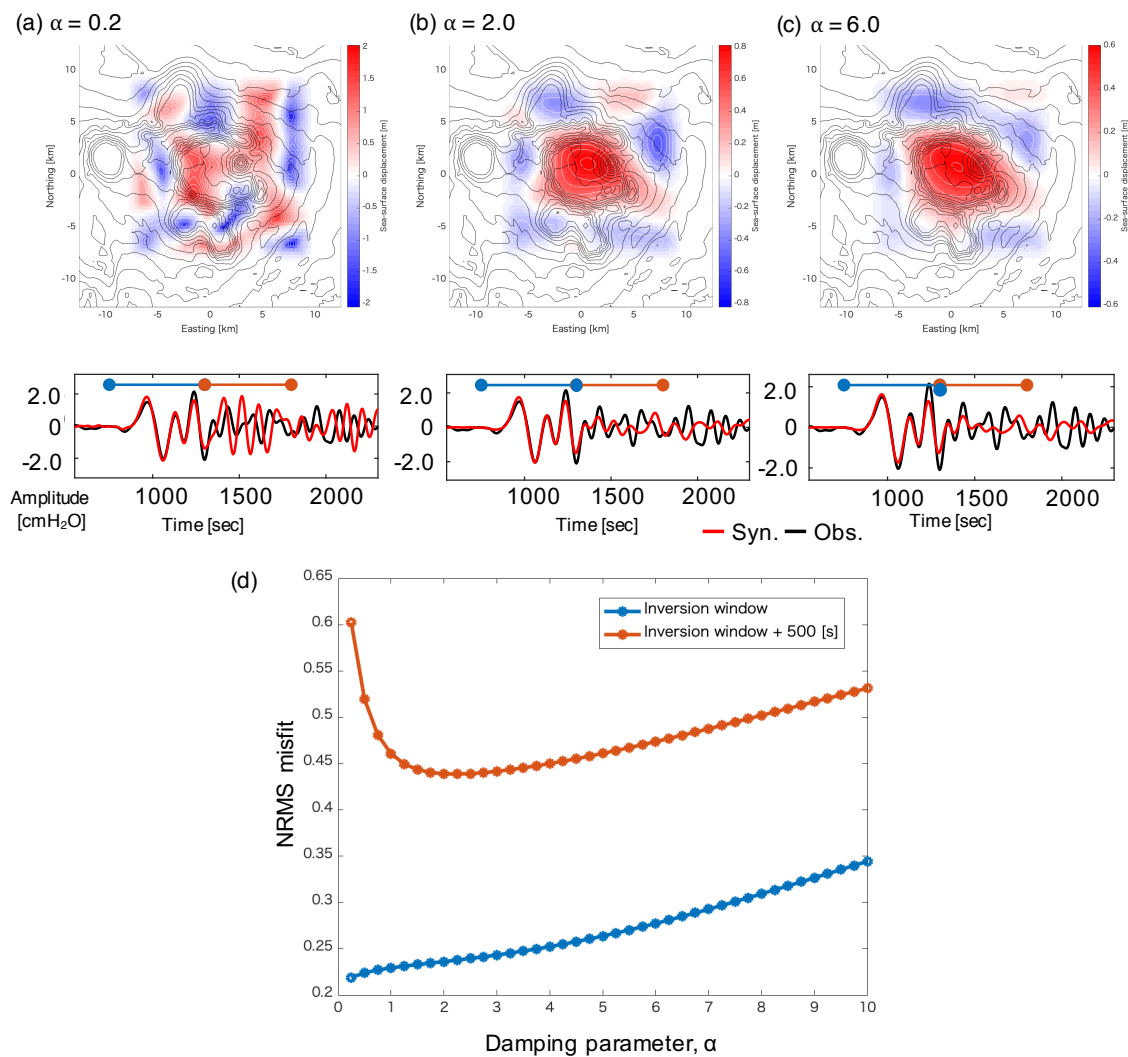


**Fig. 3.3 Selection of a damping parameter**

(a) NRMS misfit values as functions of a damping parameter  $\alpha$ . Blue and orange lines are computed for two datasets with different data lengths, inversion window (blue line in b) and inversion window + 500 [s] (blue + orange line in b), respectively. (b) Waveform comparisons for different damping parameters.

### 3.1.3.2 Results and resolution tests

I obtained a tsunami source model from records at all 24 stations (Fig. 3.4a). The inverted model contained a large uplift ( $\sim 80$  cm maximum) within the caldera structure and non-negligible subsidence mainly on the NE and NW sides along the exterior of the rim structure, similar to the results estimated by the tsunami source modeling (Chapter 2). The inverted model accurately reproduced the observed tsunami waveforms including later phases at all the stations (Fig. 3.4b).

I examined the robustness of the uplift and subsidence signals by conducting inversion analysis, first with only the array ( $\alpha=2.0$ ; Fig. 3.5a), then with the DONET and DSFO stations ( $\alpha=1.0$ ; Fig. 3.5b). Regardless of dataset, the central uplift within the caldera structure was stably estimated, strongly supporting a meter-scale uplift of the Smith Caldera floor. For both inversions, the uplift distributions were elongated in directions perpendicular to their station azimuths, implying that the small uplift signals along the exterior of the rim structure seen in the main result (Fig. 3.4a) may be artifacts from the central uplift due to the limited station azimuthal coverages.

On the other hand, non-negligible subsidence signals on the northern exterior along the rim were found in both cases, despite slight variations in amplitude and location. In order to confirm the robustness of the subsidence, I alternatively inverted a source model with only uplifted sea-surface displacement by imposing the non-negative condition on the damped least-square method. The inverted uplift source model, a large uplift focused within the caldera rim, showed much worse waveform fitness at the array (A01-10), particularly in the leading parts (Fig. 3.6). The NRMS misfit took a much larger value of 0.34 for this case, compared to 0.23 for the model including subsidence (Fig. 3.4a). This suggests that the earthquake actually accompanied a seafloor subsidence along the northern exterior of the rim structure.

In the dataset used here, only the DART 52404 station was located south of the source, which may have led to less reliability in the southern part of the source model. To consider the effect of station location on the inverted model, I also conducted the inversion with all stations except for DART 52404 ( $\alpha=2.0$ ; Fig. 3.5c), producing no significant change. This means that the source model was estimated mainly from records at stations belonging to the array, DONET, and DSFO, all to the NE and NW. Therefore, subsidence signals distributed on the southern side of the caldera may not be inverted reliably with the dataset available here.

## 3.1.4 Physical mechanism inferred from the inverted tsunami source model

### 3.1.4.1 Implications of the tsunami model for the physical mechanism

The tsunami source model is useful for considering the source kinematics of the 2015 Torishima earthquake that occurred at Smith Caldera. The model robustly inferred a large upward motion of the caldera floor and a downward motion at least along the northern parts of the rim structure. From the perspective of the source kinematics, I considered possible source mechanisms discussed for vertical-

CLVD earthquakes by *Shuler et al.* [2013b], including the opening/closing of a horizontal crack, a volumetric change, volume exchange between two magma reservoirs, and ring-fault slip.

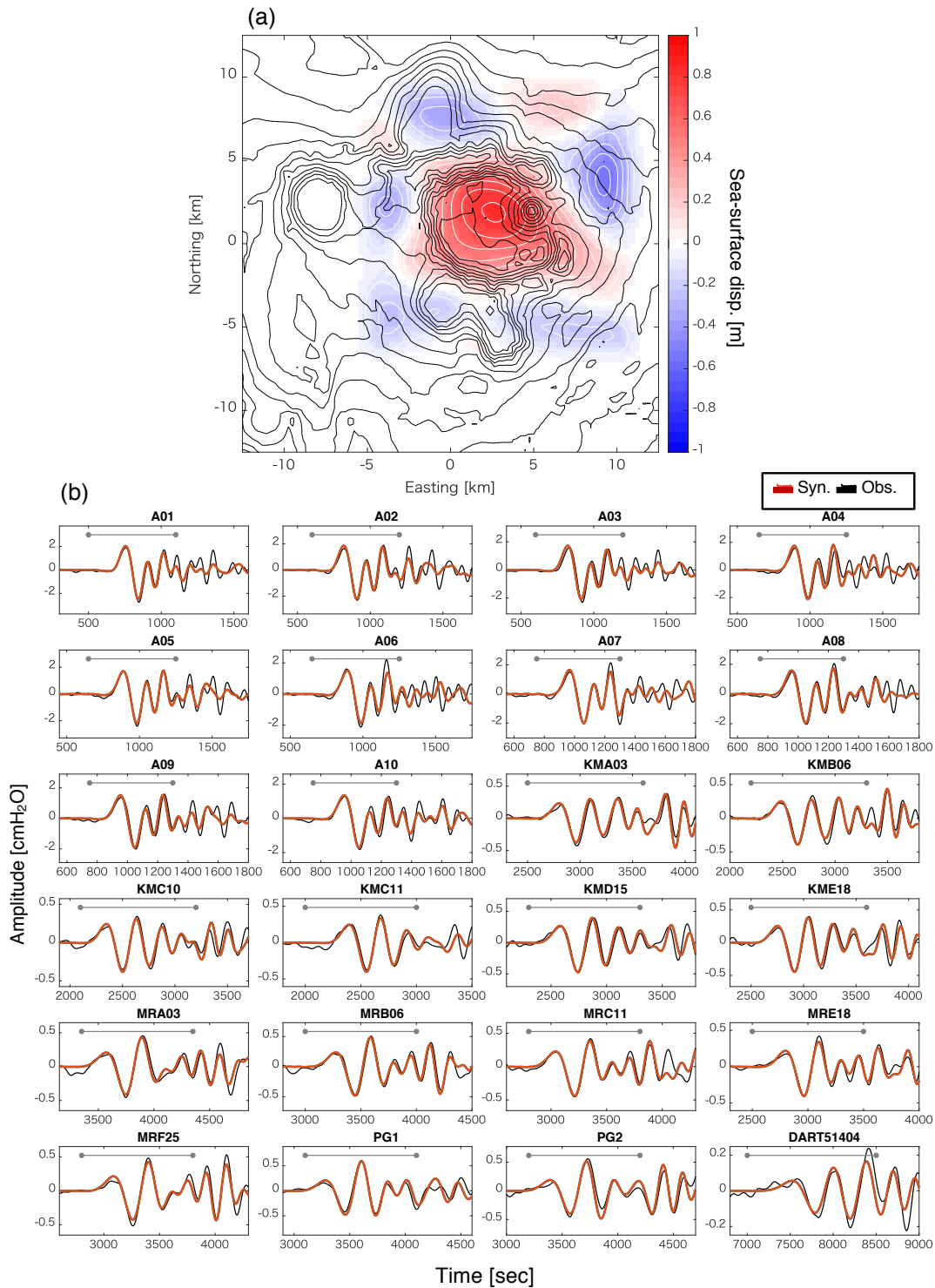


**Fig. 3.4 Inversion results using all the stations**

(a) Inverted initial sea-surface displacement, with white contour lines plotted every 0.1 m. Black contour lines are painted every 100 m of the water depth. Red and blue color represent sea-surface uplift and subsidence, respectively. (b) Waveform comparison of synthetic (red) and observed waves (black).

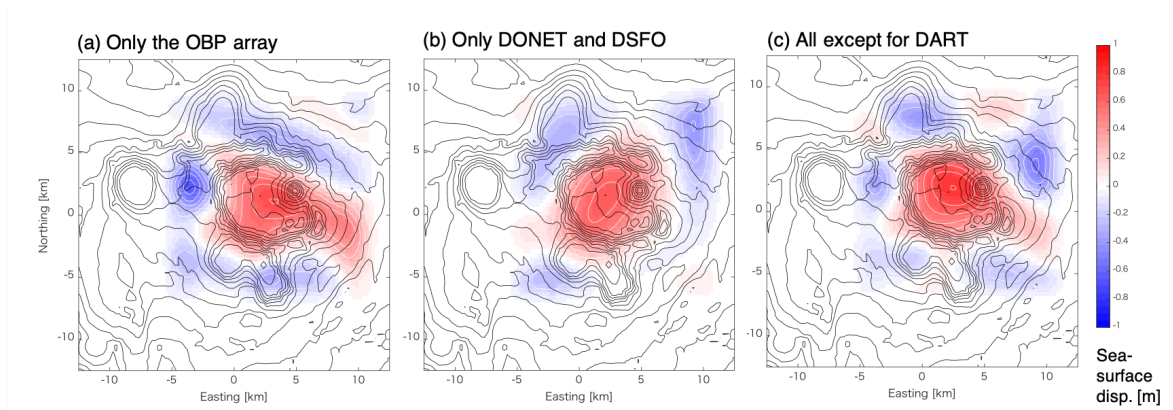


**Fig. 3.5 Inversion results using different datasets**

Initial sea-surface displacement inverted from (a) only the array, (b) only DONET and DSFO, and (c) all stations except for DART. The damping parameter was selected as 2.0, 1.0, and 2.0 for (a), (b) and (c), respectively.

The first key feature of the 2015 Torishima earthquake kinematics was large uplift at the meter scale, focused on the caldera floor. This uplift may be explained by explosive volume change at shallow depth below the caldera structure. The vertical opening of a shallow horizontal crack driven by high-pressurized magma inside [Fukao *et al.*, 2018] is a possible candidate for this type of mechanism. However, the other key feature of the source kinematics, non-negligible subsidence confined to the rim structure, cannot be generated by such an explosive volumetric source. Among other possible mechanisms, a volume- or pressure-exchange source connecting two reservoirs may cause uplift and subsidence in nearby zones. Although the movement of magmatic fluid is unlikely to occur within the source duration estimated by Shuler *et al.* [2013b] as  $\sim 10$  s, a pressure propagation or volcanic gas movement between reservoirs could occur together with seismic excitations during a short source time. In such a case, it is reasonable to assume that a shallow reservoir inflates just below the caldera while another deeper one deflates due to the volume or pressure exchange. Nevertheless, considering the subsidence estimated within a narrow area along the caldera rim, the deflating reservoir would have to be located at very shallow depth along the rim structure as well, otherwise subsidence would be expected to be spread broadly around the caldera. This possibility cannot be excluded, since little is known about the subsurface structures of Smith Caldera. However, I consider such a complicated system composed of two separate reservoirs unrealistic at shallow depth.

Apart from the above mechanisms related to volumetric changes or exchanges, a ring-fault rupture is more likely to generate such rapid seafloor deformation consisting of upward and downward motion with a clear transition boundary along the rim structure. Generally, ring-fault structures in caldera volcanoes are formed within the structural boundary along the rim during the collapse of a caldera block [e.g. Cole *et al.*, 2015; Geyer and Martí, 2014; and references therein]. When a ring-fault system causes a brittle rupture in a dip-slip direction as the caldera block moves upward, the resultant deformation consists of caldera-floor uplift and subsidence along the rim, which is consistent with the kinematics inferred from the tsunami model. In addition, the ring-fault slip can generate seismic radiation with a vertical-CLVD

focal mechanism [e.g. *Ekström, 1994*]. Therefore, the ring-fault mechanism is the most plausible explanation for the earthquake physics suggested by the source kinematics inferred from tsunami records, as well as its focal mechanism.

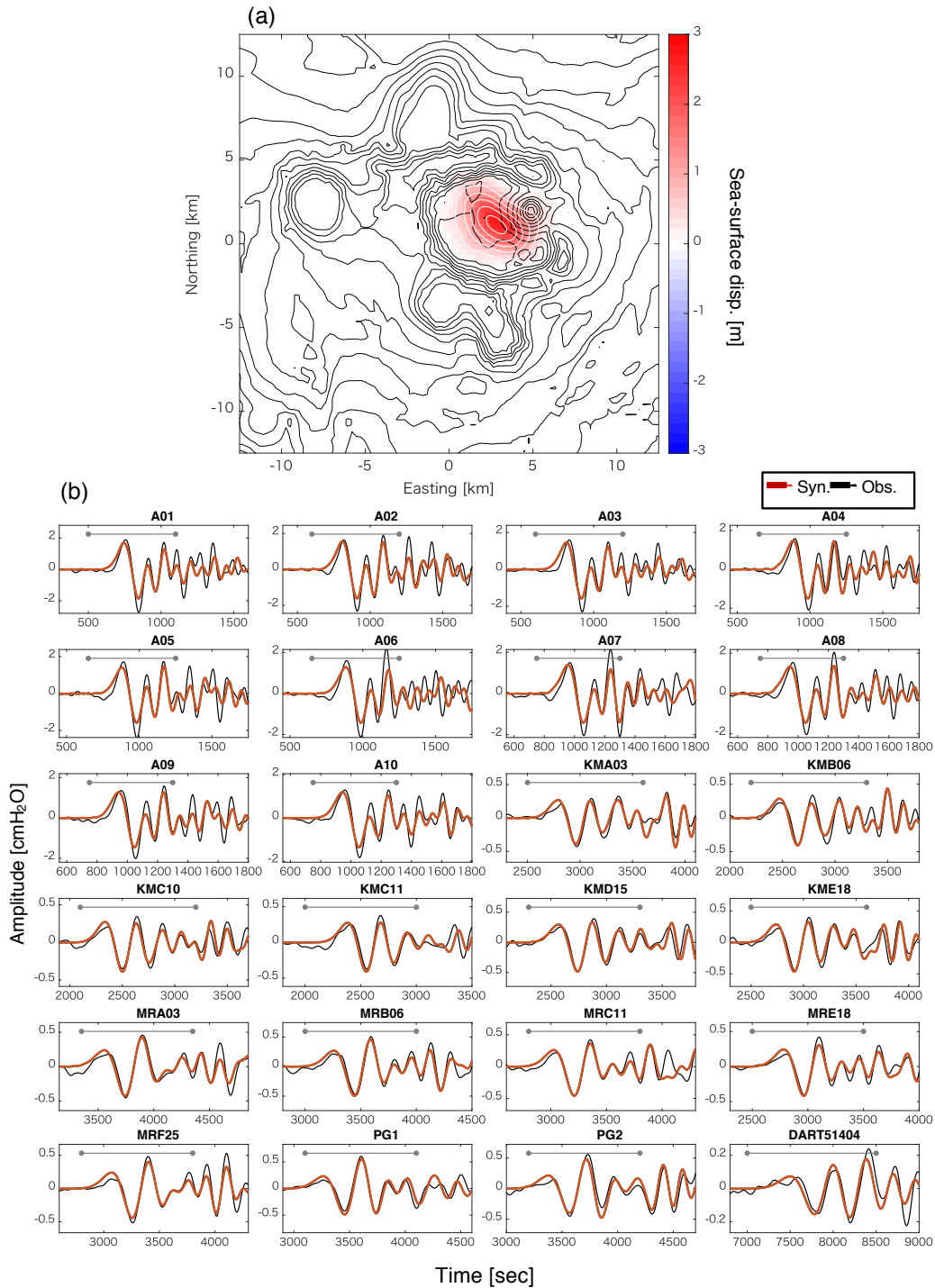


**Fig. 3.6 Inversion result assuming uplifted sea-surface displacement**

(a) Inverted initial sea-surface uplifted displacement, with white contour lines plotted every 0.5 m. Black contour lines are painted every 100 m of the water depth. (b) Waveform comparison of synthetic (red) and observed waves (black).

### 3.1.4.2 Hypothetical source model of the 2015 Torishima earthquake

Here, I hypothesize a physical mechanism related to the composite fault system, involving the opening of a shallow horizontal crack filled with high-pressure magma and the rupture of an intra-caldera ring-fault system (Fig. 3.7a). The composite fault system is equivalent to the structural boundary of the subsurface caldera block. Motion of a subsurface caldera block interacting with the composite fault structures has been suggested by many volcanological studies on a type of volcanic unrest called “resurgence,” which have been documented at several volcanoes such as Iwo-Jima, Tanna, Campi Flegrei, Ischia, and Toba [Acocella *et al.*, 2015; references therein]. Resurgence is characterized by the large uplift of a caldera floor, up to a few meters over a span of weeks to years, reaching a thousand meters over hundreds to thousands of years [Acocella, 2019]. This uplift is mainly caused by magmatic pressure or volumetric changes in shallow magma chambers below calderas. Many studies based on field observations and numerical/analogue experiments have also revealed that pre-existing ring-fault structures play an important role in promoting the upward motion of a caldera block [e.g. De Natale and Pingue, 1993; Acocella and Funiciello, 1999; Acocella *et al.*, 2001]. Although most previously observed resurgence activities did not accompany notable seismic energy release, a few seismic events were observed at Sierra Negra caldera, Galápagos, in an analogous way to the interacting fault system. These were attributed to an instantaneous ring-fault rupture initiated by high-pressure magma accumulated in a shallow sill-like chamber [e.g. Amelung *et al.*, 2000; Jónsson, 2009].

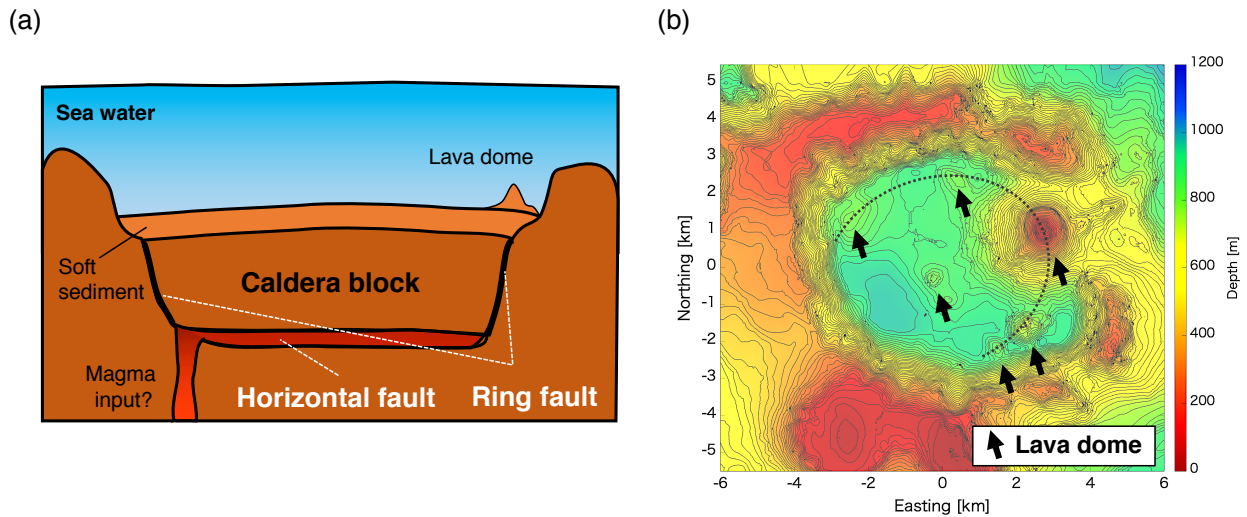


**Fig. 3.7 Hypothesized subsurface structures of Smith Caldera**

(a) Schematic illustration of the hypothetical structures of Smith Caldera. (b) Surface structure of Smith Caldera. Black arrows represent lava domes pointed out by Tani *et al.* [2008]. Dotted line represents an approximate trace of the subsurface ring fault extended to seafloor. Contour lines of bathymetry are plotted every 20 m. The bathymetry data is obtained from the M7000 model.

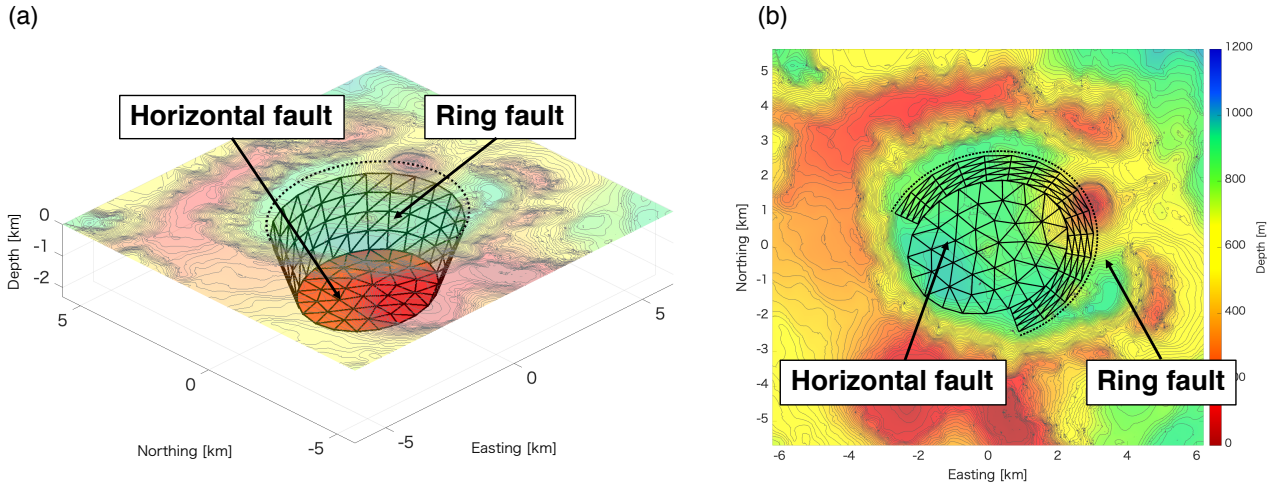


**Fig. 3.8 Model setting of the composite fault system discretized by triangular meshes**

(a) Perspective view of Smith Caldera. Transparent and red-colored meshes represent the ring fault and the horizontal fault, respectively. Dotted line represents an approximate trace of the subsurface ring fault extended to seafloor. The subsurface ring fault extends from 0.3 km depth to deeper with a uniform dip angle. (b) Map view. The surface trace of the ring fault has an ellipse shape with radius of  $3.2 \times 2.7$  km. The ellipse is rotated in contour-clockwise by  $20^\circ$  around the central point at  $140.0454^\circ\text{E}$ ,  $31.4816^\circ\text{N}$ .

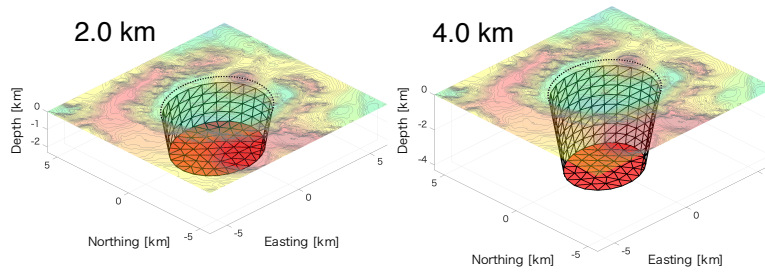
At Smith Caldera, it is reasonable to consider the existence of a subsurface caldera block whose structural boundary forms the composite fault system, considering surface structures on the caldera floor. The high-resolution bathymetry data from the caldera contains six cone structures on the caldera floor (Fig. 3.7b), some of which were identified as young dacitic lava domes by rock sampling [Tani *et al.*, 2008]. At several caldera volcanoes, such as Ichia, Long Valley and Valles, lava domes formed by post-caldera eruptions tend to be emplaced within calderas as they connect to subsurface ring-fault structures, along which renewed magma may have intruded up to the surface [e.g. Phillips, 1974; Gudmundsson *et al.*, 1997; Acoccela *et al.*, 2001; Cole *et al.*, 2005]. The inferred ring-fault structure forming a subsurface caldera block may thus have the potential to cause seismic ruptures. On the other hand, although there is no direct evidence of the existence of a horizontal fault, recharged magma intruding below the caldera block may be indicated by different observations, such as characteristic surface structures indicating post-caldera eruptions, seawater color changes found around the caldera (reported by the Hydrographic and Oceanographic Department, Japan Coast Guard), and T-phase signals following the 1996 Torishima earthquake [Sugioka *et al.*, 2000]. Therefore, magma accumulated in the horizontal fault may have acted as a driving force causing the upward motion of the block at the time of the 2015 Torishima earthquake.

## 3.2 Inversion of tsunami waveforms for fault slips

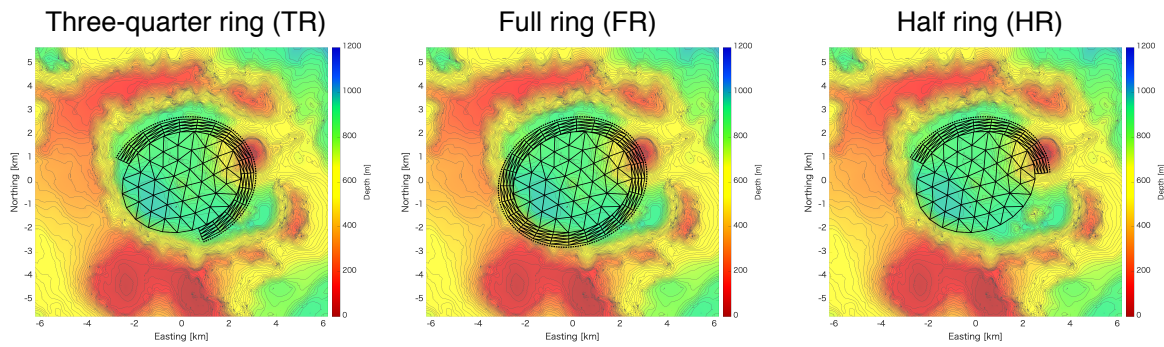
In this section, I use tsunami records to construct slip models in order to examine the validity of the hypothetical physical mechanism (subsurface composite fault motion of the caldera block consisting of both dip slip on the ring fault and tensile opening of the horizontal fault). By trying multiple fault

geometries, I also investigate detailed fault parameters, such as the dip angle and ruptured portion of the ring fault as well as the thickness of the caldera block.

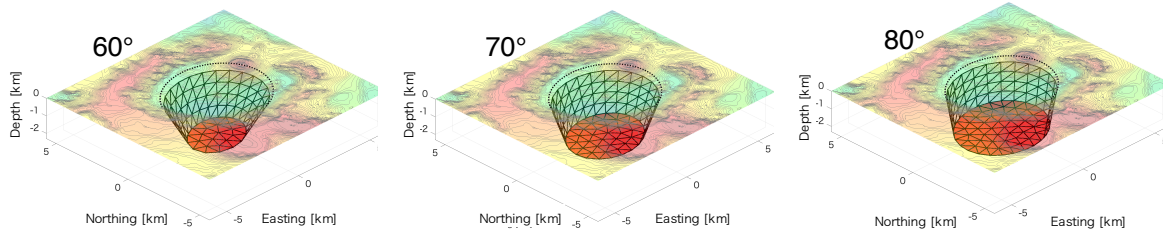
(a) Thickness of caldera block



(b) Ruptured portion of ring fault



(c) Dip angle of ring fault



(d) Fault models

Model #	1	2	3	4	5	6	7	8	9	10	11	12	13	14	15	16	17	18
Thickness [km]	2.0					2.0					2.0					4.0		
Ruptured portion	TR					FR					HR					TR	FR	HR
Dip angle [°]	60	65	70	75	80	60	65	70	75	80	60	65	70	75	80	80	80	80

**Fig. 3.9 Variable fault parameters and assumed fault models**

(a) Thickness of the subsurface caldera block; 2.0 km or 4.0 km. (b) Ruptured portion of the subsurface ring fault; Full ring (FR), Three-quarter ring (TR), and half ring (HR), (c) Dip angle of the ring fault; 60-80° in interval of 5°. (d) Fault parameters of the assumed 18 fault models.

## 3.2.1 Seafloor deformation modeling

### 3.2.1.1 Fault models

Based on the hypothetical physical mechanism, I modeled the composite fault system using discrete triangular dislocation (TD) elements with a triangulation method and an open-source code DistMesh [Persson and Strang, 2004] in MATLAB (Fig. 3.8). In the model setting, the ring fault extended with a uniform dip angle from at a shallow depth (300 m for simplicity) below-surface to the horizontal fault lying at an assumed bottom depth of the caldera block (Fig. 3.8a). The ring fault location was set up such that its trace (extended to the caldera surface) formed a rotated ellipse connecting the peripheral lava domes (Fig. 3.8b).

Due to uncertainties in the subsurface geometry of Smith Caldera, I tested 18 fault models with variable fault parameters (Fig. 3.9): (a) thickness of the caldera block: 2 km or 4 km, (b) ruptured portion of the ring fault: three-quarter ring (TR), full ring (FR), or half ring (HR), (c) dip angle of the ring fault: from 60–80° at 5° interval for models with 2 km thickness. For those with 4 km thickness, dip angle was set at 80° so that the horizontal fault size was comparable to that of the caldera block's upper surface (Fig. 3.9a). It is uncertain whether ruptures occurred partially or entirely along the ring fault structure. Therefore, I assumed three cases for ruptured portions (Fig. 3.9b), all of which contained ruptures at least on the northern portion of the ring-fault structure, because seafloor subsidence on the sides was confirmed by the previous tsunami analysis.

The ring fault's inward dip angle (Fig. 3.9c) was set on the basis of insights into caldera volcanism and the focal mechanism. Many field studies and analogue/numerical experiments on caldera collapse processes have indicated that ring-fault systems are optimally formed with a steep dip angle [e.g. Geyer and Martí, 2014; Cole *et al.*, 2005]. The inward dip angle was based on a vertical-CLVD focal mechanism with a dominant tension axis (vertical-T CLVD mechanism). Ekström [1994] theoretically demonstrated that these mechanisms are generated by upward motion of caldera block along an inward-dipping ring fault or downward motion along an outward-dipping ring fault. Given that the tsunami source model showed upward motion of the caldera block, the ring fault must have been inward-dipping to accommodate a vertical-T CLVD focal mechanism. A vertical fault was excluded on seismological grounds because pure dip slip on a vertical fault excites little long-period seismic energy due to the aseismic properties of  $M_{xz}$  and  $M_{yx}$  at shallow depth [e.g. Kanamori and Given, 1981].

### 3.2.1.2 Modeling of seafloor deformation

For the computation of seafloor deformation excited by slip on the composite fault system, I used the triangular dislocation (TD) method [Nikkho and Walter, 2015], which is capable of conducting deformation modeling on complex or arbitrary curved geometries, unlike other methods using rectangular dislocation meshes such as Okada [1982]. To model a motion of the caldera block, I simply assumed purely tensile opening or closing on the horizontal fault and purely dip slip motion (reverse or normal faulting)

on the ring fault. I regarded two neighboring TD elements forming a rhombus as one subfault on the ring fault, while each TD element was considered as one subfault on the horizontal fault. I assumed a Poisson's ratio of 0.25, a typical value for a shallow crust. For simplicity, the topography was considered to be a flat surface on the caldera floor. Although neglecting topography generally leads to misevaluations of surface vertical displacement on a slope [McTigue and Segall, 1988], the effect on similar caldera structures is < 10% [Ronchin et al., 2015].

### 3.2.2 Methods

To obtain slip distributions on the assumed fault models, I conducted slip inversions using the tsunami records from the array, DONET, DSFO off Muroto Cape, and DART (also used for the tsunami source modeling in Chapter 3.2; Fig. 3.1). The tsunami inversion procedure generally consists of two steps: (1) synthesize tsunami Green's functions from each subfault and (2) obtain slip distributions by solving the inverse problem relating subfault slips to tsunami records. To test multiple fault models composed multiple subfaults (over ~100 for each), I developed a new inversion method using efficient computations of tsunami Green's functions.

#### 3.2.2.1 Four-step computation of tsunami Green's functions from subfault slip

First, tsunami Green's functions were computed to relate subfault slips on fault models to tsunami records. In the conventional tsunami slip inversion method [e.g. Satake, 1988], the number of required tsunami simulations over the entire region is [*the number of fault models*] x [*the number of subfaults*] (Fig. 3.10a). Hence, the computation of tsunami Green's functions is generally the most time-consuming in the inversion method. In this case, using the sophisticated tsunami model with dispersion and other effects would require a long time.

To avoid this inefficiency in the conventional method, I invented a new method to compute tsunami Green's functions, the "four-step computation of tsunami Green's functions" approach (Fig. 3.10b). Because all the physical values considered here (i.e., slip amount, sea-surface displacement, and tsunamis in the deep ocean) are related in linear formulations, it is possible to reduce the computation time by utilizing this linearity.

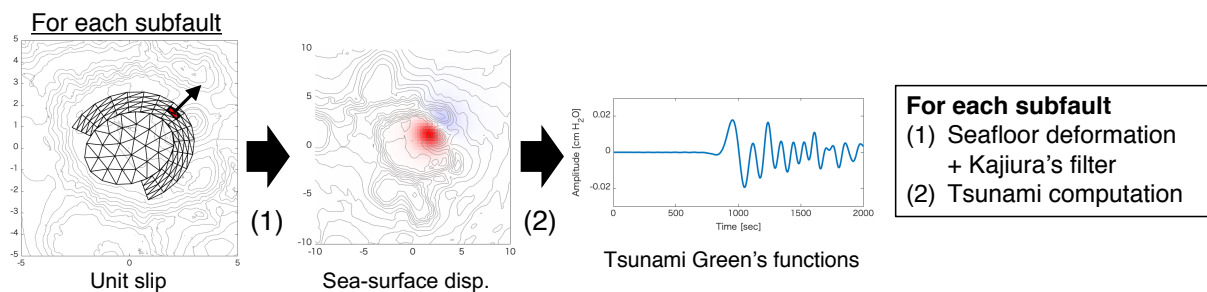
In the first step, tsunami Green's functions of unit sources of sea-surface displacement were prepared by simulating tsunami propagations from unit sources densely distributed in the source region. A dataset of the synthetic waveforms at the  $j$ th station from the  $k$ th unit source was restored as the "first tsunami Green's functions,"  $g_j^k(t)$ . Here, the spatial distribution of the  $k$ th unit source was expressed by  $\eta^k(x, y)$ . In this case, I reused the tsunami Green's functions from the 113 unit sources with cosine shapes that were computed in Chapter 3.1 (Fig. 3.2).

In the second step, tsunami Green's functions from subfaults were computed for each subfault, without a tsunami simulation. First, sea-surface displacement excited by unit slip on each subfault was

computed. Next, vertical seafloor displacement was computed by the TD method [Nikkho and Walter, 2015], then transformed into vertical sea-surface displacement by applying the Kajiura's filter to remove short-wavelength components of seafloor displacement [Kajiura, 1963]. An approximate water depth of 800 m over the caldera floor was assumed for this purpose (Eqs. 3.1,3.2). Then, the spatial field of theoretical sea-surface displacement excited by the  $i$ th subfault was restored as  $d_i(x, y)$ .

In the third step, the spatial distribution of the theoretical sea-surface displacement  $d_i(x, y)$  excited by unit slip of the  $i$ th subfault was reconstructed by summation of assumed unit sources of sea-surface displacement  $\eta^k(x, y)$ . The weighting factors of the  $k$ th unit source,  $m_i^k$ , were computed by solving the linear inverse problem:

(a) Conventional computation



(b) Four-step computation

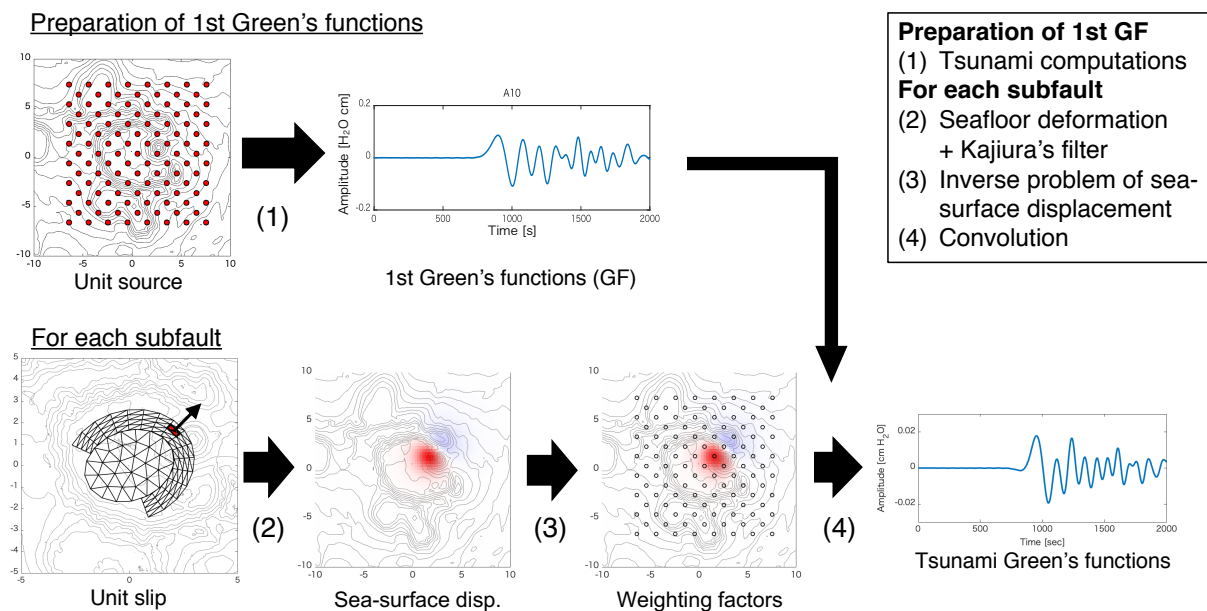


**Fig. 3.10 Procedures to compute tsunami Green's functions**

(a) Conventional computation method of tsunami Green's functions [e.g. Satake, 1989]. (b) Four-step computation method of tsunami Green's functions used in this study. It is noted that, after preparing the 1st Green's functions in first step, no tsunami simulation is required any more to compute tsunami Green's functions from unit slips from subfaults (See text).

$$d_i(x, y) = m_i^k \eta^k(x, y). \quad \text{Eq. 3.8}$$

In the final step, tsunami Green's functions from unit slip on the  $i$ th subfault were computed by convolution of the weighting factor  $m_i^k$  and the first tsunami Green's functions  $g_j^k(t)$  on unit sources of sea-surface displacement:

$$G_{ij}(t) = m_i^k g_j^k(t), \quad \text{Eq. 3.9}$$

where at  $G_{ij}(t)$  is the tsunami Green's functions at  $j$ th station from unit slip on  $i$ th subfault.

In this new inversion method, the number of tsunami simulations was equivalent to the number of unit sources (113, here). This is far smaller than [*the number of fault models*] x [*the number of subfaults*], which is ~1,800 if each of the 18 fault models contain ~100 subfaults. Thus, the new method makes it possible to test the inversion analysis by assuming multiple fault models with numbers of subfaults. Moreover, because I reused the tsunami Green's functions from the unit sources in Chapter 3.2, no additional tsunami simulations were required here.

### 3.2.2.2 Inverse problem

Slip distributions on fault models were obtained by solving the observation equations with the damped least-square method:

$$\begin{bmatrix} \mathbf{b} \\ \mathbf{0} \end{bmatrix} = \begin{bmatrix} \mathbf{G} \\ \alpha \mathbf{I} \end{bmatrix} \mathbf{s}^T, \quad \text{Eq. 3.10}$$

where  $\mathbf{b}$  ( $= w_j b_j$ ) is the column vector of the observed waveforms  $b_j$  weighted by  $w_j$  at the  $j$ th station ( $j = 1, 2, \dots, M$ ) (Eq. 3.4),  $\mathbf{G}$  is the matrix of the tsunami Green's functions  $G_{ij}$  weighted by  $w_j$  ( $j = 1, 2, \dots, N$ ),  $\mathbf{s}$  ( $= s_i$ ) is the unknown row vector of slip amounts of the  $i$ th subfault,  $\mathbf{I}$  is the identity matrix, and  $\alpha$  is the damping parameter. To obtain a smooth source model, I set a proper damping parameter  $\alpha$  as 0.3 in the same way as explained in Chapter 3.2.2; this was used for all inversion results given in the next subsection.

The new inversion method proposed here has an advantage over another efficient method, “two-step slip inversion” [e.g. *Ho et al.*, 2017; *Gusman et al.*, 2018; *Hossen et al.*, 2018]. In that method, the initial sea-surface displacement is first inverted from tsunami records, then inverted to slip distributions. However, because the inversion of initial sea-surface displacement has no constraint from fault geometries, artifact signals resulting from a limited azimuthal coverage of stations or noises are likely to arise regardless of geometry, as shown in Chapter 3.2. Hence, the slip inversion method relating fault slips indirectly to tsunami records may result in misvaluations of slip distributions. On the other hand, the proposed method can relate slips on assumed fault models directly to tsunami records, making it possible to evaluate slips on fault models without contamination by artifacts from sea-surface displacement models. However, if unrealistic source structures are assumed, tsunami signals are imposed on them, leading to misunderstandings of the source. Hence, source structures should be considered carefully by estimating

the initial sea-surface displacement before the application of this method, as done in Chapter 3.1. It is noted that slip patterns with smaller scales than unit source sizes may not be resolved by the method due to the approximation of sea-surface displacements, which is discussed in Chapter 3.2.4.

### 3.2.3 Results

The main purpose of the slip inversion analysis was to examine whether the hypothetical source mechanisms were reasonable or not. Figure 3.11 shows the inverted slip distributions for the 18 fault models, while Table 3.1a presents the maximum and minimum amounts for the ring and horizontal faults with the NRMS misfit between synthetic and observed tsunami waveforms. In terms of the waveform fitness, all the slip distributions on the 18 assumed fault models sufficiently reproduced tsunami records at the observation networks with NRMS values of 0.24–0.28. Figures. 3.12–3.14 show the resulting sea-surface displacements and waevform comparisons for Models 4 (2 km/TR/75°), 9 (2 km/FR/75°), and 14 (2 km/TR/75°), which explained the tsunami records with good agreement. All the slip models had common features in their resultant initial sea-surface displacements (large uplift on the northeastern part of the caldera floor and clear subsidence along the rim structure on the same side), regardless of variable fault parameters. Therefore, the hypothetical composite models can reasonably explain tsunami records in a quantitative manner.

In the following sub-subsections, I consider optimal fault geometries from the point of view of the waveform fitness and slip distributions.

**Table 3.1 Results of the inversion of tsunami waveforms**

(a) Maximum and minimum amounts of ring-fault slips and tensile opening of the horizontal fault, and tsunami NRMS misfit in the inversion time window for 18 fault models.

Model #	Thick-ness [km]	Portion	Dip [°]	Slip amount [m]				Tsunami NRMS
				Ring fault		Horizontal fault		
				max	min	max	min	
1	2.0	TR	60	3.98	-0.32	-0.01	-2.98	0.272
2			65	3.33	-0.04	0.39	-3.20	0.264
3			70	3.30	0.09	1.38	-3.18	0.261
4			75	3.21	0.00	2.26	-3.19	0.259
5			80	3.43	-0.03	2.28	-3.36	0.257
6		FR	60	3.76	-0.44	-0.72	-3.40	0.262
7			65	4.06	-0.71	0.52	-2.93	0.254
8			70	4.25	-1.20	1.57	-2.50	0.250
9			75	3.96	-1.40	2.30	-1.98	0.247
10			80	3.52	-1.44	2.46	-1.65	0.245
11		HR	60	3.98	1.00	1.60	-3.10	0.274
12			65	3.50	0.38	0.64	-3.03	0.269
13			70	3.59	-0.22	1.74	-2.82	0.267
14			75	4.00	-0.51	2.84	-2.80	0.265
15			80	4.42	-0.63	2.80	-3.04	0.263
16	4.0	TR	80	4.66	-1.74	3.71	-4.12	0.258
17		FR	80	4.27	-2.73	2.09	-2.60	0.252
18		HR	80	5.47	-3.03	4.08	-3.04	0.265

### 3.2.3.1 Thickness of the caldera block

Despite the good waveform fittings, the slip distributions of the fault models with a caldera block thickness of 4.0 km were phenomenologically unnatural. Figure 3.15 compares slip distributions for two fault models with different block thicknesses, Models 5 (2 km/TR/80°) and 16 (4 km/TR/80°). Model 5 represents thrust-faulting over most of the ring fault (Fig. 3.15a) while Model 16 has incompatible slip directions above and below the middle of the block (Fig. 3.15b). Because I hypothesized that the caldera moved upward overall as a block, these bimodal slips (upward and downward) on the ring fault were contradictory to the hypothesis. This contradiction was commonly found in all the slip models with a block thickness of 4 km, regardless of other fault parameters (Models 16–18 in Fig. 3.11). As this suggests that the subsurface caldera block of Smith Caldera is as thin as ~2.0 km, I only considered slip models with a block thickness of 2.0 km (Models 1–15) from this point onward.

### 3.2.3.2 Ruptured portion of the ring fault

I next considered the ruptured portion of the ring fault. Although the tsunami NRMS misfits showed slightly better waveform fitness from FR > TR > HR (Table 3.1a), the better fitness of the FR models may have been due to the larger numbers of fault parameters, or subfaults. Regardless of the ruptured portions, the slip models reproduced the observed tsunami waveforms sufficiently (Fig. 3.12–3.14), making it difficult to constrain the ruptured portion of the ring fault only from the tsunami waveforms. However, it is notable that even though the ring fault was assumed to extend to the SW part of the rim, the modeled initial sea-surface displacement was not significant above that part (compare Fig. 3.12b and Fig. 3.13b). This implies that a notable ring-fault slip did not occur there, which is considered further in Chapter 3.3.

### 3.2.3.3 Dip angle of the ring fault

The ring fault dip angle slightly affected the tsunami waveform fitness, as inferred from the minor decrease in NRMS misfits with steeper dip angle in all cases with the TR, FR, and HR models (Table 3.1a). This suggested that the ring fault was likely to have a steeper dip angle. Moreover, although the hypothetical mechanism requires an inflated source to move a caldera block upward, slip models with a dip angle smaller than 65° did not contain an inflated source (Models 1, 2, 6, 7, 11, and 12). This may also imply that the dip angle is steeper than 70°.

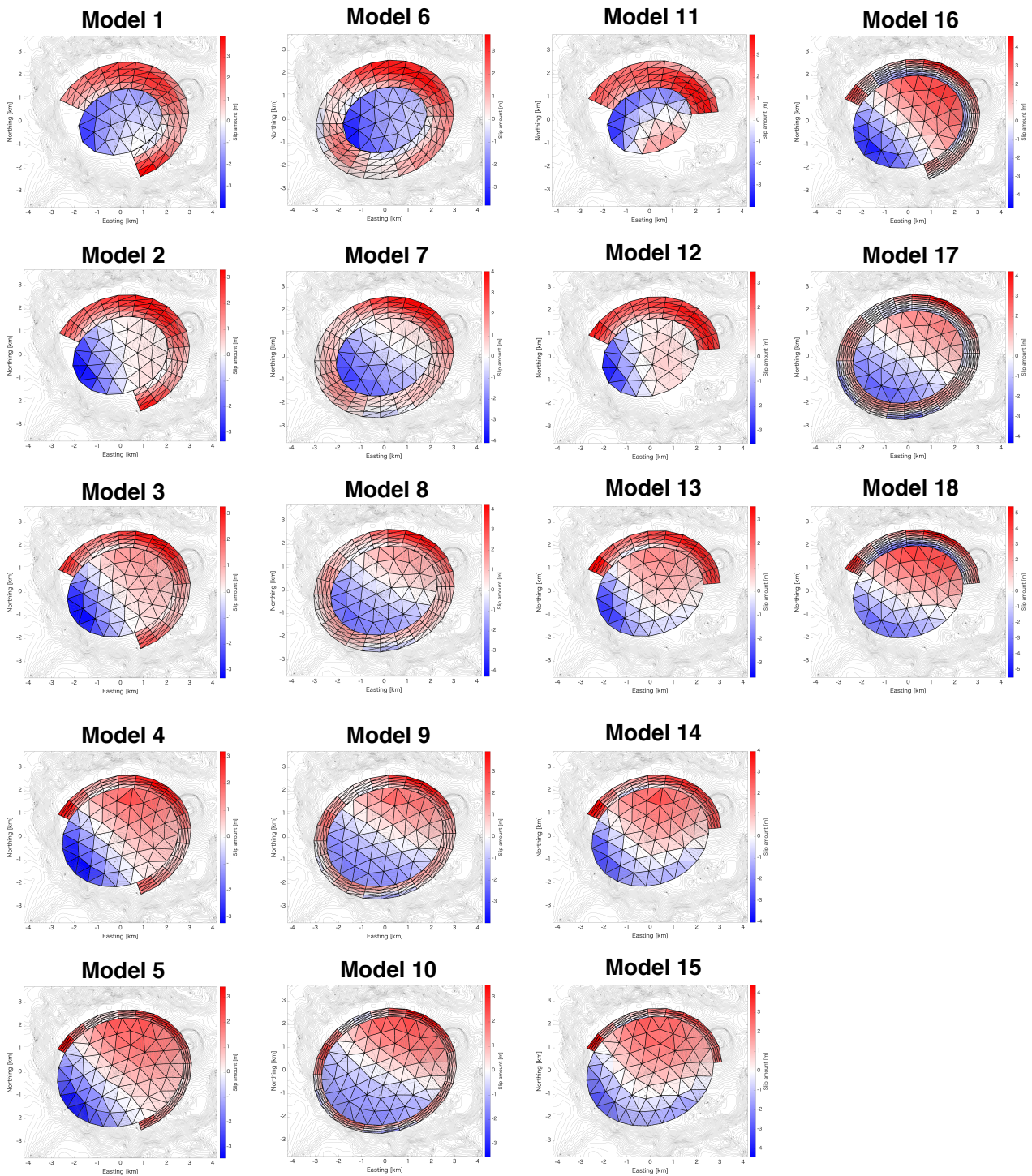


**Fig. 3.11 Slip distributions of the 18 fault models**

Colors represents amounts of dip slip of the ring fault, and opening of the horizontal fault, respectively. Red color represents a fault motion with a sense of upward motion of the caldera block, while blue color does in turn (i.e. Ring fault: Red and blue represents thrust and normal faulting, respectively. Horizontal fault: Red and blue represents opening and closing faulting, respectively).

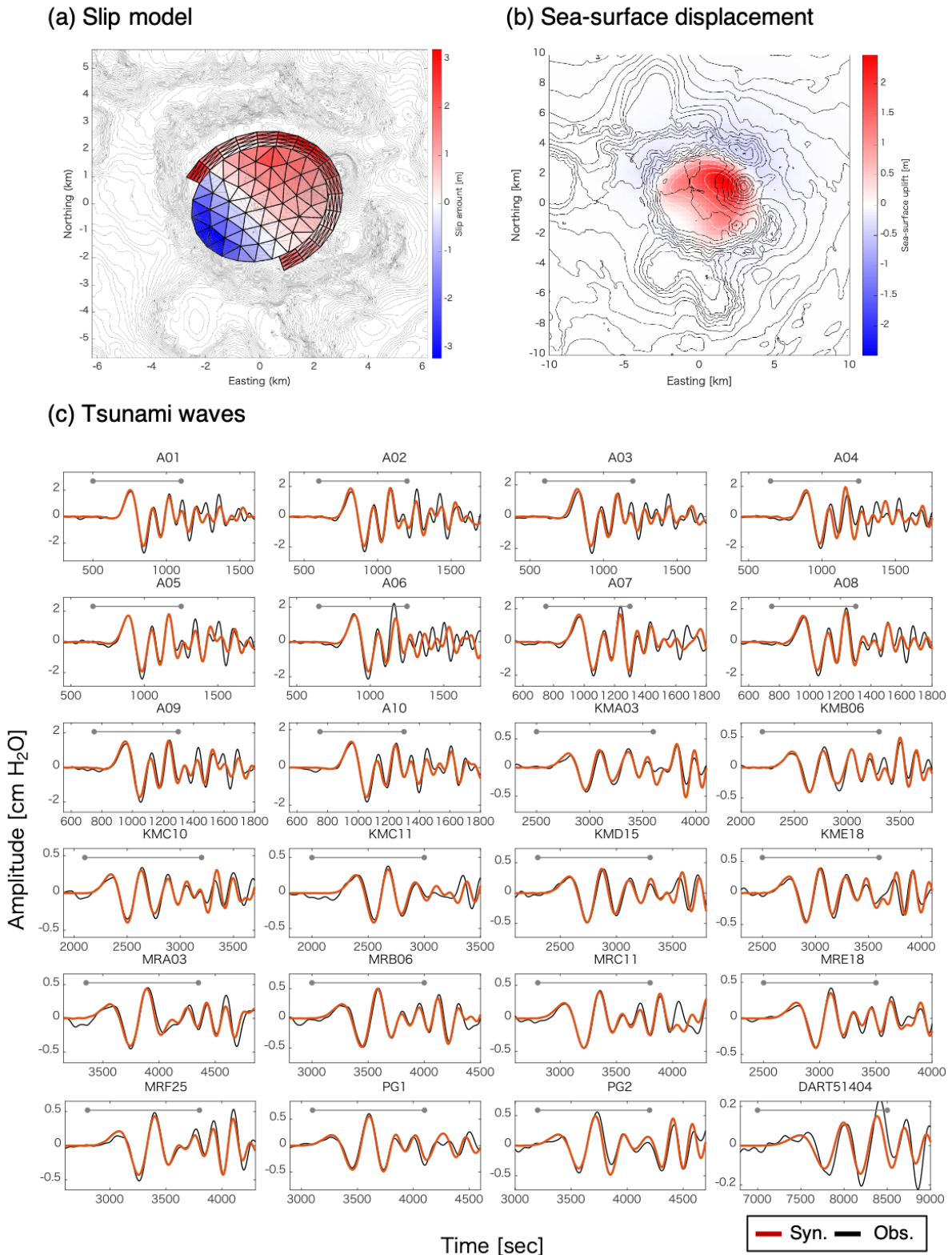
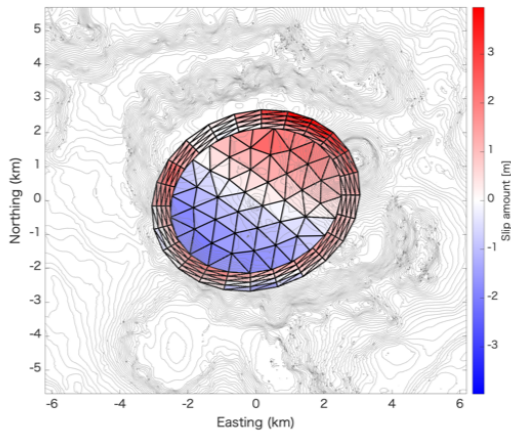


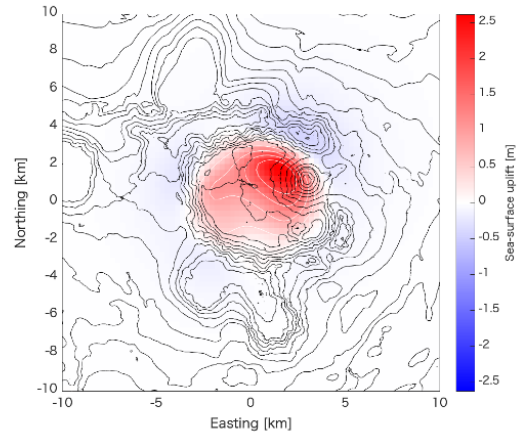
**Fig. 3.12 Slip inversion results of Model 4 (2 km/TR/75°)**

(a) Slip model. Color representations follow the caption of Fig. 3.11. (b) Inverted initial sea-surface uplifted displacement. (c) Waveform comparison of synthetic (red) and observed waves (black).

(a) Slip model



(b) Sea-surface displacement



(c) Tsunami waves

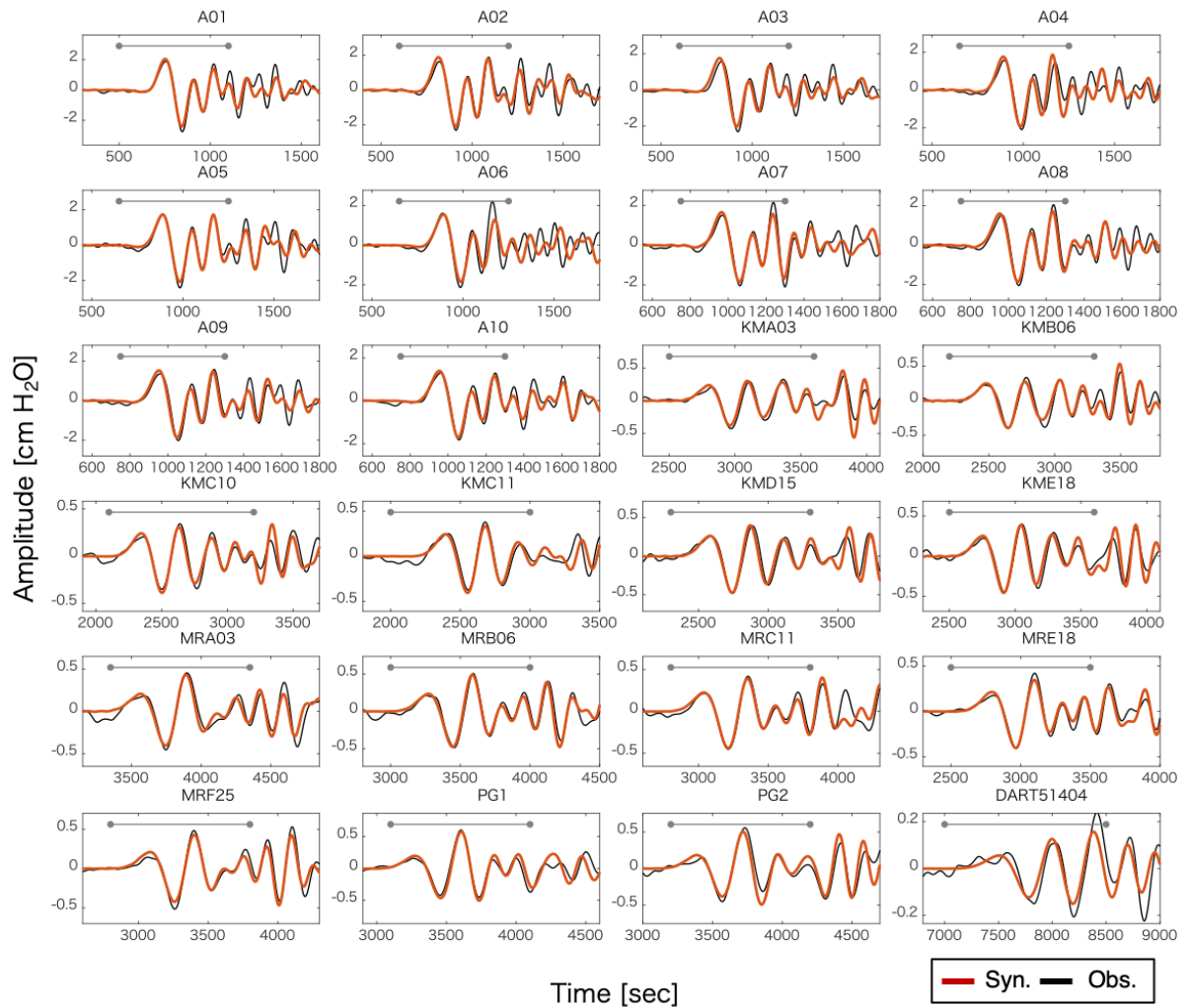
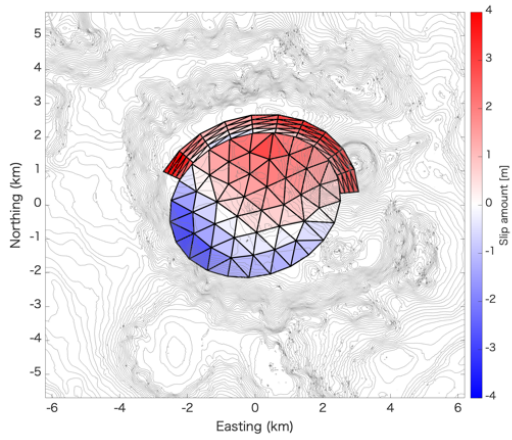


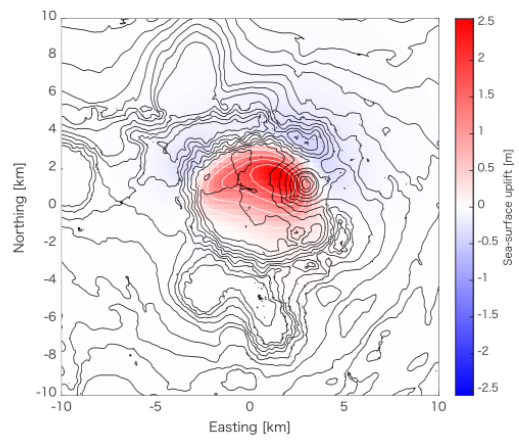
**Fig. 3.13 Slip inversion results of Model 9 (2 km/FR/75°)**

Same as Fig. 3.12.

(a) Slip model



(b) Sea-surface displacement



(c) Tsunami waves

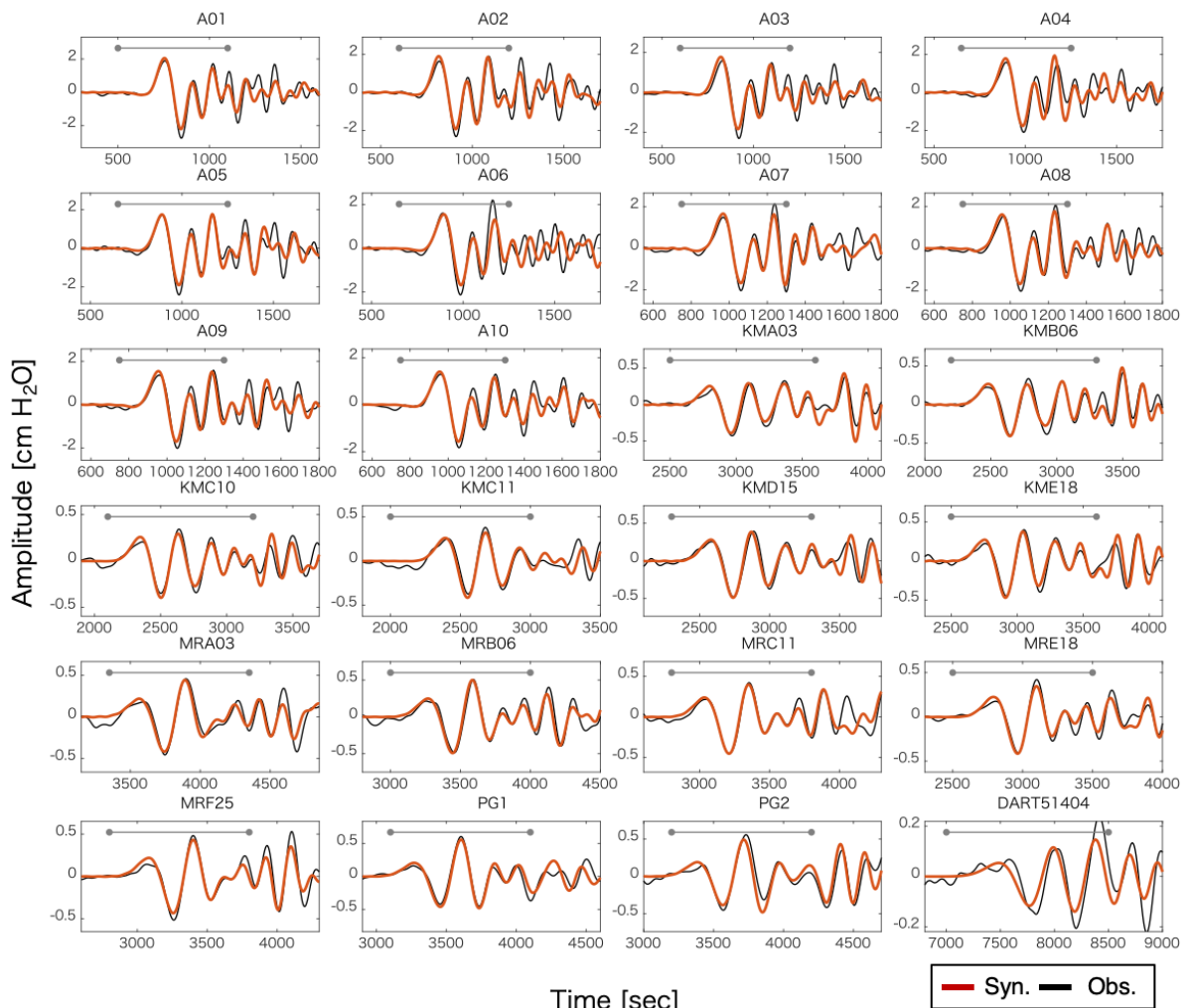
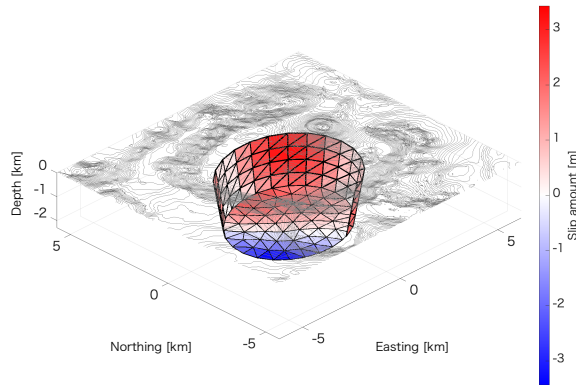


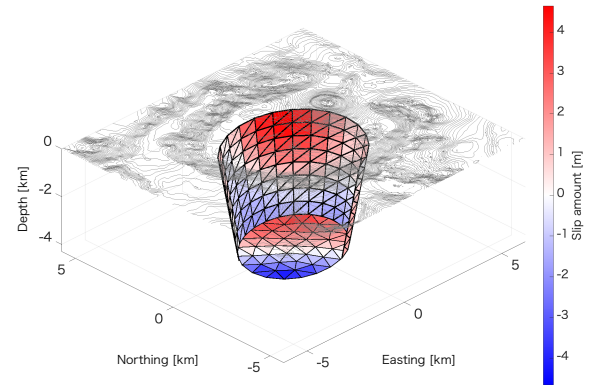
Fig. 3.14 Slip inversion results of Model 14 (2 km/HR/75°)

Same as Fig. 3.12.

(a) 2.0 km thickness



(b) 4.0 km thickness

**Fig. 3.15 Slip models with different block thickness**

Slip models of (a) Model 5 (2 km/TR/80°) and (b) Model 16 (4 km/TR/80°). Color representations follow the caption of Fig. 3.11.

### 3.2.4 Singular value decomposition

In general, the slip inversion problem is a function of instability. Since data have noise and models contain errors or approximations, inverted solutions contain artifacts due to small perturbations caused by such imperfections, and it is critical to suppress solutions sensitive to small perturbations. To evaluate the stability of the inverted solutions, I conducted singular value decomposition analysis (SDV) [e.g. *Menke, 2012*].

Based on the tsunami Green's functions from subfault slips  $\mathbf{G}$  [ $N$  rows  $\times$   $M$  columns] defined in Eq. 3.5, the matrix can be uniquely decomposed into:

$$\mathbf{G} = \mathbf{U}\mathbf{A}\mathbf{V}^T, \quad \text{Eq. 3.11}$$

where  $\mathbf{U}$  [ $N+1, M$ ] and  $\mathbf{V}$  [ $M, M$ ] are orthonormal matrixes, and  $\mathbf{A}$  is a diagonal matrix composed of singular values  $\lambda_i$  ( $i=1, 2, \dots, M$ ;  $\lambda_1 > \lambda_2 > \dots > \lambda_M$ ). Columns of  $\mathbf{V}_{(i)}$  of matrix  $\mathbf{V}$  are called singular vectors. In general, the solution of the inverse problem, or slip modes, can be expressed as a linear combination of singular vectors  $\mathbf{V}_{(i)}$ . Slip patterns constructed by singular vectors with relatively large singular values can be regarded as reliable, while others with smaller singular values (generally,  $< 1\%$  of the maximum  $\lambda_1$ ) are very sensitive to small errors in data and models.

I used SVD analysis of the tsunami Green's functions to consider the reliability of the solutions. For example, consider Model 4 (2 km/TR/75°; Fig. 3.12). Fig. 3.16a shows the singular values of the Green's functions, which decrease rapidly from the maximum ( $\lambda_1=6.278$ ) to around 1% of the maximum at  $i=11$  ( $\lambda_{11}=0.072$ ). Fig. 3.16c shows solutions reconstructed by contributions of singular vectors only up to  $i=1, 5, 10, 20, 50$ , and 100. The inverted solution shown in Fig. 3.16b was mostly expressed as singular vectors with singular values  $> 1\%$  of the maximum  $\lambda_i$ , and was not contributed to by patterns with near-zero singular values. This indicates that the overall pattern of the slip model was well-resolved from the

dataset, and that the damped least-square method (Eq. 3.5) successfully suppressed slip patterns sensitive to small perturbations due to data and model imperfections. However, more detailed slip patterns may not be resolved only with the tsunami dataset available here and the inversion method containing approximations of sea-surface displacement to compute tsunami Green's functions efficiently.

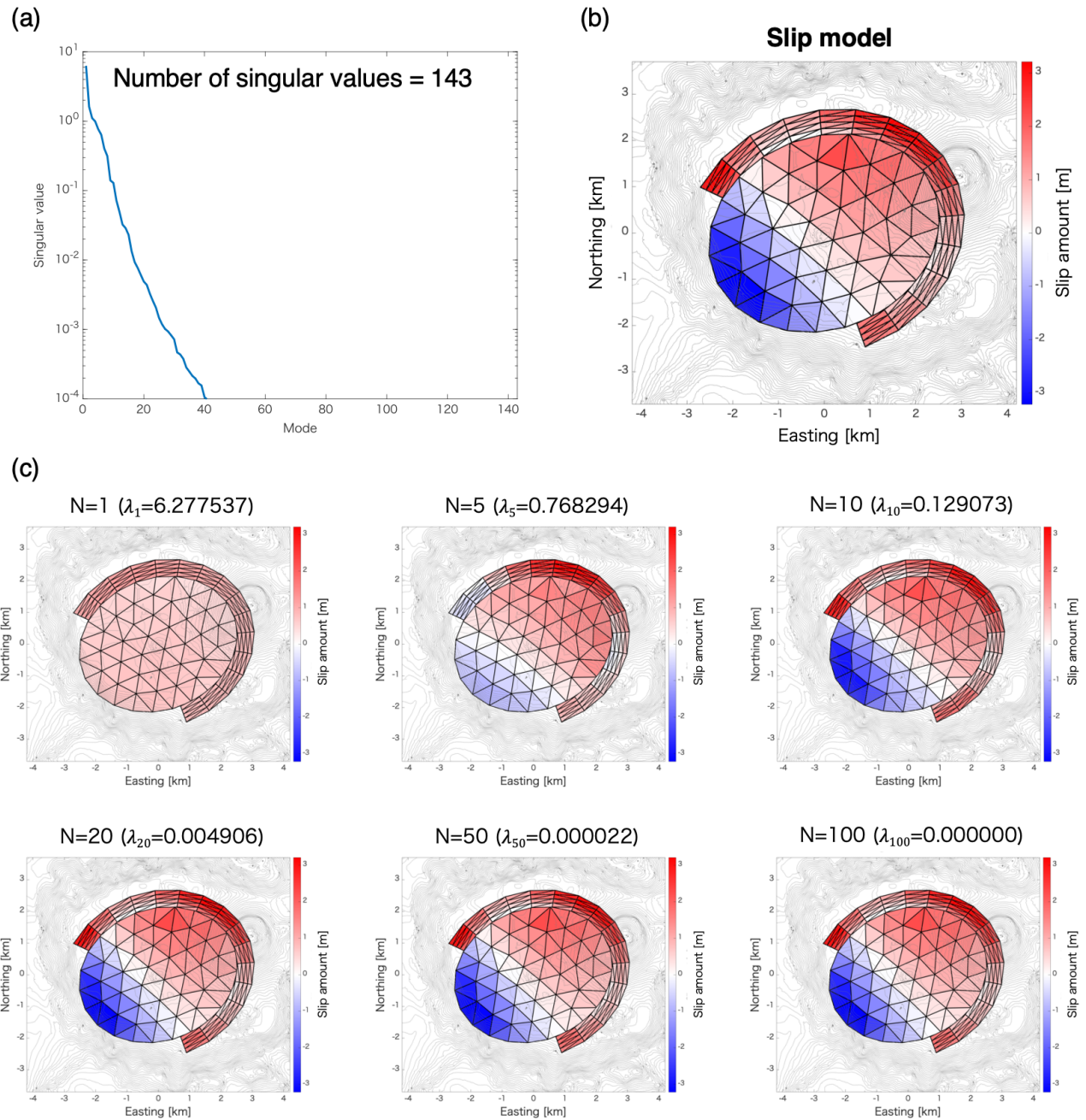


**Fig. 3.16 Singular value decomposition**

(a) Singular values of matrix of the tsunami Green's functions from subfault slips of Model 5. (b) The solution of the inverse problem assuming Model 5. (c) Reconstructions of the solution only with singular vectors up to  $i=1, 5, 10, 20, 50,$  and  $100,$  respectively.

### 3.3 Forward modeling of long-period seismic waves

In the previous section, I successfully modeled slip models based on the hypothetical physical mechanism, which explained the observed tsunami records and was phenomenologically reasonable. In this section, I conduct forward modeling of long-period seismic waves excited by the slip models. By comparing synthetic seismic waves with the observed records at regional seismic stations, I examine the validity of the slip models in a quantitative manner using seismic waves. The fault geometries are also pursued on the basis of the waveform fitting level. Note that the slip models were inverted only from tsunamis, not seismic waves.

#### 3.3.1 Methods and Data

##### 3.3.1.1 Moment tensor modeling of slip models

I first obtained moment tensors of the slip models by summing up moment tensors of slip on each subfault (Fig. 3.17a). The coordinate system was the same as that used in the Harvard Centroid Moment Tensor project:  $(r, \theta, \phi)$  for [up, south, east]. A composite moment tensors of slip models  $\mathbf{M}$  was computed as:

$$\mathbf{M} = \mathbf{M}_{RF} + \mathbf{M}_{HF} = \sum \mathbf{m}_{RF}^k + \sum \mathbf{m}_{HF}^l, \quad \text{Eq. 3.12}$$

where  $\mathbf{M}_{RF}$  and  $\mathbf{M}_{HF}$  represents a moment tensor of slips on a ring fault and a horizontal fault, respectively,  $\mathbf{m}_{RF}^k$  and  $\mathbf{m}_{HF}^l$  are the moment tensors on each subfault, and superscripts  $k$  and  $l$  are the number of subfaults. Moment tensors of subfault dip-slip on the ring fault  $\mathbf{m}_{RF}^k$  were computed with the slip amount and strike, dip, and rake ( $90^\circ$ ) angles following *Aki and Richards* [1980]. Their seismic moments were  $m_0 = \mu \times \Delta u_k \times S_k$ , where  $\Delta u$  and  $S$  are slip amount and area, subscript  $k$  represents the number of subfault on the ring fault, and  $\mu$  is rigidity (31.85 GPa, here). The moment tensors of subfault slips on the horizontal fault  $\mathbf{m}_{HF}^l$  were computed as:

$$\mathbf{m}_{HF}^l = \begin{bmatrix} M_{rr} & M_{\theta r} & M_{\phi r} \\ M_{r\theta} & M_{\theta\theta} & M_{\phi\theta} \\ M_{r\phi} & M_{\theta\phi} & M_{\phi\phi} \end{bmatrix} = \Delta u_l \times S_l \times \begin{bmatrix} \lambda + 2\mu & 0 & 0 \\ 0 & \lambda & 0 \\ 0 & 0 & \lambda \end{bmatrix}, \quad \text{Eq. 3.13}$$

where  $\Delta u$  and  $S$  are the slip amount and area of each subfault of the horizontal fault, respectively [e.g. *Kawakatsu and Yamamoto*, 2007]. Lamé's constant  $\lambda$  is assumed as 29.9 GPa, computed with the shear velocity in the velocity structure used in this study (explained in the following sub-subsection).

A scalar seismic moment of a moment tensor was computed following the definition given by *Silver and Jordan* [1982] and *Dahlen and Tromp* [1998]:

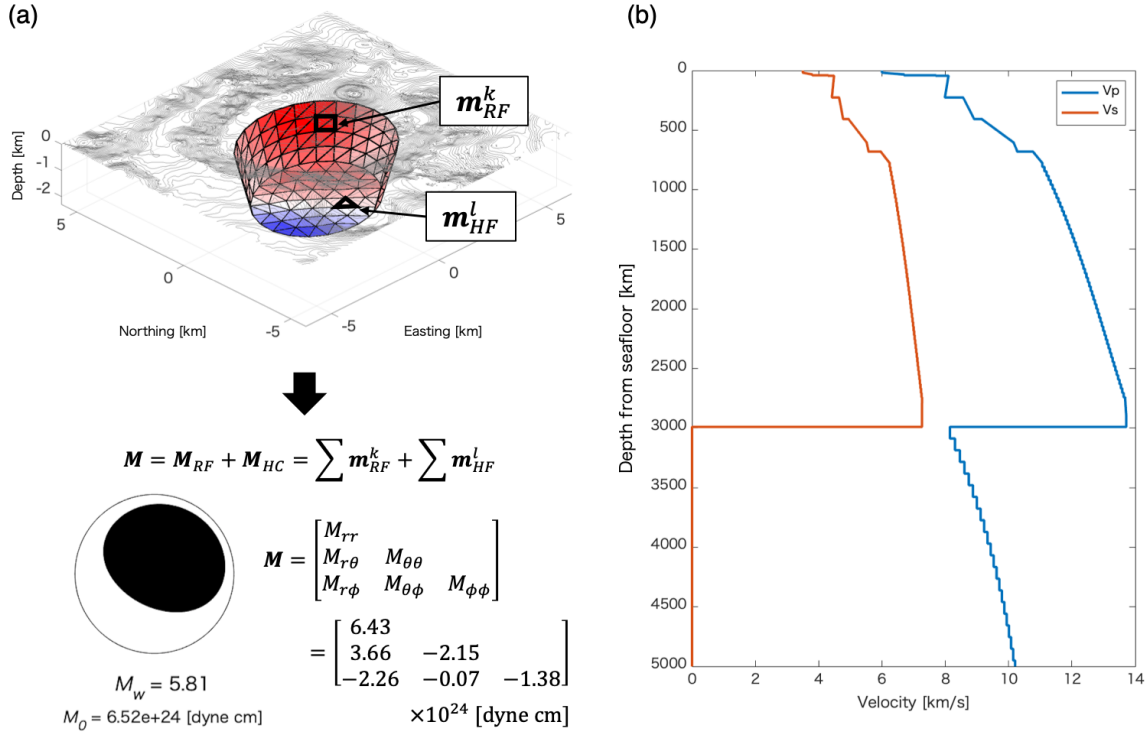


**Fig. 3.17 Computation of moment tensor from a slip model and 1-D velocity structure**

(a) Moment tensor modeling of slip models (see text). Model 4 (TR/75°/2 km) is shown as an example. (b) 1-D velocity structure used in this study.

$$M_0 = \sqrt{\sum_{ij} M_{ij} M_{ij} / 2}, \quad \text{Eq. 3.14}$$

Their moment magnitudes were then computed as:

$$M_w = \frac{2}{3} (\log_{10} M_0 - 16.10), \quad \text{Eq. 3.15}$$

with  $M_0$  in the [dyne cm] scale [e.g. *Kanamori, 1977; Hanks and Kanamori, 1979*].

### 3.3.1.2 Forward simulations of long-period seismic waves

I then computed the long-period seismic waves of the slip models by assuming the moment tensors as initial conditions. W-phase package code was used for the computation process, including filtering, data screening, and convolution of Green's functions [*Kanamori and Rivera, 2008; Hayes et al., 2009; Duputel et al., 2012*]. Green's functions were computed with *Herrmann's* [2013] implementation of the integral wavenumber method over the one-dimensional velocity structure of Japan's crust model (Fig. 3.17b). The centroid location was set as the center of Smith Caldera (140.053° E, 31.485° N) and the depth was assumed as 1.5 km below the seafloor. Both the half duration and the centroid time shift were assumed to be 5 s, as obtained by the W-phase inversion (Chapter 5.2). In the filtering procedure, long-period

seismic signals were extracted from synthetic displacement records by applying the one-pass and fourth-order Bandpass Butterworth filter with corner frequencies of 0.004 and 0.0167 Hz (band-pass period from 60–250 s).

I used long-period energy from 60–250 s in the W-phase of the seismic waves to quantify the waveform fitness between the model and data with the normalized root-mean-square (NRMS) misfit:

$$\frac{1}{N_s} \rho_i = \frac{1}{N} \sum_{i=1}^{N_s} \frac{\|\mathbf{s}_w^i - \mathbf{d}_w^i\|}{\|\mathbf{s}_w^i\|}, \quad \text{Eq. 3.16}$$

where  $\mathbf{s}_w^i$  and  $\mathbf{d}_w^i$  are the synthetic and observed records in the W-phase of seismic waves, respectively, which were determined following the definition of *Kanamori and Rivera* [2008] at  $i$ th channels ( $i=1, 2, \dots, N_s$ ).  $\rho_i$  is the NRMS error at a single channel. Only channels with good quality were used to compute seismic NRMS misfits, which can be well modeled by the zero-trace W-phase inversion using only  $\rho_i < 0.9$ .

One advantage of using the W-phase is the fast propagation speeds from 4.5–9 km/s [e.g. *Kanamori and Rivera*, 2008]. Given that the 2015 Torishima earthquake had a source size of  $\sim 7$  km and a short rupture duration of  $\sim 10$  s, as inferred from the W-phase inversion analysis described in Chapter 5.2, it is reasonable to describe the source models as moment tensors by point-source approximation. Another advantage derives from the fact that major energy was confined to mantle depth, where lateral heterogeneity was relatively small. Thus, waveforms in the phases were not affected by complex structures related to the shallow crust or oceanic layers, enabling an examination of the validity of source models without concerns regarding other effects such as uncertain velocity structures or complex topography around the caldera.

### 3.3.1.3 Broad-band seismic records

For waveform comparisons of synthetic waveforms with the observations, I used broad-band seismic records (LH channel) of the 2015 Torishima earthquake observed at F-net stations in Japan [*NIED*, 2019b]. To compensate for the azimuthal coverage of the stations, I also used LH- and BH-channel data from seismic stations of the Global Seismograph Network (GSN) downloaded from the Incorporated Research Institutions for Seismology (IRIS). All datasets were composed of stations within  $30^\circ$  of the epicentral distances. After performing the same filtering as used for the simulated data, observed velocity records were integrated to determine displacement.

## 3.3.2 Results

Table 3.1b shows moment magnitudes, scalar seismic moments, moment tensors, and seismic NRMS misfits for the 15 models with 2 km thick caldera blocks (Model 1–15). Their moment magnitudes were similar (5.7–5.9) and slightly larger than that of the reported GCMT solution (Table 1.1a). The focal mechanism and the fitness of long-period seismic waveforms for Model 5 (2 km/TR/ $75^\circ$ ) is presented in Fig. 3.18, showing a vertical-CLVD type similar to the GCMT solution (Fig. 1.1). The fitness of the seismic waves was quite good at most stations, demonstrating the plausibility of the slip model.

**Table 3.2 Results of the forward modeling of long-period seismic waves**

Moment magnitude, scalar seismic moment, and moment tensors, and seismic NRMS misfit of 15 models with 2-km thick caldera block. Stations (channels) used to compute seismic NRMS misfits are

Model #	Portion	Dip [°]	$M_w$	$M_\theta$ [ $10^{24}$ dyne cm]	Moment tensor [10 <sup>24</sup> dyne cm]						Seismic NRMS
					$M_{rr}$	$M_{\theta\theta}$	$M_{\phi\phi}$	$M_{r\theta}$	$M_{r\phi}$	$M_{\theta\phi}$	
1	TR	60	5.89	8.66	1.00	-9.42	-6.49	2.48	-1.62	-0.55	0.639
2		65	5.84	7.36	2.46	-7.04	-4.98	3.17	-1.94	-0.23	0.557
3		70	5.81	6.49	4.42	-4.52	-3.20	3.51	-2.16	-0.11	0.443
4		75	5.81	6.52	6.43	-2.15	-1.38	3.66	-2.26	-0.07	0.354
5		80	5.85	7.45	8.50	0.11	0.50	3.74	-2.29	-0.04	0.686
6	FR	60	5.93	9.87	-0.98	-10.58	-8.20	2.30	-1.13	0.83	0.645
7		65	5.88	8.46	-0.25	-8.50	-7.17	2.72	-1.12	1.04	0.579
8		70	5.81	6.61	1.44	-6.09	-5.35	2.82	-1.14	0.73	0.488
9		75	5.75	5.25	3.31	-3.76	-3.39	2.79	-1.13	0.42	0.393
10	80	5.74	5.08	5.55	-1.35	-1.17	2.73	-1.12	0.21	0.533	
11	HR	60	5.85	7.61	3.35	-7.01	-5.07	3.71	-0.91	0.42	0.562
12		65	5.84	7.27	4.43	-5.33	-3.77	4.53	-1.06	0.39	0.493
13		70	5.84	7.27	6.31	-3.08	-2.12	4.94	-1.20	0.35	0.400
14		75	5.87	7.93	8.25	-0.92	-0.41	5.17	-1.25	0.27	0.453
15		80	5.91	9.14	10.17	1.09	1.33	5.31	-1.23	0.18	1.068

**Station List**

AOG (LHE, LHN, LHZ) HJO (LHE, LHN, LHZ) KZS (LHE, LHN, LHZ) KNY (LHE, LHN, LHZ) FUJ (LHE, LHN, LHZ) SGN (LHE, LHN, LHZ) KIS (LHE, LHN, LHZ)  
NAA (LHE, LHN, LHZ) KMT (LHE, LHN, LHZ) TTO (LHN, LHZ) TSK (LHE, LHN, LHZ) ONS (LHN, LHZ) OSW (LHN, LHZ) NOK (LHE, LHN, LHZ)  
TGA (LHE, LHN, LHZ) KNM (LHE, LHN, LHZ) ABU (LHE, LHN) ASI (LHZ) MAJO (LH1, LHZ) ISI (LHE, LHZ) YMZ (LHE, LHN, LHZ)  
UMJ (LHE, LHN, LHZ) SRN (LHE, LHN, LHZ) HRO (LHN, LHZ) YAS (LHN, LHZ) YZK (LHE, LHN, LHZ) KZK (LHN, LHZ) OKW (LHE, LHN, LHZ)  
TSA (LHE, LHN, LHZ) NRW (LHZ) WJM (LHE, LHN, LHZ) SBT (LHN, LHZ) TGW (LHZ) KSK (LHE, LHN, LHZ) YSI (LHZ)  
NSK (LHE, LHN, LHZ) SAG (LHE, LHN, LHZ) TKO (LHE, LHZ) KSN (LHE, LHN, LHZ) INN (LHE, LHN, LHZ) TAS (LHE, LHZ) TYS (LHE, LHN, LHZ)  
YTY (LHE, LHN, LHZ) SIB (LHZ) KYK (LHE, LHZ) GJM (LHN, LHZ) SBR (LHE, LHN, LHZ) IYG (LHE, LHN, LHZ) STM (LHZ)  
TMR (LHE, LHN, LHZ) AMM (LHZ) KMU (LHN, LHZ) KGM (LHZ) HID (LHZ) HSS (LHZ) URH (LHZ)  
KSR (LHZ) INCN (LHZ) KNP (LHZ) NOP (LHN, LHZ) SHR (LHZ) NKG (LHZ) MDJ (LH1, LHZ)  
YSS (LHZ) GUMO (LHZ) BJT (LH1)

### 3.3.2.1 Dip angle of the ring fault

Comparing the seismic NRMS misfits for Models 1–15, it is notable that the misfits changed significantly with the ring fault’s dip angle (Table 4.1b). For example, models with TR portions (Models 1–5) had misfit value changes from 0.639 to 0.354, the same as for FR (Models 6–10) and HR (Models 11–15). Figure 3.19 demonstrates that the synthetic wave amplitudes of Model 1 (2 km/TR/60°) were much larger than for Model 5 (2 km/TR/80°) by ~3 times, despite their similar seismic magnitudes (5.89 and 5.85, respectively). This major difference in amplitude levels can be attributed to the aseismic properties of  $M_{r\theta}$  and  $M_{r\phi}$  at shallow depth [e.g. Kanamori and Given, 1981]. The moment tensor components were more dominant for dip slips with steeper dip angles, resulting in less seismic properties of models with steeply dipping ring faults; this is further discussed in Chapter 5.2.

The sensitivity of the seismic amplitudes can be therefore be used to constrain the optimal dip angle of the ring fault. I next examined the optimal dip angles for the TR, FR, and HR models; because these had smaller values at dip angles of 75°, 75°, and 70°, respectively (Table 4.1b), I assumed fault models with different dip angles by 1° intervals in the angle ranges (TR: 70–80°, FR: 70–80°, HR: 65–75°). I then inverted the slip distributions by the tsunami waveform inversion and computed long-period seismic waves. Finally, I calculated the seismic NRMS misfits for the slip models with 1° interval dip angles (Fig. 3.20a-c). In all cases, small NRMS misfit values were confined to within a few degrees of the dip angle of the ring fault. Therefore, the optimal dip angles can be determined as 75°, 76°, and 72° for the TR, FR, and HR models, respectively.

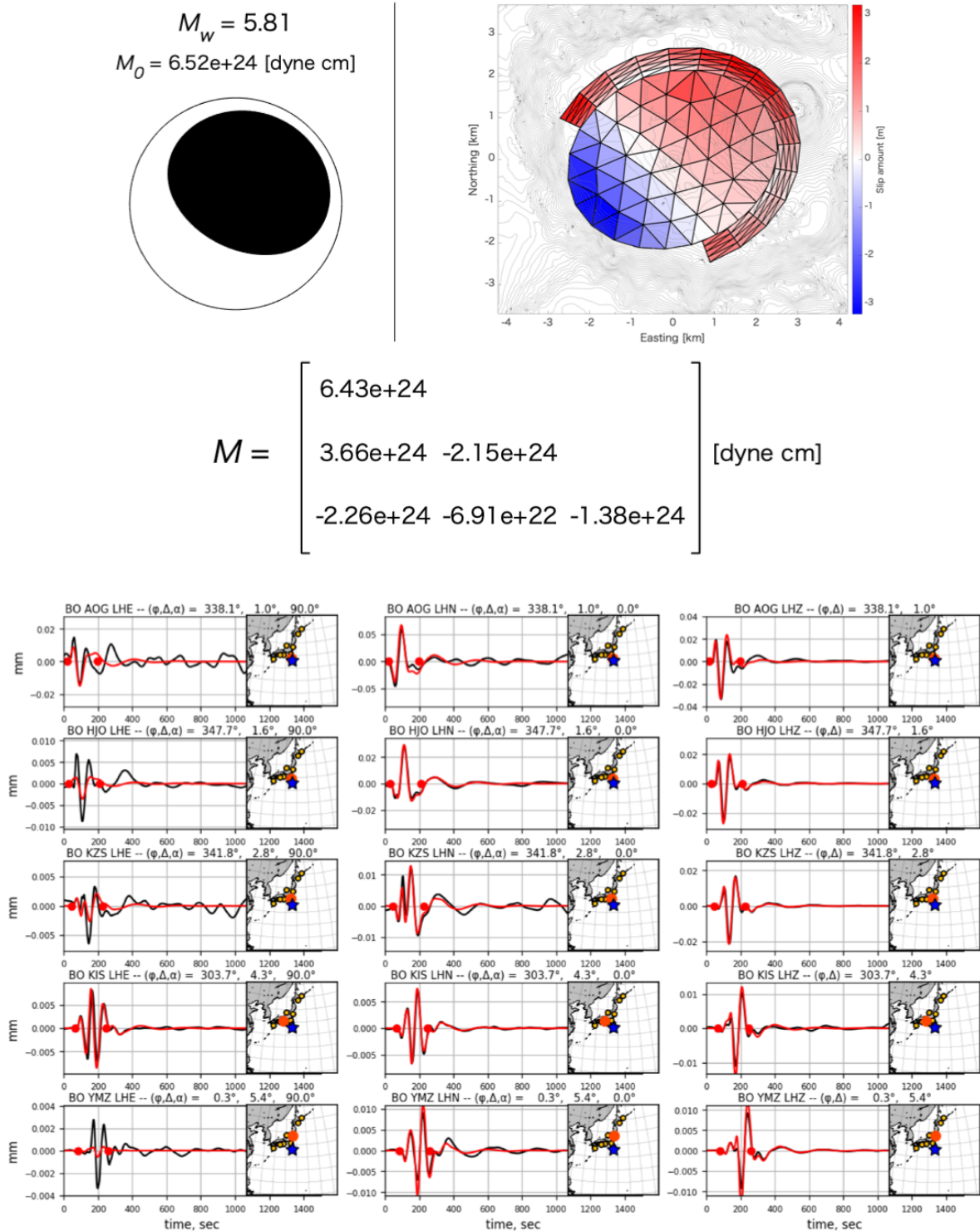


**Fig. 3.18 Long-period seismic waves of the best TR model (TR/75°/2 km)**

Moment tensor, slip model, and waveform comparisons are shown. Red and black lines represent synthetic and observed waveforms, respectively. Blue star and big orange circle represent locations of the epicenter (Smith Caldera) and a station, in inset figures. Tsunami and seismic NRMS misfits for the model are shown in Fig. 3.20e-f.

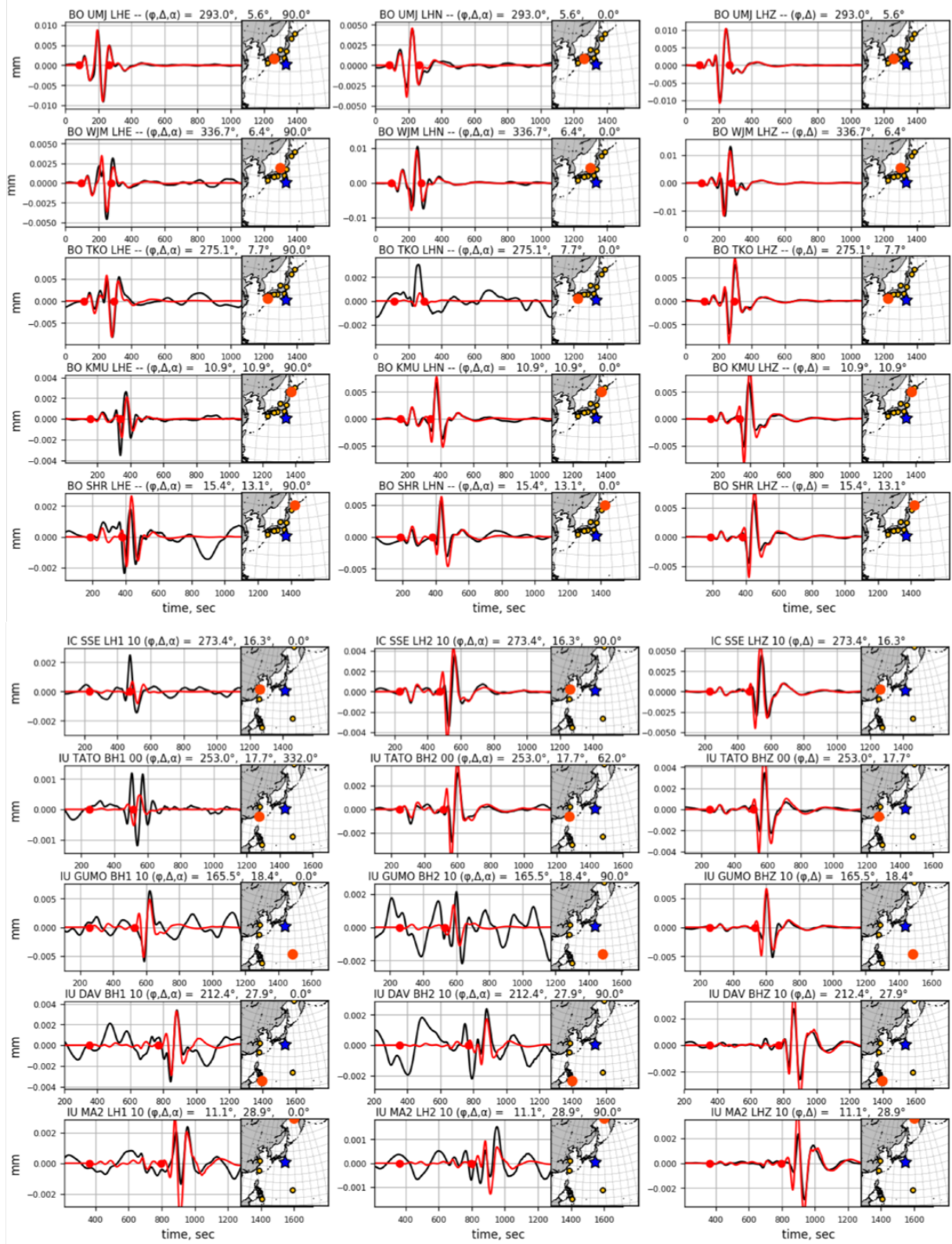
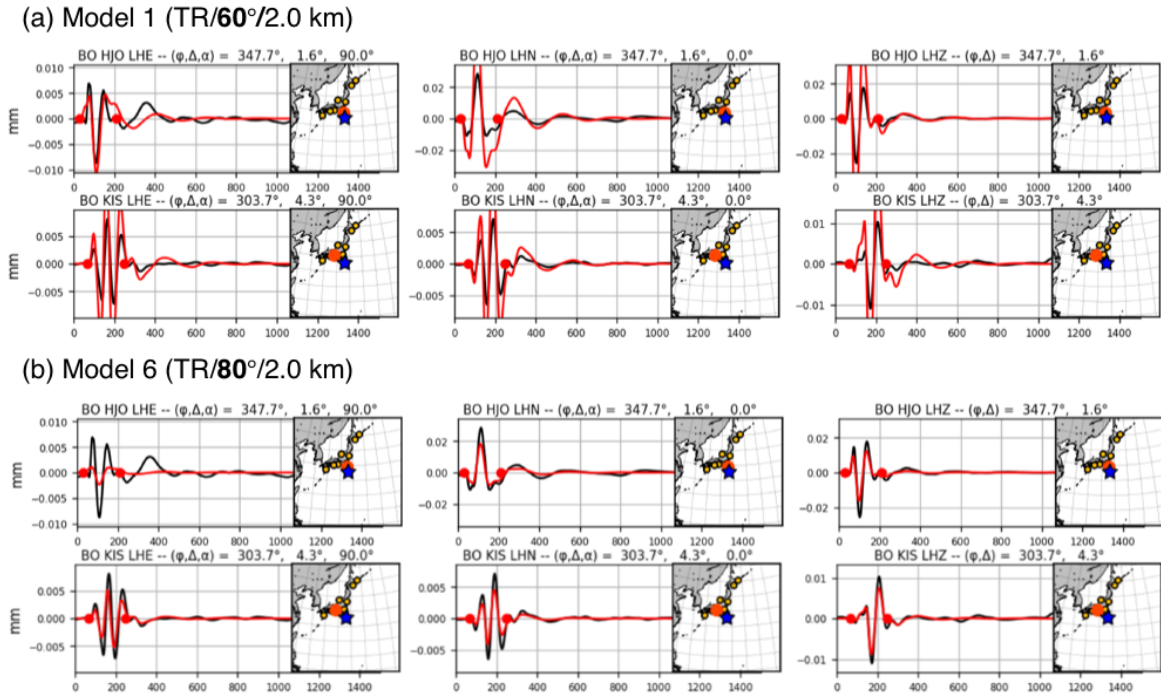


Fig. 3.18 Long-period seismic waves of the best TR model (TR/75°/2 km) (Continued)



**Fig. 3.19 Seismic waves of slip models with different ring-fault dip angles**

Waveform comparisons of Model 1 (TR/60°/2 km) and Model 6 (TR/80°/2 km). It is noted that amplitude levels of synthetic waves (red) are significantly different from model to model, despite their similarities in waveforms, or phases and polarities.

### 3.3.2.2 Ruptured portion of the ring fault

Here, I discuss three models: “best TR” (2 km/TR/75°, equivalent to Model 5), “best FR” (2 km/TR/76°), and “best HR” (2 km/HR/72°) as constructed above. Slip inversion results, moment tensor information, and tsunami and seismic NRMS misfits for these are shown in Fig. 3.20e-f. Based on the seismic NRMS misfits, the seismic wave fitness of the best TR model was clearly better than the others when using their optimal dip angles (Fig. 3.20d). Ruptured portions of the ring fault significantly affected the waveforms of the horizontal components of the long-period seismic waves, but less so the vertical components. Overall, for the best models shown in Fig. 3.18, 21-22, the vertical component waveforms (third column) showed good agreement at all stations. On the other hand, the horizontal component waveforms were significantly different from model to model (first and second columns). The horizontal-component waveforms showed better fitting for the best TR model than the FR and HR models, which can be seen clearly in the EW component at stations HJO, KZS, YMZ, KMU, SHR, and SSE, and the NS component at station TKO. This indicated that the best TR model (2 km/TR/75°) was the most likely kinematic source model of the 2015 Torishima earthquake of the three considered here.

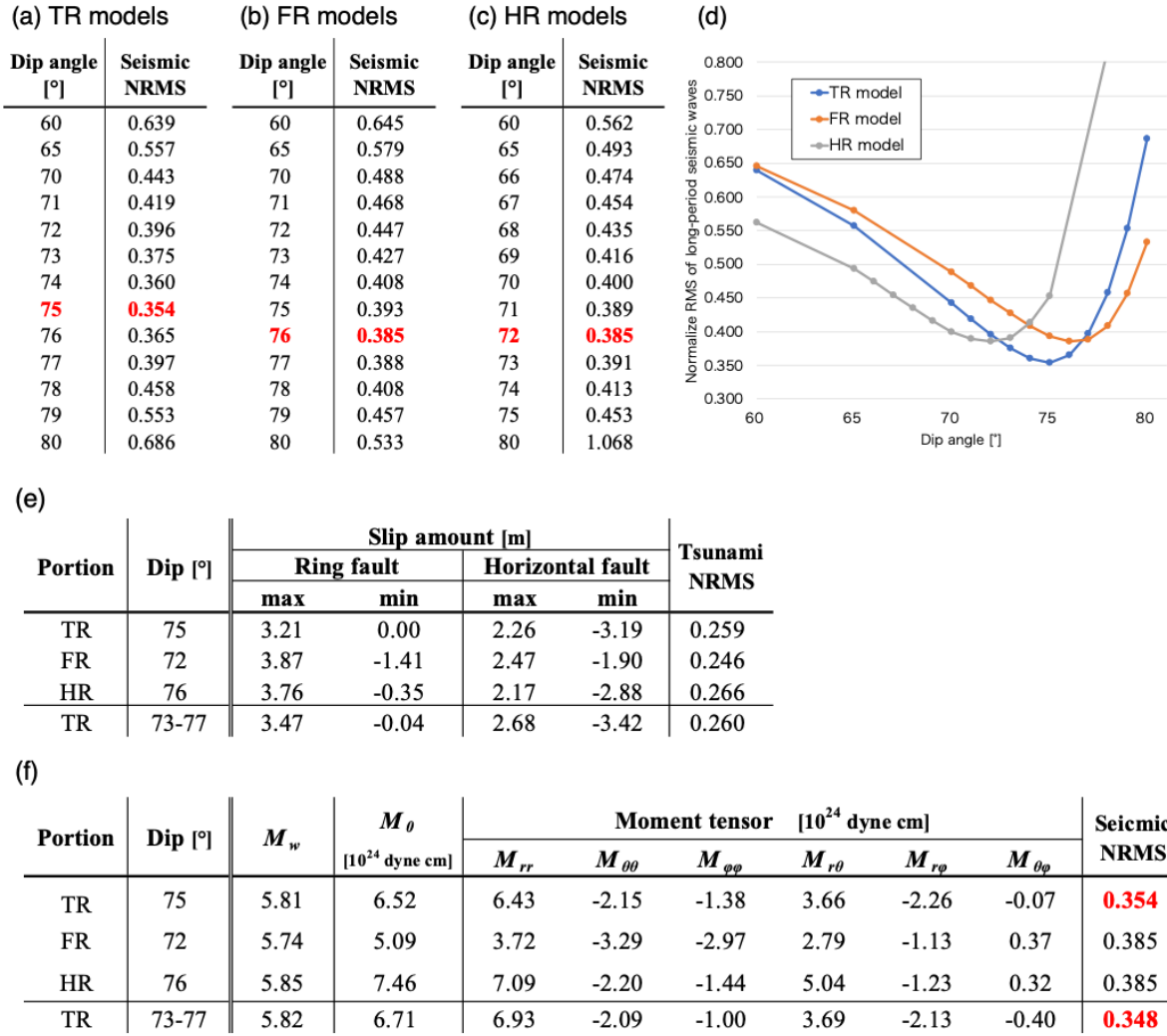


**Fig. 3.20** Grid-search for the best dip angle and best TR/FR/HR and heterogeneous-TR models

(a-c) Seismic NRMS misfits of different dip angles of (a) TR models, (b) FR models, and (c) HR models. (d) Comparisons of NRMS misfits for TR/FR/HR models. (e) Maximum and minimum amounts of ring-fault slips and tensile opening of the horizontal fault, and tsunami NRMS misfit and (f) Moment magnitude, scalar seismic moment, and moment tensors, and seismic NRMS misfit of the best-dip TR/FR/HR models and heterogeneous-dip TR model.

### 3.3.2.3 Possible constraints on fault geometries from long-period seismic waves

The significant variations in waveforms and amplitude levels, depending on the fault geometries, ruptured portions, and dip angles of the ring fault, implied the possibility that long-period seismic wave information could constrain source geometry. This is discussed in Chapter 5.2 by considering the characteristics of seismic radiation for idealistic fault models; note that the contributions to long-period seismic waveforms by the tensile opening/closing of the horizontal fault were negligible compared to those by slips on the ring fault.

### 3.3.2.4 Heterogeneity of the fault geometries

Even for the best TR model, the fitness of the seismic waveforms of horizontal components at some stations were relatively bad (Fig. 3.18). However, the fitness can be improved significantly by including a little heterogeneity in the TR model. Assuming a dip angle of  $77^\circ$  on the NE part and  $73^\circ$  on the other parts, I conducted the same analysis involving the inversion of tsunami waveforms and forward modeling of long-period seismic waves. In addition to good agreement in tsunami waveforms with the tsunami NRMS misfit of 0.260 (Fig. 3.23c, Fig. 3.20e), the fitness of the long-period seismic waves was significantly improved compared to the uniformly dipping model (compare Fig. 3.18 and Fig. 3.23). The seismic NRMS misfit was also smaller for the heterogeneous model (0.348) than uniform model (0.354; Fig. 3.20f). These results confirmed that the hypothetical mechanism was able to reproduce long-period seismic waves at high levels at all stations with sufficient azimuth coverage. The reason for the clear differences in waveform between the uniformly dipping model (the best TR model) and the heterogeneous-dip TR model will be discussed in Chapter 5.2.

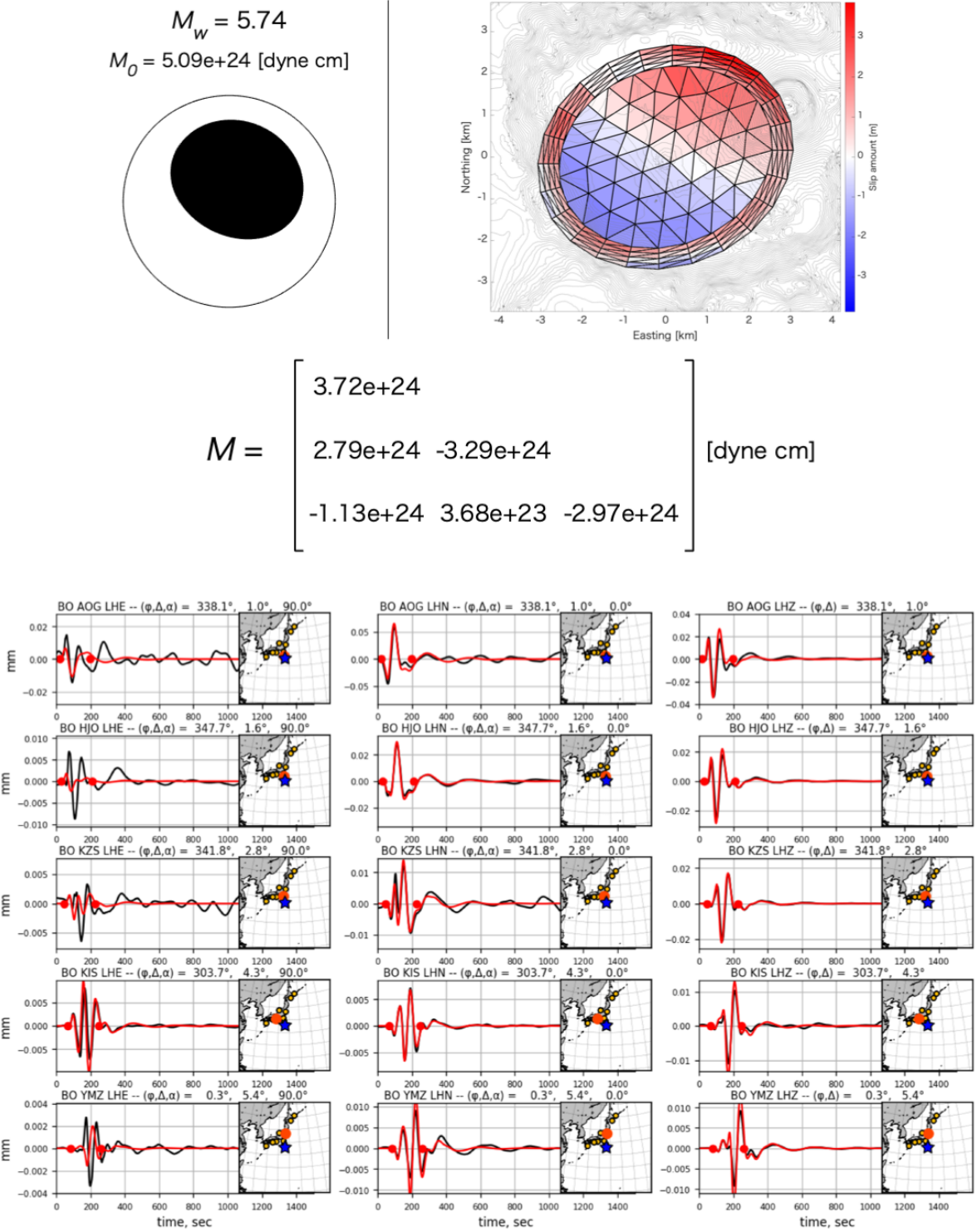


**Fig. 3.21 Long-period seismic waves of the best FR model (FR/76°/2 km)**  
 See the caption of Fig. 3.18. Tsunami and seismic NRMS misfits for the model are shown in Fig. 3.20e-f.

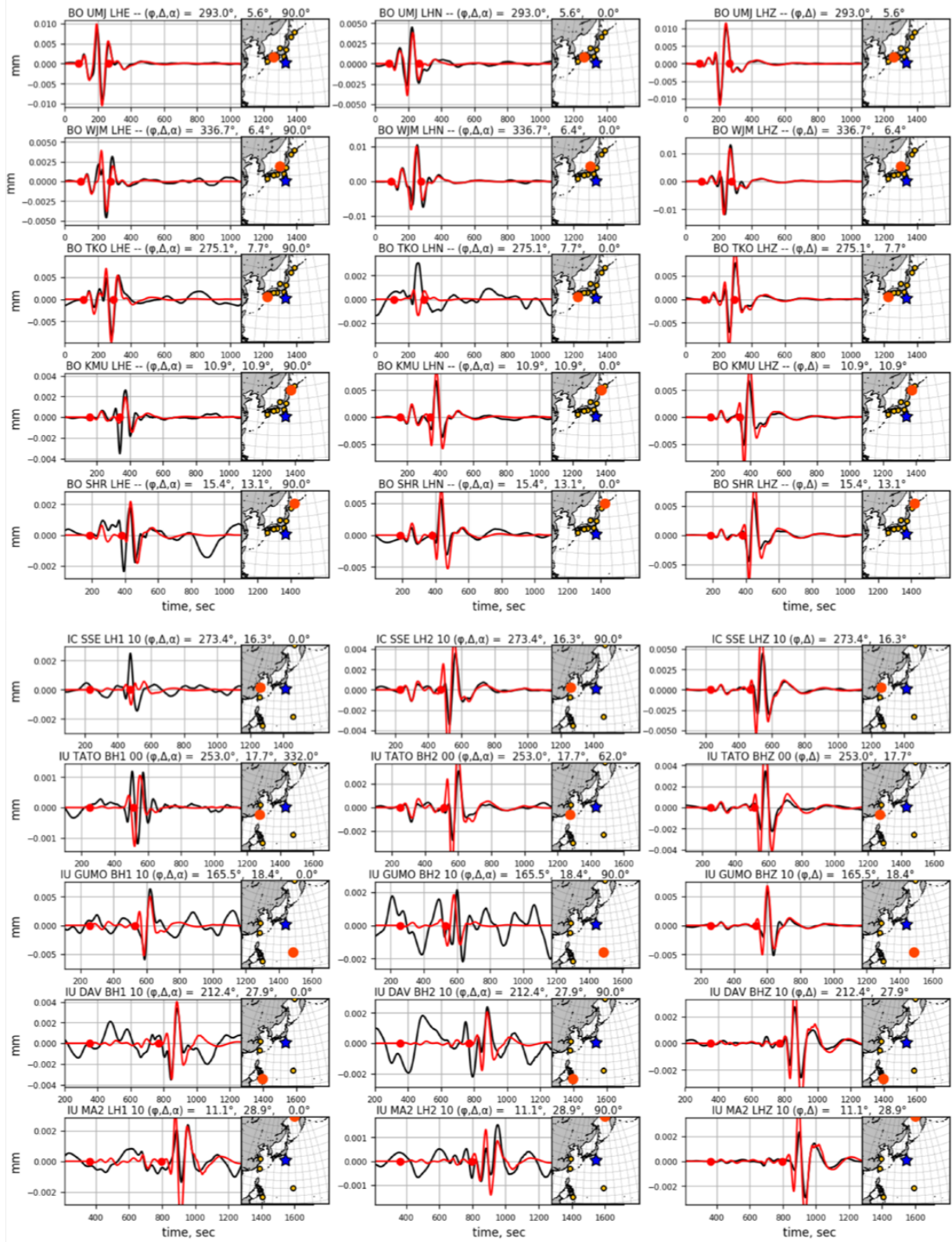
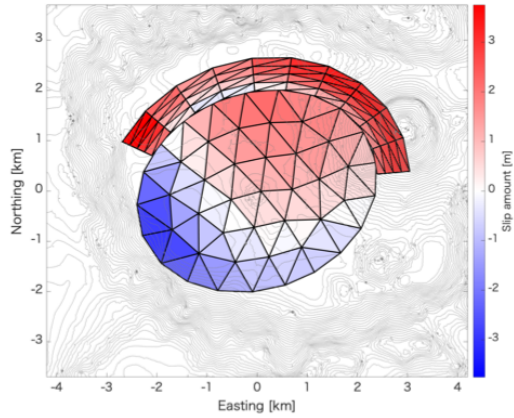
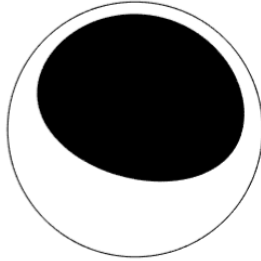


Fig. 3.21 Long-period seismic waves of the best FR model (Continued)

$$M_w = 5.85$$

$$M_0 = 7.46e+24 \text{ [dyne cm]}$$



$$M = \begin{bmatrix} 7.09e+24 & & \\ 5.04e+24 & -2.20e+24 & \\ -1.23e+24 & 3.16e+23 & -1.44e+24 \end{bmatrix} \text{ [dyne cm]}$$

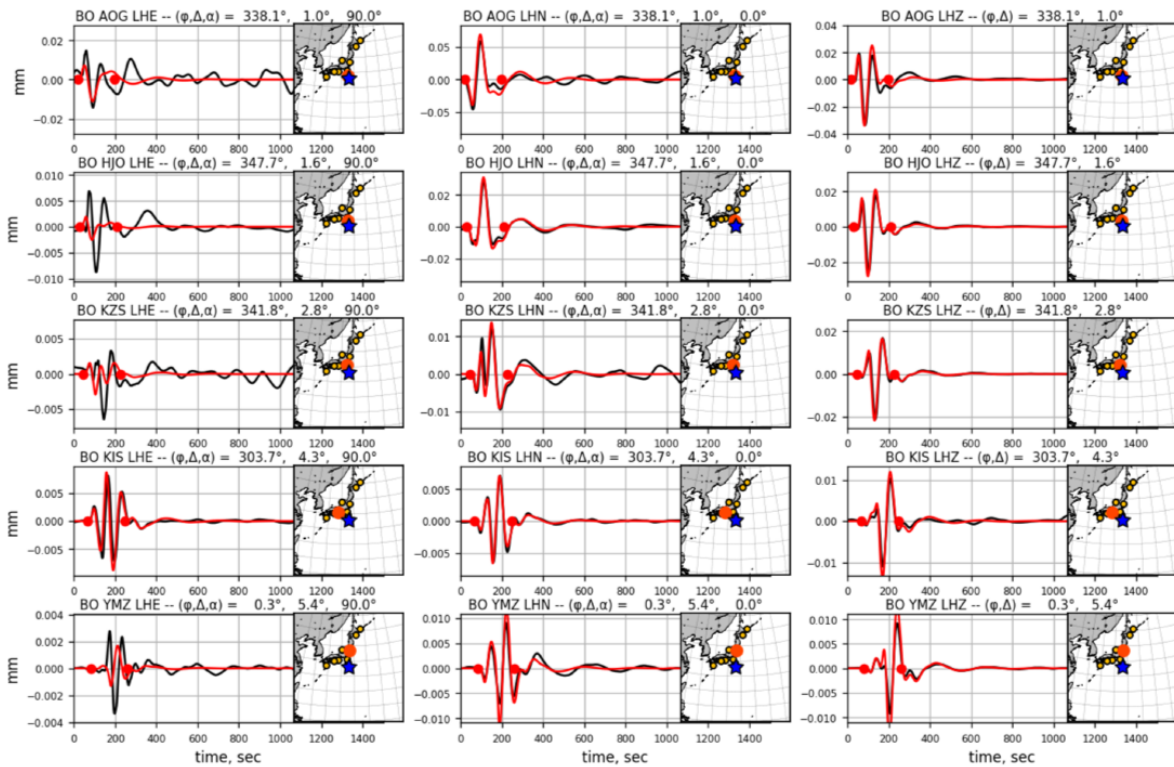


**Fig. 3.22 Long-period seismic waves of the best HR model (HR/72°/2 km)**

See the caption of Fig. 3.18. Tsunami and seismic NRMS misfits for the model are shown in Fig. 3.20e-f.

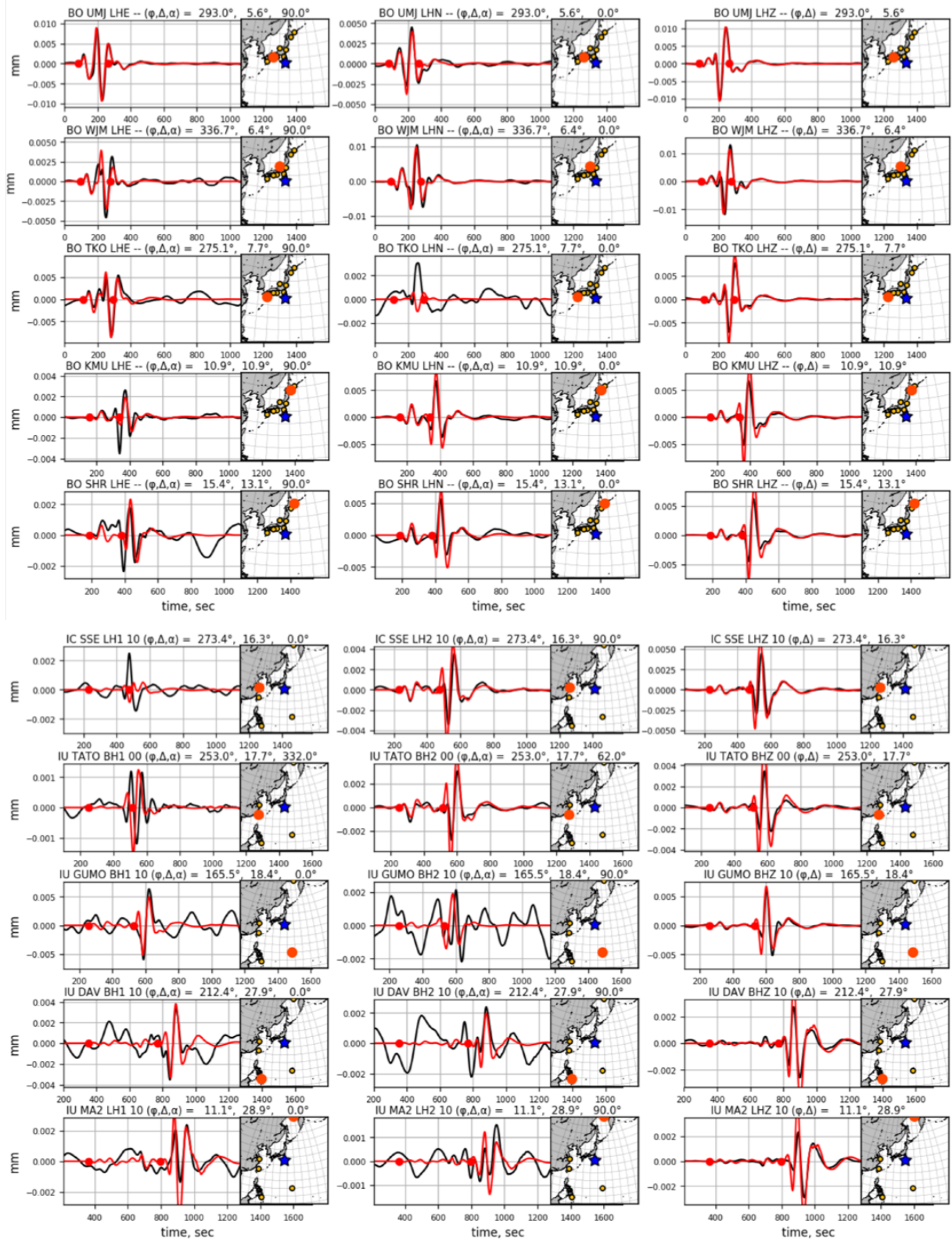
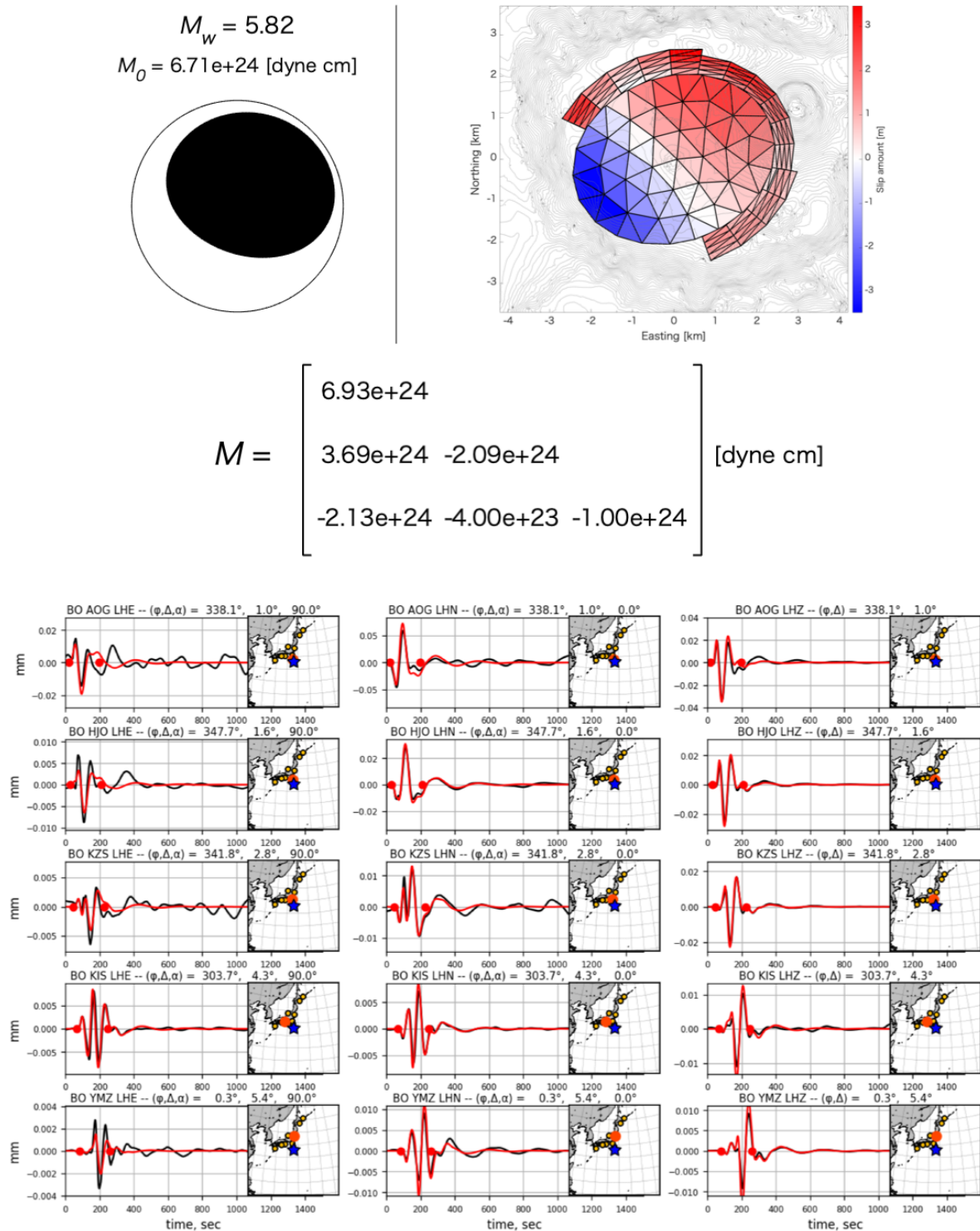


Fig. 3.22 Long-period seismic waves of the best HR model (Continued)



**Fig. 3.23 Long-period seismic waves of the heterogeneous-dip TR model (TR/73-77°/2 km)**

See the caption of Fig. 3.18. Tsunami and seismic NRMS misfits for the model are shown in Fig. 3.20e-f.

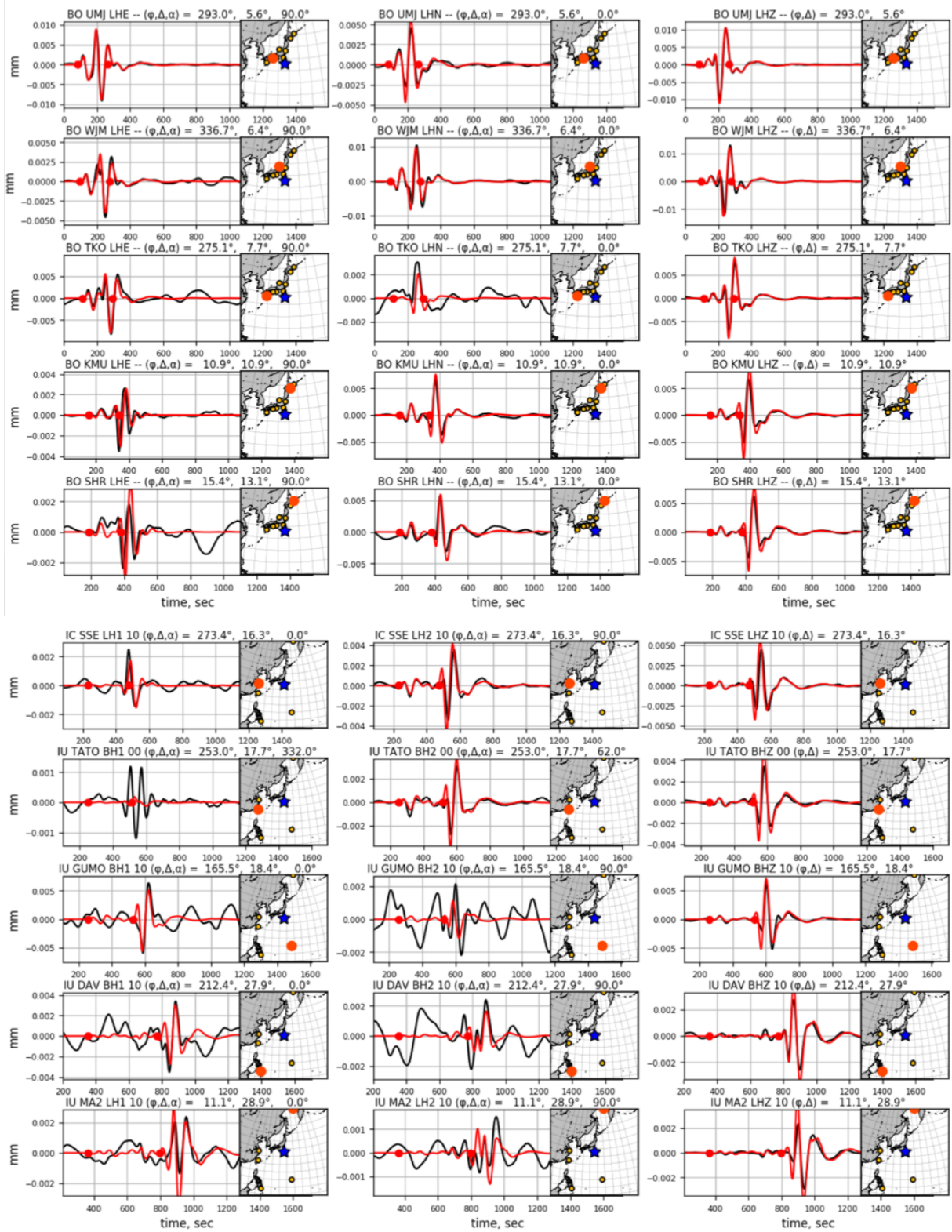


Fig. 3.23 Long-period seismic waves of the heterogeneous-dip TR model (TR/73-77°/2 km)  
(Continued)

### 3.4 Summary of Chapters 2 and 3

To this point, I have explored a kinematic source model for the 2015 Torishima volcanic tsunami earthquake. In Chapter 2, I examined the tsunami source using two different tsunami simulation methods, (1) ray tracing and (2) numerical simulations with variable parameters and simple assumptions, as part of a collaborative study [Fukao *et al.*, 2018]. The advantages of using tsunami records from the array included their location close to the epicenter, deployment on the deep ocean bottom, high-sampling-rate gauges, and dense distribution. These beneficial observational conditions enabled us to determine the following characteristics of the tsunami source for the 2015 Torishima earthquake: (1) the peak of the uplifted source was placed within the rim structure of Smith Caldera, (2) the large caldera uplift ( $> 1.0$  m) was estimated with a horizontal size comparable to that of Smith Caldera, and (3) a small peripheral subsidence was also revealed, at least on the NE side of the caldera. However, limitations of methods and data (i.e., the assumed axially symmetric source shape and the limited station coverage to the NNE) did not yield sufficient information regarding heterogeneity nor a unique solution for the source model. Thus, further investigation of the tsunami source was required for kinematic source modeling containing subsurface fault geometries.

Therefore, in Chapter 3, I began by exploring a more reliable tsunami source model that included spatial heterogeneity using the tsunami waveform inversion with additional tsunami data and more accurate simulations. By performing additional inversion tests with different datasets or the non-negative condition for sea-surface displacement, I confirmed the following nature of the seafloor deformation excited by the earthquake: (1) large uplift was concentrated within the rim structure, whose peak location shifted NE from the center of the caldera, (2) peripheral seafloor subsidence outside of and along the rim structure was confirmed to the northern parts, and (3) signals on the southern rim may have low reliability

Based on these results and other prior information, I hypothesized a physical mechanism of slippage on a subsurface composite fault system consisting of the ring fault and the horizontal fault, representing motion of a subsurface caldera block. I then assumed multiple fault models containing different fault parameters with discrete triangular meshes. For each model, I conducted slip inversion using a new computation method for tsunami Green's functions. All the assumed models reproduced the observed tsunami waves sufficiently. However, from the perspectives of the caldera block kinematics, slip models estimated with a block thickness of 2.0 km were phenomenologically reasonable while those with 4.0 km thickness were not, making it possible to constrain the caldera block geometry with tsunami records.

Finally, I conducted forward modeling of long-period seismic waves using the slip models. Waveforms of the vertical components of seismic waves were not different from model to model, while those of the horizontal components were significantly affected by the ruptured portion of the ring fault. Based on the waveform fitting levels, it was most probable that the dip slip occurred on the three-quarter

portion of the ring fault. On the other hand, the dip angle of the ring fault influenced the amplitude levels of the long-period seismic waves, which enabled me to constrain the dip angle as  $\sim 75^\circ$ . The fitting level of long-period seismic waves were greatly improved by incorporating a slight heterogeneity in the ring fault into the model with a three-quarter ring fault. Therefore, I successfully constructed a kinematic source model of the 2015 Torishima volcanic tsunami earthquake that fully explained both the tsunamis and long-period seismic wave records. The physical mechanism and related features are discussed in Chapter 5.



# ***Chapter 4 Kinematic source modeling for the 2017 Curtis volcanic tsunami earthquake***

In this chapter, I explore a kinematic source model for the 2017 Curtis volcanic tsunami earthquake in New Zealand by taking a similar approach to that used in Chapters 2 and 3. I first examine the tsunami source location by assuming simple uplift sources placed around the reported earthquake locations. After estimating the initial sea-surface displacement by the inversion of tsunami waveforms, I assume possible source geometries with consideration of bathymetric structures around the tsunami source. I then invert slip distributions of assumed fault modes from tsunamis and compute long-period seismic waves.

## **4.1 Data and tsunami simulations**

### **4.1.1 Tsunami data**

For analysis of tsunami waveforms from the 2017 Curtis earthquake, I used sea-level records with a sampling rate of one sample/minute at six tide gauge stations (Fig. 1.3). I extracted tsunami signals from these records by removing tidal signals approximated as polynomial functions. The obtained tsunami signals were dominated by wave periods ranging from  $\sim 200$ – $400$  s (blue line in Fig. 1.4).

### **4.1.2 Tsunami simulation**

For tsunami computations, I used the simulation code JAGURS [Baba *et al.*, 2015] to solve the standard Boussinesq-type equations expressed by Eqs. 2.6–2.8. For bathymetry data, I prepared the nested grid data with grid sizes changing from 30 arcsec ( $\sim 750$  m) in the deep ocean to 1.1 arcsec ( $\sim 28$  m) in nearshore areas around the tide gauges (Fig. 4.1). For the widest region, I used GEBCO\_2014 [Weatherall *et al.*, 2015], and prepared finer topographic/bathymetric data processed from 250 m spacing bathymetric data obtained from the New Zealand Regional Bathymetry product developed by NIWA [2016] around the source region to incorporate structural effects near the source. To include nearshore effects around the tide

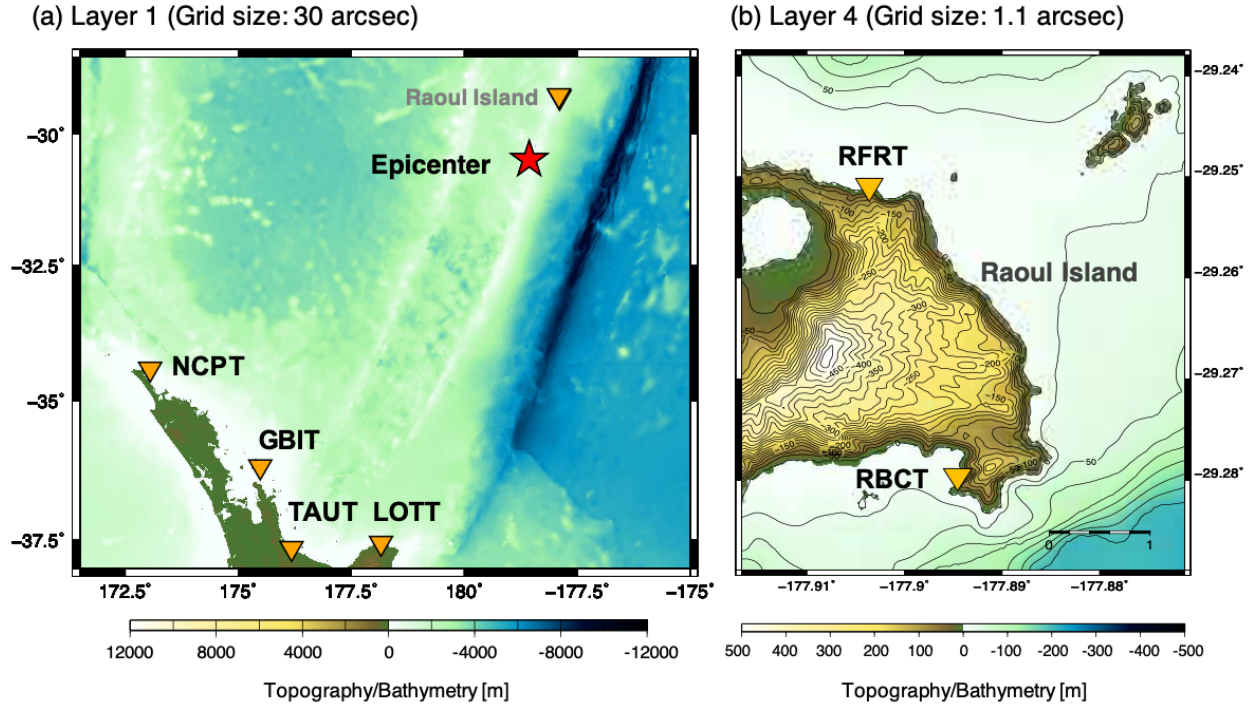


**Fig. 4.1 Nested bathymetry data and tide-gauge stations used for tsunami simulations**

(a) Bathymetry of Layer 1. Orange triangles and red star represent tide-gauge stations and epicenter of the 2017 Curtis earthquake, respectively. (b) Bathymetry data of Layer 4 around Raoul Island, where RFRT and RBCT tide-gauge stations are deployed. Fine bathymetry data in Layer 4 was used for nearshore regions around all the tide-gauge stations.

gauges correctly, I prepared finer data ( $\sim 28$  m) by combining digital topographic data on land and bathymetric data obtained by interpolating data digitized by bathymetric lines on analogue charts around all tide gauge stations used. All original data for nearshore regions was downloaded from the Land Information of New Zealand (LINZ) department. In coastal regions, I incorporated the nonlinear effects of tsunami propagation only for forward simulations in Chapter 4.2, while disregarding them in the inversion analysis in Chapters 4.3 and 4.4 because synthetic waveforms at tide-gauge stations did not change even when including nonlinear effects.

## 4.2 Estimation of tsunami source area

### 4.2.1 Methods

First, in order to roughly estimate the tsunami source area of the 2017 Curtis earthquake, I conducted forward simulations of tsunami waveforms from nine simple tsunami source models of initial sea-surface displacements with a spatial interval of  $0.1^\circ$  ( $\sim 10$  km) (Fig. 4.2a). Each tsunami source model was defined with a Gaussian-shaped uplift, whose displacement  $h_0(r)$  was expressed as:

$$h_0(r) = A \left[ \exp \left\{ - \left( \frac{2r}{R} \right)^2 \right\} \right], \quad \text{Eq. 4.1}$$

where  $r$  is the distance from the center and  $A$  and  $R$  represent a peak amplitude (1.5 m, here) and a 2-sigma length of the Gaussian function (7.0 km, here), respectively (Fig. 4.2b). I assumed uplifted displacement as the tsunami source, because the largest pulse started with an upswing motion at most stations (Fig. 1.4). The rise times of the sea-surface uplifts were assumed as 8.0 s, based on a source duration time for the 2009 Curtis earthquake estimated by moment tensor inversion using teleseismic body waves by *Shuler et al.* [2013].

## 4.2.2 Results

The synthetic tsunami waveforms changed sensitively by location, enabling the source area to be constrained by comparison with observed waveforms at the six tide gauge stations. Synthetic waveforms radiated from Location 5 showed the best agreements at the tide gauge stations in terms of arrival times of major waves, amplitudes, and phases (Fig. 4.2c-d; Fig. 4.3). These results indicated that the Curtis earthquake occurred near Location 5, where Curtis and Cheeseman Islands are emergent on the sea surface (Fig. 1.3c, Fig. 4.2a). Note that the earthquake locations for the 2009 and 2017 Curtis earthquakes reported

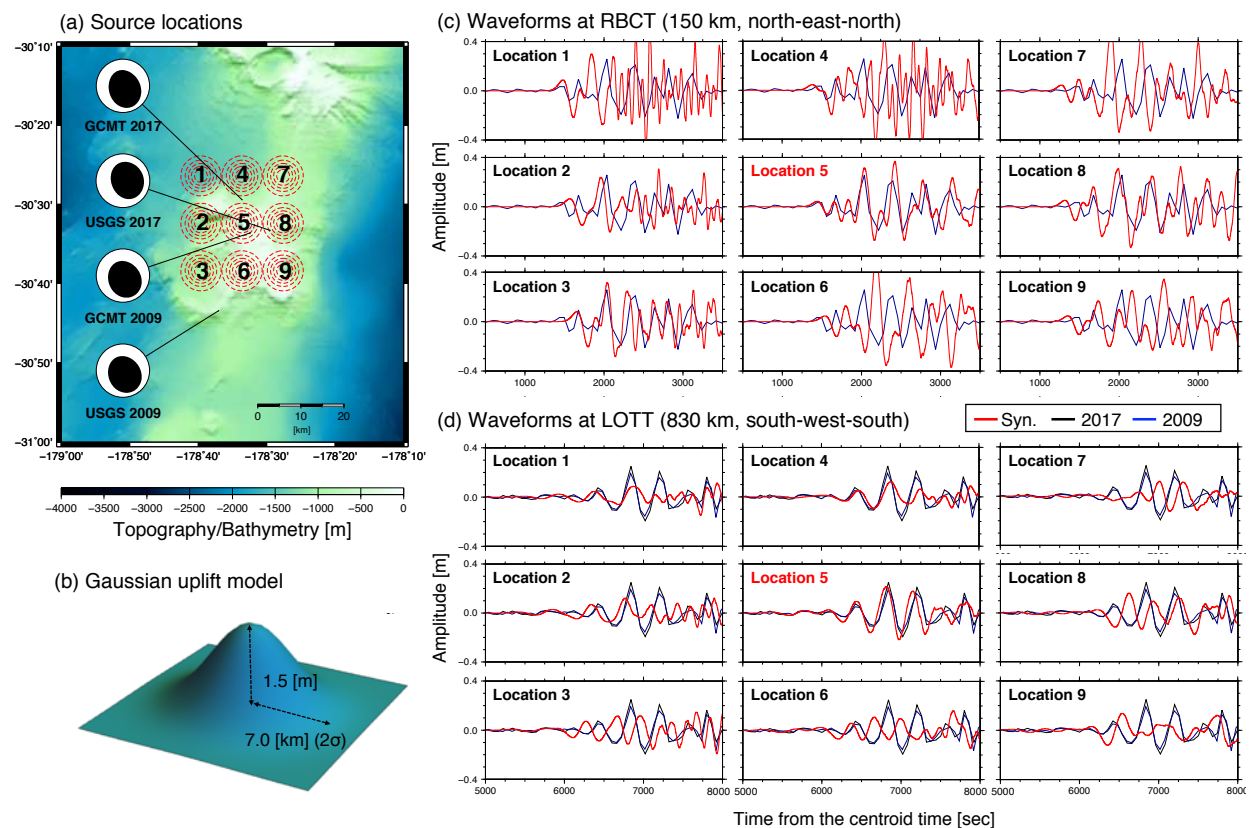


**Fig. 4.2 Estimation of the tsunami source region**

(a) Source locations of assumed Gaussian-shaped models. Red dashed circles represent approximate sizes of the sources. Focal mechanisms of the 2017 and 2009 Curtis earthquakes reported by GCMT and USGS are shown with a line pointing at the reported source locations. (b) Shape of the assumed source model. (c-d) Comparisons of synthetic (red) and observed (black and blue) waveforms at (c) RBCT and (d) LOTT stations from the assumed nine source locations.

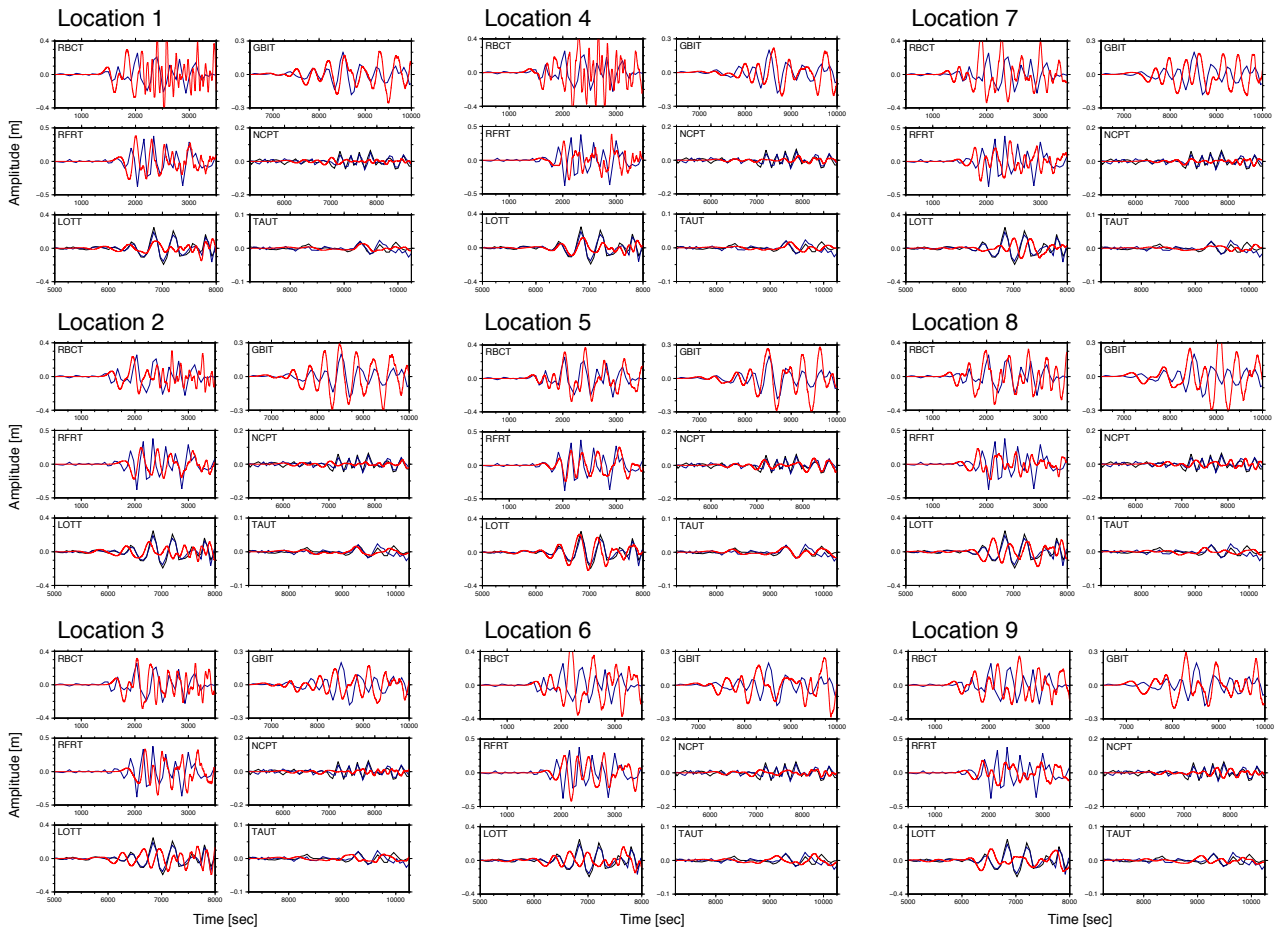


**Fig. 4.3 Waveforms of the Gaussian-shaped uplift models**

Comparisons of synthetic (red) and observed (black and blue) waveforms at tide-gauge stations from the assumed nine source locations.

by GCMT and USGS were scattered around the submarine volcanic rise in intervals of  $\sim 10\text{--}30$  km (Fig. 4.2a), likely due to highly heterogeneous velocity structures along the volcanic ridge. However, my results demonstrate the advantages of utilizing tsunami simulations, as I was able to successfully locate the tsunami source area of the 2017 Curtis earthquake close to Curtis and Cheeseman Islands.

## 4.3 Inversion of tsunami waveforms for initial sea-surface displacement

### 4.3.1 Methods

#### 4.3.1.1 Inverse problem

I then estimate the initial sea-surface displacement of the 2017 Curtis earthquake by the inversion of tsunami waveforms. Based on the estimated source area, I assumed a source region of 25 km

× 25 km square around Curtis and Cheeseman Islands and distributed 181 unit sources of initial sea-surface displacement with 1.25 km intervals (Fig. 4.4), each of which was formulated as:

$$\eta_i(x, y) = 0.25 \times \left[ 1.0 + \cos \frac{\pi(x - x_i)}{L} \right] \times \left[ 1.0 + \cos \frac{\pi(y - y_i)}{L} \right], \quad \text{Eq. 4.2}$$

$$(|x - x_i|, |y - y_i| \leq L),$$

where  $\eta_i$  is the initial distribution of the  $i$ th unit source with the central location at  $(x_i, y_i)$  in kilometers ( $i = 1, 2, \dots, N$ ) with a source size of  $L$  (1.25 km, here). I computed synthetic waveforms from the  $i$ th unit source at the  $j$ th stations ( $j = 1, 2, \dots, M$ ) to obtain tsunami Green's functions  $\mathbf{g} = g_{ij}(t)$ . The rise time for each unit source was set as 10 s, given that the moment tensor inversion using the W-phase of the seismic waves indicated a source duration of 10 s (see Chapter 5.2).

I then followed the inversion method used for the 2015 Torishima earthquake (Chapter 3.1.2). I solved the observation equation (Eq. 3.5) by the damped least-square method, which was formulated by observed tsunamis and tsunami Green's functions normalized by the inverse RMS value of the observed records (Eq. 3.4). By taking the waveform fitness of the later phases after the inversion time window into account in the same way as done in Chapter 3.2, the damping parameter  $\alpha$  was determined to be 0.3, providing smooth solutions without unrealistic patterns.

In the inversion analysis, I did not use tsunami records at tide-gauge stations NCPT and TAUT (Fig. 4.1a), because they had low S/N ratios and complex bay shapes around the tide gauges. The synthetic waveforms were not significantly influenced by the detailed shapes of the assumed tsunami sources at these two stations. Therefore, I do not further mention tsunami waveforms at these two stations, but focus on those at the other stations (RBCT, RFRT, LOTT, and GBIT) (Fig. 4.1a).

#### 4.3.1.2 Incorporation of tsunami travel-time delays

Of the four stations used here, LOTT and GBIT were further from the epicenter, with epicentral distances around 830 km for both. At these distant locations, short-period tsunamis (200–400 s) are generally influenced by the elasticity of the Earth, the compressibility and density stratification of seawater, and the gravity potential change [e.g. *Watada et al.*, 2014; *Ho et al.*, 2017], resulting in non-negligible travel time delays (Appendix 1). Although I developed a phase correction method for short-period tsunamis, this requires an approximation of the tsunami ray path as a single path. Complex ray paths bending along the Kermadec ridge made it difficult to apply this method to the two far-field stations. Instead, I incorporated the effects more simply by grid-searching for delay times that improved waveform fittings. In order to find the optimal delay times due to these effects, I shifted the travel time of tsunami Green's functions by from 0 to 70 s in 5 s intervals for each station and computed the NRMS misfit in the inversion time window. Figure 4.5 shows the NRMS misfit values as a function of delay times at stations LOTT and GBIT; the minimum values occurred for travel-time delays of 25 and 45 s, respectively.

### 4.3.2 Results

As a consequence of the inversion, two tsunami source models for initial sea-surface displacements were estimated using the travel-time delays at stations LOTT and GBIT (Fig. 4.6a). The model incorporating these effects had a smoother and more focused uplift with a maximum amplitude signal of  $\sim 1.2$  m to the west of Curtis and Cheeseman Islands and smaller peripheral subsidence of  $\sim 60$  cm to the south. I conducted another inversion without the travel-time shift (Fig. 4.6b), in which the waveform fitness was clearly worse with an NRMS misfit of 0.44 (the value with the travel-time delay was 0.37). This indicated that including the travel-time delay effects allowed a more reliable tsunami source model to be obtained (Fig. 4.6a).

The estimated uplift area was consistent with the caldera-like topographic structure. Figure 4.7 compares the tsunami source model (Fig. 4.6b) with the topography of the submarine volcanic edifice below Curtis and Cheeseman Islands. The dome-like structure below the island is surrounded by topographic depressions with  $\sim 400$  m water depth, strongly suggesting a caldera collapse event in the past. The existence of a submarine caldera around the islands was mentioned in the *Global Volcanism Program* [2009], which hereafter I call “Curtis Caldera”. The main uplift area was estimated to be focused on the southwest part of the caldera, and its boundary to the peripheral subsidence was traced closely along the rim structure. These characteristics of seafloor deformation as inferred from tsunami records were quite similar to those of the 2015 Torishima earthquake. Although the uplifted area leaked out of the rim to the north and east, the smaller signals were artifacts because of low-sampling tide-gauge records (one sample every minute) used for the inversion.

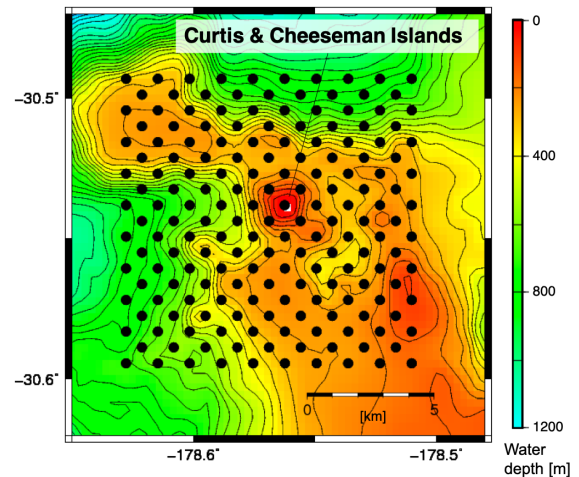


**Fig. 4.4 Unit sources distributed around Curtis and Cheeseman Islands**

Distributions of assumed unit sources of initial sea-surface displacement. Black dots represent central locations of unit sources of initial sea-surface displacement. Each unit source has a cosine-tapered shape with a horizontal source size of  $1.25 \times 1.25$  km. Contour lines of the water depth are painted every 50 m.

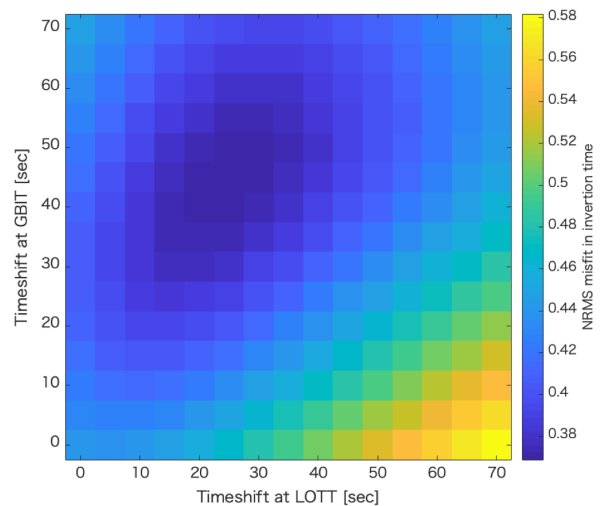


**Fig. 4.5 Grid-search results of travel time delays at LOTT and GBIT stations**

NRMS misfit value as a function of delay times at LOTT and GBIT stations, which takes the minimum value at time delays of 25 s at LOTT and 45 s at GBIT.

To examine the robustness of the peripheral subsidence to the south, I inverted a source model only with uplifted sea-surface displacement by imposing the non-negative condition on the damped least-square method to solve the observation equation (Eq. 3.5). Figure 4.6c shows the inverted uplift source model and comparisons of the synthetic and observed waveforms. The waveform fitting level did not

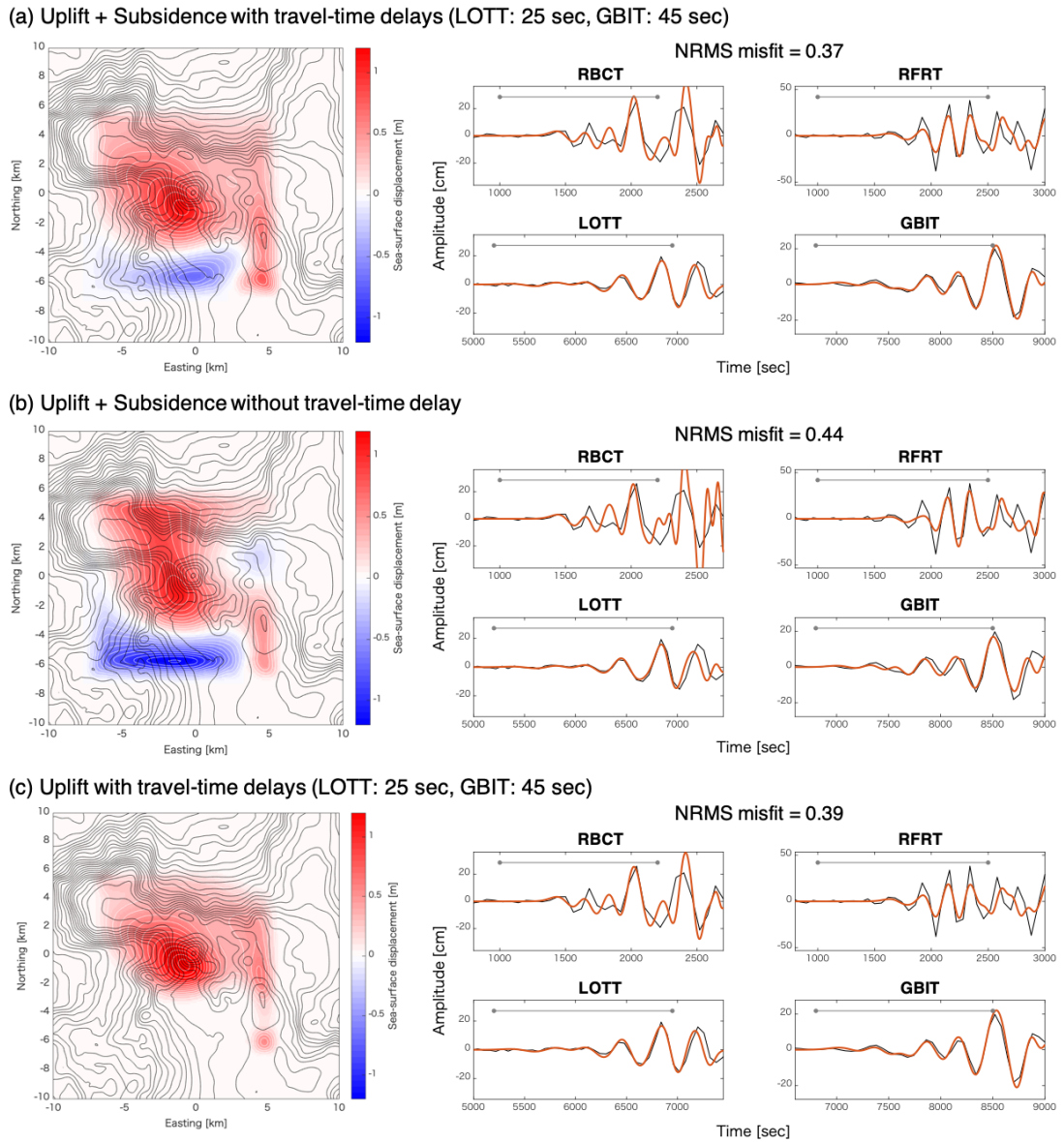


**Fig. 4.6 Results of inversions for the initial sea-surface displacement**

Initial sea-surface displacement and tsunami waveforms inverted by three different methods. (a-b) Inversion allowing sea-surface uplift and subsidence (a) without travel-time delay, and (b) with travel-time delays by 25 s at LOTT station and 45 s at GBIT station. (c) Inversion allowing only sea-surface uplift with travel-time delays by 25 s at LOTT station and 45 s at GBIT station. Initial sea-surface displacements are shown with white contour lines every 0.5 m uplift or subsidence, and black contour lines every 50 m of the water depth. Synthetic and observed waveforms were represented by red and black lines, respectively. Gray lines represent the time window of data used for the inversion.

change significantly, compared to the model with subsidence (Fig. 4.6a). This indicated that the peripheral subsidence to the south did not have much effect on tsunami waveforms at the stations used here. Therefore, the amplitude and location of the subsidence were not resolved well. This was probably because such short-wavelength subsidence cannot have clear signals in waveforms at faraway stations such as LOTT and GBIT due to strong dispersion during long-distant propagation. The low-sampling records may have also limited the resolution. However, the model still estimated large uplift with a clear zero-amplitude boundary on the southwestern part of the caldera rim, indicating a clear transition of the source kinematics along the rim.

### 4.3.3 Physical mechanism inferred from the inverted tsunami model

Based on these results, I hypothesized a physical mechanism composed of a volumetric change in a shallow horizontal fault filled with magma and a rupture of a ring fault for the 2017 Curtis earthquake. The tsunami source revealed that the Curtis earthquake shared common features with the Torishima earthquake; both were characterized by meter-scale seafloor uplift concentrated above a submarine caldera floor with a clear uplift boundary along the rim structure. Considering the analogy with a kinematic source for the Torishima earthquake as modeled in Chapter 3, a ring-fault rupture may have occurred on the SW side of Curtis Caldera, interacting with a magma-filled subsurface horizontal crack (or fault).

Although little information is available regarding Curtis Caldera, it is notable that several features indicated post-caldera activities including resurgence. In general, resurgence can occur due to high-pressurized magma in a sill-like chamber and reactivation of the ring fault [Acoccela *et al.*, 2015;

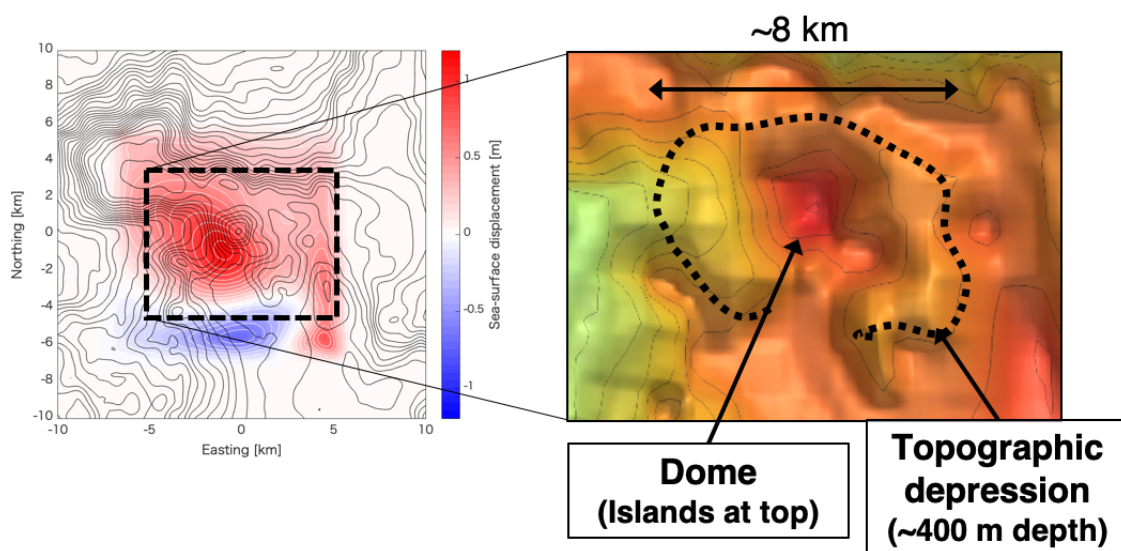


**Fig. 4.7 Caldera-like structure around the tsunami source region**

Comparison of the tsunami source (left) and the topographic structures around Curtis and Cheeseman Islands (right). The bathymetry data was New Zealand Regional Bathymetry (2016) [NIWA, 2016], which was visualized with QGIS.

references therein], as explained in Chapter 3.1.4. One feature indicating resurgence activities at Curtis Caldera was a topographic rise of 300–400 m found in the center (Fig. 4.7). Several volcanoes sometimes activated by resurgence have shown similar structures called “resurgent domes,” such as Long Volley and Valles [e.g. *Acocella et al*, 2001]. *Doyle et al.* [1979] found that long-term large uplift took place on and around Curtis Island on the basis of several observations, such as a water-depth survey around the islands and radiocarbon dating of barnacles on the wall above sea level. They reported ~7 m uplift from 1929 to 1964, and ~18 m in the last 200 years, strongly indicating a resurgent doming processes within the caldera structure. Active fumaroles in its crater (300 m × 200 m) were also found, which are common at geothermal and volcanic vents at the summits of resurgent domes [e.g. *Molin et al.*, 2003]. Observations of T-wave signals from near the islands just before the 2009 Curtis earthquake [*Global Volcanism Program*, 2009] suggested that magma input into the chamber may have continued in recent decades, potentially causing uplift of the caldera floor. These features around the submarine caldera may support the hypothetical source mechanism with regard to a subsurface interactive system.

## 4.4 Kinematic source modeling

I next explore a kinematic source model of the 2017 Curtis volcanic tsunami earthquake by taking a similar approach to that used for the 2015 Torishima earthquake in Chapters 3.2 and 3.3. The main purpose of kinematic source modeling for the Curtis earthquake is to explain both the tsunami and long-period seismic wave records, rather than pursuing detailed fault parameters, because limited information on subsurface fault geometries for Curtis Caldera makes it difficult to constrain detailed structures even if tsunami and seismic waves are utilized.

### 4.4.1 Methods

#### 4.4.1.1 Reference fault model

I first assumed a reference fault model composed of a ring fault and a horizontal fault, by discretizing the structural boundaries of a subsurface caldera block with discrete triangular dislocation (TD) elements. The model had a partial ring fault structure with a uniformly inward-dipping angle of 70°, extending from 0.5 km to 3.5 km depth, whose down-dip edge connected to the ellipse-shaped fault lying horizontally that was equivalent to the bottom of the subsurface caldera block (Fig. 4.8a). The ruptured portion of the ring fault was assumed to be on the SW side of the caldera, on the basis of the tsunami source model inverted in the previous section (Fig. 4.7).

To find a kinematic source model, I used the reference model to conduct the inversion of tsunami waveforms for fault slips and the forward modeling of long-period seismic waveforms at regional seismic stations. This analysis was repeated through the trial-and-error method while modifying the geometry of the horizontal fault and dip angle of the ring fault, in order to obtain fault parameters achieving sufficient fitting levels with the synthetic and observed records for both of tsunamis and long-period

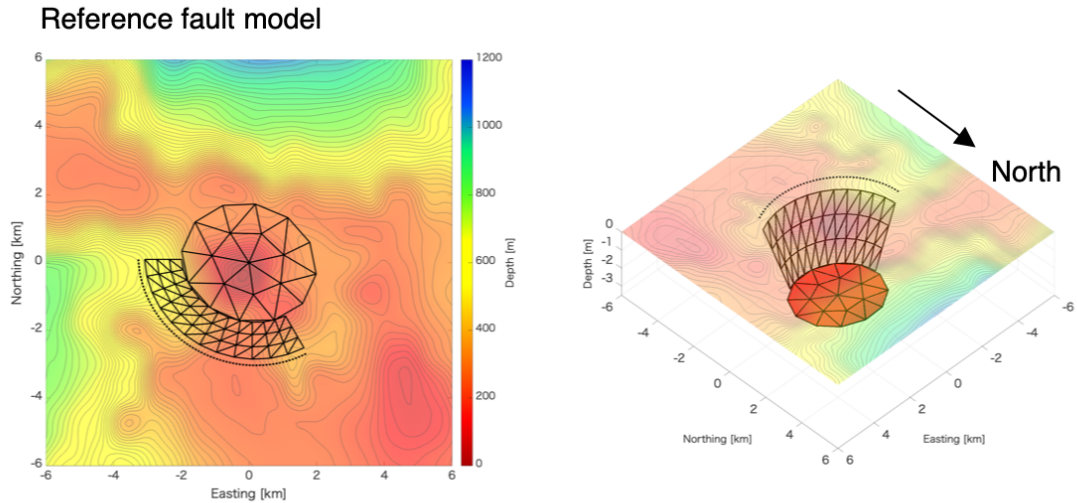


**Fig. 4.8 Reference and modified fault models**

(a) Geometry of the reference fault model: The ring fault has a uniform dip angle of  $70^\circ$  as its trace extended to seafloor forms an ellipse shape with radius of  $3.3 \text{ km} \times 3.0 \text{ km}$  rotated clockwise by  $20^\circ$  around the central point at  $178.56^\circ\text{W}$ ,  $30.535^\circ\text{S}$ . (2) Geometry of the modified fault model: The ring fault has a uniform dip angle of  $70^\circ$  as its trace extended to seafloor forms an ellipse shape with radius of  $3.8 \text{ km} \times 3.5 \text{ km}$  rotated clockwise by  $20^\circ$  around the central point at  $178.56^\circ\text{W}$ ,  $30.532^\circ\text{S}$ .

seismic waves. Only an inward-dipping ring fault was considered because a vertical-CLVD type moment tensor with a dominant tension axis (Fig. 1.3) can be generated only in the case of an inward dip when a caldera block moves upward [Ekström, 1994; Shuler et al., 2013].

#### 4.4.1.2 Inversion of tsunami waveforms for fault slips

For the assumed fault models, I estimated slip distributions from the tsunami records at the tide-gauge stations (Fig. 4.1) by conducting the inversion using four-step computations of the tsunami Green's functions developed in Chapter 3.2. I first prepared the "first tsunami Green's functions" by reusing the functions from unit sources of initial sea-surface displacement used in Chapter 4.3 (Eq. 4.2; Fig. 4.4). Second, vertical sea-surface displacement excited by subfault slips were computed by the TD method [Nikkho and Walter, 2015] and the Kaiura's filter [Kajiura, 1963]. In the process, I simply assumed a flat seafloor with water depth of 400 m. Third, I solved the inverse problem to reconstruct the displacement fields with the unit sources (Eq. 4.2) and obtained weighting factors of each unit source. Finally, I obtained tsunami Green's functions from subfault slips at the tide-gauge stations by convolving the weighting factors and the first tsunami Green's functions from unit sources. For the Green's functions, I incorporated the travel-time delays by shifting synthetic waveforms by 25 s and 45 s at stations LOTT and GBIT, respectively, as estimated in the previous section.

Using the tsunami Green's functions, I next solved the observation equation (Eq. 3.10) to obtain slip distributions on assumed fault models. I determined a proper damping parameter by taking a balance between smoothly distributed slips and tsunami waveform fitting levels. Figure 4.9 compares slip distributions and synthetic waveforms of the inversion results with damping parameters of 0.05, 0.2, and 0.4, respectively. When using 0.05, the waveform fitting was high, while large slips were unnaturally distributed on the ring fault (Fig. 4.9a). On the other hand, when using 0.4, the synthetic waves were smaller than the observed records. although slips were smoothly distributed along the fault structures (Fig. 4.9c). To find a balance between the two criteria, I selected a damping parameter of 0.2 for the inversion analysis (Fig. 4.9b), using the same value for all models shown here because the trend did not change for individual models.

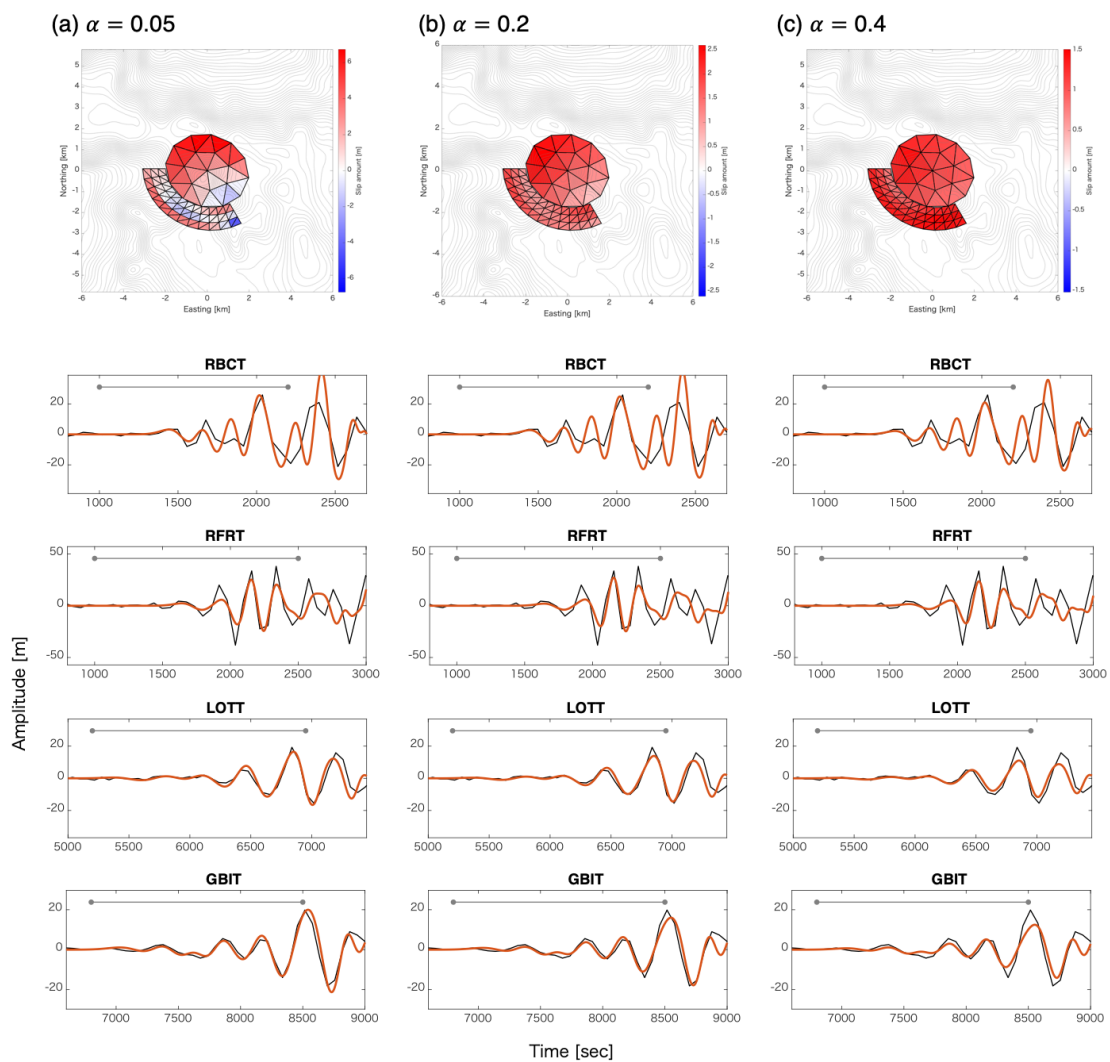


**Fig. 4.9 Selection of a proper value of damping parameter for the slip inversion**

(a-c) Comparisons of (top) slip distributions and (bottom) waveforms for different damping parameters. Color representations in slip distributions follow the caption of Fig. 4.10. Red and black lines represent synthetic and observed tsunami waveforms, respectively.

### 4.4.1.3 Forward modeling of long-period seismic waves

Using the slip distributions on the assumed fault models, I computed a moment tensor, seismic moment, and moment magnitude by following the method explained in Chapter 3.3.1.1. I then computed long-period seismic waves at the regional stations using the W-phase package [Kanamori and Rivera, 2008; Hayes *et al.*, 2009; Duputel *et al.*, 2012]. Green's functions were computed with the PREM velocity model based on normal mode theory [e.g. Takeuchi and Saito, 1972; Saito, 1988; Woodhouse, 1988]. The centroid location was assumed at the approximate center of Curtis Caldera (178.56°W, 30.54°S) with a depth of 2.5 km below the seafloor. Both the half duration and the centroid time shift were assumed to be 5 s, as obtained by the moment tensor inversion using the W-phase of the seismic waves (Chapter 5.2).

To compare the synthetic waveforms with the observed seismic records, I used the LH and BH channels at seismic stations of the Global Seismograph Network (IU), New Zealand National Seismograph network (NZ), Australian National Seismograph Network (AU), and GEOSCOPE (G) from the IRIS. All stations were located within epicentral distances of 30°. The one-pass and forth-order Bandpass Butterworth filters, with corner frequencies at 0.007 and 0.0174 Hz (band-pass period ranging from 57–143 s), were used for both the observed and synthetic waveforms to extract long-period components. I computed the seismic NRMS misfit in the W-phase using Eq. 3.16 to quantify the waveform fitness.

## 4.4.2 Results

### 4.4.2.1 Reference fault model

I first conducted the inversion of tsunami waveforms for slip distributions on the reference model (Fig. 4.10). The inverted slip distributions were composed of large thrust faulting on the ring fault with the maximum amount of ~2.0 m and opening of the horizontal fault as large as 2.6 m (Fig. 4.10a: Table 4.1a). The estimated sea-surface displacement reached ~2.7 m along the ring fault (Fig. 4.10b), which reproduced the observed tsunamis with good agreement (Fig. 4.10c). Thrust slip on the ring fault and opening of the horizontal fault were equivalent to moment tensors of  $M_w$  5.75 and 6.00, respectively, and the composite moment tensor of the slip model ( $M_w$  6.05) was dominated by an explosive isotropic component (Fig. 4.11a). Assuming the composite moment tensor as an initial condition, long-period seismic waves of the slip model were then synthesized and compared with the observed records (Fig. 4.11b). Although seismic signal phases were similar between the synthetic and observed waveforms, synthetic signal amplitudes were clearly smaller. The seismic NRMS misfit was as large as 1.431 (Table 4.1a), indicating that the slip model lacked seismic radiation energy.

### 4.4.2.2 Modified fault models

To obtain comparable amplitude levels in the synthetic seismic waves to those of the observations, I constructed two modified fault models (Fig. 4.12) by changing the dip angle of the ring fault or the thickness of the caldera block (or depth of the horizontal fault) from the reference model. The first was a “modified-dip fault model” with a gentler ring fault dip angle of 60°, compared to the reference

**Table 4.1 Results of the inversion of tsunami waveforms and their tsunami and seismic NRMS errors**

(a) Maximum and minimum amounts of ring-fault slips and tensile opening of the horizontal fault, and tsunami NRMS misfit in the inversion time window of the reference, modified-dip, modified-thickness, and half-ring models.

(b) Moment magnitude, scalar seismic moment, and moment tensors, and seismic NRMS misfit. Stations (channels) used to compute seismic NRMS misfits are listed below.

(a)

Model	Thick-ness [km]	Dip [°]	Slip amount [m]				Tsunami NRMS
			Ring fault		Horizontal fault		
			max	min	max	min	
Reference	3.0	70	1.99	0.93	2.60	0.65	0.46
Mod-dip	3.0	60	2.30	-0.05	2.62	1.09	0.45
Mod-thickness	5.0	70	2.02	0.45	1.71	1.06	0.44
Half ring	3.0	60	2.14	0.01	1.92	0.86	0.43

(b)

Model	Thick-ness [km]	Dip [°]	$M_w$	$M_0$ [ $10^{25}$ dyne cm]	Moment tensor [ $10^{25}$ dyne cm]						Seismic NRMS
					$M_{rr}$	$M_{\theta\theta}$	$M_{\phi\phi}$	$M_{r\theta}$	$M_{r\phi}$	$M_{\theta\phi}$	
Reference	3.0	70	6.05	1.51	1.97	0.37	0.48	-0.35	0.19	0.08	1.431
Mod-dip	3.0	60	6.02	1.35	1.83	0.20	0.23	-0.22	0.18	0.15	<b>0.870</b>
Mod-thickness	5.0	70	6.01	1.30	1.60	0.02	0.15	-0.53	0.32	0.13	<b>0.861</b>
Half ring	3.0	60	5.97	1.15	1.59	0.01	0.00	-0.13	0.23	0.01	0.916

**Seismic Station List**

OUZ (LHZ) URZ (LH1, LHZ) BKZ (LHE, LHZ) HIZ (LHE, LHN, LHZ) NFK (BHZ) SNZO (LH2, LHZ) QRZ (LHZ) KHZ (LHZ) NIUE (BHE, BHN, BHZ) RPZ (LHZ)  
 DZM (BHZ) NOUC (LHN, LHZ) FUTU (LHZ) ODZ (LHE, LHZ) AFI (LHZ) LHI (BHZ) RAR (LH1, LHZ)

model's 70° (Fig. 4.12a). The second was a “modified-thickness fault model” with a thicker caldera block of 5.0 km, compared to the reference fault model's 3.0 km, but with the same dip angle of 70° (Fig. 4.12b). Along with the parameter modifications, I also corrected the size and central location of the horizontal fault to retain a size comparable to that of the topographic structure of the caldera.

Using the modified-dip fault model (Fig. 4.12a), I obtained a kinematic source model by the inversion of tsunami waveforms, which yielded sufficient fitting of both synthetic tsunamis and long-period seismic waves to the observations. The overall results of the inversion for this fault model were similar to those for the reference model, in terms of slip distributions and amounts, resultant sea-surface displacements, and tsunami waveform fittings at the tide-gauge stations (Fig. 4.13, Table 4.1a). On the other hand, the fitness of long-period seismic waves was significantly improved with similar amplitude levels, with a smaller seismic NRMS misfit of 0.870 compared to the reference model's 1.431 (Fig. 4.14b: Table 4.1b). Although the horizontal components of the observed records were contaminated by noise (probably due to oceanic waves hitting the coasts) larger seismic signals following the W-phase time window (indicated by red circles in the waveforms) also showed good agreement with those of synthetic waveforms at most stations.

For the modified-thickness fault model (Fig. 4.12b), the inverted slip distribution are overall similar to that of the reference fault model despite smaller opening amount of the horizontal fault (Fig. 4.15a). Synthetic tsunami waveforms were similar to those observed (Fig. 4.15c). Moreover, the fitting of the synthetic long-period seismic waveforms to the observations was with an NRMS misfit of 0.861 and

was improved when compared to the reference model (Fig. 4.16b, Table 4.1b). The moment magnitude of the horizontal fault was 0.13 smaller as a  $M_w$  value, while that of the ring fault was 0.13 larger (Fig. 4.16a), compared to those of the reference model (Fig. 4.11a).

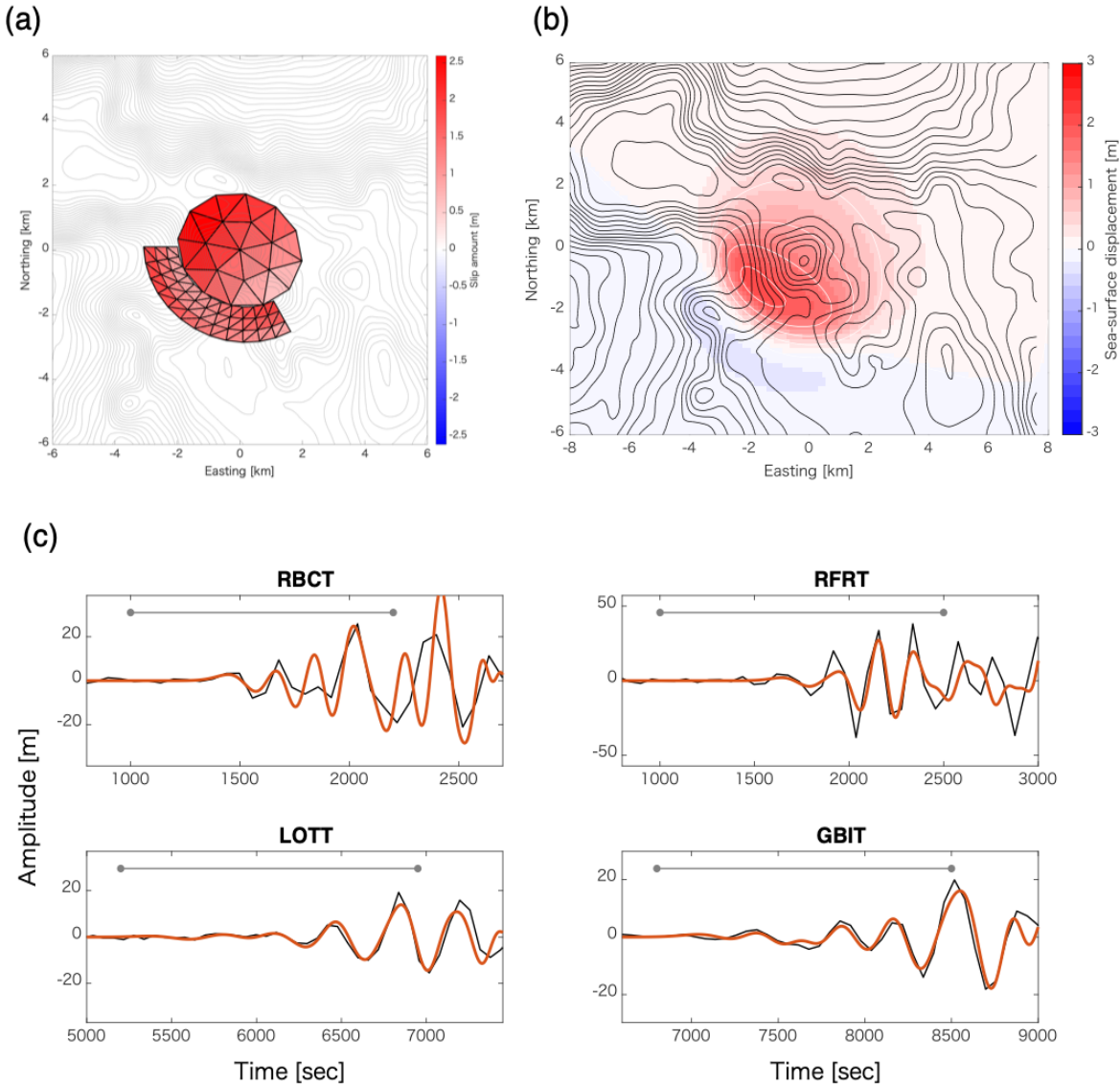


**Fig. 4.10 Inversion results with the reference fault model**

(a) Slip distributions: Colors in slip distributions represent amounts of dip slips on the ring fault, and tensile opening of the horizontal fault, respectively. Red color represents a fault motion with a sense of upward motion of the caldera block, while blue color does in turn (i.e. Ring fault; Red and blue represents thrust and normal faulting, respectively; Horizontal fault; Red and blue represents opening and closing faulting, respectively). (b) Initial sea-surface displacement of the inverted slip model, with white contour lines plotted every 0.5 m uplift or subsidence. Black contour lines are plotted every 50 m of the water depth. (c) Waveform comparison of the computation (red) and observations (black). Gray lines represent the time window used for the inversion.

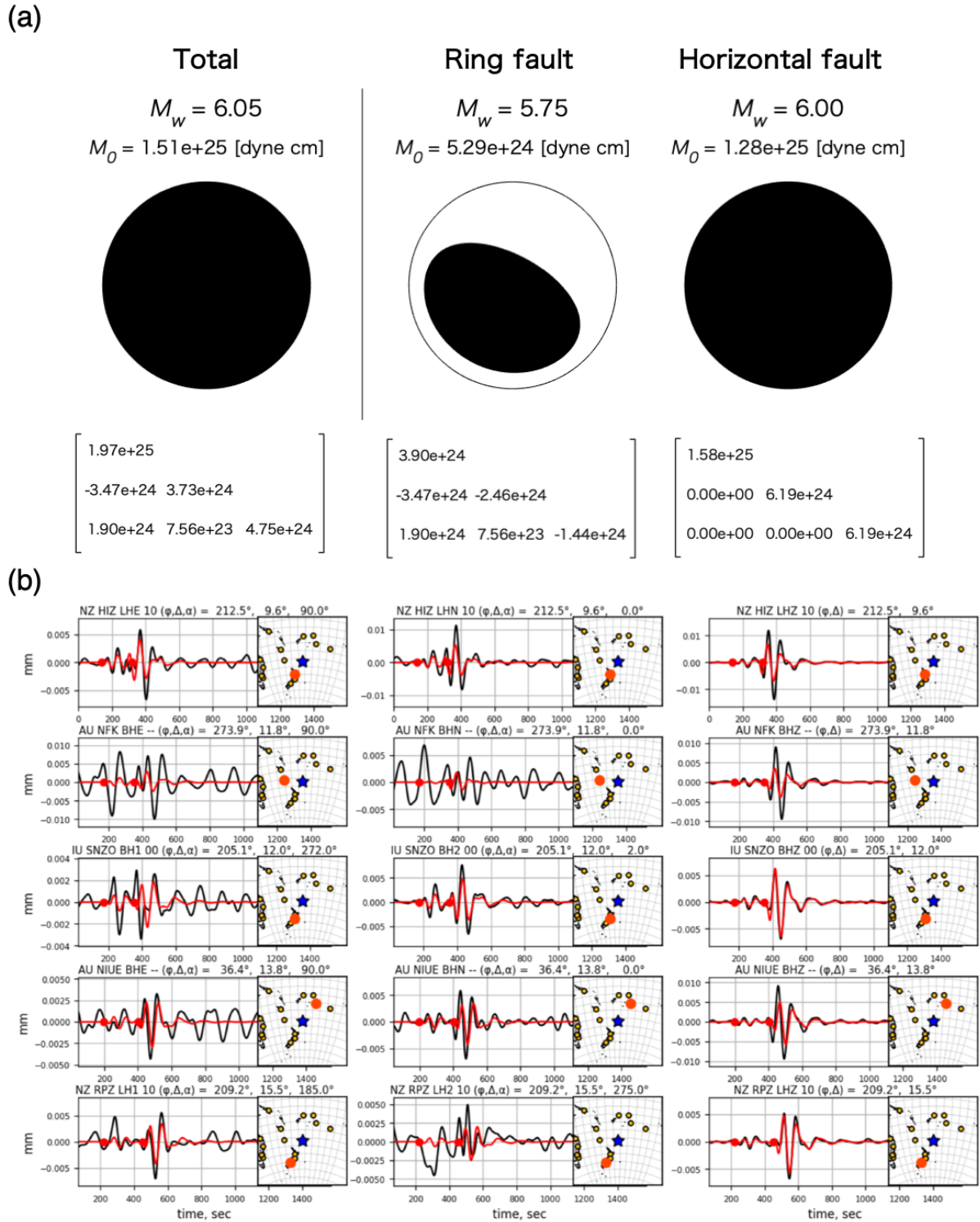


**Fig. 4.11 Moment tensor and long-period seismic waves of slip distributions of the reference fault model**

(a) Composite moment tensor of slip model (left), and partial moment tensors of slips on the ring fault (middle) and on the horizontal fault (right). (b) Waveform comparisons. Red and black lines represent synthetic and observed waveforms, respectively. In inset figures, blue star and big orange circle represent locations of the epicenter (Curtis Caldera) and a station, respectively.

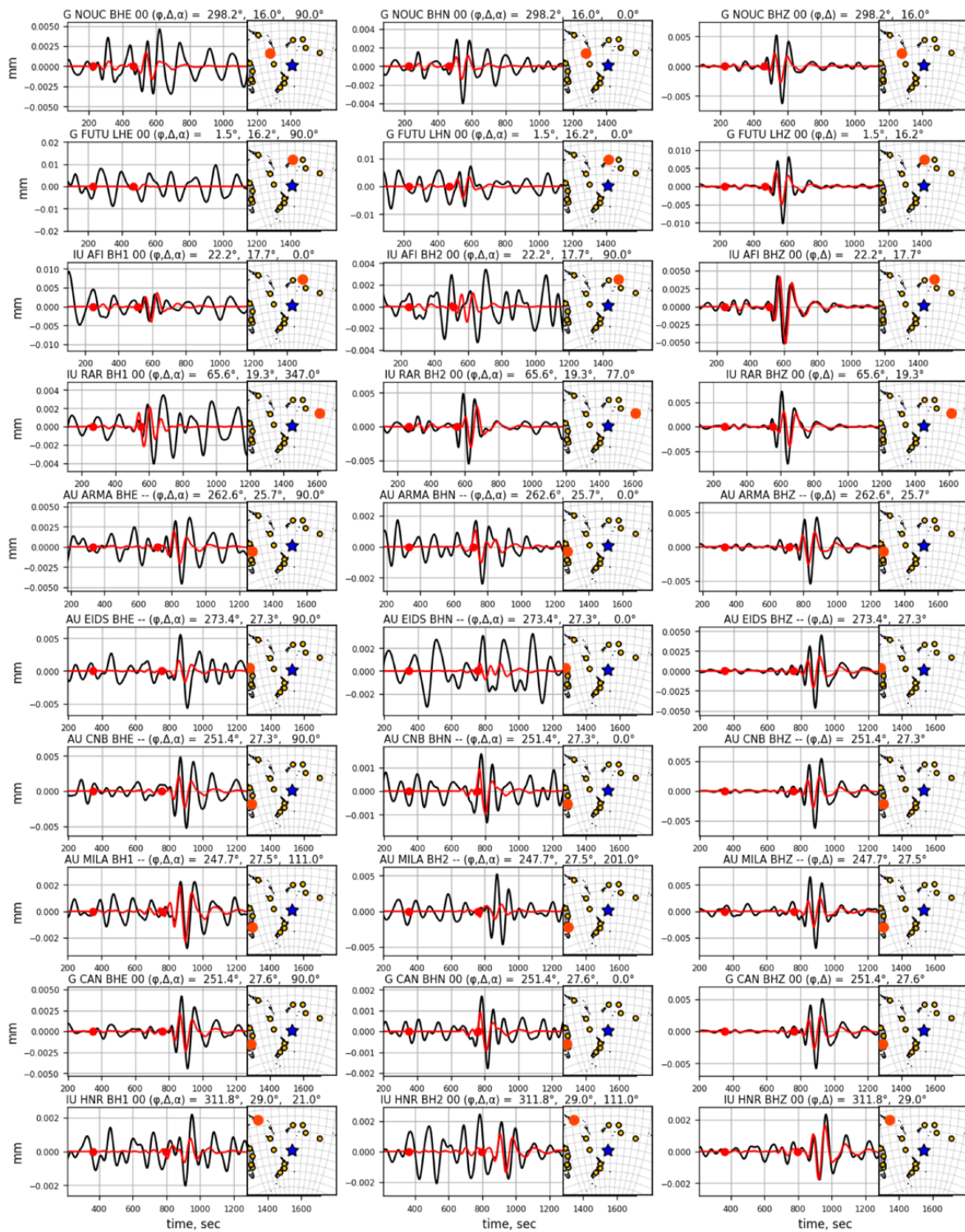
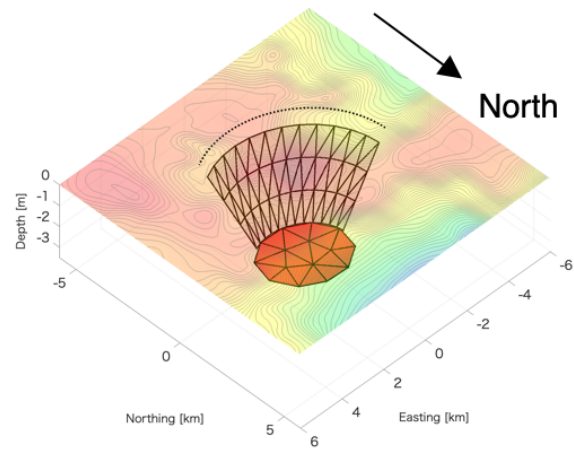
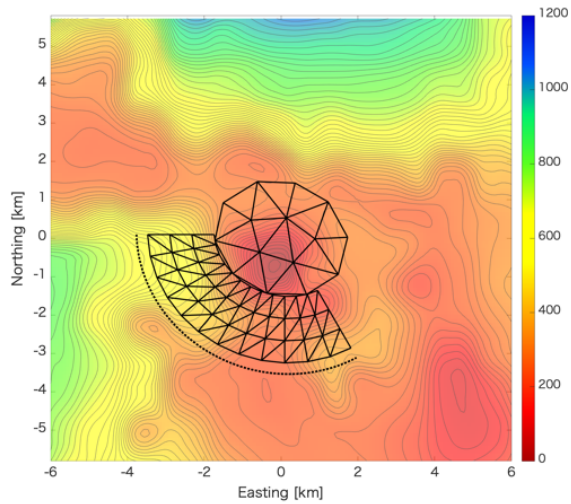
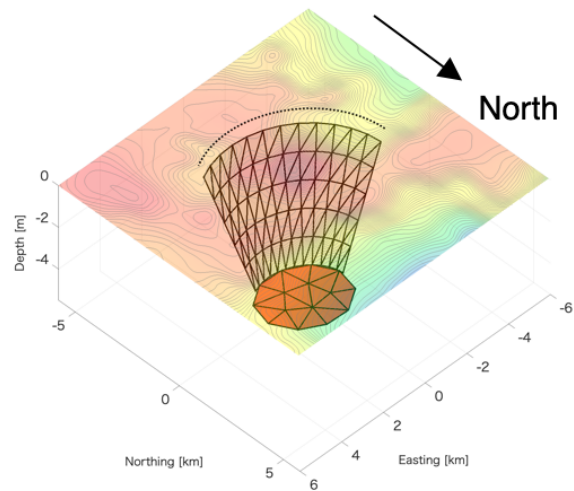
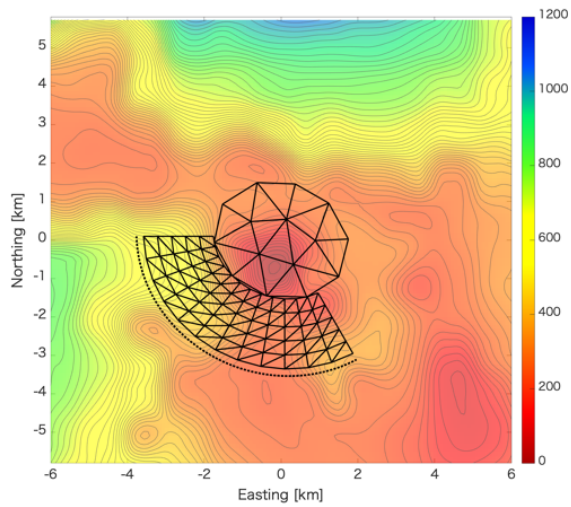


Fig. 4.11 (Continued)

(a) Modified-dip fault model



(b) Modified-thickness fault model



**Fig. 4.12 Modified fault models**

For both of the two modified models, the ring fault is emplaced as its trace extended to seafloor forms an ellipse shape with radius of  $3.8 \times 3.5$  km rotated clockwise by  $20^\circ$  around the central point at  $178.56^\circ\text{W}$ ,  $30.532\text{S}$ . (a) Modified-dip fault model: The ring fault has a uniform dip angle of  $60^\circ$ , and caldera block thickness is 3.0 km. (b) Modified-thickness fault model: The ring fault a uniform dip angle of  $70^\circ$ , and the caldera block thickness is 5.0 km.

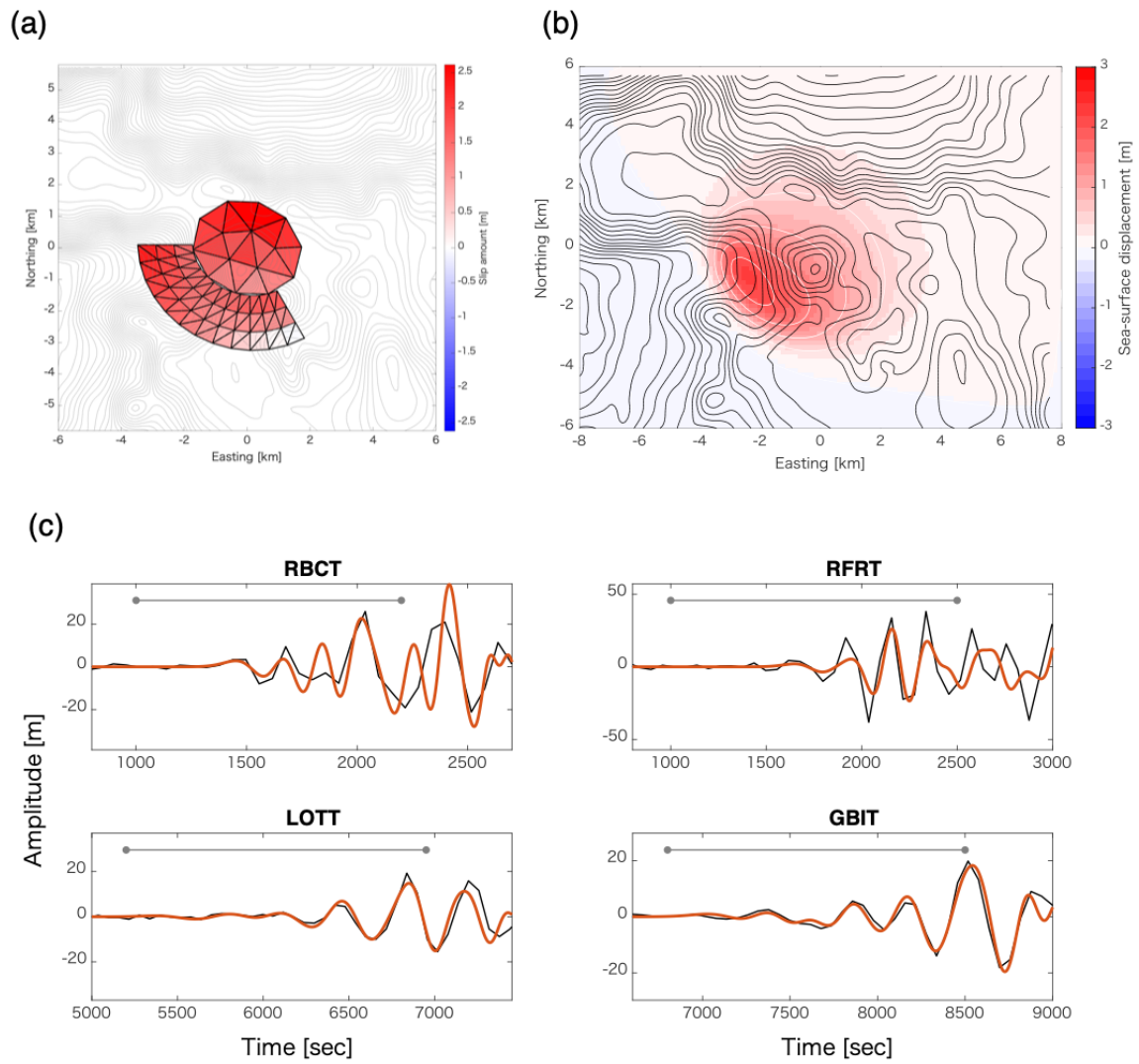
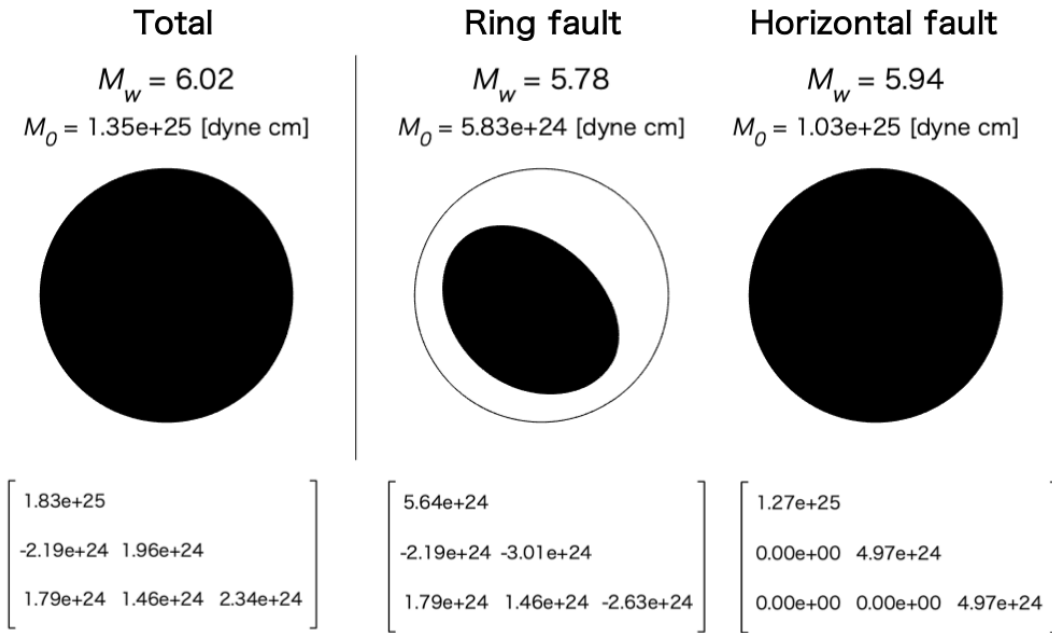


**Fig. 4.13 Inversion results with the modified-dip fault model**

Same as Fig. 4.10, but for the modified-dip fault model (Fig. 4.12a).

(a)



(b)

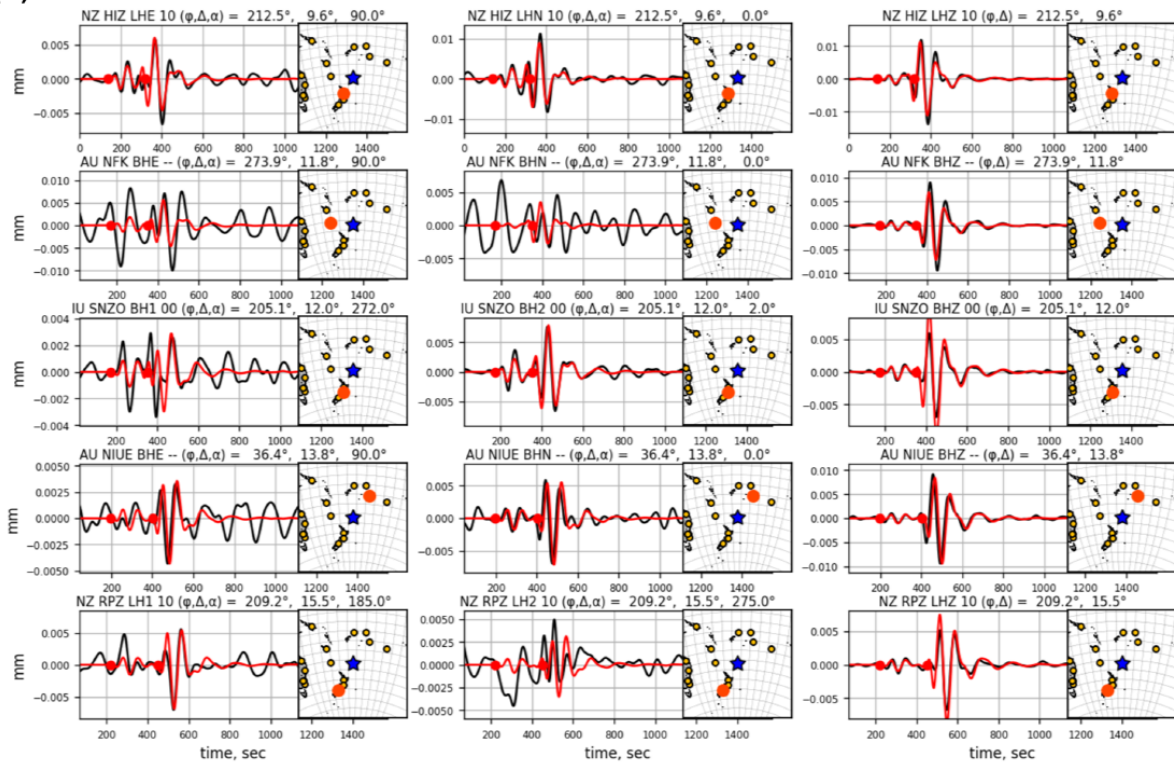


**Fig. 4.14 Moment tensor and long-period seismic waves of slip distributions of the modified-dip fault model**

Same as Fig. 4.11, but for the slip model on the modified-dip fault model (Fig. 4.13a).

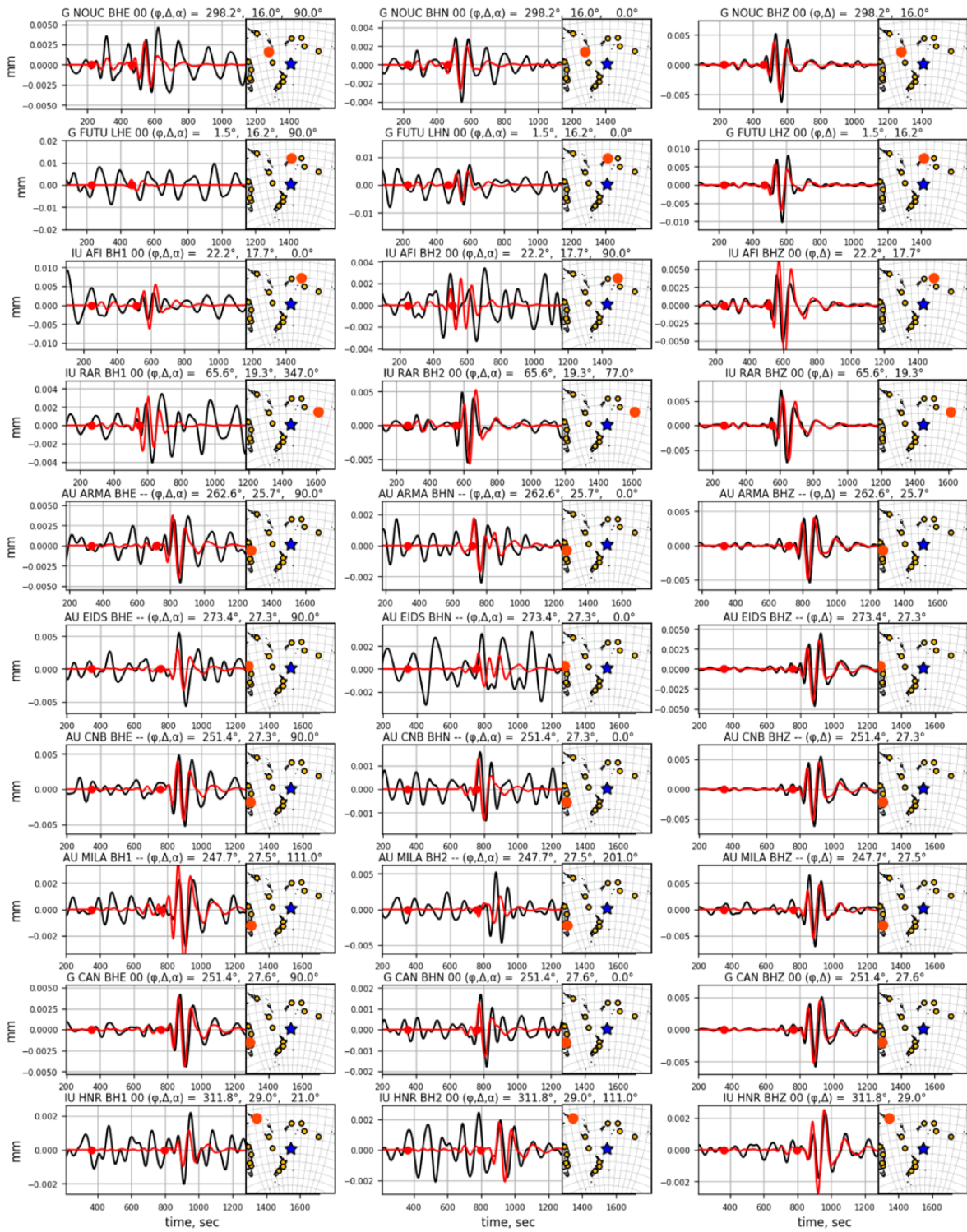
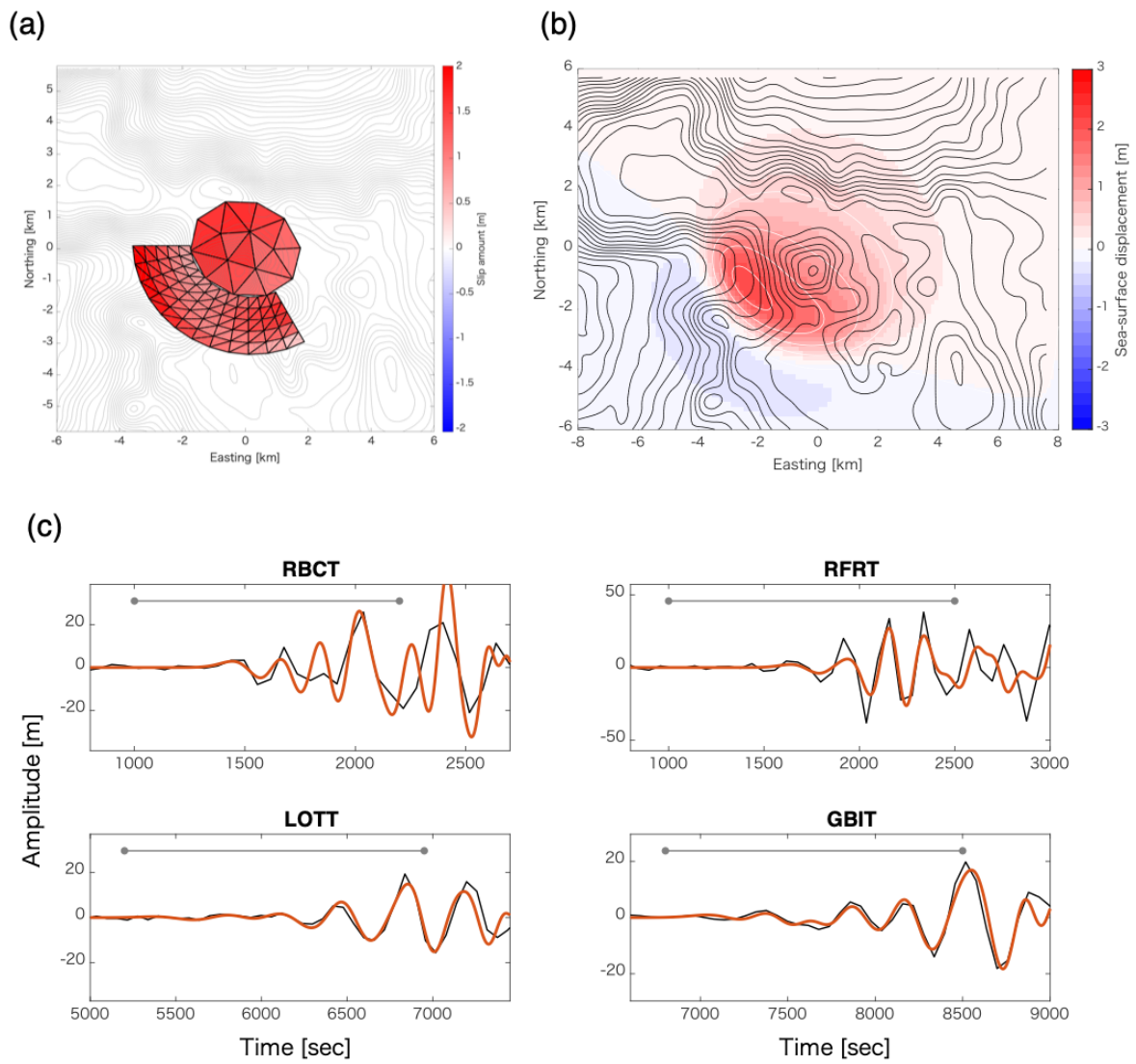
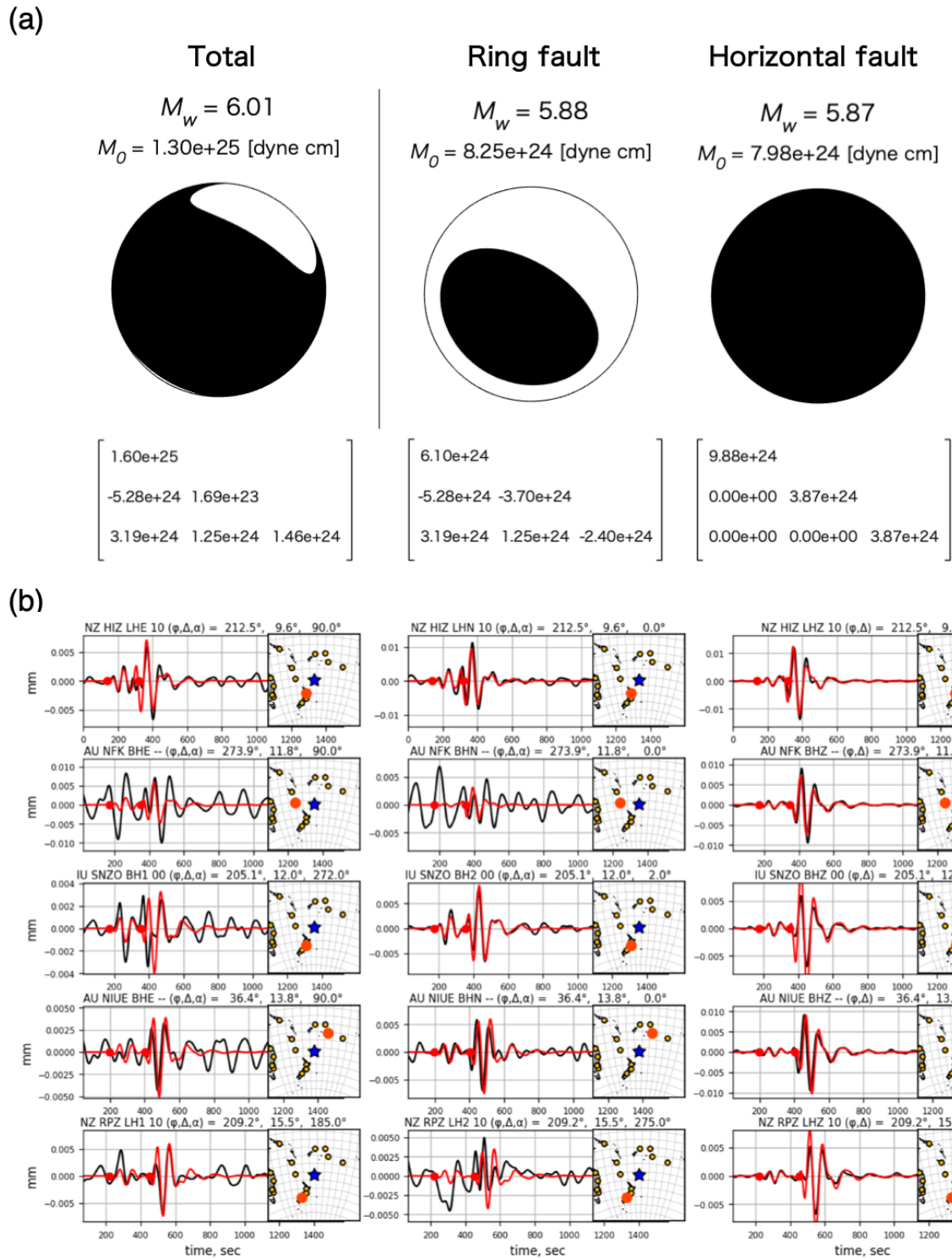


Fig. 4.14 (Continued)



**Fig. 4.15 Inversion results with the modified-thickness fault model**  
 Same as Fig. 4.10, but for the modified-thickness fault model (Fig. 4.12b).



**Fig. 4.16 Moment tensor and long-period seismic waves of slip distributions of the modified-thickness fault model**

Same as Fig. 4.11, but for the slip model on the modified-thickness fault model (Fig. 4.15a).

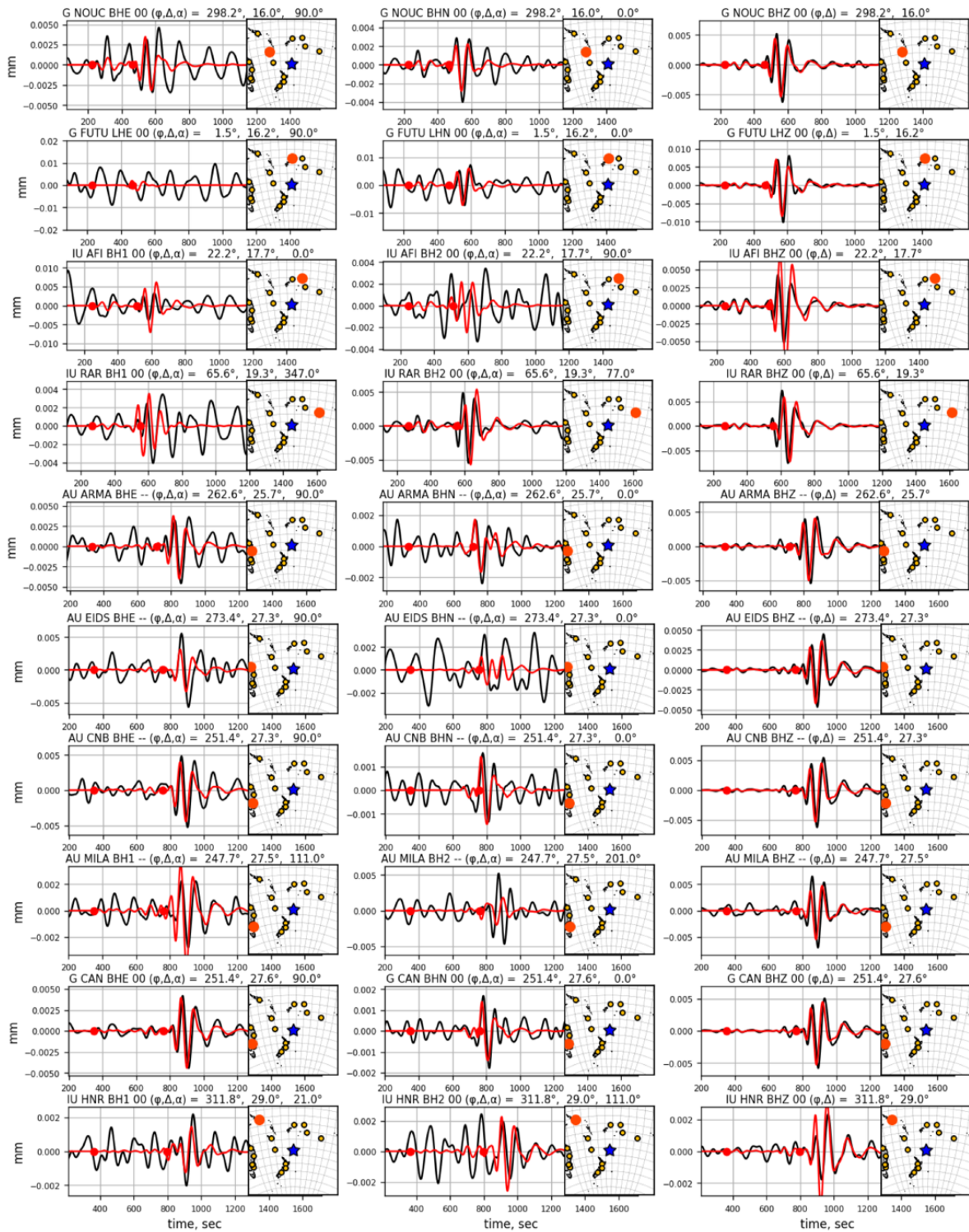
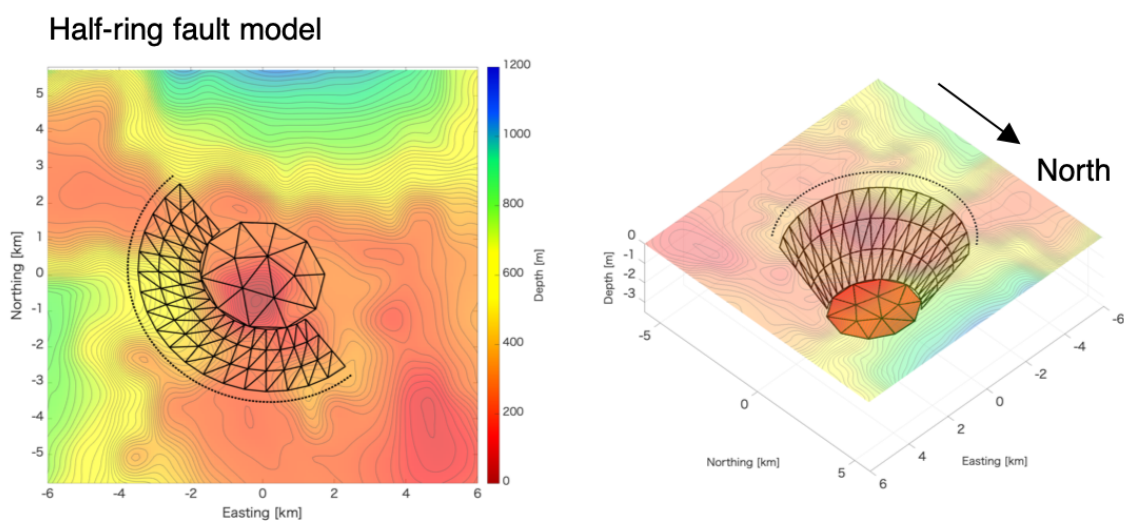


Fig. 4.16 (Continued)

### 4.4.2.3 Ruptured portion of the ring fault

Apart from the fault parameters discussed above, a ruptured portion of the ring fault affects long-period seismic waves, particularly their horizontal components. By changing the ruptured portion of the modified-dip fault model (Fig. 4.12a), I assumed a half-ring fault model and conducted the relevant analysis (Fig. 4.17). The resulting inversion of tsunami waveforms produced an inverted slip model with a maximum slip amount of 2.14 m (Fig. 4.18a), explaining recorded tsunami waveforms sufficiently (Fig. 4.18c, Table 4.1a). However, the fitness of the long-period seismic waves was worse when the ring fault extended along half the rim (NRMS=0.916), compared to the modified-dip fault model (NRMS=0.861; Table 4.1b). This can be seen in some of the NS components at stations ARMA, CNB, and CAN (compare Fig. 4.14b and Fig. 4.19c), indicating that ring-fault ruptures possibly occurred in shorter portions than the half ring. The seismic energy elimination could be explained by the cancellation of moment release from different portions of the curved ring fault, as suggested by *Ekström* [1994]. Effects of ring-fault geometries on long-period seismic energy release are discussed further in Chapter 5.2.



**Fig. 4.17 Half-ring fault model**

The ring fault a uniform dip angle of  $60^\circ$ , and the caldera block thickness is 3.0 km. the ring fault is emplaced as its trace extended to seafloor forms an ellipse shape with radius 3.5–3.8 km rotated clockwise by  $20^\circ$  around the central point at  $178.56^\circ\text{W}$ ,  $30.532\text{S}$ .

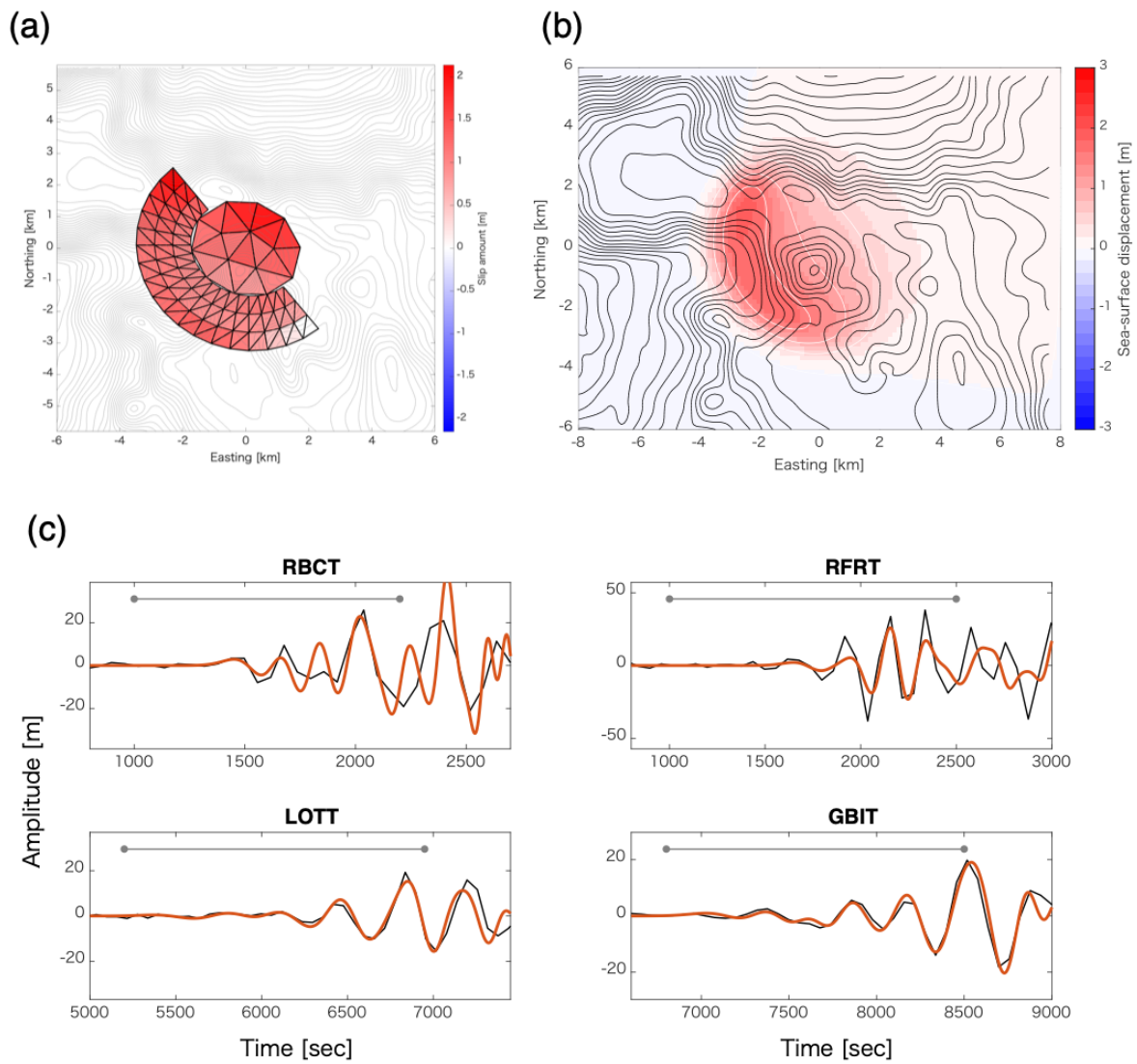


**Fig. 4.18 Inversion results with the half-ring fault model**

Same as Fig. 4.10, but for the modified-thickness fault model (Fig. 4.17b).

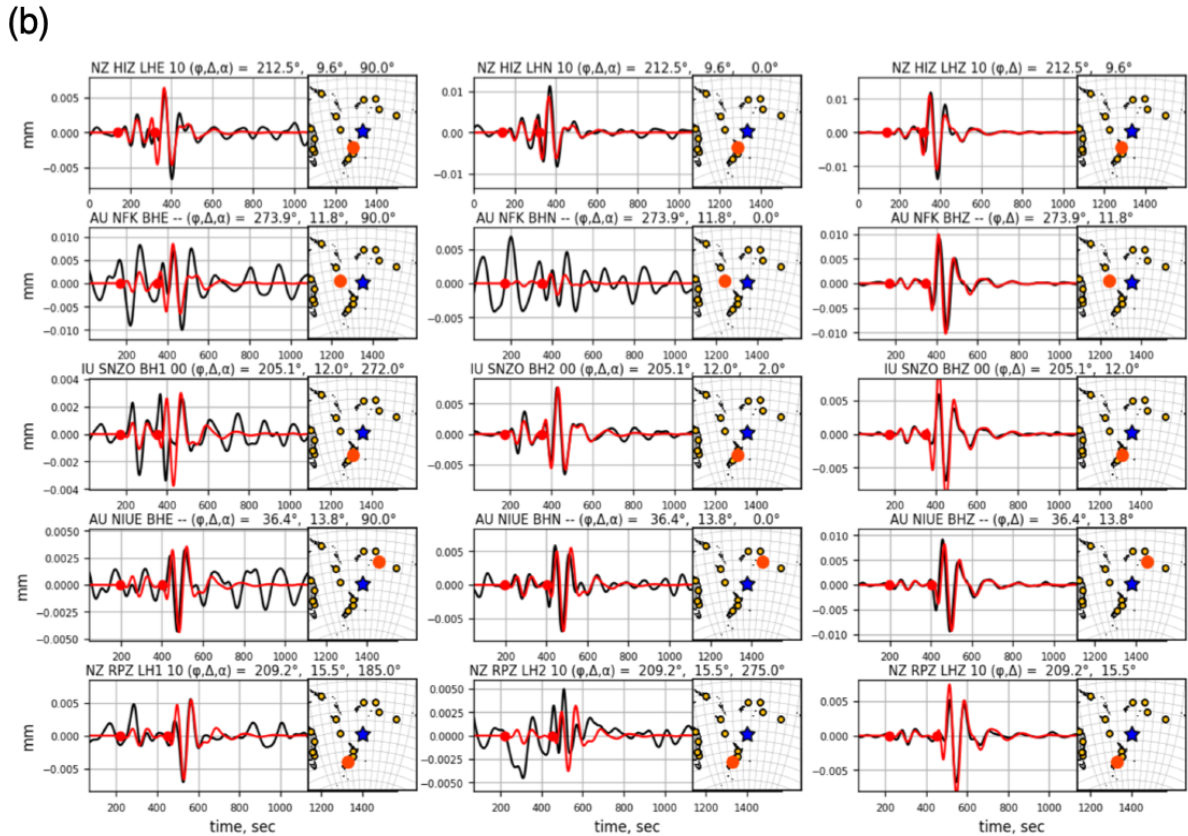
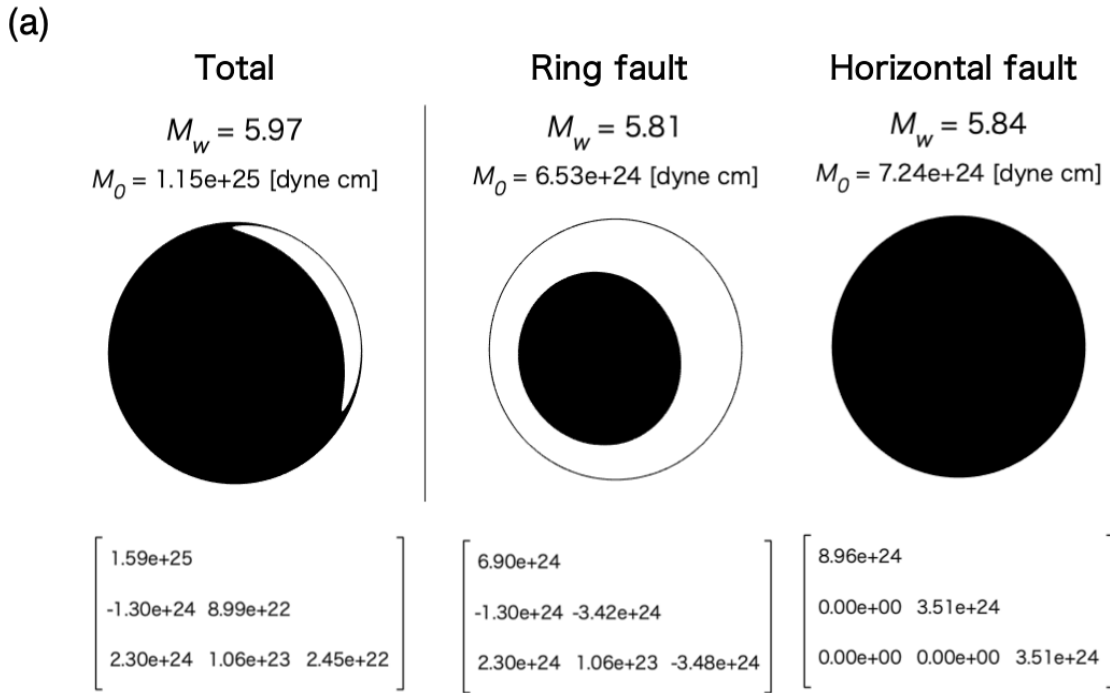


**Fig. 4.19 Moment tensor and long-period seismic waves of slip distributions of the half-ring fault model**  
 Same as Fig. 4.11, but for the slip model on the modified-thickness fault model (Fig. 4.18a).

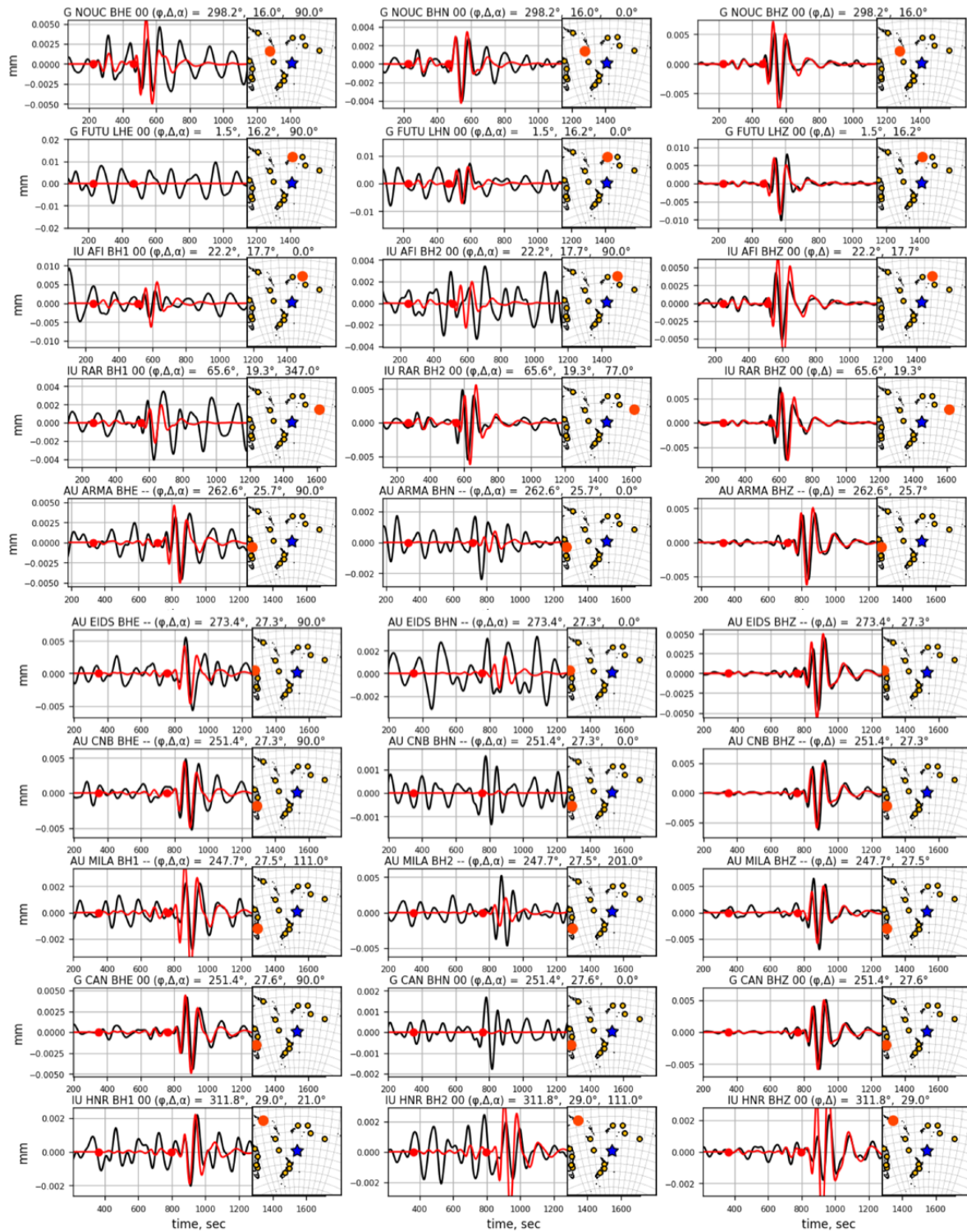


Fig. 4.19 (Continued)

### 4.4.3 Discussion

I successfully constructed two kinematic source models that sufficiently reproduced observed records of tsunamis and long-period seismic waves (modified-dip model: Fig. 4.13-4.14; modified-thickness model: Fig. 4.15-4.16). Both models showed thrust faulting with a few-meter slip on the ring fault on the southwest of the caldera accompanied by an opening of the horizontal fault. These results strongly suggest that the hypothetical physical mechanism, composed of a volumetric change in a shallow horizontal crack filled with magma and a rupture of the ring fault, was reasonable for the 2017 Curtis earthquake as well as the 2015 Torishima earthquake. The physical mechanism and other features are further discussed in Chapter 5, together with the source model of the Torishima earthquake.

The resolution and reliability of the inverted source model of the 2017 Curtis earthquake were worse compared to those of the 2015 Torishima earthquake, probably because of the 4–6 tsunami records available only with low sampling rates at remote tide-gauge stations and low S/N ratios in seismic records. For example, the opening amount on the horizontal fault may have been overestimated. As shown in Fig. 4.6, the inverted initial sea-surface displacements consisted of uplift distributed broadly around the caldera structure, which may be attributed to the low-sampling tide-gauge records used for the inversion. Such a broad deformation can be optimally explained by tensile opening of the horizontal fault rather than dip slips on the ring fault. In addition, larger uncertainties in prior information for the subsurface geometries of Curtis Caldera made it more challenging to determine detailed fault parameters, as seen in the wide possible ranges of fault parameters (such as a ring fault dip angle from 60–70° and a caldera thickness from 3.0–5.0 km). In order to obtain a source model with higher reliability and resolution, further explorations will be required with better circumstances for tsunami and earthquake observations, and with direct surveys of bathymetry or subsurface structures in order to extract better information regarding the caldera structures.

## 4.5 Summary of Chapter 4

In this chapter, I pursued a kinematic source model of the 2017 Curtis volcanic tsunami earthquakes. To model sources of the earthquake, I used tsunami waveforms recorded at tide-gauge stations on the North Island and remote islands of New Zealand. I first conducted forward tsunami simulations from Gaussian-shaped uplift sources distributed around earthquake locations reported for the Curtis earthquakes in 2009 and 2017 by the USGS and GCMT. By comparing synthetic waveforms with these observations, I determined a tsunami source area near Curtis and Cheeseman Islands.

Next, I conducted an inversion of tsunami waveforms to estimate initial sea-surface displacement by the 2017 Curtis earthquake. Inclusions of tsunami travel-time delays at remote tide-gauge stations improved the waveform fitting levels. The results showed that large uplift was excited by the earthquake on the southwest part of a submarine caldera surrounding Curtis and Cheeseman Islands. Indirect evidence of resurgence in the submarine caldera, such as large cumulative long-term uplift and a

dome structure with volcanic vents on the caldera floor, implied the existence of ring-fault structures and a sill-like magma-filled chamber.

Given this context, I assumed a composite fault model consisting of a partial ring fault on the southwest side and a horizontal fault below the submarine caldera. Using the inversion of tsunami waveforms for slip distributions and forward modeling of long-period seismic waves, I successfully obtained two slip models explaining the tsunami and long-period seismic records. Although the lack of prior information on subsurface structures of the submarine caldera made it difficult to constrain the detailed geometries, the 2017 Curtis earthquake was successfully explained using a composite source model of thrust faulting on a partial ring fault and opening of a horizontal fault, similar to that of the 2015 Torishima earthquake.



# ***Chapter 5    General discussion***

## **5.1    Physical mechanism of volcanic tsunami earthquakes**

In previous chapters, I explored kinematic source models of the 2015 Torishima and 2017 Curtis volcanic tsunami earthquakes to determine the physical mechanisms related the source process. I first investigated the seafloor deformation of the earthquakes by using different types of tsunami source modeling. The tsunami analysis revealed occurrences at submarine volcanoes with caldera structures that similarly excited meter-scale uplift of a caldera floor with a clear boundary of the uplifted area along the topographic rim structure. Outside the rim, peripheral subsidence along the rim structure was robustly confirmed with high-quality OBP records at relatively nearby stations for the Torishima earthquake; this may have been true for the Curtis earthquake as well.

The inferred seafloor deformation associated with submarine calderas motivated me to hypothesize a physical mechanism: instantaneous ruptures consisting of a shallow horizontal crack opening filled with high-pressure magma and a ring fault slip. To examine the validity of this hypothesis, I assumed a composite fault model of a dip-slipping ring fault and a tensile-opening or -closing horizontal fault, which may have existed below the submarine calderas. The inversion of tsunami waveforms for fault slips enabled me to construct slip distributions at arbitrary assumed composite fault geometries. By examining fittings of synthetic long-period seismic waveforms to the observed records, I succeeded in constructing kinematic source models both for the Torishima and Curtis earthquakes, which accurately reproduced tsunami and long-period seismic wave records. Quantitative validations using the two types of the observations strongly supported the hypothetical physical mechanism.

The kinematic source models made it possible to quantitatively interpret the physical mechanism of volcanic tsunami earthquakes including concrete fault geometries. Here, I discuss the mechanism mainly by considering a kinematic source model for the best TR model (Fig. 5.1a-b, Fig. 3.12, 3.18), which was constructed for the 2015 Torishima earthquake, because the model was validated from better observational circumstances in terms of the number and quality of tsunami and long-period seismic records as well as detailed topographic structures around Smith Caldera.

Slip distributions of the kinematic source model showed complex fault behaviors on the composite fault model (Fig. 5.1d). Thrust faulting was estimated on the three-quarter ring fault with a maximum slip amount of ~2.7 m on the NE part and the ring-fault edges. On the side of the ring fault, the vertical opening of the horizontal fault was estimated with a slip amount comparable to that on the ring fault. The ring-fault thrust slips and vertical opening of the horizontal fault on the NE side consistently indicated an upward motion of the subsurface caldera block. On the other hand, the source model showed a closing of the horizontal fault on the SW side, implying a downward motion of the caldera block, in the opposite sense of that on the NE side.

The kinematic source models of the 2017 Curtis volcanic tsunami earthquake (Fig. 4.13a or Fig. 4.15a) were slightly different from those of the 2015 Torishima earthquake, in that a vertical opening was estimated entirely on the former's horizontal fault. However, detailed features like the closing of the fault could not be resolved from the limited and low-sampling tsunami records of the Curtis earthquake. Therefore, considering other common features clearly shared by the two earthquakes, I simply assumed that the Curtis earthquake had a physical mechanism equivalent to that of the Torishima earthquake.

Based on the kinematic source model of the Torishima earthquake, I therefore suggest a scenario involving ruptures on the composite fault system below the caldera as follows (Fig. 5.1c-d):

1. Preparation process before a volcanic tsunami earthquake (Fig. 5.1c)

Prior to the occurrence of a volcanic tsunami earthquake, magma ascending from depth intrudes continuously or intermittently into a shallow horizontal fault, or a sill-like crack below a subsurface caldera block. The accumulated magma increases internal pressure within the crack, causing shear stress on a pre-existing ring fault structure. At this moment, strength of the ring fault is still high enough to accommodate magma below the caldera block, allowing an increase in the internal magma pressure.

2. Occurrence of a volcanic tsunami earthquake (Fig. 5.1d)

When the shear stress on the ring fault generated by the over-pressurized crack reaches a critical threshold, a rupture initiates and propagates along the ring fault with a thrust-faulting sense. The crack is successively forced to open along the ring fault mainly due to sudden stress changes accompanying the ring-fault rupture. The opening of the crack on one side causes deflation of the magma inside, resulting in consecutive crack closing on the other side.

This proposed scenario speculates that a ring-fault fracture acts as the trigger of instantaneous ruptures on the composite fault system, successively promoting the opening/closing of the crack filled with magma. However, this study did not have sufficient temporal resolution to demonstrate this, as only long-period properties of tsunamis and seismic waves were analyzed. A deeper understanding of the initiation and propagation of such ruptures will require analyses of higher-frequency seismic waves, in-situ observations at submarine calderas, or improved dynamics of the rupture's interactions with magma and intra-caldera fault systems, but these efforts are beyond the scope of this study.

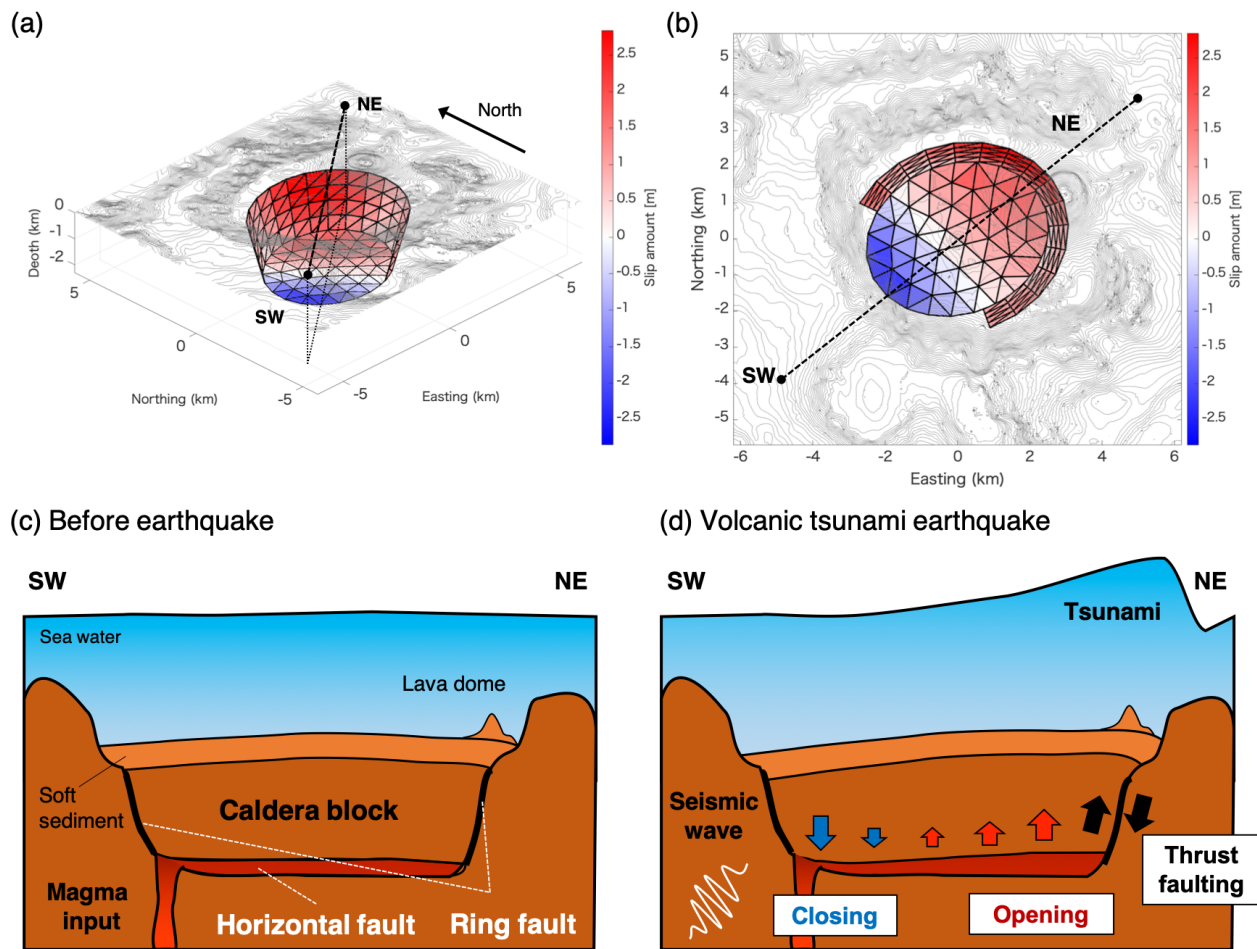


**Fig. 5.1 Interpretation of the physical mechanism with a rupture scenario of volcanic tsunami earthquake**

(a-b) The kinematic source model of the 2015 Torishima earthquake. (c-d) Schematic illustrations of the physical mechanism of volcanic tsunami earthquakes. (c) Preparation process before an earthquake. (d) Coseismic ruptures. See text in Chapter 5.1 for the details.

To develop this scenario, I referred to a similar phenomenon observed at an inland shield volcano, the Sierra Negra volcano in the Galápagos [Reynolds *et al.*, 1995]. Its summit caldera, with a size of  $10 \text{ km} \times 7 \text{ km}$ , contains an intra-caldera sinuous fault system on the west and south portions of the caldera floor. Along this sinuous fault, thrust faulting events called *trapdoor faulting* were reported, including a few  $M_w$  5-class earthquakes from 1997 to 1998 (the exact time is not clear), and in 2005 and 2018 [e.g. Amelung, 2000; Chadwick *et al.*, 2006; Jónsson, 2009; Amelung *et al.*, 2018]. Large asymmetric uplifts of the caldera floor were observed during the occurrence of such trapdoor faulting. For example, a GPS station along the southern fault recorded an 84 cm uplift within 10 s of the event on April 16, 2005 [Chadwick *et al.*, 2006]. Sudden crack closing due to sudden magma deflation may have accompanied the trapdoor faulting, as indicated by subsidence of a few centimeters recorded by GPS stations on the northern part of the caldera floor [Jónsson, 2009]. Since an inflating sill-like magma reservoir lying at  $\sim 2 \text{ km}$  depth below the floor was inferred from elastic deformation prior to the trapdoor faulting [Amelung, 2000; Yun

*et al.*, 2006], the rupture on the sinuous fault may have occurred due to stress fields generated by a high-pressurized sill-like magma reservoir [Jónsson, 2009; Gregg *et al.*, 2018]. An event on October 22, 2005 was characterized by a moment tensor with a dominant vertical-CLVD component as reported by the GCMT and USGS; this was also listed in Shuler *et al.* [2013a]’s catalogue as a vertical-CLVD earthquake.

Therefore, I conclude that the physical mechanism of volcanic tsunami earthquakes is equivalent to that of trapdoor faulting, considering the common features in source structures, rupture properties, deformation, and earthquake characters. This analogy implies that magma intrudes into a horizontal crack at shallow depth below the seafloor and increases stress levels in submarine calderas prior to volcanic tsunami earthquakes. Jónsson [2009] computed stress fields and the Coulomb Failure Stress change generated by inflating a sill-like magma reservoir and indicated that the pressure source may promote thrust faulting on steeply inward-dipping faults within the caldera floor. The author also suggested that intra-caldera faulting events in turn relieve magma pressure inside a reservoir, which may postpone eruptions by allowing accommodations of large quantities of magma. Given this analogy with such well-monitored trapdoor faulting events in a subaerial caldera, it seems reasonable to speculate that stress interactions between magma inside a crack and faulting of a ring fault system could control volcanic activities at submarine calderas such as the Smith and Curtis calderas, where volcanic tsunami earthquakes regularly occur.

## 5.2 Long-period seismic waves excited by volcanic tsunami earthquakes

In Chapters 3 and 4, I succeeded in reproducing long-period seismic waves of volcanic tsunami earthquakes by modeling the moment tensors of the kinematic source models. In this section, I investigate the seismic radiation properties of volcanic tsunami earthquakes, primarily based on a kinematic source model for the 2015 Torishima earthquake composed of thrust faulting on a ring fault and tensile opening and closing of a horizontal fault (Fig. 5.1a-b). As the complicated instantaneous fractures make it difficult to directly interpret the properties of seismic radiation, I first consider observable elements of the moment tensors and then investigate their associations with the earthquake source.

### 5.2.1 Observable moment tensor elements

#### 5.2.1.1 Theory

The modeling studies revealed that volcanic tsunami earthquakes occurred at very shallow depth ( $< \sim 5$  km). It is quite significant that some types of moment tensors contained by volcanic tsunami earthquakes might be unobservable in long-period seismic energy due to very shallow source depth near the solid surface [e.g. Kanamori and Given, 1981; Dahlen and Tromp, 1998; Fukao *et al.*, 2018]. Generally, the dynamic boundary condition of the solid free surface imposes zero traction on the surface, resulting in nearly-zero strain

at shallow depth:

$$(\lambda + 2\mu)\epsilon_{rr} + \lambda\epsilon_{\theta\theta} + \lambda\epsilon_{\phi\phi} \approx 0, \quad \text{Eq. 5.1}$$

and

$$\epsilon_{r\theta} = \epsilon_{r\phi} \approx 0, \quad \text{Eq. 5.2}$$

where  $\epsilon$  represents the strain tensor and  $\lambda$  and  $\mu$  are Lamé's constants. Because the contributions of a moment tensor  $\mathbf{M}$  to seismic waves are proportional to  $\mathbf{M}:\epsilon^*$  (superscript \* indicates a complex conjugate), the strain-free conditions near the solid surface make some types of fractures aseismic for long-period seismic energy. Equation 5.1 indicates that a fracture near the crust's surface with a moment tensor proportional to  $\begin{bmatrix} \lambda + 2\mu & & \\ 0 & \lambda & \\ 0 & 0 & \lambda \end{bmatrix}$  releases little long-period seismic energy, which is equivalent to that of a tensile opening of a horizontal fault [Fukao *et al.*, 2018]. On the other hand, Equation 5.2 indicates that moment tensors proportional to  $\begin{bmatrix} 0 & & \\ 1 & 0 & \\ 0 & 0 & 0 \end{bmatrix}$  and  $\begin{bmatrix} 0 & & \\ 0 & 0 & \\ 1 & 0 & 0 \end{bmatrix}$  at shallow depth do not contribute much to long-period seismic waves, which represent pure dip slips on a vertical fault [Kanamori and Given, 1981].

In the following subsections, I investigate this theory based on a kinematic source model of the 2015 Torishima earthquake (the TR model), which I here refer to simply as the “Torishima source model” (Fig. 3.12a; Fig. 5.1a-b).

### 5.2.1.2 Seismic radiations by tensile opening of a horizontal crack

The tensile-opening fractures on the horizontal fault of volcanic tsunami earthquakes do not excite long-period seismic waves as considered by Eq. 5.1. To confirm this, I computed long-period seismic waves excited by the moment tensor of the horizontal fault rupture in the Torishima source model (Fig. 5.2b). Figure 5.3 shows that long-period seismic waves were negligibly small compared to the observed records, even at F-net stations with epicentral distances shorter than  $5^\circ$ .

Apart from the low-seismic excitation property, the instantaneous occurrence of horizontal fault opening and closing may cancel out moment releases of volcanic tsunami earthquakes. The Torishima source model contained opening activity equivalent to  $M_w$  5.85 ( $M_0 = 7.58 \times 10^{24}$  [dyne cm]) with a positive volume change of  $10.5 \times 10^6$  [m<sup>3</sup>] and closing activity equivalent to  $M_w$  5.80 ( $M_0 = 6.23 \times 10^{24}$  [dyne cm]) with a negative volume change of  $8.63 \times 10^6$  [m<sup>3</sup>]. These comparable slips in opposite directions canceled out their moment tensors, resulting in a smaller moment magnitude  $M_w$  5.35 ( $M_0 = 1.35 \times 10^{24}$  [dyne cm]). Such complex ruptures related to magma depressurization inside a horizontal fault (or crack) may make the rupture even more aseismic.

### 5.2.1.3 Seismic radiations by dip slips on a ring fault

In contrast to the above, the zero-stress condition (Eq. 5.2) predicts that moment tensors representing pure dip slip on a vertical fault do not produce long-period seismic waves, which may closely affect seismic excitation properties of volcanic tsunami earthquakes that contain dip slip along a ring fault.

However, because of the curved fault structure, the moment tensor of the ring fault slip is too complicated to interpret directly with itself, as seen in that of the Torishima source model (Fig. 5.2b).

In order to understand the seismic radiation of this complex source, I decomposed the moment tensor into four elements: isotropic (*ISO*), vertical-CLVD (*CLVD*), and two double-couple (DC) elements representing pure strike slip (*Strike-DC*) and pure dip slip (*Dip-DC*) (Fig. 5.4). To obtain these four elements, diagonal components ( $M_{rr}$ ,  $M_{\theta\theta}$ ,  $M_{\phi\phi}$ ) were first newly defined as ( $M_{ISO}$ ,  $M_{CLVD}$ ,  $M_D$ ) by following *Kawakatsu* [1996]:

$$M_{ISO} = \frac{1}{3}(M_{rr} + M_{\theta\theta} + M_{\phi\phi}), \quad \text{Eq. 5.3}$$

$$M_{CLVD} = \frac{1}{3}(2M_{rr} - M_{\theta\theta} - M_{\phi\phi}), \quad \text{Eq. 5.4}$$

$$M_D = \frac{1}{2}(M_{\theta\theta} - M_{\phi\phi}). \quad \text{Eq. 5.5}$$

Note that the polarity of the vertical-CLVD component was opposite to that of *Kawakatsu* [1996]'s definition.

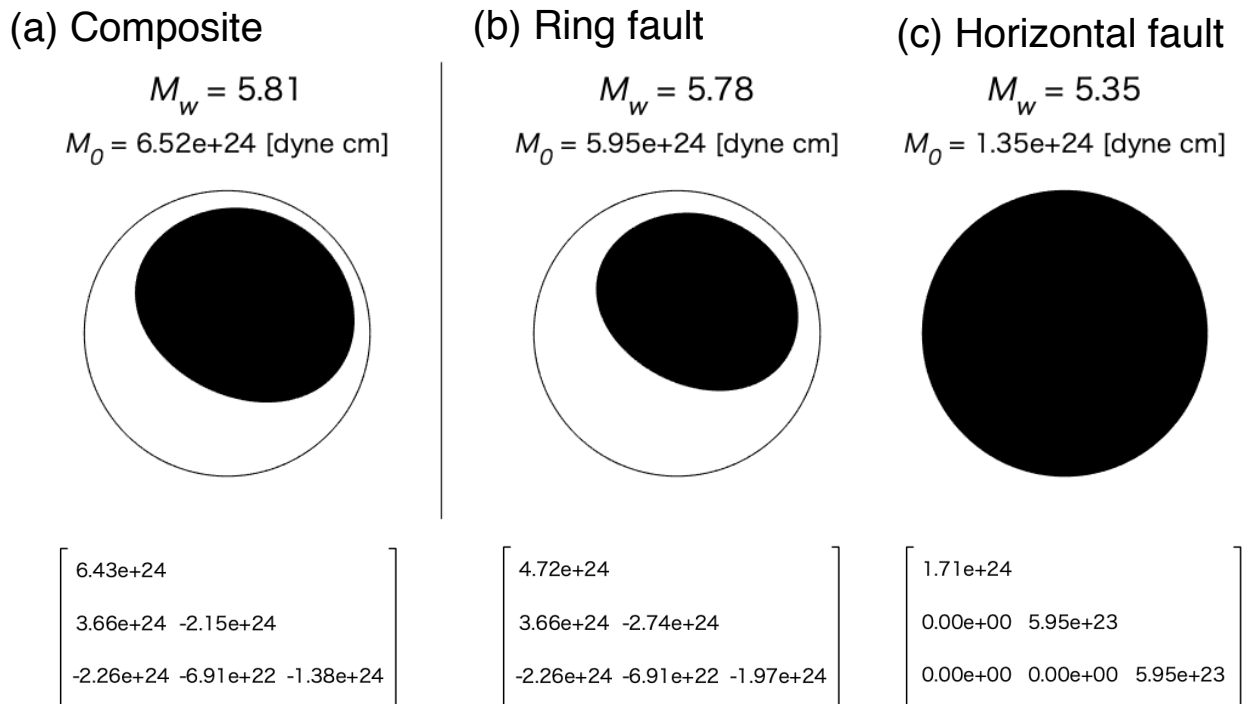


**Fig. 5.2 Moment tensor of the Torishima source model**

(a) Composite moment tensor of slip model. (b-c) partial moment tensors of slips on the ring fault (b) and on the horizontal fault (c). Moment tensors shown in the bottom has a unit of [dyne cm].

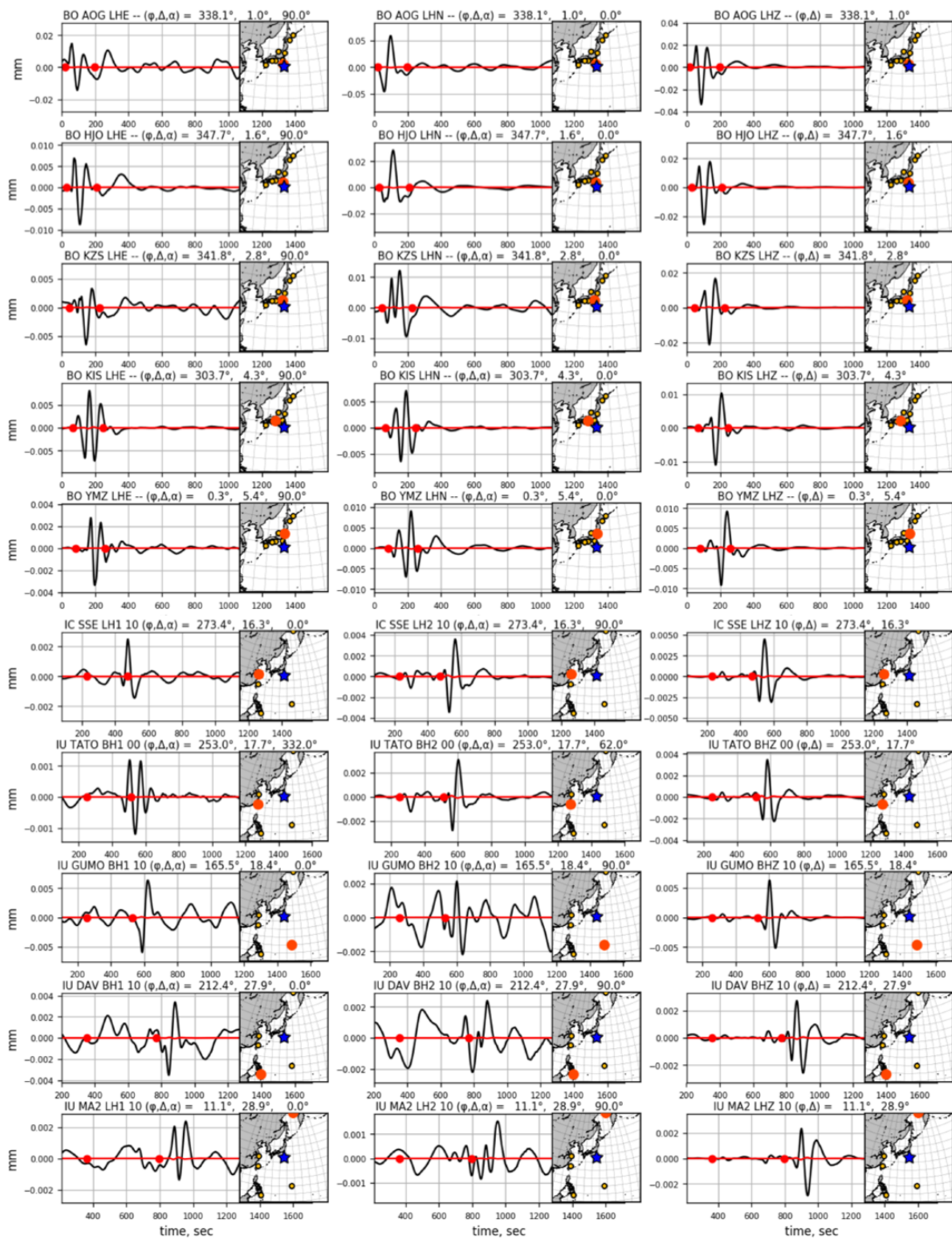


**Fig. 5.3 Long-period seismic waves excited by fractures of the horizontal fault of the Torishima source model**

Red and black lines represent synthetic and observed waveforms, respectively. Blue star and big orange circle represent locations of the epicenter (Smith Caldera) and a station, in inset figures.

$$\begin{aligned}
M_{ISO} &= \frac{1}{3}(M_{rr} + M_{\theta\theta} + M_{\phi\phi}) \longrightarrow \text{●} \quad \text{ISO} &= M_{ISO} \begin{bmatrix} 1 & & \\ 0 & 1 & \\ 0 & 0 & 1 \end{bmatrix} \\
M_{CLVD} &= \frac{1}{3}(2M_{rr} - M_{\theta\theta} - M_{\phi\phi}) \longrightarrow \text{⊙} \quad \text{CLVD} &= M_{CLVD} \begin{bmatrix} 1 & & \\ 0 & -1/2 & \\ 0 & 0 & -1/2 \end{bmatrix} \\
\left. \begin{array}{l} M_D \\ M_{\theta\phi} \end{array} \right\} &\longrightarrow \text{⊗} \quad \text{Strike-DC} &= M_D \begin{bmatrix} 0 & & \\ 0 & 1 & \\ 0 & 0 & -1 \end{bmatrix} + M_{\theta\phi} \begin{bmatrix} 0 & & \\ 0 & 0 & \\ 0 & 1 & 0 \end{bmatrix} \\
\left. \begin{array}{l} M_{rt} \\ M_{r\phi} \end{array} \right\} &\longrightarrow \text{⊕} \quad \text{Dip-DC} &= M_{rt} \begin{bmatrix} 0 & & \\ 1 & 0 & \\ 0 & 0 & 0 \end{bmatrix} + M_{r\phi} \begin{bmatrix} 0 & & \\ 0 & 0 & \\ 1 & 0 & 0 \end{bmatrix}
\end{aligned}$$

**Fig. 5.4 Decomposition of moment tensor**

See text in Chapter 5.2.1.2.

Then, two independent DC elements with  $M_D$  and  $M_{\theta\phi}$  components were combined into a new DC element, *Strike-DC*, which represented a pure strike slip on a vertical planar fault with an arbitrary strike direction. The other DC elements with  $M_{r\theta}$  and  $M_{r\phi}$  were combined into another new element, *Dip-DC*, which was equivalent to pure dip slip on a vertical fault with an arbitrary strike direction. I thus obtained four newly defined elements: two non-DC elements (*ISO* and *CLVD*) and two DC elements (*Strike-DC* and *Dip-DC*).

To quantify the contributions of these four elements to a seismic moment, I defined a relative seismic moment  $m_i$  for each element:

$$m_i = \frac{|M_i|}{M_{Total}} \times 100 [\%], \quad \text{Eq. 5.6}$$

where  $i$  represents the moment tensor elements (*ISO*, *CLVD*, *Strike-DC*, or *Dip-DC*), and the total seismic moment was defined as:

$$M_{Total} = |M_{ISO}| + |M_{CLVD}| + M_{Strike-DC} + M_{Dip-DC}, \quad \text{Eq. 5.7}$$

where  $M_{Strike-DC} = \sqrt{M_D^2 + M_{\theta\phi}^2}$  and  $M_{Dip-DC} = \sqrt{M_{rt}^2 + M_{r\phi}^2}$ .  $M_{Total}$  was defined differently from the seismic moment  $M_0$  of the moment tensor (Eq. 3.14) in order to quantify the relative contributions of each element in terms of percentage.

Using this moment-tensor decomposition, a partial moment tensor from the ring fault of the Torishima model was decomposed into *ISO*, *CLVD*, *Strike-DC*, or *Dip-DC* elements (Fig. 5.5). Their relative seismic moments indicated dominant *CLVD* (50.1%) and *Dip-DC* (45.7%) elements with a slight

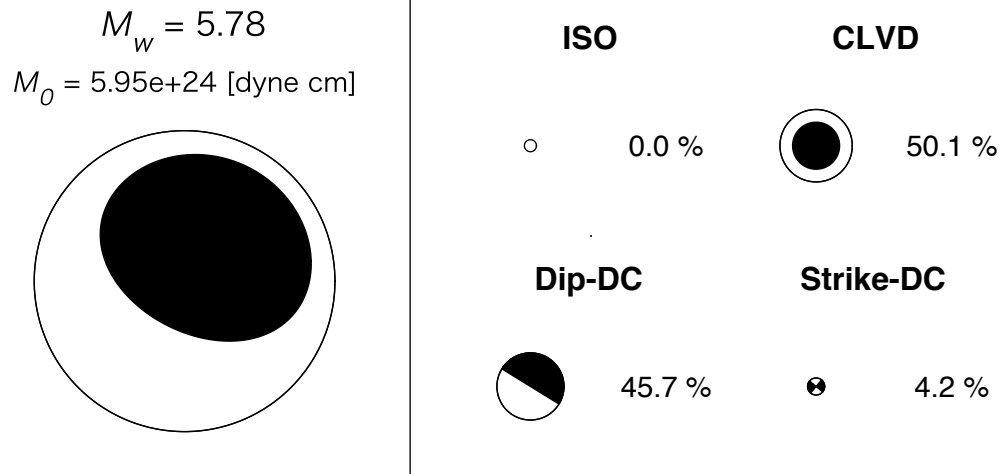


**Fig. 5.5 Decomposition of the moment tensor from the ring fault of the Torishima source model**

See text in Chapter 5.2.1.3.

*Strike-DC* (4.2%) element. The *ISO* element was not present because the ring fault slip consisted of multiple dip-slipping planar faults.

It is notable that almost half of the seismic moment contributing to the *Dip-DC* element could not excite long-period seismic energy. To confirm this inefficient seismic excitation, I synthesized long-period seismic waves only with the *Dip-DC* element, equivalent to  $M_w$  5.69 ( $M_0 = 4.30 \times 10^{24}$  [dyne cm]). Figure 5.6 compares synthetic waves from the *Dip-DC* element with the observed records. The amplitude levels of these synthetic waves were much lower than those of the observations, even at stations located along the maximum radiation azimuth of the Rayleigh waves (such as station DAV). Therefore, even though the ring-fault slip had a large *Dip-DC* element at its source, little long-period seismic energy was released from the element.

## 5.2.2 Moment tensor inversion using W-phase of seismic waves

Thus, the *CLVD* and *Strike-DC* elements from the ring fault slip only contributed to long-period seismic energy, despite the complicated moment tensor estimated for volcanic tsunami earthquakes. In turn, this implied that only those two elements could be directly determined by using long-period seismic waves. To confirm this, I conducted moment-tensor (MT) inversion using the W-phase of seismic waves for the 2015 Torishima earthquake [Kanamori and Rivera, 2008; Hayes et al., 2009; Duputel et al., 2012]. I used the seismic records from F-net and GSN that were applied to the forward modeling of long-period seismic waves in Chapter 3.3. Of these, only data with good quality was used for the MT inversion. Because the *ISO* element inherent in the tensile opening of a horizontal fault may not radiate long-period seismic energy, the zero-trace condition  $M_{rr} + M_{\theta\theta} + M_{\phi\phi} = 0$  was assumed. I used the same Green's functions as those used for the forward modeling in Chapter 3.3. Based on the source model, the centroid was fixed at 2.5 km depth below the center of Smith Caldera (140.053°E, 31.485°N). To utilize long-period seismic energy, I applied the one-pass and forth-order Bandpass Butterworth filter with corner frequencies at 0.004 and 0.0167 Hz (band-pass period from 60–250 s). The optimum time-shift and half duration were simply

assumed to be the same and determined by the grid-search method. I also computed the posterior correlation matrix and relative standard deviations of the moment-tensor components to examine their constraints.

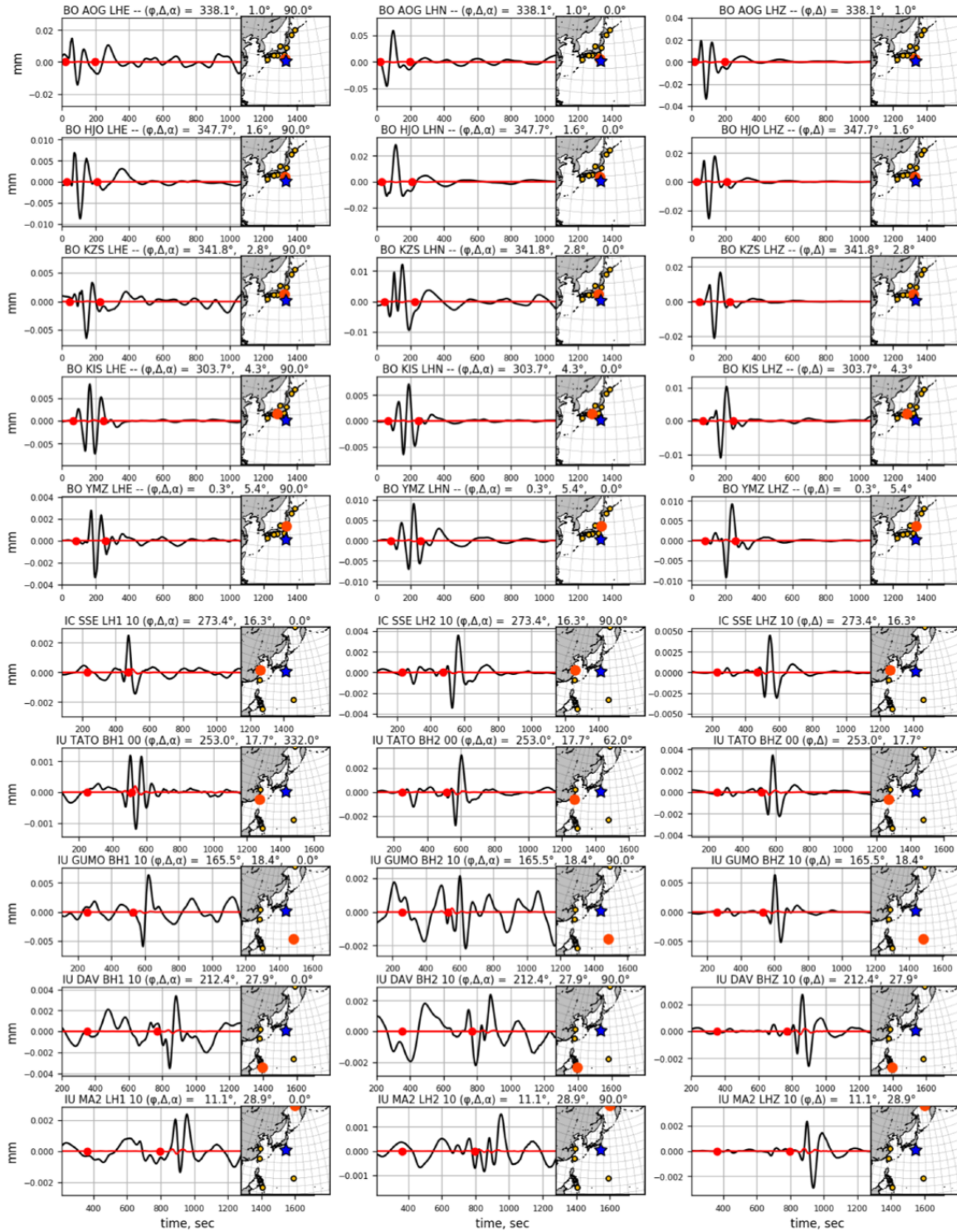


**Fig. 5.6 Long-period seismic waves excited by the *Dip-DC* element of the Torishima source model**  
 Red and black lines represent synthetic and observed waveforms, respectively. Blue star and big orange circle represent locations of the epicenter (Smith Caldera) and a station, in inset figures.

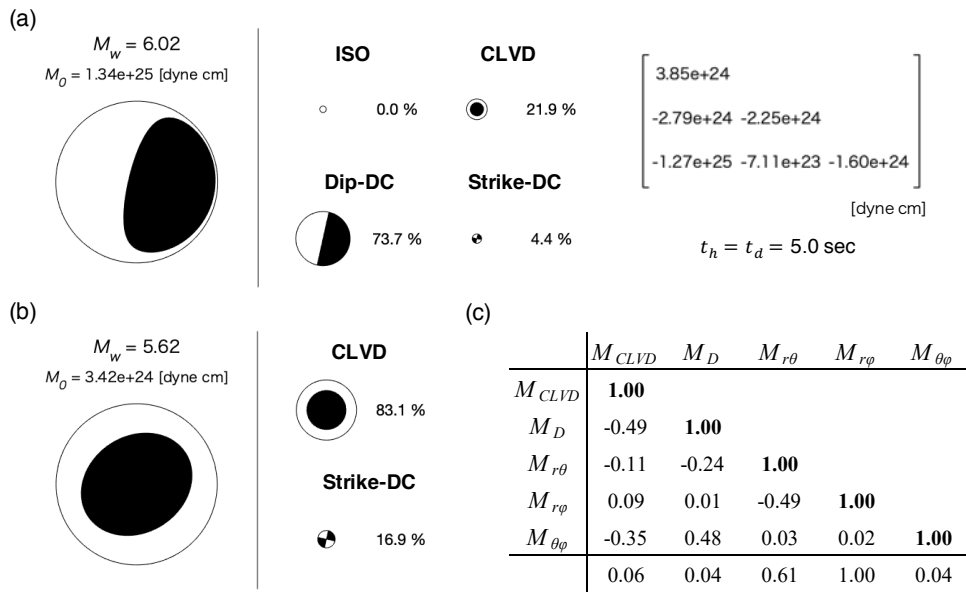


**Fig. 5.7 MT inversion using W-phases of seismic waves for the 2015 Torishima volcanic tsunami earthquake**

(a) Solution of the MT inversion. (b) Observable moment-tensor elements without the *Dip-DC* element. (c) Posterior correlation matrix and relative standard deviations of moment-tensor components in the bottom row. The model performance is shown in Fig.A2.1.

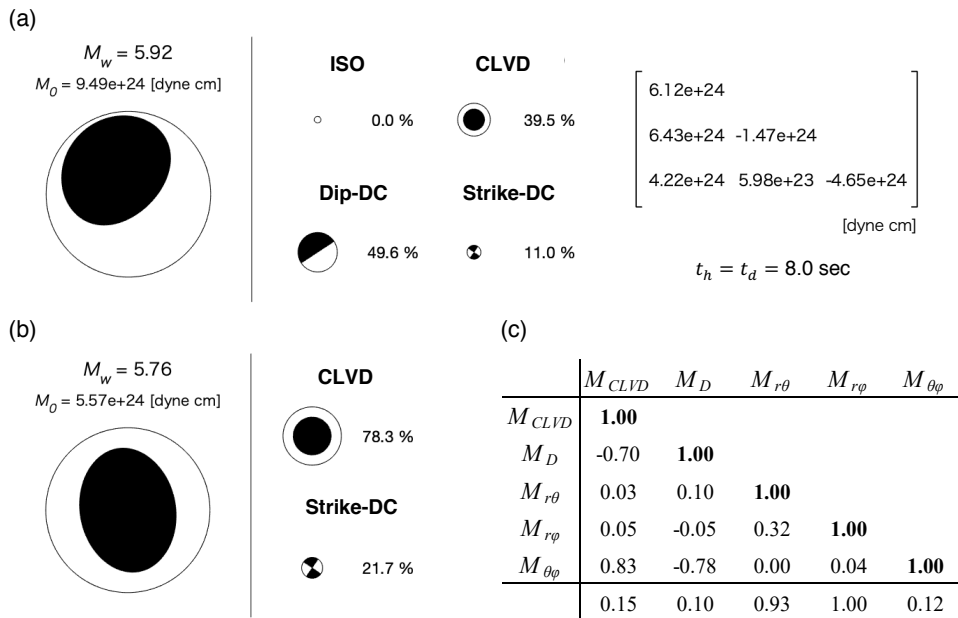


**Fig. 5.8 MT inversion using W-phases of seismic waves for the 2017 Curtis volcanic tsunami earthquake**

(a) Solution of the MT inversion. (b) Observable moment tensor elements without the *Dip-DC* element. (c) Posterior correlation matrix and the relative standard deviations of moment tensor components in the bottom row. The model performance is shown in Fig.A2.2.

I obtained a resulting moment tensor (Fig. 5.7a) that achieved sufficient fitting levels of long-period seismic waves (Fig-A2.1 in Appendix 2). The half duration was estimated as 5 s, indicating a  $\sim 10$  s source duration of the rupture of the ring fault structure. The most dominant element in the moment tensor was the *Dip-DC* element with a relative seismic moment of 73.3%. However, the posterior relative standard deviations of the two components ( $M_{r\theta}$ ,  $M_{r\phi}$ ) showed the largest values among all the components (Fig. 5.7c), indicating that the *Dip-DC* element was poorly resolved because of low seismic excitation. On the other hand, the other moment-tensor components corresponding to the *CLVD* and *Strike-DC* elements were much better constrained (Fig. 5.7c), indicating that only the two moment-tensor elements generated by ring-fault slips could be constrained by the MT inversion analysis using long-period seismic waves.

I also conducted the MT inversion with the zero-trace condition for the 2017 Curtis volcanic tsunami earthquake using regional stations as in Chapter 4.3 (Fig-A2.2 in Appendix 2). The centroid was assumed at 2.5 km depth below the seafloor at the center of Curtis Caldera ( $178.56^\circ\text{W}$ ,  $30.54^\circ\text{S}$ ). The band-pass filter had corner frequencies at 0.007 and 0.0174 Hz (band-pass period ranging from 57–143 s). The inverted moment tensor solution showed a dominant *Dip-DC* element (Fig. 5.8) but the corresponding components ( $M_{r\theta}$ ,  $M_{r\phi}$ ) had relatively larger posterior standard deviations than the others, implying poor constraints on the *Dip-DC* element, as for the 2015 Torishima earthquake. The half duration was estimated as 8.0 s.

### 5.2.3 Relationship of long-period seismic waves to ring-fault slips

Next, I assessed how long-period seismic waves were related to the source geometries of the ring-fault slip. In Chapters 3 and 4, I showed that these geometries were sensitive to long-period seismic wave excitations. First, the dip angle of the ring fault changed the amplitude levels. Second, the ruptured portions of the ring fault significantly influenced the horizontal components of the waveforms. These implied that fault parameters of the ring fault can be inferred by analysis of long-period seismic records.

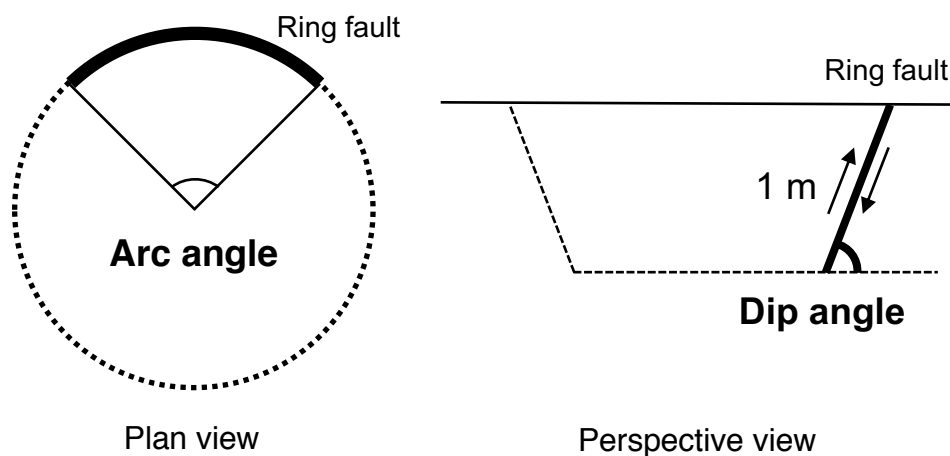


**Fig. 5.9 Modeling of the ring-fault slip**

See text in Chapter 5.2.3.

Here, I consider seismic radiation properties of ring-fault ruptures by taking an approach similar to *Ekström* [1994] and *Shuler et al.* [2013b]. I assume an idealized ring-fault slip, that is, a pure thrust uniform slip along a circular ring fault and sum up partial moment tensors of discretized planar faults with varying strike angles. Because long-period seismic waves are considered here, the seismic source can be modeled as a moment tensor under the point-source assumption. The ring fault has two variable fault parameters: dip and arc angles (Fig. 5.9). The inward-dipping ring fault is only considered here, as this is equivalent to the structures estimated for the 2015 Torishima and the 2017 Curtis volcanic tsunami earthquakes.

### 5.2.3.1 Radiated seismic energy of ring-fault slip

Seismic energy radiation by the ring-fault slip itself was eliminated due to partial cancellations of long-period seismic waves from different portions [*Ekström*, 1994; *Shuler et al.*, 2013b]. These cancellation effects were examined by computing the normalized seismic moment of a thrust-slipping ring fault with 45–90° dip angles and 0–360° arc angles:

$$\frac{M_0}{\sum_i \Delta M_0^i} \quad \text{Eq. 5.8}$$

where  $M_0$  is the seismic moment of the composite moment tensor and  $\Delta M_0^i$  is the partial moment tensor of the  $i$ th discretized planar fault. Figure 5.10a shows that the normalized seismic moment decreased overall as the ring fault extended, regardless of dip angle, while the cancellation ratio was much larger when the dip angle was more vertical.

This property can be understood easily by decomposing the moment tensor. Figure 5.11a shows the composite moment tensors of the ring-fault slip with a dip angle of 70° and an arc angle of 90° on the north, south, east, and west portions. As the ring fault extends, because the *CLVD* element gets larger because it is identical regardless of its portion or direction (Fig. 5.11b). On the other hand, the tension-axis (and pressure-axis) directions of the *DC* elements were different from portion to portion. Therefore, the *DC* elements were partially or totally cancelled from the other portions, resulting in the elimination of the seismic moment (Fig. 5.11b). Because the *DC* elements were more dominant in dip slip on a steeply dipping planar fault (Fig. 5.10b), the cancellation was more significant for steeply dipping ring faults, causing more aseismic ruptures.

In addition to the moment cancellation, the minor seismic excitation of the *Dip-DC* element made the ring fault slip even more aseismic. I therefore examined the contributions of the observable *CLVD* and *Strike-DC* elements in the composite moment tensor of the ring-fault slip. Fig. 5.10c shows the relative seismic moments of the observable elements to the total seismic moment on ring faults with 45–90° dip angles and 0–360° arc angles. Overall, the ratio of the observable elements increased as arc angle increased beyond 180°, because the polarities of the unobservable *Dip-DC* elements on portions facing each other were totally reversed, resulting in cancellation of the element (Fig. 5.11b). On the other hand, as the dip

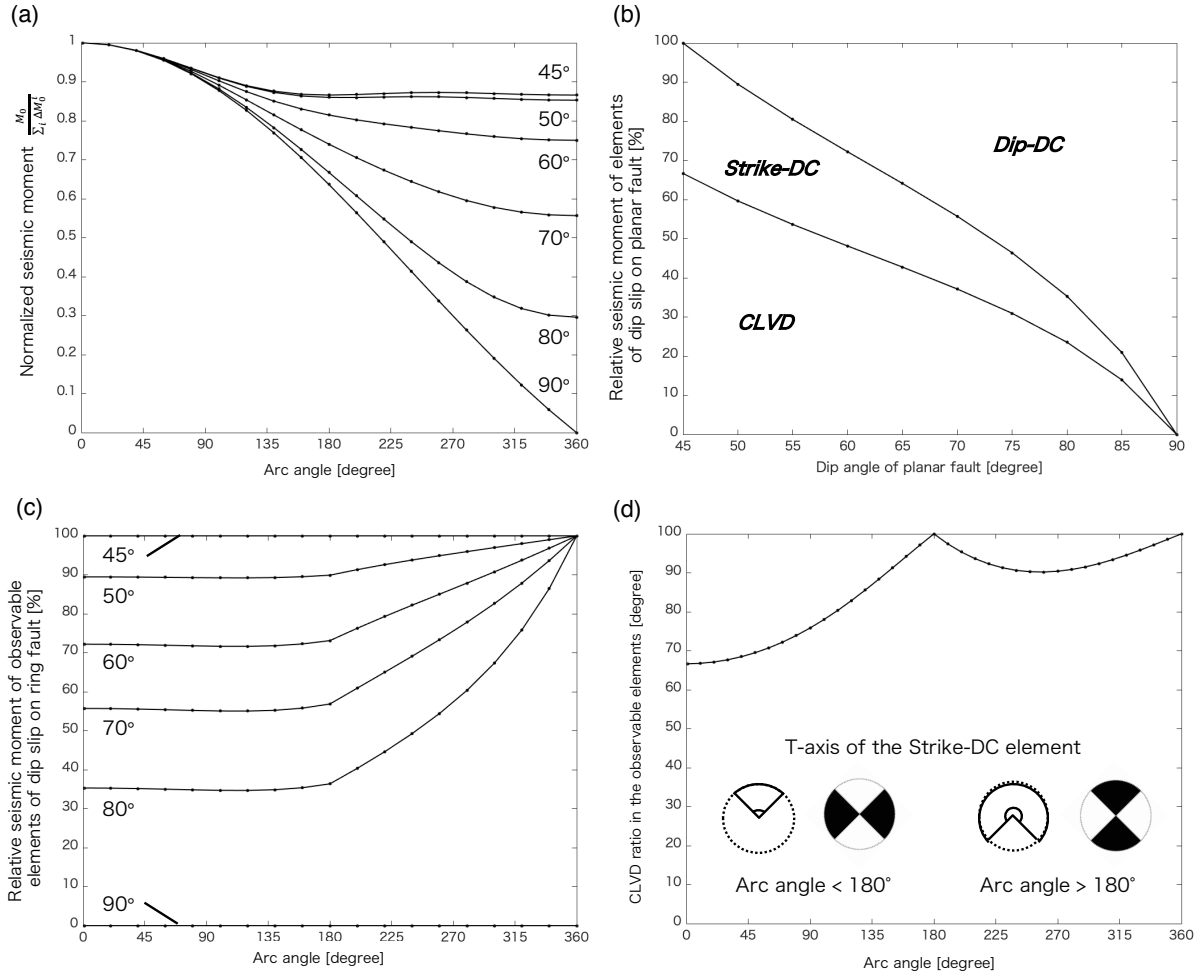


**Fig. 5.10 Seismic radiation properties of ring-fault slips**

(a) Normalized seismic moment computed by Eq. 5.4. (b) Ratio of the *CLVD*, *Strike-DC*, and *Dip-DC* elements contained in a pure dip slip of a planar fault. (c) Relative seismic moment of the observable elements (*CLVD* + *Strike-DC*) to the total seismic moment. (d) The *CLVD* ratio in the observable elements computed with Eq. 5.7.

angle became more vertical, the observable elements were less dominant. In the end-member cases, the vertical ring fault did not contain the observable elements at all, while the 45° dipping ring fault was entirely composed of them.

Therefore, dip slip on a steeply dipping ring fault released even less seismic energy, together with the cancellation of long-period seismic waves from the DC elements of different portions. For example, I considered two ring faults with dip angles of 60° and 80°, both having the same arc angle of 225°. For the 60° case, the cancellation reduced the seismic moment by ~20% (Fig. 5.10a) and only ~77% of the seismic moment radiated long-period seismic energy (Fig. 5.10c); 61% of the total seismic moment of slips on the ring fault ( $\sum_i \Delta M_0^i$ ) contributed to the seismic radiations. For the 80° case, ~47% of the seismic moment was cancelled out by curved faults (Fig. 5.10a), and the observable elements were equivalent to only ~45% of the remaining moment (Fig. 5.10c); only ~24% of the total slips radiated seismic energy. These properties of seismic energy release and the sensitivity to dip angle could be

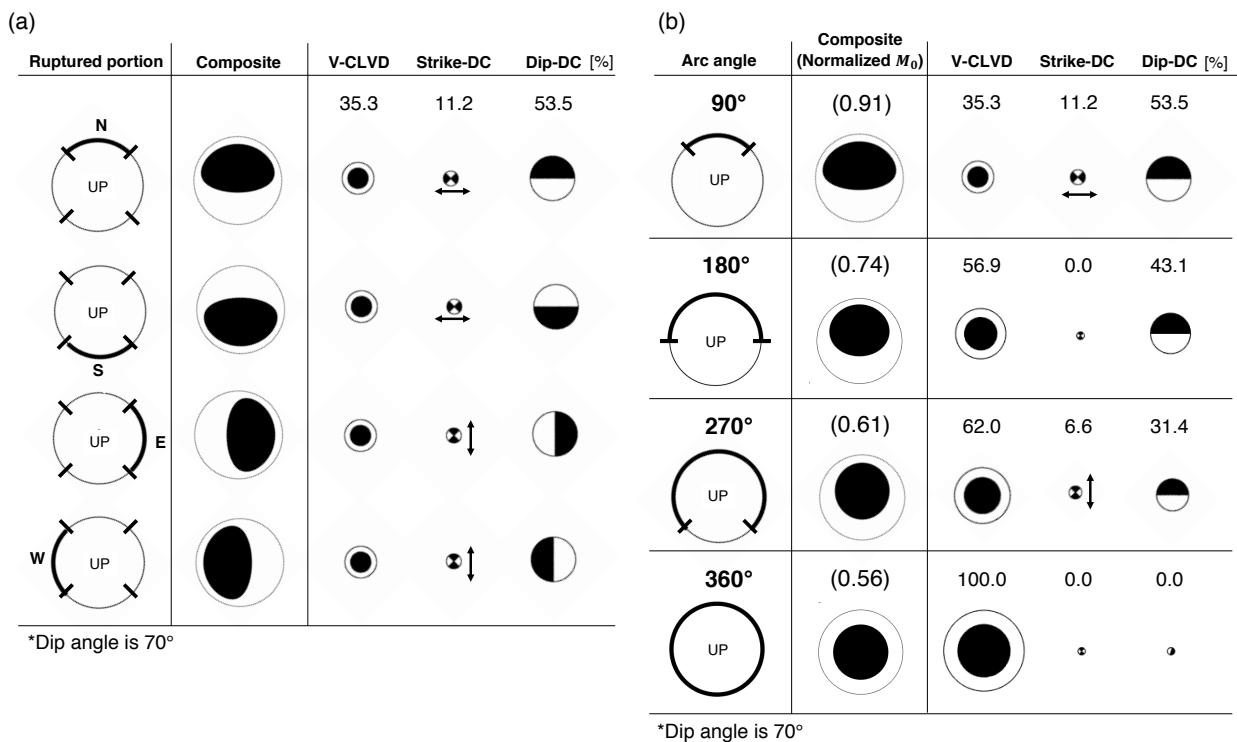


**Fig. 5.11 Moment tensors of the ring-fault slip with different geometries**

(a) Moment tensors of ring-fault slips with a 90° arc-angle on different sides. Relative seismic moments of each decomposed element are written in the three columns on the right. (b) Moment tensors of ring-fault slips with arc angles with 90°, 180°, 270° and 360°. In the second column, normalized seismic moments (Eq. 5.6) are written with composite moment tensors.

attributed to the significant changes in amplitudes of synthetic long-period seismic waves for the kinematic source modeling of the 2015 Torishima volcanic tsunami earthquake (Fig. 3.19).

The cancellation and aseismic characters associated with the DC elements could be attributed to peculiar moment tensors dominated by the vertical-CLVD components estimated for volcanic tsunami earthquakes (Fig. 1.1, Fig. 1.3), and even for vertical-CLVD earthquakes possibly related to ring-fault fractures [e.g. *Ekström*, 1994; *Nettles and Ekström*; 1998, *Shuler and Ekström*, 2009; *Shuler et al.*, 2013b]. This could also explain the absence of long-period Love waves caused by the 1984 Torishima volcanic tsunami earthquake [*Kanamori et al.*, 1993]. In the moment tensor inversion methods employed for earthquake monitoring system, the source depth is assumed to be deeper than 10 km to avoid poor constraints on components of the *Dip-DC* elements, or  $M_{r\theta}$  and  $M_{r\phi}$  (e.g. USGS [*Kanamori and Rivala*, 2008], GCMT [*Ekström et al.*, 2012]), resulting in small ratios of the element. However, it is probably substantially impossible to resolve the element due to its aseismic character.

### 5.2.3.2 Associations of observable moment-tensor elements to ring-fault geometries

I have already shown that long-period seismic waves excited by the ring-fault slip were only contributed to by the *CLVD* and *Strike-DC* elements of the moment tensor, which could be well-constrained by the moment tensor inversion. Here, I suggest that two physical parameters obtained from the observable elements can serve as indicators of ring-fault arc angles and fault orientations.

The first indicator is the ratio of the *CLVD* to the observable elements, which reflects the arc angle of the ring fault:

$$\frac{|M_{CLVD}|}{|M_{CLVD}| + M_{Strike-DC}} \times 100 [\%]. \quad \text{Eq. 5.9}$$

As explained above, the *Strike-DC* elements on different ring-fault portions can partially or totally cancel out each other, while the *CLVD* elements along the portions accumulate. Because of their different properties, the *CLVD* ratio changes as the arc angle of the ring fault extends (Fig. 5.10d). As the arc angle approaches 180°, the *CLVD* ratio increases from 66.6% to 100%. From 180° to 360°, it decreases to a local minimum of 90% at ~255°, then increases to 100% at 360°. The *CLVD* ratio reaches 100% at both 180° and 360°, indicating zero *Strike-DC* element, since the *Strike-DC* element vanishes completely every 180° due to the cancellation of two neighboring 90° arc ring fault portions (Fig. 5.11). When the ring fault has a uniform dip, the dimensionless value keeps the same relationship to the arc angle regardless of its dip angle, because each partial planar-fault slip with an arbitrary uniform dip angle always has the *CLVD* element at a ratio of 2:1 to the *Strike-DC* (Fig. 5.10b). In addition, the ratio is independent of slip amount on the ring fault or its diameter, due to its dimensionless property. Therefore, the *CLVD* ratio helps to estimate the extension of the ring fault regardless of its variable seismic energy release.

The other indicator is the tension-axis (T-axis) direction of the *Strike-DC* element, which infers the fault orientation of the central portion of the ring fault. Figure 5.11b shows the decomposition of theoretical moment tensors for four cases with arc angles of 90°, 180°, 270°, and 360°. In the two end-member cases (180° and 360°), the cancellation resulted in no contribution to the moment tensor of the *Strike-DC* element (2nd and 4th row in Fig. 5.11b; line in Fig. 5.10d). In the other cases, the *Strike-DC* element contained in a moment tensor carried information about the ring-fault geometry. Up to 180° arc angle, the T-axis of the *Strike-DC* element had a direction that was consistent with the fault orientation of the central part of the ring (top row in Fig. 5.11b; inset figure in Fig. 5.10d). On the other hand, when the arc angle was larger than 180°, the T-axis direction was vertical to the fault orientation of the central portion of the ring fault (inset figure in Fig. 5.10d, bottom row in Fig. 5.11b). Beyond 180° arc angle, the central portion with an 180° arc angle did not contribute to the *Strike-DC* element due to total cancellation, while the other portions generated the *Strike-DC* element with a T-axis direction vertical to that of the central portion.

These two indicators are thus useful for estimating ruptured portions of the ring fault. In particular, the arc angle and the fault orientation of a ring-fault slip with an arc angle  $< \sim 135^\circ$  can be constrained well by combining these indicators. Because the CLVD ratio significantly changes from  $0^\circ$  to  $\sim 135^\circ$  of arc angle and corresponds to a single value (Fig. 5.10d), arc angles up to  $135^\circ$  can be uniquely determined by the ratio. When the arc angle is smaller than  $180^\circ$ , the fault orientation of the central portion of the ring fault can be estimated as it is horizontal to the T-axis direction of the *Strike-DC* element. On the other hand, if the arc angle is  $> \sim 135^\circ$ , constraints on the ring-fault geometry from the indicators are relatively weaker. First, the CLVD ratio changes slowly only within 90–100%, and two or three arc angles ranging from  $135$ – $360^\circ$  correspond to one CLVD ratio (Fig. 5.10d), making it difficult to constrain the arc angle identically. Without a constraint on the arc angle, it is possible to estimate two fault directions for the central portion of the ring from the T-axis of the *Strike-DC* element.

It is substantially impossible to determine on which side of the ring fault a slip occurs using only a moment-tensor analysis of long-period seismic waves, because of the aseismic *Dip-DC* element. Figure 5.11a shows that ring-fault slips on two facing sides (i.e., north and south or east and west) differ only with the *Dip-DC* element and share the same observable *CLVD* and *Strike-DC* elements. Because the *Dip-DC* element cannot be well-constrained due to its aseismic property, it is still uncertain on which side the ruptured ring fault extends even though the arc angle and fault orientation of the ring fault can be estimated by the two indicators.

Because of the aseismic property of the *Dip-DC* moment-tensor element, it seems that the dip angle of the ring fault cannot be constrained from long-period seismic waveform analysis. However, against expectations, the sensitivity of the dip angle to released seismic energy can be used to constrain this indirectly based on the amplitude levels of long-period seismic waves in combination with constraints from other observations. Generally, amplitude levels of long-period seismic waves excited by the ring-fault slip have a trade-off relationship between fault size, slip amount, and dip angle. If two of these three parameters are available from other observations, the third can be estimated by using amplitude levels. For example, when modeling the 2015 Torishima volcanic tsunami earthquake, the ring-fault arc angle and width were constrained mainly by fitting the horizontal component of the long-period seismic waveforms and the slip amount on the geometry was estimated by the inversion of tsunami waveforms. Therefore, by fitting amplitude levels of synthetic long-period waveforms to the observations, the dip angle was successfully constrained within a narrow range using this relationship. On the other hand, the Curtis earthquake had larger uncertainties in its ring-fault geometry, resulting in relatively weak constraints on its dip angle.

### 5.2.3.3 Other effects

The above discussions are based on the assumption of idealistic cases for ring-fault slip with homogeneous properties all along the ring fault, such as slip amount, dip angle, curvature (circular ring), fault width, and shear modulus. However, these properties may be more heterogeneous in reality, causing

variations in seismic contributions by different ring fault portions. For example, heterogeneously dipping ring-fault slip also has variations along the fault in terms of contribution to seismic energy because of the aseismic *Dip-DC* element. In addition, when the ring fault forms an ellipse rather than a circle, the DC elements from a fault orientation parallel to the long axis may be radiated more when compared to the short axis. Thus, it is necessary to carefully consider such complexities in the source geometry in real-world cases.

Apart from the seismic radiation of the ring fault, it is also possible that the *ISO* element from other sources including a positive volumetric change may decrease the CLVD ratio. *Kawakatsu* [1996] showed that long-period body waves and surface waves caused by the *ISO* and *CLVD* elements of shallow earthquakes were very similar to each other, which is well-known for the relationship between the elements. Figure 5.12 compares long-period waveforms, including those for both body and surface waves, caused by

the *ISO* (positive volumetric change) and *CLVD* (vertical-CLVD with a vertical tension-axis) elements. When an active source causing upward motion of the caldera block has a crack-like geometry, it may be aseismic because of the free-surface effect, as confirmed in Chapter 5.2.1. On the other hand, if the volumetric-change source has a more spherical geometry, it may contain more of the *ISO* element and contribute to seismic energy by partially canceling out energy radiated by the *CLVD* element of the ring fault slip. However, it is difficult to resolve contributions of the *ISO* element of a volumetric source because of the waveforms correlated with the *CLVD* element [*Kawakatsu*, 1996]. The volumetric change effect may be resolved seismologically by analyzing first-motion polarities of many P-waves radiated from the source with different take-off angles [*Kawakatsu*, 1996], though this is challenging for volcanic tsunami earthquakes occurring offshore and far from developed seismic networks.

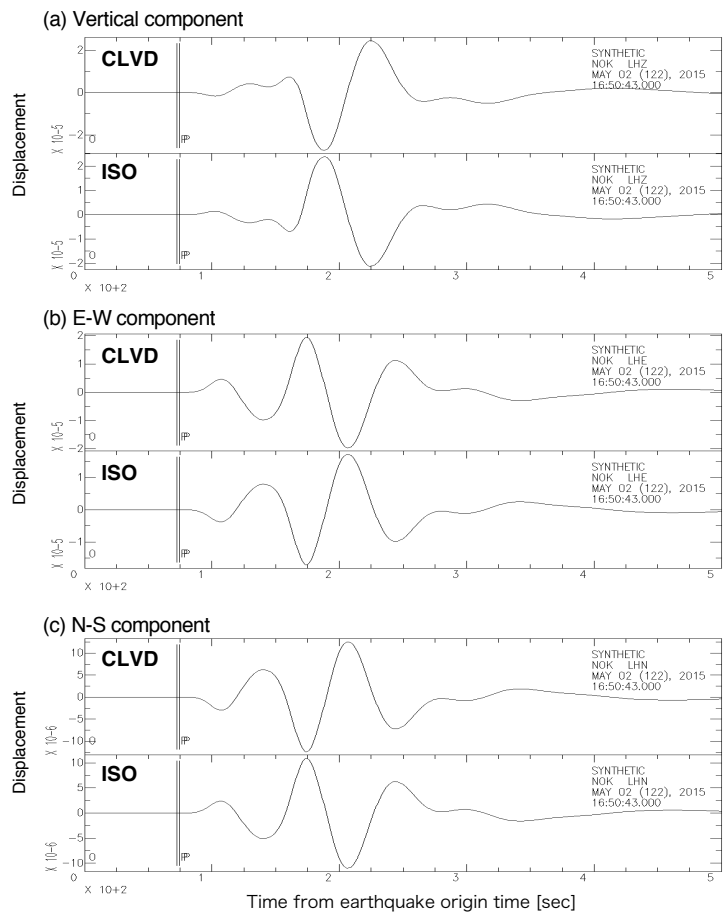


**Fig. 5.12 Waveforms of the ISO and CLVD elements at source depth 2.0 km**

Moment tensor are assumed as  $(M_{rr}, M_{\theta\theta}, M_{\phi\phi}) = (1.0, -0.5, -0.5) \times 10^{25}$  [dyne cm] for the CLVD source, and  $(M_{rr}, M_{\theta\theta}, M_{\phi\phi}) = (1.0, 1.0, 1.0) \times 10^{25}$  [dyne cm] for the ISO source.

Therefore, to capture detailed information, including heterogeneous geometries of ring-fault slip and other volumetric sources, it is critical to combine seismic analysis with other geophysical observations, such as geological or geodetical observations, or seafloor deformation analysis using tsunami waves. Surveys of subsurface structures using active seismic sources of seismic topography will be also useful for understanding earthquake sources through direct observations of source geometries, such as ring-fault systems and magma chamber geometries.

## 5.2.4 Usefulness of observable moment-tensor elements for the kinematic source modeling of volcanic tsunami earthquakes

To this point, I have demonstrated that long-period seismic waveforms of ring-fault slips are associated with the source geometries of the *Strike-DC* and *CLVD* moment-tensor elements, allowing the source geometries of volcanic tsunami earthquakes to be successfully constrained by analyzing long-period seismic waveforms in combination with inversions of tsunami waveforms. Here, I consider how source geometries including ruptured portions, or arc angles, of the ring faults of the 2015 Torishima and 2017 Curtis volcanic tsunami earthquakes could be successfully constrained by long-period seismic waveform analysis. I also examine a moment tensor of a trapdoor faulting event at the Sierra Negra caldera to allow comparison with its intra-caldera sinuous fault geometry.

### 5.2.4.1 The 2015 Torishima volcanic tsunami earthquake

In the source modeling approach for the kinematic source model of the 2015 Torishima earthquake, I estimated slip distributions on assumed fault geometries composed of a dip-slipping ring fault and a tensile opening/closing horizontal fault. Because the seismic contributions of the horizontal slip could be disregarded, it was reasonable to consider seismic radiations of volcanic tsunami earthquakes by focusing only on the ring fault. In Chapter 3.2, based on the inversion of tsunami waveforms for fault slips, I obtained three slip models with ring faults with different ruptured portions, or arc angles: TR (three-quarter ring), FR (full ring), and HR (half ring) (Fig. 5.13b-d). By analyzing fitting levels in horizontal components of long-period seismic waves, I suggested that the TR model was most preferable for the source model of the earthquake based on waveform fitting levels in horizontal components.

It was possible to constrain the ring fault geometry with horizontal components of long-period seismic waves because the radiation patterns of the shear waves were very sensitive to the T-axis direction of the *Strike-DC* element, which was closely related to the geometry. Figure 5.13 compares the observable moment-tensor elements of the slip models with those of the solution of the MT inversion using the W-phase of the seismic waveforms (Fig. 5.13a; see Chapter 5.2.2), which contains a *Strike-DC* element with a T-axis oriented in the NE-SW direction. In terms of the T-axis direction, the TR model (Fig. 5.13b) was more similar to that of the solution of the MT inversion than the other two models (Fig. 5.13c-d). Therefore, the TR model showed the best waveform fitness (particularly of horizontal motions) of the three models, as compared in Chapter 3.3 (Fig. 3.20).

This is consistent with what is expected from the relationship between the ring-fault geometry and the T-axis direction of the *Strike-DC* element. In the previous subsection, I demonstrated that the T-axis of the element was parallel to the fault orientation of the central portion of the ring fault when the arc angle was  $< 180^\circ$ , but perpendicular when the arc angle was  $> 180^\circ$  (Fig. 5.10d). The tsunami analysis indicated a large rupture on the northeastern portion with a NW-SE fault orientation that was perpendicular to the T-axis direction of the MT solution (NE-SW). Therefore, to produce the *Strike-DC* element, the ring-fault rupture must have extended over  $180^\circ$  of arc angle around the central portion on the northeast side of the ring fault.

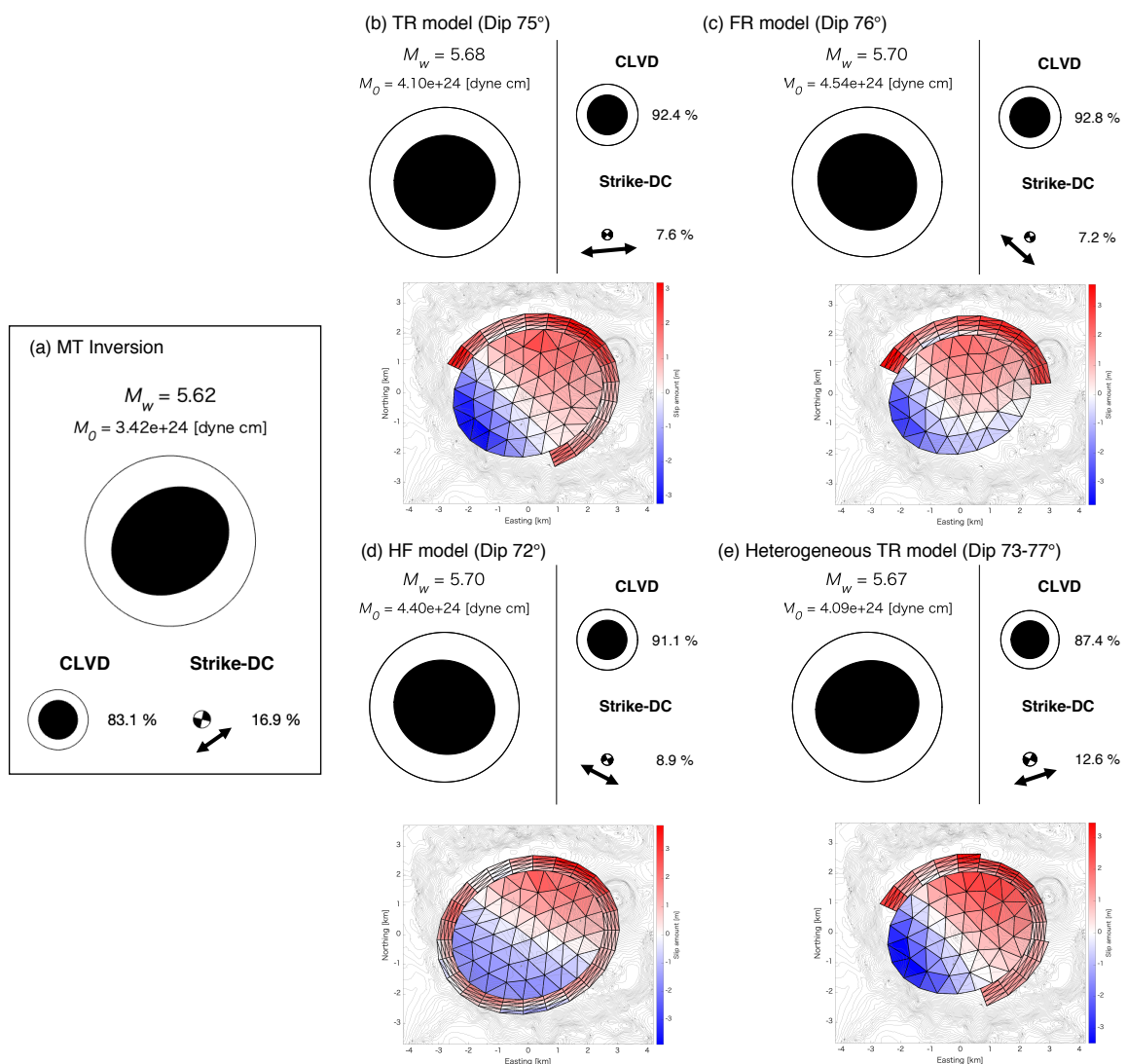


**Fig. 5.13 Observable moment-tensor elements of slip models of the 2015 Torishima volcanic tsunami earthquakes**

(Top) Observable moment tensor elements, composed only of the *CLVD* and *Strike-DC* elements. (bottom) Slip models from plan view. (a) MT inversion, (b) the best TR model (Fig. 3.18), (c) the best FR model (Fig. 3.21), (d) the best HR model (Fig. 3.22) and (e) heterogeneous-dip TR model (Fig. 3.23).

However, the MT solution still showed a T-axis direction of the *Strike-DC* element (NE-SW) different from that of the TR model (NE-SW), and its CLVD ratio (83.1%) was much smaller (by ~9%) than that of the source model (92.4%) (Fig. 5.13). The larger *Strike-DC* element with a NE-SW T-axis direction may imply relatively larger seismic contributions by ring-fault portions with a fault orientation parallel to the direction, due to heterogeneities along the ring fault. One possible cause is a heterogeneously dipping ring fault causing varied seismic radiation rate along the ring fault. I demonstrated that the heterogeneous-dip TR model, with a steeper dip angle on the northeastern side of the ring fault (Fig. 5.13e), improved fitting levels of long-period seismic waveforms in horizontal components compared to the TR model with a uniform dip (Fig. 3.23; Fig. 3.20e-f; Chapter 3.3.2.4). Because the model had smaller seismic contributions from the northeastern side with a *Strike-DC* element with a T-axis direction of NW-SE, the CLVD ratio and the T-axis direction of the *Strike-DC* element were similar to the MT solution. The deviations of the MT solution from the homogeneous slip model could be explained by other heterogeneities related to fault width (or thickness of a caldera block), or physical fault properties along the ring fault. The seismic radiation efficiency may also vary with temperature, due to hot magma distributed heterogeneously below the ring fault. However, it is difficult to determine exact causes without detailed information regarding subsurface structures in the caldera.

#### 5.2.4.2 The 2017 Curtis volcanic tsunami earthquake

Figure 5.14 shows the observable moment-tensor elements for two slip models with different ring-fault arc angles from the 2017 Curtis earthquake: the modified-dip fault model with an arc angle of  $120^\circ$  (Fig. 5.14b) and the half-ring fault model with an arc angle of  $180^\circ$  (Fig. 5.14b). These two models contained significantly different CLVD ratios in the two observable elements (79.3% and 98.4%, respectively), which is consistent with the CLVD ratio diagram of a ring-fault slip with different arc angles (Fig. 5.10d). Such deviations in the ratio of the *CLVD* and *Strike-DC* elements can be attributed to significant differences in the horizontal-component amplitudes of synthetic seismic waveforms for the two models; this enabled me to determine that the modified-dip fault model with a  $120^\circ$  arc angle was a more preferable source model (Chapter 4.4.2.3). The CLVD ratio of the moment tensor obtained by the MT inversion using the W-phase of seismic waves (Fig. 5.14a; Chapter 5.2.2) was more consistent with this model, further supporting its choice. This implies the usefulness of the CLVD ratio for estimation of source geometry for earthquakes related to ring-fault slips.

The T-axis of the *Strike-DC* element in the MT inversion solution close to a N-S orientation and slightly deviated from that of the modified-dip fault model (Fig. 5.14). This may imply that the ring-fault structure was located along the western side with a fault orientation parallel to that, although it was difficult to distinguish the two different cases from long-period seismic records containing relatively high-level noises in its horizontal components. Due to poor S/N ratios at many stations, horizontal-component waveforms from only a few stations were used for the MT inversion of the W-phase inversions of the 2017 Curtis earthquake (Fig-A2.2 in Appendix 2). In order to constrain the ring-fault geometry more accurately, other phases of seismic waves with better qualities are needed.

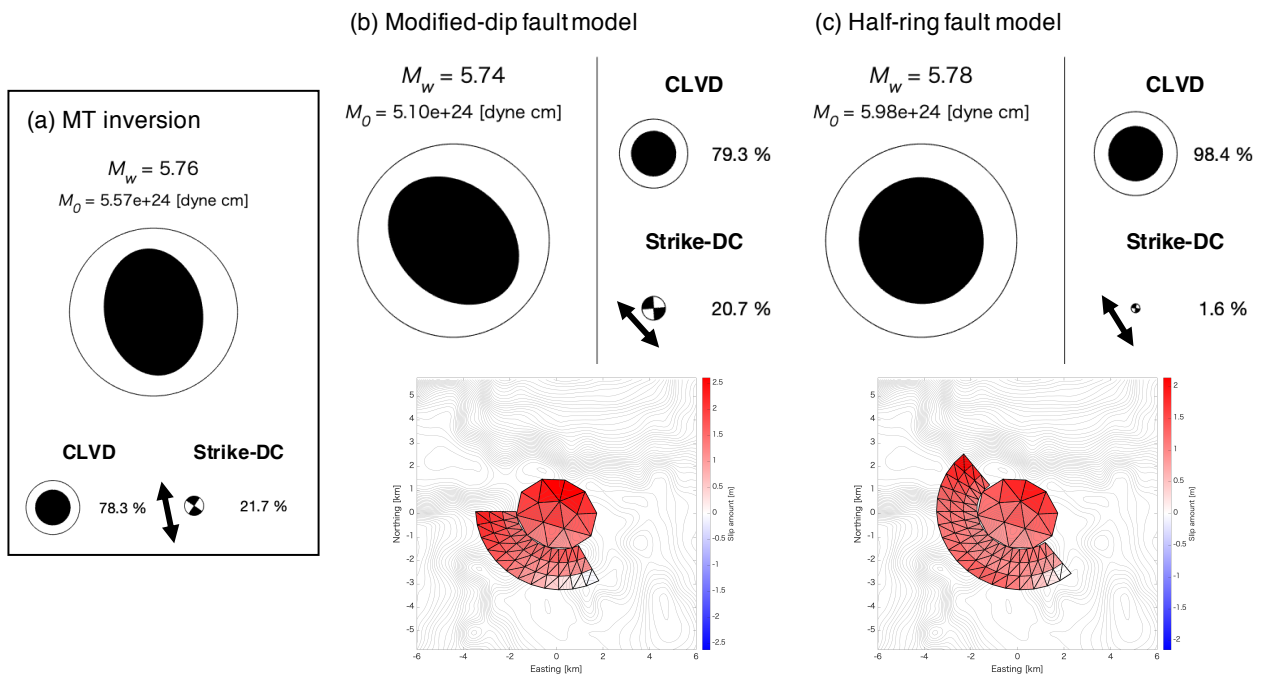


**Fig. 5.14 Observable moment-tensor elements of slip models of the 2017 Curtis volcanic tsunami earthquakes**

(Top) Observable moment tensor elements, composed only of the *CLVD* and *Strike-DC* elements. (bottom) Slip models from plan view. (a) MT inversion, (b) Modified-dip fault model, and (c) half-ring fault model.

### 5.2.4.3 Trapdoor faulting event at Sierra Negra caldera

For comparison, I also considered a  $M_w$  5.5 trapdoor faulting event on October 22, 2005 at the Sierra Negra caldera, Galápagos [e.g. *Jónsson*, 2009]. This event may have shared a physical mechanism related to a ring-fault fracture with volcanic tsunami earthquakes, as discussed in Chapter 5.1. I downloaded the zero-trace centroid moment tensor from the GCMT catalogue (Fig. 5.15a), and decomposed it into the *CLVD*, *Strike-DC*, and *Dip-DC* elements. Fig. 5.15b shows the observable moment tensor, composed of 77.3% *CLVD* element and 22.7% *Strike-DC* element with a T-axis slightly tilted clockwise from the E-W direction. If the seismic release is attributed to the ring fault slip, the *CLVD* ratio diagram with the T-axis of the *Strike-DC* element (Fig. 5.10d) indicates a  $\sim 100^\circ$ -arc ring fault oriented E-W, which is almost consistent with expectations for a trapdoor faulting event along the vertical scarp fault on the southwest of the caldera as reported by *Geist et al.* [2008]. The T-axis almost perpendicular to E-W may be explained by the sinuous fault structure extending longer in that direction than south. This consistency supports the idea that moment tensors estimated from seismic waves reflect source geometries of ruptures related to ring faults through the observable elements.

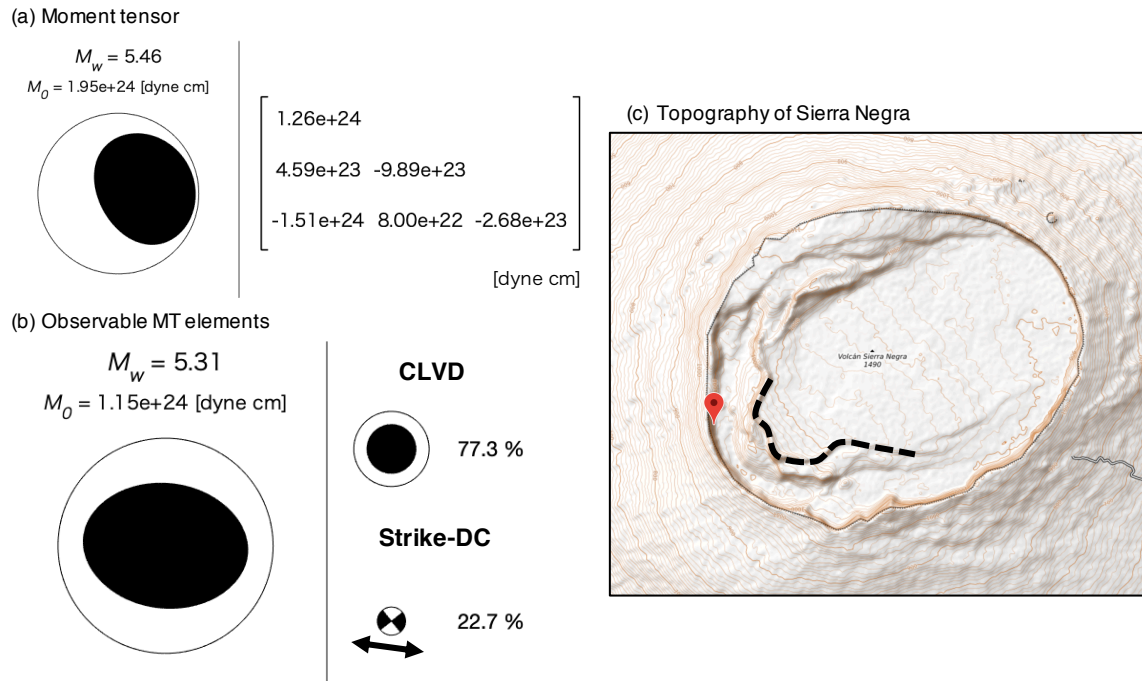


**Fig. 5.15 Moment tensor of a trapdoor faulting event on 22 October 2005 and intra-caldera fault of Sierra Negra**

(a) Moment tensor reported by the GCMT catalogue. (b) Observable elements of moment tensor. (c) The topography of Sierra Negra caldera. The dashed line represents a vertical scarp fault reported in *Geist et al.* [2008]. The topographic map of Sierra Negra caldera was obtained in Worldwide Elevation Finder ([http://elevation.maplogs.com/poi/sierra\\_negra\\_ecuador.237123.html](http://elevation.maplogs.com/poi/sierra_negra_ecuador.237123.html)).

### 5.3 Recurrent volcanic tsunami earthquakes

Throughout the previous section, I showed that source geometries of volcanic tsunami earthquakes can be estimated by focusing on well-constrained elements of their moment tensor solutions, the *CLVD* and *Strike-DC* elements. I next used these properties to consider similarities and differences of recurrent volcanic tsunami earthquakes. In addition to the events analyzed in this study, four other Torishima volcanic earthquakes occurred at Smith Caldera in 1984 ( $M_w$  5.6), 1996 ( $M_w$  5.7), 2006 ( $M_w$  5.6), and 2018 ( $M_w$  5.4), while another Curtis volcanic tsunami earthquake occurred in 2009 ( $M_w$  5.8) at Curtis Caldera (Table 1.1). I conducted zero-trace MT inversion using the W-phase of the seismic waves for the remaining volcanic tsunami earthquakes, except for the 1984 Torishima event because of lack of high-quality records, by following the procedures given in Chapter 5.2.2. Then, the observable *CLVD* and *Strike-DC* elements were extracted by removing the *Dip-DC* element from the solution.

Figure 5.16 compares the moment tensors and their observable elements of the Torishima earthquakes in 1996, 2006, and 2018 with those of the 2015 earthquake. In terms of the CLVD ratio and T-axis direction of the *Strike-DC* element, the 1996 and 2006 events were quite similar to those of the 2015 event (83–85% CLVD ratio, NEE-SWW T-axis of the *Strike-DC*), indicating that the 1996 and 2006 events shared identical ring-fault ruptures with the 2015 event, despite slight differences in magnitude. Therefore,

	Moment tensor		Observable	
<b>2015</b>	$M_w = 6.02$ $M_0 = 1.34e+25$ [dyne cm]	$\begin{bmatrix} 3.85e+24 & & \\ -2.79e+24 & -2.25e+24 & \\ -1.27e+25 & -7.11e+23 & -1.60e+24 \end{bmatrix}$ [dyne cm] $t_h = t_d = 5.0$ sec	$M_w = 5.62$ $M_0 = 3.42e+24$ [dyne cm]	<b>CLVD</b>  83.1 % <b>Strike-DC</b>  16.9 %
<b>1996</b>	$M_w = 5.99$ $M_0 = 1.22e+25$ [dyne cm]	$\begin{bmatrix} 3.84e+24 & & \\ 2.71e+24 & -2.21e+24 & \\ -1.13e+25 & -6.91e+23 & -1.64e+24 \end{bmatrix}$ [dyne cm] $t_h = t_d = 5.3$ sec	$M_w = 5.62$ $M_0 = 3.41e+24$ [dyne cm]	<b>CLVD</b>  83.7 % <b>Strike-DC</b>  16.3 %
<b>2006</b>	$M_w = 5.88$ $M_0 = 8.36e+24$ [dyne cm]	$\begin{bmatrix} 2.86e+24 & & \\ -1.57e+24 & -1.89e+24 & \\ -7.81e+24 & -2.35e+23 & -9.70e+23 \end{bmatrix}$ [dyne cm] $t_h = t_d = 8.0$ sec	$M_w = 5.54$ $M_0 = 2.53e+24$ [dyne cm]	<b>CLVD</b>  84.7 % <b>Strike-DC</b>  15.3 %
<b>2018</b>	$M_w = 5.58$ $M_0 = 2.95e+24$ [dyne cm]	$\begin{bmatrix} 1.03e+24 & & \\ -8.65e+23 & -9.08e+23 & \\ -2.64e+24 & -6.08e+22 & -1.19e+23 \end{bmatrix}$ [dyne cm] $t_h = t_d = 4.0$ sec	$M_w = 5.26$ $M_0 = 9.75e+23$ [dyne cm]	<b>CLVD</b>  72.0 % <b>Strike-DC</b>  28.0 %

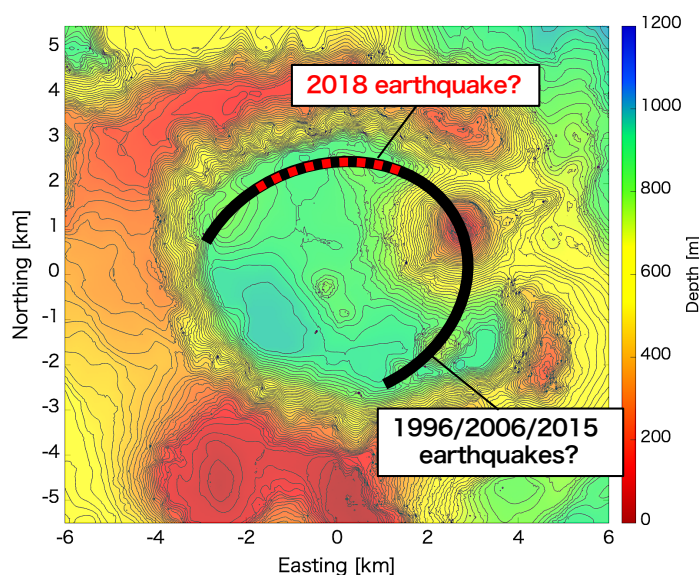
**Fig. 5.16 Moment tensors of recurrent volcanic tsunami earthquakes at Smith Caldera**

(Left) Event year. (Middle) Moment tensor solution of the zero-trace moment tensor inversion using W-phase of seismic waves. The matrix represents moment tensor in the coordinate system  $(r, \theta, \phi)$ .  $t_h$  and  $t_d$  represent grid-searched half duration and centroid time shift, which assumed to be the same. (Right) The observable moment tensor, without the *Dip-DC* element.

I suggest that fractures including thrust slips along the three-quarter ring fault may have repeatedly occurred almost every decade from 1996 to 2015 (Fig. 5.17). This also implies that stable or intermittent magma input into a shallow magma reservoir below reaches a critical threshold pressure needed to break out of the ring fault every decade, which may result in a  $\sim 10$  yr cycle of recurrent volcanic tsunami earthquakes. This interval may correspond to the time required to accumulate high-pressurize magma within a shallow chamber that can initiate ruptures of the intracaldera ring fault.

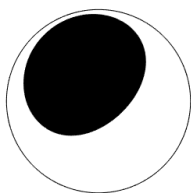
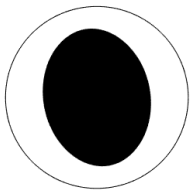
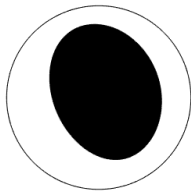
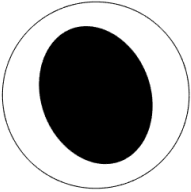
On the other hand, only the 2018 Torishima earthquake had a clearly smaller CLVD ratio (72%) and a *Strike-DC* element with a T-axis oriented in E-W direction, slightly deviating from the other events. Based on the CLVD ratio diagram (Fig. 5.10d), a CLVD ratio of 72% is equivalent to a ring fault slip with a  $\sim 90^\circ$  arc angle, and the *Strike-DC* T-axis direction infers rupture along a ring fault mainly orientated E-W. The 2018 earthquake occurred just three years after the 2015 event, and was significantly different from the other events with a roughly decadal period (1984, 1996, 2006, and 2015). Considering the peculiarities of the 2018 event, I suggest that the 2018 earthquake may have occurred on a small portion on the northern ring fault that was not broken by the 2015 earthquake (Fig. 5.17), which explains its smaller magnitude. Relatively high shear stress on the surrounding portion, even after the 2015 earthquake, may have shortened the earthquake interval significantly compared to past events.

Recurrences of similar fractures to the 2015 volcanic tsunami earthquake can also be inferred from topographic features of Smith Caldera. The source model revealed that the ring-fault rupture accompanied shallow crack opening on the NE side and closing on the SW side (Fig. 3.12a). The topography of the caldera floor showed clearly higher elevations on the NE side (by  $\sim 80$  m) than the SW side (Fig. 5.17), which is correlated with vertical displacements on the caldera floor expected from the source model (Fig. 5.1b). Such a correlation between the topography and the recurrent trapdoor faulting was also suggested for the Sierra Negra caldera [Amelung *et al.*, 2000], indicating that volcanic tsunami earthquakes equivalent to trapdoor faulting have occurred many times at Smith Caldera since the Torishima earthquake was first recognized in 1984.



**Fig. 5.17 Estimated geometries of the ring fault ruptured by recurrent Torishima volcanic tsunami earthquakes at Smith Caldera**

Solid black line represents an estimated ruptured portion of the 1996, 2006 and 2015 Torishima earthquakes, and dashed red line represents that of the 2018 earthquake. The contour lines are plotted every 20 m water depth.

	Moment tensor	Observable
2017	$M_w = 5.92$ $M_0 = 9.49 \times 10^{24}$ [dyne cm]  $\begin{bmatrix} 6.12 \times 10^{24} & & \\ 6.43 \times 10^{24} & -1.47 \times 10^{24} & \\ 4.22 \times 10^{24} & 5.98 \times 10^{23} & -4.65 \times 10^{24} \end{bmatrix}$ [dyne cm] $t_h = t_d = 8.0$ sec	$M_w = 5.76$ $M_0 = 5.57 \times 10^{24}$ [dyne cm]  <b>CLVD</b> 78.3 % <b>Strike-DC</b> 21.7 % 
2009	$M_w = 5.83$ $M_0 = 6.98 \times 10^{24}$ [dyne cm]  $\begin{bmatrix} 7.32 \times 10^{24} & & \\ 1.24 \times 10^{24} & -2.14 \times 10^{24} & \\ -1.74 \times 10^{24} & 1.26 \times 10^{24} & -5.19 \times 10^{24} \end{bmatrix}$ [dyne cm] $t_h = t_d = 7.0$ sec	$M_w = 5.81$ $M_0 = 6.64 \times 10^{24}$ [dyne cm]  <b>CLVD</b> 78.7 % <b>Strike-DC</b> 21.3 % 

**Fig. 5.18 Moment tensors of recurrent volcanic tsunami earthquakes at Curtis Caldera**

Same as Fig. 5.16, but for the Curtis earthquakes.

Figure 5.18 compares the moment tensor of the 2009 Curtis earthquake with the analyzed event in 2017. Even though the unresolved *Dip-DC* element makes the focal mechanisms of the two earthquakes look different, they are quite similar to each other in terms of the observable moment tensor elements, with  $\sim 76\%$  CLVD ratios and *Strike-DC* elements with a T-axis direction of NNW-SSE. Therefore, I suggest that quite similar fractures on an almost identical ring-fault geometry are present at both Curtis and Smith Calderas. *Doyle et al.* [1979] reported large long-term uplift around Curtis and Cheeseman Islands that accumulated during tens or hundreds of years, also implying recurrent volcanic tsunami earthquakes not recognized in the past.

## 5.4 Causes of tsunami earthquake characteristics

The peculiarities of volcanic tsunami earthquakes can be characterized by disproportionately large tsunamis relative to their intermediate-class seismic magnitudes of  $M_w$  5–6. As shown in Chapter 1.1, tsunami magnitudes  $M_t$  of the 2015 Torishima and the 2017 Curtis earthquakes were estimated as 7.5 and 7.8, respectively, larger than their seismic wave magnitudes  $M_s$  by 1.8 and 1.6, respectively. These large deviations create problems for accurate real-time tsunami forecasts based on seismic information. *Satake and Kanamori* [1991] suggested that the focusing of tsunami energy along shallow ridge structures played an important role in tsunami amplifications at tide-gauge stations deployed along the ridge. However, Fig. 1.5 showed that observed tsunami amplitudes of the two volcanic tsunami earthquakes were much larger than empirically estimated even where tide-gauge stations were not located along a ridge system. This

implies that tsunami earthquakes are more likely to be caused by their abnormal earthquake source rather than the focusing effect. Here, I consider possible causes of the unique characteristics of volcanic tsunami earthquakes, which are inherent to their abnormal physical mechanism of instantaneous fractures of a ring fault and a horizontal crack at very shallow depth.

One of possible main causes of tsunami earthquakes is slip along a curved ring-fault system, as some previous studies have suggested [e.g. *Ekström*, 1994; *Shuler et al.*, 2013b]. I demonstrated that ring-fault slips canceled out long-period seismic energy release due to the cancellation of double-couple elements from different ring-fault portions. On the other hand, thrust slips on a curved fault system focus seafloor deformation inside the ring fault, or on the caldera floor, resulting in short-wavelength tsunamis with large amplitudes, compared to typical planar fault geometries. Therefore, the ring-fault slip mechanism has a lower efficiency in terms of seismic excitation but causes tsunami amplifications in a focused area, compared to a slip on a planar fault with an equivalent fault size.

The shallow source depth is also significant. As discussed in Chapter 5.2, a depth  $< \sim 5$  km makes some types of fractures related to volcanic tsunami earthquakes aseismic. First, vertical opening/closing of a shallow crack lying horizontally excites little long-period seismic energy. Second, the *Dip-DC* moment tensor element contained by the dip slip on a ring fault is also aseismic at shallow depth, making the ring fault fracture even more aseismic together with its cancellation of the DC elements along a curved fault system. Despite these less seismic properties, short-period tsunamis can be excited efficiently by such a shallow source [e.g. *Ward*, 1982].

Thus, both effects play an important role in amplifying and focusing tsunamis in a source area with a certain caldera size, which may explain the significant gaps between seismic and tsunami magnitudes. In general, an earthquake contributes to tsunami energy by displacing a large volume of sea water, which is characterized by  $[amplitude] \times [source\ size]$ . Therefore, when the earthquake energy is evaluated from tsunami observations, tsunami wavelengths or periods proportional to the source size must be considered as well as amplitudes. In contrast to typical tsunamigenic earthquakes on planar fault structures, the peculiar source mechanism of volcanic tsunami earthquakes focuses the earthquake energy within a relatively small area, which is transformed into short-period tsunamis with larger amplitudes. However, the empirical relationship with tsunami magnitude (Eq. 1.1) [*Abe*, 1981] was derived only from amplitudes of long-period tsunamis caused by typical tsunamigenic earthquakes ( $M_w$  7.5-8.2). The direct employment of this relationship, dismissing period information of shorter-period tsunamis from volcanic tsunami earthquakes, leads to significant overestimations of earthquake energy and results in large gaps between seismic and tsunami magnitudes. This implies that the incorporation of source-size information of tsunamis, as well as amplitudes, is required for more accurate evaluation of the earthquake energy from tsunami waves.

Apart from the characteristic source properties of volcanic tsunami earthquakes, peculiar fracture phenomena may accompany large slips, when compared to typical tectonic earthquakes. In Fig.

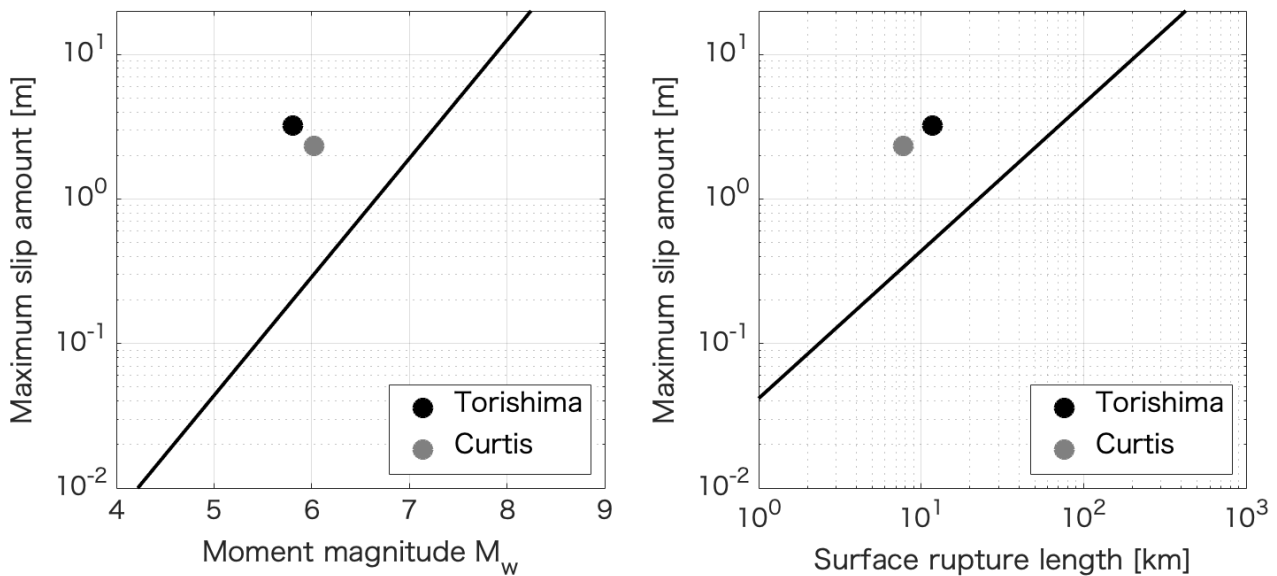


**Fig. 5.19 Comparison of volcanic tsunami earthquakes with a scaling law of global earthquakes.**

Comparisons of the 2015 Torishima and the 2017 Curtis volcanic tsunami earthquakes. For the Torishima earthquake, earthquake parameters (maximum slip amount, moment magnitude, and surface rupture length) of Model 5 (Table 3.1) are plotted. For the 2017 Curtis earthquake, those of the modified-dip model (Table 4.1) are plotted. The lines represent scaling laws proposed by [Wells and Coppersmith, 1994].

5.19, maximum slip amounts from the 2015 Torishima earthquake and 2017 Curtis earthquake are compared to the scaling law for global earthquakes with magnitudes greater than 4.5 as suggested by [Wells and Coppersmith, 1994]. Both earthquakes had larger maximum slip amounts by one order of magnitude, compared to the average of global earthquakes with similar moment magnitudes (Fig. 5.19a) and similar fault lengths (Fig. 5.19b). Such large ruptures that exceed the scaling law may be attributed to special environments with very localized stress caused by a sub-caldera pressure source or rupture amplifications related to interactions with pressurized magma. Thus, abnormally large slips also contributed to larger tsunamis than expected from seismic magnitudes alone.

Soft sediment layers, possibly lying at shallow depth below caldera floors, might result in enhancement of tsunami excitation [Okal, 1988]. Magma below the caldera structure may make the ring fault fracture less seismic by reducing the fault strength with its hot temperature [Jónsson, 2009]. Hence, many peculiar features of the atypical physical mechanism of volcanic tsunami earthquakes, such as curved fault structures, shallow source depth, focused seafloor displacement, and magma-related fractures, may contribute to the distinct tsunami earthquake characteristic of large tsunamis disproportional to seismic magnitude.

## 5.5 Future studies

This research lays the groundwork for further exploration of various topics related to earthquake physics, volcanology, and tsunami risks. Here, I consider some of these possibilities along with potential applications of the source modeling approach developed in this study.

### 5.5.1 Dynamics of volcanic tsunami earthquakes

I successfully constructed kinematic source models of volcanic tsunami earthquakes. However, these models were described with final slip distributions under the assumption of instantaneous fractures throughout the composite fault system, and long-period seismic wave analysis was conducted with the point-source assumption. These assumptions regarding the source rupture limited the discussion of rupture dynamics to speculations based on an analogy to a trapdoor faulting event observed at a subaerial caldera. Therefore, for a deeper understanding of the fractures, it will be important to investigate how these fractures were initiated and propagated over the structures. It would be useful to utilize higher-frequency seismic waves to resolve ruptures along the ring fault structures with  $\sim 5$  km source size during  $\sim 10$  s. The source structures constructed in this study will also enable us to construct more elaborate kinematic source modeling, including temporal slip history. The physics-based dynamic earthquake simulation can also be useful for understanding rupture processes of volcanic tsunami earthquakes. During the fracture processes, it is expected that the two different source systems, or the fracture of the ring fault and crack oscillations filled with magma, may interact with each other. Development of a new dynamic rupture simulation that incorporates this process could allow better predictions of rupture processes of volcanic tsunami earthquakes otherwise invisible from remote observations.

In addition, triggering processes and conditions of volcanic tsunami earthquakes are not well-understood. Some studies have suggested that intra-caldera fault ruptures are most likely triggered by over-pressurized sill-like magma chamber based on numerical modeling of stress field at calderas [e.g. *Jónsson, 2009; Gregg et al., 2018*]. Such numerical modeling approaches help constrain the (possibly large) volume of magma accumulated below submarine calderas before these earthquakes. Moreover, it is notable that instantaneous ruptures with  $M_w$  5–6 class earthquakes do not occur in every caldera volcano, although aseismic caldera-floor uplift has been widely observed [e.g. *Acocella, 2019; references therein*]. It is unclear what controls the seismic or aseismic properties of caldera uplift phenomena. The advancement of numerical simulations relating magma pressurization and intra-caldera fractures may lead to new insights into the diversity of caldera volcanism.

### 5.5.2 Submarine caldera volcanology

Throughout this source modeling study of the two volcanic tsunami earthquakes, I suggested their close association with magma fluid accumulating below the submarine calderas. Similarities in recurrent earthquakes inferred from the moment tensor analysis also indicated quasi-regular earthquake

cycles at 10 yr intervals due to magma input into a shallow magma reservoir system, as discussed in Chapter 5.3. To understand this magma accumulation process, *in-situ* seafloor observations at the submarine calderas using ocean-bottom seismometers or pressure gauges is a promising direction for future research. These instruments are very effective at monitoring microearthquakes or seafloor deformation undetectable from remote stations, which potentially occur during their inter-seismic processes. Such monitoring may lead to the detection of magma chamber inflation or activation of ring-fault systems, or even predictions of volcanic unrest at submarine volcanoes, as implemented with dense seafloor cabled observation networks at the Axial Seamount on Juan de Fuca Ridge [e.g. *Nooner and Chadwick, 2012; Wilcock et al., 2016; Levy et al., 2018; Arnulf et al., 2018*]. Remote hydrophonic records are also useful for detecting smaller-magnitude earthquakes at volcanoes, thanks to the efficient propagation of T-waves [e.g. *Sugioka et al., 2000*].

### **5.5.3 Tsunami risk evaluations**

From the perspective of tsunami risk evaluation, it is critical to develop a technique for forecasting tsunami arrivals at coastal cities based on seismic analysis. Recently, data assimilation has been applied to real-time tsunami forecasting, which does not require knowledge of the tsunami source [e.g. *Maeda et al., 2015; Wang et al., 2018*]. However, few offshore tsunami observation networks have been deployed around remote islands where large tsunamis have been observed due to volcanic tsunami earthquakes, such as Hachijojima Island. Therefore, the conventional tsunami forecasting system based on seismic analysis is still the most useful. The present study overcame the challenge of quantitatively relating tsunamis to seismic magnitudes through kinematic source models. Because their recurrence properties implied that the source geometry may not change dramatically throughout long periods, it is possible to evaluate tsunami risks for different-sized volcanic tsunami earthquakes potentially occurring at submarine volcanoes in future. On the other hand, it may be possible that volcanic activity shifts to different stages including dyke intrusions and caldera collapses, as observed at several calderas such as Bardarbunga [e.g. *Gudmundsson et al., 2016*], Kilauea [e.g. *Neal et al., 2019*] or Miyakejima Island [e.g. *Kumagai et al., 2001; Geshi et al., 2002*]. Tsunami modeling studies considering such possible scenarios may be also important for evaluating potential risks related to such active submarine calderas with recurrent volcanic tsunami earthquakes.

### **5.5.4 Application of the kinematic source modeling approach**

An interdisciplinary approach for earthquake sources, combining seismic and tsunami data, can be applied to similar vertical-CLVD earthquakes on subaerial calderas by replacing tsunami data with geodetic data, such as Global Positioning System (GPS) or Interferometric Synthetic Aperture Radar (InSAR) data. Such data help us to estimate slip distributions on possible fault geometries. By analyzing long-period seismic data, it is possible to validate the estimated source models and constrain their geometries with additional information obtained by the observable moment-tensor elements. Moreover, if vertical-CLVD earthquakes are focused at calderas with the specific characteristics of ring-fault structures

and a magma chamber, long-period seismic waves can enable us to examine physical properties of intra-caldera systems (such as frictional strength) that are poorly understood. On the other hand, different types of vertical-CLVD earthquakes with a vertical pressure axis are often observed during the caldera collapse process, which has been attributed to ring-fault ruptures, closing cracks, or free falls of caldera blocks [e.g. *Ekström*, 1994; *Nettles and Ekström*, 1998; *Shuler and Ekström*, 2009; *Shuler et al.*, 2013a-b; *Riel et al.*, 2015; *Duputel and Rivera*, 2019]. The application of the modeling approach used in this study, assuming specific caldera geometries, may contribute to our understanding of caldera collapse processes.



## ***Chapter 6 Major findings and conclusions***

In this thesis, I aimed to determine the unknown physical mechanism causing peculiar volcanic tsunami earthquakes recurrent at submarine volcanoes by investigating their source using interdisciplinary methods based on analyses of tsunami waveforms and long-period seismic waves. By combining the advantages of different types of geophysical data, I successfully obtained kinematic source models for two volcanic tsunami earthquakes near Torishima Island in Japan and Curtis Island in New Zealand. Based on the estimated source models, I suggested that the physical mechanism of such volcanic tsunami earthquakes is the instantaneous fracture of intra-caldera ring fault structures and a shallow horizontal crack filled with magma. This mechanism explained many distinct features of these events, such as vertical-CLVD-type moment tensors, specific tsunami earthquake characteristics, and the recurrence of similar earthquakes.

In Chapter 2, I investigated the initial sea-surface displacement caused by the 2015 Torishima volcanic tsunami earthquake by using high-quality tsunami data recorded by the array of OBP gauges deployed only ~100 km from the epicenter. Using the ray-tracing method for dispersive tsunamis, the peak location of the uplifted source was constrained within the rim structure of a submarine caldera, Smith Caldera, with better accuracy than earthquake locating systems using regional or faraway seismic data. By reproducing observed tsunami waveforms with an axially symmetric tsunami source, I revealed that the earthquake caused meter-scale seafloor uplift on the caldera floor and smaller peripheral subsidence along the rim structure. These results suggested that the earthquake occurred in close association with subsurface structures of Smith Caldera, such as shallow horizontal crack and intra-caldera ring-fault structures.

In Chapter 3, I explored a kinematic source model of the 2015 Torishima earthquake. In order to obtain more detailed information of seafloor deformation caused by the earthquake, I estimated the initial sea-surface displacement by using the inversion of tsunami waveforms with additional OBP records observed in a wide oceanic region south of Honshu Island, Japan. To improve the accuracy of tsunami waveform computations, I used a new phase correction method for short-period tsunamis (developed in Appendix 1). The results confirmed that large uplift was focused on the northwestern side of the caldera floor and peripheral subsidence could be traced along the rim structure, mainly on the same side.

Based on the heterogeneous tsunami source model, I hypothesized a physical mechanism for the instantaneous fracturing of sub-caldera structures composed of dip slips of an inwardly down-dipping ring fault and tensile opening of a shallow horizontal fault lying at a few kilometers' depth below the caldera floor. I modeled multiple fault models with different fault parameters by discretizing the fault structures with triangular dislocation elements. To relate the tsunami waveforms directly to fault slips in the fault models, I developed a new inversion method using an efficient computation technique for tsunami Green's functions from subfault slips. Applying this new method allowed the construction of slip distributions on multiple fault models that reproduced the tsunami waveform records. The depth of the horizontal fault was considered as very shallow ( $\sim 2$  km) because slip distributions were phenomenologically reasonable in the case, while other fault parameters such as the dip angle and ruptured portions of the ring fault were not constrained well.

I then aimed to validate the hypothetical physical mechanism and constrain the fault parameters by comparing synthetic long-period seismic waveforms predicted for the multiple inverted slip models with observed records at broad-band seismic stations of the F-net and GSN. I modeled their moment tensors by summing up partial contributions of subfault slips under the point-source assumption. Of the slip models with different fault parameters, the best fittings for the synthetic and observed long-period seismic waveforms was a model composed of 1–3 m thrust slips on the ring fault with a dip angle of  $75^\circ$  along a three-quarter portion of the rim structure and instantaneous opening on the northeastern side and closing on the southwestern side of a horizontal fault with comparable maximum slip amounts of  $\sim 2$  m. Thus, I finally obtained a kinematic source model for the 2015 Torishima earthquake that reproduced both the tsunami and long-period seismic wave records sufficiently, validating the hypothetical physical mechanism. A kinematic source model with slip distributions on a concrete fault structure was thus successfully established based on quantitative assessments using different datasets incorporating different geophysical phenomena.

In Chapter 4, I took a similar approach for the 2017 Curtis volcanic tsunami earthquake. Using tsunami records at tide-gauge stations, I roughly estimated the tsunami source area of the earthquake by computing synthetic tsunami waveforms from Gaussian-shaped uplift sources distributed in intervals of  $1^\circ$  and located it very near Curtis Island. Then, I inverted the tsunami waveforms to estimate the initial sea-surface displacement generated by the earthquake around the island. Consequently, meter-scale seafloor uplift was focused to the southwest of the island with a clear boundary of the uplifted area on its southern side. The caldera-like topographic features just below the uplifted sea surface strongly suggested that the Curtis earthquake also occurred with a similar mechanism to that of the 2015 Torishima earthquake. Hence, I assumed composite fault models composed of an inward ring fault along the southwestern part of the caldera rim structure and a horizontal fault lying at shallow depth of  $\sim 3$ – $5$  km. While changing detailed fault parameters, I estimated slip distributions on the fault models by inversion using the tsunami waveforms, then synthesized long-period waveforms at regional broad-band seismic stations. By taking a trial-and-error approach to find the best fault parameters, I obtained several kinematic source models that

explained tsunami and seismic data; these indicated that the Curtis earthquake had a physical mechanism quite similar to that of the Torishima earthquake.

In Chapter 5, I discussed the physical mechanism of volcanic tsunami earthquakes based on the kinematic source models established for the two earthquakes. I attributed the earthquakes to the sudden rupture of an intra-caldera inward-dipping ring fault promoted by an inflated sill-like magma reservoir at shallow depth below a submarine caldera floor. In the proposed scenario, as magma accumulates inside the shallow reservoir, shear stress on the ring fault generated by the inflated reservoir increases until it reaches a critical threshold needed to initiate the fracture of the ring fault. When the ring fault rupture starts, the sill-like reservoir is forced to open along the ring fault, while rapid depressurization of inner magma due to the volumetric change forced by the rupture cause deflation of the reservoir on the other side. This fracture process is quite similar to that of *trapdoor faulting* events observed at the Sierra Negra caldera, Galápagos. This analogy implies that abundant magma recharged below the submarine caldera increased local stress levels of intra-caldera structures, generating atypical volcanic earthquakes with intermediate-class magnitudes.

I also considered the properties of volcanic tsunami earthquakes from the perspectives of long-period seismic radiation, recurrence of similar earthquakes, and causes of the tsunami earthquake characteristics. It is significant that the crack opening/closing is aseismic and parts of the moment release by the ring-fault fracture do not contribute to long-period seismic waves, because of the shallow source depth of the volcanic tsunami earthquakes. However, I demonstrated that ring-fault geometries such as an arc angle and a fault orientation can be constrained from observable elements obtained with moment-tensor analysis using long-period seismic waves. By analyzing the observable moment-tensor elements, I suggested that most of the recurrent volcanic tsunami earthquakes shared very similar fault geometries at the submarine calderas. The characteristics of tsunami earthquakes were thus explained by their aseismic properties and short-wavelength and large-amplitude tsunamis due to seafloor deformation that were focused over a caldera structure.

Therefore, in this study, I successfully determined a physical mechanism for volcanic tsunami earthquakes that explains many key features while providing new insights into seafloor phenomena at remote submarine calderas. The methods and results presented here will enhance the scientific understanding of geophysical fields including volcanology, seismology, and oceanography.



# *Acknowledgements*

First of all, I would like to express my deep gratitude to my supervisor, Kenji Satake. Since I started my research career about six years ago, he helped me various supports by providing knowledgeable ideas, proper instructions, and great opportunities to communicate with excellent geoscientists all over the world. I am very honored to be a member of his world-wide laboratory dealing with various geoscience problems, which enabled me to progress my interdisciplinary project efficiently and actively with many collaborators.

I am deeply thankful to Shingo Watada for his supports. Whenever I had challenging problems in my research project, he helped me with his insightful ideas to solve them. I also appreciate to all my research collaborators: Yoshio Fukao, Hiroko Sugioka, Aki Ito, Hajime Shiobara, Hiroo Kanamori, Luis Rivera, Zhongwen Zhang, Kazushige Obara, Takuto Maeda and Ryota Takagi. I am also thankful to many great scientists who provided me instructive advices: Kiwamu Nishida, Hitoshi Kawakatsu, Yasuyuki Kano, Toshitaka Baba, Naotaka Y. Chikasada, Tatsuhiko Saito, Tatsuya Kubota, Shunsuke Takemura, Nana Yoshimura, Masakazu Fuji, Mikhail A. Nosov, Sigurjón Jónsson, Teh-Ru Alex Song, Eric Dunham, Paul Segall and others.

Thank you to all members of Satake Laboratory including post members and visitors: Satoko Murotani, Aditya Gusman, Mohammad Heidarzadeh, Iyan E. Mulia, Takeo Ishibe, Tomoko Goto, Masaki Yamada, Ryoichi Nakamura, Tomoya Harada, Satoshi Kusumoto, Tungcheng Ho, Yifei Wu, Yuchen Wang, Patricio Winckler Grez, Lingling Ye, Marco Quiroz, Kirill Sementsov, Md. Jakir Hossen, Siraput Jongaramrungruang, Florian Millet and others. I also thankful to all the staffs in ERI, including Mayumi Takashima who helped me to attend scientific conferences, and Shigeki Nakagawa, Miki Uehara and Yukiko Minamoto, who helped me whenever I had troubles with my computer environments.

Data of tsunami, seismic, topography and bathymetry were provided by JMA, Japan Agency for Marine-Earth Science and Technology (JAMSTEC), the Marine Information Research Center of the Japan Hydrographic Association, Hydrographic and Oceanographic Department of Japan Coast Guard, the Geospatial Information Authority of Japan, GEBCO, NIWA, LINZ, NIED and IRIS. I appreciate the effort of all who maintains the networks. I also thank the shipboard scientists and technical staffs of cruise YK14-07 and cruise YK15-08 of R/V Yokosuka (JAMSTEC) to deploy and collect the array stations.

This work was supported by Japan Society for the Promotion of Science (JSPS) Grants-in-Aid for Scientific Research (KAKENHI) grant number JP17J02919. My travel to California Institute of Technology was funded by the KAKENHI and the Oversea Internship Program of ERI.

I am also thankful to members of Dissertation Committee, Takashi Furumura, Takao Ohminato, Yosuke Aoki, Ryosuke Ando, and Kenji Satake, for reviewing and providing valuable comments to improve this thesis.

I appreciate to my colleagues from the undergrad department, Ryo Kurihara and Masatoshi Ohashi, and all the friends of ERI FC Ladies. Thank you to my friends in Room 1-616 in ERI, HyeJeong Kim, Satoru Baba, Yuki Kawano, Michelle Legler, Kota Fukuda, Naoto Yokotani, and Xiaoli Wan. Thank you to friends in Caltech SeismoLab, Voon Hui Lai, Yuan-Kai Liu, Zhichao Shen, Jorge Castillo, Zhe Jia and others, for sharing the best summertime in California with me. I also thankful to an administrative assistant in Caltech SeismoLab, Donna Mireles, and my Airbnb host, Carolyn Sykes, for helping my days in Pasadena. Thank you to all my friends, including my best friend, Yuki Haba, who always stayed on my side. I appreciate to my Korean parents-in-law and family-in-law, who always continue sending big loves from Seoul. Thank you to my parents for always supporting me with the bottomless love. Finally, I would like to express my biggest gratitude to the precious one, YoungJoo, for bringing full of loves and smiles to my life.

## References

- [1] Abe, K. (1981), Physical size of tsunamigenic earthquakes of the northwestern Pacific. *Phys. Earth Planet. Inter.*, **27**: 194-205.
- [2] Acocella, V., Funiciello, R. (1999), The interaction between regional and local tectonics during resurgent doming: the case of the island of Ischia, Italy. *J. Volcanol. Geotherm. Res.*, **88**, 109–123.
- [3] Acocella, V., Cifelli, F., Funiciello, R. (2001), The control of overburden thickness on resurgent domes: insights from analogue models. *J. Volcanol. Geotherm. Res.*, **111**, 137–153.
- [4] Acocella, V., Di Lorenzo, R., Newhall, C., and Scandone, R. (2015), An overview of recent (1988 to 2014) caldera unrest: knowledge and perspectives. *Rev. Geophys.*, **53**, 896–955. doi: 10.1002/2015RG000492.
- [5] Aki, K., and P. G. Richards (1980), *Quantitative Seismology*, W.H. Freeman and Company.
- [6] Amelung, F., Jónsson, S., Zebker, H., Segall, P. (2000), Widespread uplift and ‘trapdoor’ faulting on Galápagos volcanoes observed with radar interferometry. *Nature* **407**, 993–996.
- [7] Amelung, F., Brothelande, E., Mirzaee, S., La Femina, P. C., Ruiz, G., Vajedian, S., Motagh, M., Ruiz, M. C., Mothes, P. A., Hernandez, S., Cesca, S., Dahm, T., Bell, A. F. (2018), Ground Deformation associated with the 2018 eruption of Sierra Negra volcano and the source mechanism of the initial M5.3 earthquake, AGU 2018 Fall Meeting, V31C-07, Washington, D.C.
- [8] Arnulf, A., Harding, A., and Kent, G. (2018), Three-dimensional P-wave velocity structure of axial volcano on the Juan de Fuca ridge (investigators: Adrien F. Arnulf, Alistair Harding, Graham Kent). Palisades, NY: Interdisciplinary Earth Data Alliance (IEDA). <https://doi.org/10.1594/IEDA/324420>.
- [9] Baba, T., Takahashi, N., Kaneda, Y., Ando, K., Matsuoka, D., and Kato, T. (2015), Parallel implementation of dispersive tsunami wave modeling with a nesting algorithm for the 2011 Tohoku tsunami. *Pure Appl. Geophys.*, **172**(12), 3455–3472. <https://doi.org/10.1007/s00024-015-1049-2>.
- [10] Bernard, E., and C. Meinig (2011), History and future of deep-ocean tsunami measurements. In *Proceedings of Oceans' 11 MTS/IEEE, Kona, IEEE, Piscataway, NJ, 19–22 September 2011*, No. 6106894, 7 pp.
- [11] Chadwick, W. W., D. J. Geist, S. Jónsson, M. Poland, D. J. Johnson, and C. M. Meertens (2006), A volcano bursting at the seams: Inflating, faulting, and eruption at Sierra Negra volcano, Galápagos, *Geology*, **34**(12), 1025–1028, doi:10.1130/G22826A.1.

- [12] Chadwick, W. W., Nooner, S. L., Butterfield, D. A., and Lilley, M. D. (2012), Seafloor deformation and forecasts of the April 2011 eruption at Axial Seamount. *Nature Geoscience*, **5**(7), 474–477. <https://doi.org/10.1038/ngeo1464>.
- [13] Chouet, B. A. (1996), New methods and future trends in seismological volcano monitoring, in *Monitoring and Mitigation of Volcano Hazards*, edited by R. Scarpa and R. I. Tilling, pp. 23–97, Springer-Verlag, Berlin.
- [14] Chikasada, N. Y. (2019), Short-Wavelength Tsunami Observation Using Deep Ocean Bottom Pressure Gauges, International Society of Offshore and Polar Engineers, <https://www.onepetro.org/conference-paper/ISOPE-I-19-707>.
- [15] Cole, J.W., Milner, D.M., Spinks, K.D. (2005), Calderas and caldera structures: a review. *Earth Science Reviews*, **69**, 1–96.
- [16] Contreras-Arratia, R., and J., W. Neuberg (2019), Complex seismic sources in volcanic environments: Radiation modelling and moment tensor inversions, *J. Volcanol. Geotherm. Res.*, **381**, 262-272, <https://doi.org/10.1016/j.jvolgeores.2019.06.005>.
- [17] Dahlen, F.A. and Tromp, J. (1998), *Theoretical Global Seismology*, Princeton University Press, Princeton, NJ.
- [18] De Natale, G., Pingue, F. (1993), Ground deformation in collapsed calderas structures. *J. Volcanol. Geotherm. Res.*, **57**, 19–38.
- [19] Doyle, A. C., R. J. Singleton, and J. C. Yaldwyn (1979), Volcanic activity and recent uplift on Curtis and Cheeseman Islands, Kermadec Group, Southwest Pacific, *J. Royal Soc. New Zealand*, **9**(1), 123–140.
- [20] Duputel, Z., L., Rivera, H., Kanamori, and G., Hayes (2012), W phase source inversion for moderate to large earthquakes (1990–2010), *Geophys. J. Int.*, **189** (2), 1125–1147, <https://doi.org/10.1111/j.1365-246X.2012.05419.x>
- [21] Duputel, Z., and L. Rivera (2019), The 2007 Caldera Collapse of Piton de la Fournaise Volcano: Source Process from Very-Long-Period Seismic Signals. *Earth Planet. Sci. Lett.*, v. **527**, pp. 115786, <https://doi.org/10.1016/j.epsl.2019.115786>.
- [22] Ekström, G. (2006), Global detection and location of seismic sources by using surface waves, *Bull. Seism. Soc. Am.*, **96**(4A), 1201–1212, doi:10.1785/0120050175.
- [23] Ekström, G. (1994), Anomalous earthquakes on volcano ring-fault structures, *Earth Planet. Sci. Lett.*, **128**, 707–712.

- [24] Ekström, G., Nettles, M., and Dziewoński, A. M. (2012), The global CMT project 2004–2010: Centroid-moment tensors for 13,017 earthquakes. *Phys. Earth Planet. Inter.*, **200-201**, 1–9. <https://doi.org/10.1016/J.PEPI.2012.04.002>.
- [25] Frohlich, C. (1989), Note concerning possible mechanisms for non-double-couple earthquake sources, *Geophys. Res. Lett.*, **16**(6), 523–526.
- [26] Frohlich, C. (1990), Note concerning non-double-couple source components from slip along surfaces of revolution, *J. Geophys. Res.*, **95**(B5), 6861–6866.
- [27] Frohlich, C. (1994), Earthquakes with non-double-couple mechanisms, *Science*, **264**, 804–809.
- [28] Frohlich, C. (1995), Characteristics of well-determined non-double-couple earthquakes in the Harvard CMT catalog, *Phys. Earth Planet. Inter.*, **21**(4), 213–228, doi:10.1016/0031-9201(95)03031-Q.
- [29] Fukao, Y. (1979), Tsunami earthquakes and subduction processes near deep-sea trenches. *J. Geophys. Res.*, **84**: 2303–2314.
- [30] Fukao, Y., Sandanbata, O., Sugioka, H., Ito, A., Shiobara, H., Watada, S., and Satake, K. (2018), Mechanism of the 2015 volcanic tsunami earthquake near Torishima, Japan. *Science Advances*, **4**(4), eaao0219.
- [31] Sandanbata, O., S. Watada, K. Satake, Y. Fukao, H. Sugioka, A. Ito, and H. Shiobara (2018), Ray tracing for dispersive tsunamis and source amplitude estimation based on Green's law: Application to the 2015 volcanic tsunami earthquake near Torishima, south of Japan, *Pure Appl. Geophys.*, **175** 4, DOI: 10.1007/s00024-017-1746-0, 1371-1385.
- [32] Geist, D. J., K. S. Harpp, T. R. Naumann, M. Poland, W. W. Chadwick, M. Hall, and E. Rader (2008), The 2005 eruption of Sierra Negra volcano, Galápagos, Ecuador, *Bull. Volcanol.*, **70**, 655–673, doi:10.1007/s00445-007-0160-3.
- [33] Geshi, N., T. Shimano, T. Chiba, and S. Nakada (2002), Caldera collapse during the 2000 eruption of Miyakejima volcano, Japan, *Bull. Volcanol.*, **64**, 55–68.
- [34] Geyer, A., and J. Martí, (2014), A short review of our current understanding of the development of ring faults during collapse caldera formation. *Front. Earth Sci.*, **2**:22. doi:10.3389/feart.2014.00022.
- [35] Global Volcanism Program (2013), Curtis Island (242010) in *Volcanoes of the World*, v. 4.8.3. Venzke, E. (ed.). Smithsonian Institution. Downloaded 08 Nov 2019 (<https://volcano.si.edu/volcano.cfm?vn=242010>). <https://doi.org/10.5479/si.GVP.VOTW4-2013>.
- [36] Global Volcanism Program (2013), Sumisujima (284080) in *Volcanoes of the World*, v. 4.8.3. Venzke, E. (ed.). Smithsonian Institution. Downloaded 08 Nov 2019 (<https://volcano.si.edu/volcano.cfm?vn=284080>). <https://doi.org/10.5479/si.GVP.VOTW4-2013>.

- [37] Gregg, P. M., Le Mével, H., Zhan, Y., Dufek, J., Geist, D., and Chadwick, W. W., Jr. (2018), Stress triggering of the 2005 eruption of Sierra Negra volcano, Galápagos. *Geophys. Res. Lett.*, **45**, 13,288–13,297. <https://doi.org/10.1029/2018GL080393>
- [38] Gudmundsson, A., Marti, J., Turon, E. (1997), Stress fields generating ring faults in volcanoes. *Geophys. Res. Lett.*, **24**, 1559–1562.
- [39] Guðmundsson, M. T., et al. (2016), Gradual caldera collapse at Bárðarbunga volcano, Iceland, regulated by lateral magma outflow, *Science*, **353**(6296), aaf8988, doi:10.1126/science.aaf8988.
- [40] Gusman, A. R., Mulia, I. E., and Satake, K. (2018), Optimum sea surface displacement and fault slip distribution of the 2017 Tehuantepec earthquake (Mw 8.2) in Mexico estimated from tsunami waveforms. *Geophys. Res. Lett.*, **45**, 646–653. <https://doi.org/10.1002/2017GL076070>.
- [41] Hanks, T.C. and Kanamori, H. (1979), A moment magnitude scale, *J. geophys. Res.*, **84**, 2348–2350.
- [42] Hatori, T. (1985), Irregular tsunami generated by the Torishima-Kinkai earthquake on June 13, 1984 (in Japanese), *Bull. Earthquake Res. Inst. Univ. Tokyo*, **60**, 87-95.
- [43] Hayes G.P. Rivera L. Kanamori H. (2009), Source inversion of the W-Phase: real-time implementation and extension to low magnitudes, *Seismol. Res. Lett.*, **80**, 817–822.
- [44] Herrmann, R.B. (2013), Computer Programs in Seismology: An Evolving Tool for Instruction and Research. *Seismol. Res. Lett.*, **84**, 1081–1088.
- [45] Ho, T.-C., Satake, K., and Watada, S. (2017), Improved phase corrections for transoceanic tsunami data in spatial and temporal source estimation: Application to the 2011 Tohoku earthquake. *J. Geophys. Res.*, **122**, 10,155–10,175. <https://doi.org/10.1002/2017JB015070>.
- [46] Hossen, M. J., P. R. Cummins, J. Dettmer, and T. Baba (2015), Time reverse imaging for far-field tsunami forecasting: 2011 Tohoku earthquake case study, *Geophys. Res. Lett.*, **42**, 9906–9915, doi:10.1002/2015GL065868.
- [47] Hossen, M. J., Gusman, A. R., Satake, K., and Cummins, P. R. (2018), An adjoint sensitivity method applied to time reverse imaging of tsunami source for the 2009 Samoa earthquake. *Geophys. Res. Lett.*, **45**, 627–636. <https://doi.org/10.1002/2017GL076031>
- [48] Japan Meteorological Agency (2015), Analysis of earthquake near Torishima Island on 3 May 2015 (in Japanese), <https://www.data.jma.go.jp/svd/eqev/data/study-panel/tsunami/benkyokai13/shiryoku4.pdf>.
- [49] Jónsson, S. (2009), Stress interaction between magma accumulation and trapdoor faulting on Sierra Negra, Galápagos, *Tectonophysics*, **471**, 36–44.

- [50] Julian, B. R., A. D. Miller, and G. R. Foulger (1998), Non-double-couple earthquakes 1. Theory, *Rev. Geophys.*, **36**(4), 525–549.
- [51] Kajiura, K. (1963), The leading wave of a tsunami, *Bull. Earthquake Res. Institute*, **41**, 545–571.
- [52] Kanamori H (1972), Mechanism of tsunami earthquakes. *Phys. Earth Planet. Inter.*, **6**: 246–259.
- [53] Kanamori, H. (1977), The energy release in great earthquakes, *J. geophys. Res.*, **82**(20), 2981–2987.
- [54] Kanamori, H., and J. W. Given (1981), Use of long-period surface waves for rapid determination of earthquake source parameters, *Phys. Earth Planet. Inter.*, **27**, 8–31.
- [55] Kanamori, H., G. Ekström, A. Dziewonski, J. S. Barker, and S. A. Sipkin (1993), Seismic radiation by magma injection: An anomalous seismic event near Tori Shima, Japan, *J. Geophys. Res.*, **98**(B4), 6511–6522.
- [56] Kanamori H. Rivera L. (2008), Source inversion of W phase: speeding up seismic tsunami warning, *Geophys. J. Int.*, **175**(1), 222–238.
- [57] Kaneda, Y., K. Kawaguchi, E. Araki, H. Matsumoto, T. Nakamura, S. Kamiya, K. Ariyoshi, T. Hori, T. baba and N. Takahashi (2015), Development and application of an advanced ocean floor network system for megathrust earthquakes and tsunamis, Seafloor observatories, In: Favali, P. et al. (eds.), Springer Praxis Books, pp. 643-663.
- [58] Kawaguchi, K., S. Kaneko, T. Nishida and T. Komine (2015), Construction of the DONET real-time seafloor observatory for earthquakes and tsunami monitoring, Seafloor Observatories, In: Favali, P. et al. (eds.), Springer Praxis Books, pp. 211-228, doi:10.1007/978-3-642-11374-1\_10,
- [59] Kawakatsu, H. (1996), Observability of the isotropic component of a moment tensor, *Geophys. J. Int.*, **126**, 525–544.
- [60] Kawakatsu, H., and M. Yamamoto (2007), Volcano seismology, in *Treatise on Geophysics*, **4**, edited by H. Kanamori, pp. 389–420, Elsevier, Amsterdam, doi:10.1016/B978-044452748-6.00073-0.
- [61] Knopoff, L., M. J. Randall (1970), The compensated linear-vector dipole: A possible mechanism for deep earthquakes. *J. Geophys. Res.*, **75**, 4957–4963.
- [62] Konstantinou, K. I., H. Kao, C. H. Lin, and W.-T. Liang (2003), Analysis of broad-band regional waveforms of the 1996 September 29 earthquake at Bárðarbunga volcano, central Iceland: Investigation of the magma injection hypothesis, *Geophys. J. Int.*, **154**, 134–145.
- [63] Kumagai, H., T. Ohminato, M. Nakano, M. Ooi, A. Kubo, H. Inoue, and J. Oikawa (2001), Very-long-period seismic signals and caldera formation at Miyake Island, Japan, *Science*, **293**, 687–690.

- [64] Levy, S., Bohnenstiehl, D. R., Sprinkle, P., Boettcher, M. S., Wilcock, W. S. D., Tolstoy, M., and Waldhauser, F. (2018), Mechanics of fault reactivation before, during, and after the 2015 eruption of Axial Seamount. *Geology*, **46**, 447–450. <https://doi.org/10.1130/G39978.1>
- [65] Maeda, T., Obara, K., Shinohara, M., Kanazawa, T., and Uehira, K. (2015), Successive estimation of a tsunami wavefield without earthquake source data: A data assimilation approach toward real-time tsunami forecasting. *Geophys., Res., Lett.*, **42**, 7923–7932. <https://doi.org/10.1002/2015GL065588>
- [66] Menke, W. (2012), *Geophysical Data Analysis: MATLAB Edition*. Elsevier Science.
- [67] McTigue DF, Segall P (1988), Displacements and tilts from dip-slip faults and magma chambers beneath irregular surface topography. *Geophys, Res, Lett*, **15**:601–604. doi:10.1029/GL015i006p00601.
- [68] Momma, h., N. Fujiwara, K. Kawaguchi, R. Iwase, S. Suzuki and H. Kinoshita (1997), Monitoring system for submarine earthquakes and deep sea environment, Oceans '97. MTS/IEEE Conference Proceedings, Halifax, NS, Canada, pp. 1453-1459 vol.2, doi:10.1109/OCEANS.1997.624211.
- [69] Molin, P., Acocella, V. and Funicello, R. (2003), Structural, seismic and hydrothermal features at the border of an active intermittent resurgent block: Ischia Island (Italy). *J. Volcanol. Geotherm. Res.*, **121**, 65–81.
- [70] National Research Institute for Earth Science and Disaster Resilience (2019), NIED F-net, National Research Institute for Earth Science and Disaster Resilience, doi: 10.17598/NIED.0005.
- [71] National Research Institute for Earth Science and Disaster Resilience (2019), NIED DONET, National Research Institute for Earth Science and Disaster Resilience, doi: 10.17598/NIED.0008.
- [72] Neal CA, Brantley SR, Antolik L et al (2018), The 2018 rift eruption and summit collapse of Kīlauea Volcano. *Science*, **363**:367–374. <https://doi.org/10.1126/science.aav7046>
- [73] Nettles, M., and G. Ekström (1998), Faulting mechanism of anomalous earthquakes near Bárðarbunga Volcano, Iceland, *J. Geophys. Res.*, **103**(B8), 17,973–17,983.
- [74] Nikkhoo, M., Walter, T.R. (2015), Triangular dislocation: an analytical, artefact-free solution. *Geophys. J. Int.*, **201**, 1119–1141. <https://doi.org/10.1093/gji/ggv035>.
- [75] Nooner, S. L., and Chadwick, W. W. (2016), Inflation-predictable behavior and co-eruption deformation captured by cabled instruments at Axial Seamount. *Science*, **354** (6318), 1399–1403. <https://doi.org/10.1126/science.aah4666>
- [76] Okada, Y. (1992), Internal deformation due to shear and tensile faults in a half-space. *Bull. Seismol. Soc. Am.*, **82**, 1018–1040.

- [77] Okal, E. A. (1988), Seismic parameters controlling farfield tsunami amplitudes: a review, *Natural Hazards*, **1**, 67-96.
- [78] Peregrine, H. (1972), Equations for water waves and the approximations behind them, edited by R. E. Meyer, pp. 95–121, *Waves on Beaches and Resulting Sediment Transport*, Academic Press, New York.
- [79] Persson, P.-O., and G. Strang (2004), A Simple Mesh Generator in MATLAB. *SIAM Review*, **46** (2), pp. 329-345 (<https://popersson.github.io/distmesh/>)
- [80] Reynolds, R. W., D. Geist, and M. D. Kurz (1995), Physical volcanology and structural development of Sierra Negra volcano, Isabela Island, Galápagos archipelago, *Geol. Soc. Am. Bull.*, **107**(12), 1398–1410, doi:10.1130/0016-7606(1995)107<1398:PVASDO>2.3.CO;2.
- [81] Ronchin, E., Geyer, A. and Martí, J. (2015), Evaluating Topographic Effects on Ground Deformation: Insights from Finite Element Modeling, *Surv Geophys*, **36**, 513. <https://doi.org/10.1007/s10712-015-9325-3>
- [82] Phillips, W.J. (1974), The dynamic emplacement of cone sheets. *Tectonophysics*, **24**, 69–84.
- [83] Riel, B., P. Milillo, M. Simons, P. Lundgren, H. Kanamori and S. Samsonov (2015). The collapse of Bardarbunga caldera, Iceland, *Geophys. J. Int.*, **202**, pp. 446-453
- [84] Rubin, A. M. (1995), Propagation of magma-filled cracks, *Annu. Rev. Earth Planet. Sci.*, **23**, 287–336.
- [85] Saito, T., K. Satake, and T. Furumura (2010), Tsunami waveform inversion including dispersive waves: the 2004 earthquake off Kii Peninsula, Japan, *J. Geophys. Res.*, **115**, B06303, doi:10.1029/2009JB006884.
- [86] Sandanbata, O., S. Watada, K. Satake, Y. Fukao, H. Sugioka, A. Ito, and H. Shiobara (2018), Ray tracing for dispersive tsunamis and source amplitude estimation based on Green's law: Application to the 2015 volcanic tsunami earthquake near Torishima, south of Japan, *Pure Appl. Geophys.*, **175**, 4, DOI: 10.1007/s00024-017-1746-0, 1371-1385.
- [87] Satake K. (1987), Inversion of tsunami waveforms for the estimation of a fault heterogeneity—Method and numerical experiments, *J. Phys. Earth*, **35**, no. 3, 241–254.
- [88] Satake, K., and H. Kanamori (1991), Abnormal tsunami caused by the June 13, 1984, Torishima, Japan, earthquake, *J. Geophys. Res.*, **96**(B12), 19,933–19,939.
- [89] Satake, K., *Tsunamis, Treatise on Geophysics (Second edition)* (2015), pp. 477-504.
- [90] Satake, K., and A. Gusman, (2015), Abnormal tsunamis from recurrent M~6 Torishima earthquakes (abstract in Japanese), The Seismological Society of Japan, 2015 Fall Meeting (abstract number, S17-12).

- [91] Shuler, A., and G. Ekström (2009), Anomalous earthquakes associated with Nyiragongo Volcano: Observations and potential mechanisms, *J. Volcanol. Geotherm. Res.*, **181**(3–4), 219–230, doi:10.1016/j.jvolgeores.2009.01.011.
- [92] Shuler, A., M. Nettles, and G. Ekström (2013a), Global observation of vertical-CLVD earthquakes at active volcanoes, *J. Geophys. Res. Solid Earth*, **118**, 138–164, doi:10.1029/2012JB009721.
- [93] Shuler, A., G. Ekström, and M. Nettles (2013b), Physical mechanisms for vertical-CLVD earthquakes at active volcanoes, *J. Geophys. Res. Solid Earth*, **118**, 1569–1586, doi:10.1002/jgrb.50131.
- [94] Silver, P.G. and Jordan, T.H. (1982), Optimal estimation of scalar seismic moment, *Geophys. J. R. astr. Soc.*, **70**, 755–787.
- [95] Smith, I. E. M., R. N. Brothers, F. G. Muiruri, and P. R. L. Browne (1988), The geochemistry of rock and water samples from Curtis Island Volcano, Kermadec Group, Southwest Pacific, *J. Volcanol. Geotherm. Res.*, **34**, 233–240.
- [96] Sugioka, H., Y. Fukao, T. Kanazawa, and K. Kanjo (2000), Volcanic events associated with an enigmatic submarine earthquake. *Geophys. J. Int.*, **142**, 361–370.
- [97] Tani, K., Fiske, R.S., Tamura, Y., Kido, Y., Naka, J., Shukuno, H., and Takeuchi, R. (2008), Sumisu volcano, Izu-Bonin arc, Japan: site of a silicic caldera-forming eruption from a small open-ocean island, *Bull Volcanol.*, **70**: 547. Doi:10.1007/s00445-007-0153-2.
- [98] Tappin DR, Matsumoto T, Watts P, et al. (1999), Sediment slump likely caused 1998, Papua New Guinea tsunami. *Eos, Transactions American Geophysical Union*. **80**: 329, 334, 340.
- [99] Tkalcíć, H., D. S. Dreger, G. R. Foulger, and B. R. Julian (2009), The puzzle of the 1996 Bárðarbunga, Iceland, earthquake: No volumetric component in the source mechanism, *Bull. Seism. Soc. Am.*, **99**(5), 3077–3085.
- [100] Wang, Y., Satake, K., Maeda, T., and Gusman, A. R. (2017), Green's function-based tsunami data assimilation: A fast data assimilation approach toward tsunami early warning. *Geophys., Res., Lett.*, **44**, 10,282– 10,289. <https://doi.org/10.1002/2017GL075307>
- [101] Wang, Y., Satake, K., Sandanbata, O., Maeda, T., and Su, H. (2019), Tsunami data assimilation of cabled ocean bottom pressure records for the 2015 Torishima volcanic tsunami earthquake. *J. Geophys. Res. Solid Earth*, **124**, 10,413–10,422. <https://doi.org/10.1029/2019JB018056>.
- [102] Watada, S. (2013), Tsunami speed variations in density-stratified compressible global oceans. *Geophys., Res., Lett.*, **40**, 4001–4006, <https://doi.org/10.1002/grl.50785>.

- [103] Watada, S., S. Kusumoto, and K. Satake (2014), Traveltime delay and initial phase reversal of distant tsunamis coupled with the self-gravitating elastic Earth, *J. Geophys. Res. Solid Earth*, **119**, 4287–4310, doi:10.1002/2013JB010841.
- [104] Ward, S. N. (1980), Relationships of tsunami generation and an earthquake source. *Journal of Physics of the Earth* **28.5**: 441-474.
- [105] Ward S.N. (1981), On tsunami nucleation: I. A point source, *J. Geophys. Res.*, **86**, 7895, 7900.
- [106] Ward, S. N. (1982), Earthquake mechanisms and tsunami generation: the Kurile Islands event of 13 October 1963, *Bull. Seism. Soc. Am.*, **72**, 759-777.
- [107] Wells, D. L., and Coppersmith, K. J. (1994), New empirical relationships among magnitude, rupture length, rupture width, rupture area, and surface displacement. *Bulletin of the seismological Society of America*, **84**(4), 974-1002.
- [108] Wilcock, W., Tolstoy, M., Waldhauser, F., Garcia, C., Tan, Y. J., Bohnenstiehl, D. R., et al. (2016), The 2015 eruption of Axial Seamount: Seismic constraints on caldera dynamics. *Science*, **354**(6318), 1395–1399. <https://doi.org/10.1126/science.aah5563>.

## Links

- [1] JAMSTEC, Deep Sea Floor Observatory off Muroto Cape, [http://www.jamstec.go.jp/scdc/top\\_j.html](http://www.jamstec.go.jp/scdc/top_j.html)
- [2] The Marine Information Research Center of the Japan Hydrographic Association, (<http://www.mirc.jha.or.jp>).
- [3] NIWA, <https://niwa.co.nz/our-science/oceans/bathymetry>.
- [4] LINZ, <https://data.linz.govt.nz/search/?q=Chart>.
- [5] Hydrographic and Oceanographic Department, Japan Coast Guard, Smith Rock (web page in Japanese language), <https://www1.kaiho.mlit.go.jp/GIJUTSUKOKUSAI/kaiikiDB/kaiyo15-2.htm>.
- [6] DART® (Deep-ocean Assessment and Reporting of Tsunamis), <https://nctr.pmel.noaa.gov/Dart/>

## *Data resources*

Fault parameters and slip amounts of slip models proposed for the 2015 Torishima and 2017 Curtis volcanic tsunami earthquakes proposed in this thesis can be downloaded from the link below:

[http://wwweic.eri.u-tokyo.ac.jp/repository/osm3\\_VTE/](http://wwweic.eri.u-tokyo.ac.jp/repository/osm3_VTE/).

# ***Appendix 1. Phase correction method for short-period tsunamis***

## **Abstract**

The speed of tsunamis is reduced by the density-stratification, compressibility of sea water, and the self-gravitational elastic Earth. Clear waveform changes such as travel time delays and phase reversals have been observed at far-field stations over ~3000 km for major earthquakes. Recent studies pointed out that the speed deviations changes waveforms of tsunamis with dominant long-period energy over 1,000 s. However, their effects on short-period tsunamis than 1000 s have not been discussed carefully. Here I show that the speed reduction effects are not negligible and even more important at period ranges shorter than 1,000 s. Waveform changes in short-period tsunamis become clear more quickly, or during shorter-distant propagation, in comparison to longer-period tsunamis, which is confirmed quantitatively by a one-dimensional synthetic test. I modified the phase correction method to incorporate the speed reduction effects into a numerical computation of short-period tsunamis. I apply this method to a case of a short-period tsunami model of the 2015 Torishima volcanic tsunami earthquake, south of Japan. The synthetic waves with the phase correction show clear travel time delays at over 500-km distant stations from the source. Our results suggest that the effects of the self-gravitating elastic Earth and density-stratified compressible ocean plays an important role for short-period tsunami propagations. As well as the speed reduction effects, a speed error inherent in the standard Boussinesq-type tsunami model is modulated by the method, which is verified by spectrogram analysis comparing synthetic and observed tsunamis. The modified phase correction method enables us to perform more accurate computations in linear formulations, which improves waveform analysis and inversions for short-period tsunami caused by intermediate shallow earthquakes, submarine landslides, or volcanic flank collapses.

### **A1.1. Introduction**

Tsunamis are generally caused by large-scaled sea-bottom phenomena such as large earthquakes in shallow crust and contain significant long-period wave energy over 1,000 s, such as the 1960 Great Chilean Earthquake and the 2011 Tohoku-Oki Earthquake. On the other hand, tsunamis with shorter-period wave energy less than 1,000 s can be generated by various source mechanisms, such as small or inter-mediate shallow earthquakes, submarine landslides, or collapses of a volcanic flank on

seashore [Glimsdal *et al.*, 2013]. Some landslides trigger large-amplitude tsunami waves which results in severe damages, and abnormal source processes sometimes generate short-period tsunamis around broad oceanic regions, such as the 2015 Torishima volcanic tsunami earthquakes [e.g. Fukao *et al.*, 2018; Sandanbata *et al.*, 2018; Wang *et al.*, 2019]. Hence, our needs to forecast wave propagations or investigate their source mechanisms make it important to model short-period tsunamis elaborately.

Short-period tsunamis have a highly dispersion property, which is inherent in waves propagating inviscid and incompressible ocean on rigid bottom [e.g. Glimsdal *et al.*, 2013]. The dispersion effect is larger in the shorter period range and after longer propagations. Many tsunami codes are modeled by the Boussinesq-type equations incorporating the dispersion property. Recent studies have developed numerical models with more accurate dispersion properties by formulating Nwogu's [1993] equations [e.g. Pedersen and Løvholt, 2008; Grilli *et al.*, 2007; Kirby *et al.*, 2013]. On the other hand, the so-called "standard Boussinesq equations," which were derived first by Peregrine [1972], have been often employed for tsunami simulations [e.g. Saito *et al.*, 2009; Baba *et al.*, 2015]. The equations show less accurate dispersion relations in short-wavelength (or short-period) ranges, because of the lower-order approximation of the dispersion terms [e.g. Dingemans, 1997; Nwogu, 1993]. This requires careful treatments particularly when the equations are applied to computations of short-period tsunamis.

In the last decade, apart from the pure dispersion property of tsunamis, several studies revealed non-negligible influences on tsunami speed reductions caused by compressible ocean, elasticity of the Earth, gravitational changes, and density stratification of sea water [e.g. Tsai *et al.*, 2013; Allegeyer and Cummins, 2014; Watada *et al.*, 2014; Ho *et al.*, 2017; 2019]. The speed reductions caused travel-time delays as large as 15 min and significant waveform changes at far-field stations over ~3,000 km away from tsunami source locations [e.g. Watada *et al.*, 2014]. Some studies successfully obtained more reliable source models for trans-pacific tsunamis by utilizing the far-field tsunami data [e.g. Ho *et al.*, 2017; 2019]. These successes showed the importance of the speed reduction effects for computations of long-period tsunamis propagating long distances. However, the reduction effects on short-period tsunamis less than 1,000 s were not carefully discussed and often were disregarded for modeling of short-period tsunamis [e.g. Fukao *et al.*, 2018].

The main purpose of this study is to examine the influence on short-period tsunamis of the speed reductions due to the self-gravitating elastic Earth with a density-stratified compressible ocean. A theoretical analysis including a one-dimensional numerical test showed that short-period tsunamis are actually influenced by the speed reductions, even more than long-period tsunamis are. In order to incorporate the effects, the phase correction method [Watada *et al.*, 2014; Ho *et al.*, 2017] is modified for short-period tsunamis and applied to a real-case tsunami model of the 2015 Torishima volcanic tsunami earthquake proposed by Fukao *et al.* [2018]. Then, I point out non-negligible changes in their waveforms and arrival times at distant stations.

Besides the main purpose, the application range of the standard Boussinesq equations is also studied. Spectrogram analysis reveals that tsunami models based on the equations have lower limits of the valid period range, while earlier phases of synthetic waves are properly computed with theoretical dispersion relations. It is suggested that our phase correction method are useful to obtain more accuracy in earlier phases of synthetic waves with better dispersion properties, although unreliability remained in the later phases.

## A1.2. Speed of short-period tsunamis

### A1.2.1. The Boussinesq approximation of the dispersion relations

Tsunami waves have dispersive properties, in other words, the phase speed of tsunami changes depending on its frequency component. For the problem of linear gravity waves propagating on inviscid and incompressible water with uniform depth, the dispersion relation of linear gravity wave (LGW) is expressed by

$$c_{LGW} = \frac{\omega}{k} = \sqrt{\frac{g}{k} \tanh kD}, \quad \text{Eq-A1. 1}$$

where  $\omega$  and  $k$  are frequency and wavenumber, and  $D$  is water depth [e.g. *Lamb, 1932; Dingemans, 1997*]. When the wavelength is sufficiently larger than water depth ( $kD \ll 1$ ), the long-wave approximation is valid, which leads to the non-dispersive phase speed of linear long wave (LLW) expressed as

$$c_{LLW} = \sqrt{gD}. \quad \text{Eq-A1. 2}$$

On the other hand, when tsunamis have shorter-period components and propagates long distance, it is important to consider the dispersion effects [*Glimsdal et al., 2013*]. In order to incorporate the dispersion effect into numerical models, the full dispersion relation of Eq-A1. 1 needs to be expanded in terms of  $kD$ ,

$$c_{LGW} = \sqrt{\frac{g}{k} \tanh kD} = 1 - \frac{1}{3}(kD)^2 + \frac{1}{15}(kD)^4 + O(kD)^6. \quad \text{Eq-A1. 3}$$

Although models such as *Nwogu [1993]* included the approximated form the  $O(kD)^4$  term, this requires complex formulations and long computation time. Therefore, most numerical models inherit the first two terms to compute tsunami waves. Common models are linear Boussinesq-type wave models derived from *Peregrine [1972]*. Equation-A1. 3 can be rewritten by

$$1 - \frac{1}{3}(kD)^2 + \frac{1}{15}(kD)^4 + O(kD)^6 = 1 - \frac{1}{3}(kD)^2 + O(kD)^4 = \frac{1}{1 + \frac{1}{3}(kD)^2} + O(kD)^4. \quad \text{Eq-A1. 4}$$

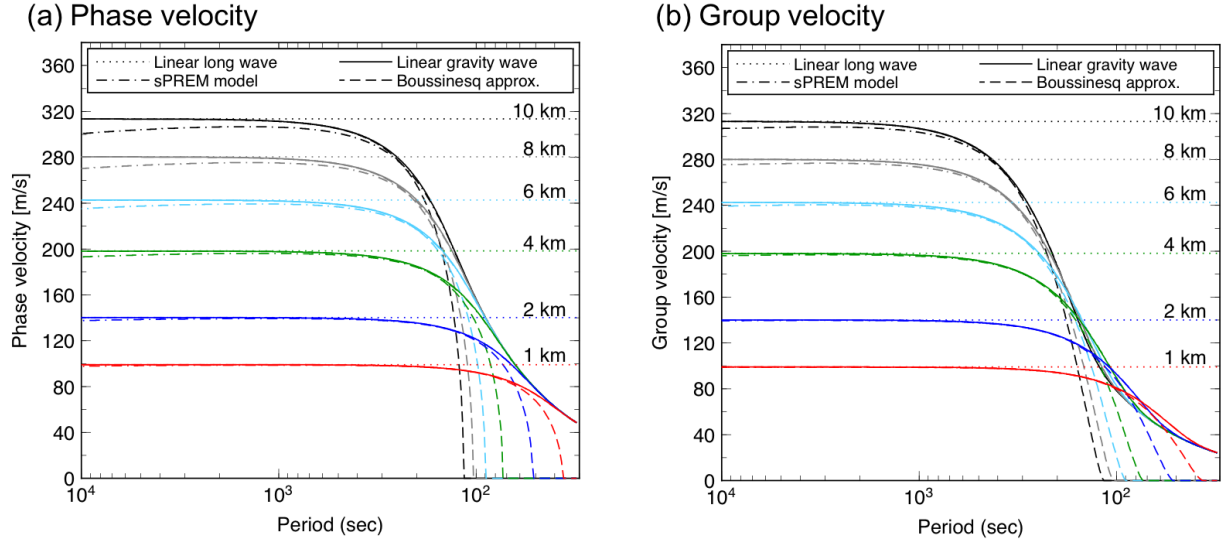


**Fig-A1.1 Phase and group speeds of different tsunami models**

(a) Phase speeds of different tsunami models. Dotted, solid, dashed-dotted, and dashed lines represent LLW, LGW, sPREM and LBW models, respectively. The numbers in kilometers shown on the right in the figure are water depths. When  $c_{LLW}$ ,  $c_{LGW}$  and  $c_{LBW}$  are computed, the gravitational accelerations values computed with sPREM models with different thicknesses of oceanic layers are used (i.e.  $g=9.8182$ ,  $9.8168$ ,  $9.8143$ ,  $9.8116$ ,  $9.8089$  and  $9.806$  m/s<sup>2</sup> at water depth of 1, 2, 4, 6, 8 and 10 km, respectively). (b) Group speeds of different tsunami models.

The dispersion relation is written in the following form;

$$c_{LBW} = \sqrt{\frac{g}{k} \tanh kD} = \sqrt{gD} \frac{1}{\sqrt{1 + \frac{1}{3}(kD)^2}}. \quad \text{Eq-A1.5}$$

By excluding the  $O(kD)^4$  terms, the phase speed is discrepant from the LGW speed at short periods. The equations are deployed by several tsunami codes such as *Saito et al.* [2010] and *Baba et al.* [2015].

I compute the dispersion curves of LGW and LBW models at uniform water depth to examine the effects the Boussinesq approximation disregarding the  $O(kD)^4$  in Eq-A1.4 (Fig-A1.1). The curves of LGW and LBW are overlapped to each other, when the wave period is long enough ( $kD \ll 1$ ). However, in the short-period range around 100 s, the phase speed of LBW is significantly reduced and shows large discrepancies from the LGW curve. The reduction is larger at the deeper water, which leads to zero speed. This indicates that the Boussinesq approximation causes significant travel-time delays of short-period wave energy, and that shortest-period energy do not propagate. Therefore, for numerical computations of short-period tsunamis propagating over deep oceans, the approximation errors need to be considered carefully.

#### A1.2.2. Speed reduction due to the self-gravitating elastic Earth with density-stratified compressible oceanic layer

The phase speeds were found to be reduced by the self-gravitating elastic Earth with density stratified oceanic layers. The effects are from (1) elasticity of the Earth, (2) compressibility of sea water, (3) gravity potential change and (4) density stratification of the ocean, all of which are not inherent in the dispersion relation of inviscid and incompressible water waves (Eq-A1. 1) [e.g. *Tsai et al.*, 2013, *Allgeyer and Cummins*, 2014, *Watada et al.*, 2014, *Ho et al.*, 2017]. *Watada et al.* [2014] developed the phase correction method including the speed reductions caused by the first three effects. *Ho et al.* [2017] calculated the phase speed of the PREM earth model with density-stratified ocean layer (stratified-PREM: sPREM) to additionally incorporate the fourth effect. Therefore, the sPREM tsunami model completely include the speed reduction effects of tsunamis mentioned above (i.e. tsunami dispersion, elasticity of the solid Earth, compressible seawater, gravitational change, and seawater density stratification). However, the reduction effects on shorter-period waves have not been discussed, because they focused on longer-period tsunamis ( $>1000$  s) [e.g. *Watada et al.*, 2014].

To investigate the reduction effects on shorter-period tsunamis, I compute the phase and group speeds of the sPREM tsunami model ( $c_{sPREM}$ ) by applying the normal mode theory to sPREM model [*Ho et al.*, 2017], and compare it with the speed of the LGW model ( $c_{LGW}$ ) (Fig-A1.1). Discrepancies in phase speeds between sPREM and LGW are large in long-period range ( $T > \sim 1000$  s), while difference is smaller at short-period range ( $T < \sim 1000$  s) (Fig-A1.2a). However, for the technical purposes of tsunami simulations such as waveform analysis or tsunami inversions, travel time delays relative to their dominant period are more important than the absolute values of speed differences. To quantify the relative travel time delays caused by the reduction effects, I compared a travel time delay normalized by wave period at uniform depth by the formula;

$$\Delta T = \left( \frac{L}{c_{sPREM}(\omega, D)} - \frac{L}{c_{LGW}(\omega, D)} \right) \times \frac{1}{T} \times 100 [\%] \quad \text{Eq-A1. 6}$$

$$= L \times \frac{\Delta c(\omega, D)}{c_{LGW}(\omega, D) - c_{sPREM}(\omega, D)} \times \frac{2\pi}{\omega} \times 100 [\%], \quad \text{Eq-A1. 7}$$

where  $T = 2\pi/\omega$  is wave period,  $\Delta c(\omega, D)$  is the absolute discrepancy of LGW and sPREM speed, and  $L$  is the propagation distance in kilometer. In Fig. A1-2b, normalized travel time differences after 100-km propagation are shown. In the short-period range, the normalized travel time delays are larger at every water depth, while smaller at long-period ranges. For example, tsunami with a period of 100 s has a normalized travel time delay of  $\sim 1.4$  % after 100 km propagation over 1-km water depth, which results in clear delay of 10 % of wave period only after  $\sim 710$  km propagation. On the other hand, the normalized travel-time delay with a period of 1,000 s is only 0.3 % of the period, which required  $\sim 3,300$  km propagation to reach travel time delay of 10 % of the period. Therefore, tsunamis with dominant shorter-period components are expected to show clear travel time delay and waveform change even at shorter distant stations less than 1,000 km away from the source, while the delay effect on long-period tsunamis are clear only at distant stations away from tsunami source. This is consistent with the fact that clear

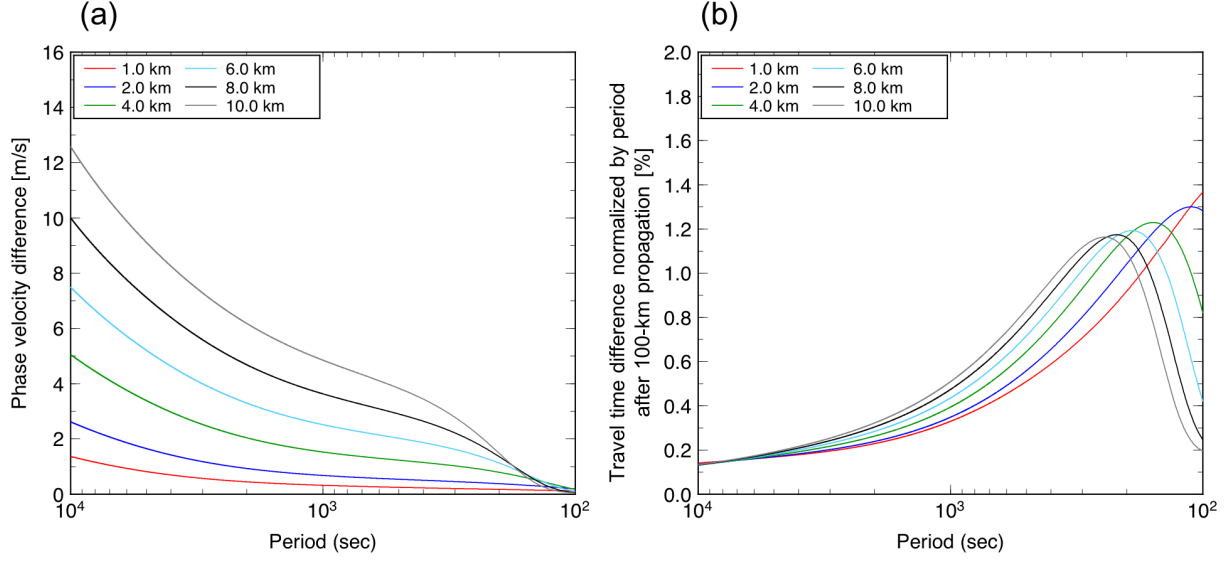


**Fig-A1.2 Speed reduction effects due to the self-gravitating elastic Earth with density-stratified compressible ocean**

(a) Phase speed discrepancy between LGW and sPREM models,  $c_{LGW} - c_{sPREM}$ , at uniform water depth. (b) Travel time delay normalized by wave period after 100-km propagation at uniform depth (see Eq-A1. 7).

tsunami waveform changes due to the reduction effects were observed only at far-fields stations over 2,800 km away from the epicenter of the 2011 Tohoku tsunami [e.g. *Ho et al.*, 2017].

To confirm the nonnegligible effects of the speed reductions on short-period tsunamis, I synthesize 1-D propagations of tsunamis with and without the effects. I assume that tsunami waves travel in the positive  $x$  direction with two types of tsunami speeds,  $c_{LGW}$  and  $c_{sPREM}$ , and compared waveforms at  $x=500, 1000, 2000,$  and  $4000$  km. The differences between the two waveforms can be regarded as the speed reduction effects during the propagations in the distances. The waveform  $u(x, t)$  observed at distance  $x$  and time  $t$  can be expressed as

$$u(x, t) = \frac{1}{\pi} \int_0^{\infty} \hat{u}(x, \omega) \cos(\Psi(x, \omega)) d\omega, \quad \text{Eq-A1. 8}$$

where  $\hat{u}(x, \omega)$  is the amplitude spectrum and  $\Psi(x, \omega)$  is the phase spectrum, which is expressed as

$$\Psi(x, \omega) = \omega t + \Psi_0 - \frac{\omega x}{c(\omega)}, \quad \text{Eq-A1. 9}$$

where  $\Psi_0 = \Psi(0, \omega) + 2\pi N$  is the initial phase spectrum at  $x=0$  and  $t=0$ , and  $N$  is an integer of phase uncertainty. The initial waveforms are assumed as

$$u(0, t) = 0.5 \times \left[ \exp\{-2\pi f(t - t_0)^2\} - \exp\left\{-2\pi f \left( t - \left( t_0 + \frac{0.4}{f_0} \right) \right)^2 \right\} \right], \quad \text{Eq-A1. 10}$$

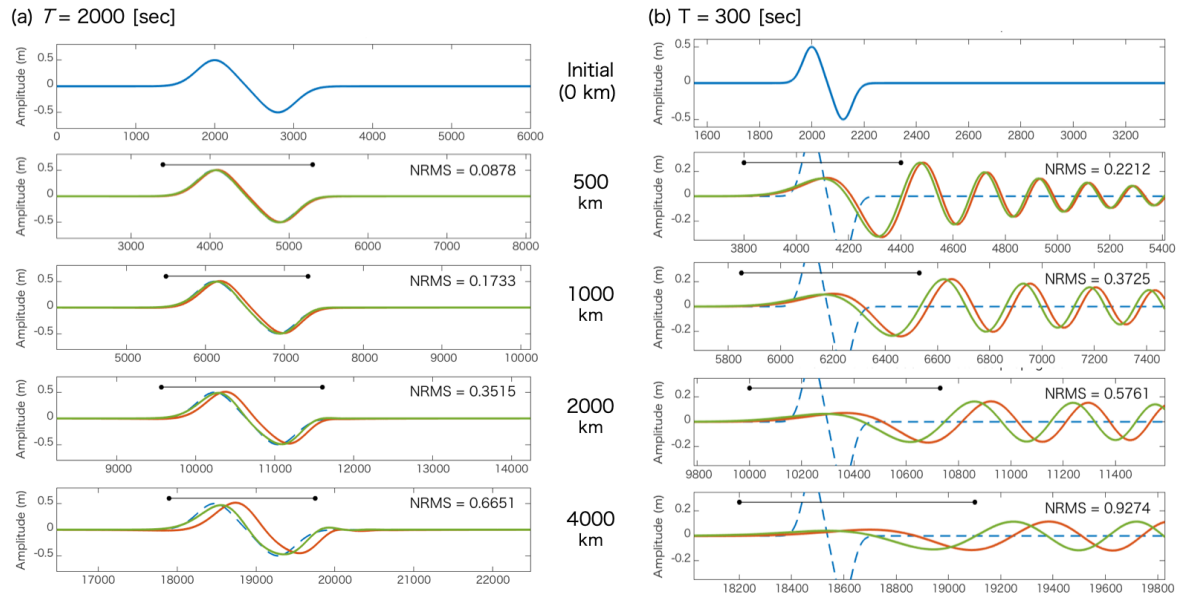


**Fig-A1.3 One-dimensional tests of tsunami propagations with and without the sPREM effects**

One-dimensional synthetic tests of (a) long-period tsunamis with 2000 s and (2) short-period tsunami with 300 s. From top to bottom figures, initial waveforms at  $x=0$  km, synthetic waveforms at  $x=500$  km, 1000 km, 2000 km, and 4000 km are shown, respectively. Blue, red, and green lines represent tsunami waveforms of the LLW, sPREM and LBW models.

where  $t_0 = 2000$  s. To compare the speed effects on tsunamis with different dominant periods,  $f$  is assumed as 0.0005 Hz ( $T=2000$  s) and 0.00333 Hz ( $T=300$  s) for long- and short-period tsunamis, respectively.

Figure A1.3 compares 1-D tsunami waveforms with wave periods of 2000 s and 300 s at different propagation distances. Compared to long-period tsunamis with 2000-sec wave period, short-period tsunamis show clear waveform differences between two types of waves propagating with  $c_{LGW}$  and  $c_{sPREM}$  even at  $x=1,000$  km. This indicates that waveforms of short-period tsunamis are more affected by the speed reduction effects. The NRMS (normalized root-mean-square) misfits between the LGW and sPREM waveforms calculated in time window including the first crest and trough mark larger values for short-period tsunamis at every distance. Therefore, it also suggests a significance of incorporation of the speed reduction effects into short-period tsunami computations.

### A1.3. Phase correction method for short-period tsunamis: The 2015 Torishima volcanic tsunami earthquake

I here develop a new tsunami computation method for short-period tsunamis to examine influences of the speed reduction effects due to the self-gravitating elastic Earth with density-stratified compressible oceanic layer on a real-case of a short-period tsunami event, the 2015 Torishima volcanic tsunami earthquake. The method is composed of the following three procedures; (1) numerically compute

tsunami propagations by solving the linear standard Boussinesq equations, (2) perform a phase correction method on the synthetic waves to obtain waveforms with the dispersion relation of the sPREM model.

The phase correction method is a noble method to compute tsunami waveforms including the speed reduction effects [Watada *et al.*, 2014; Ho *et al.*, 2017]. In the previous methods, reference synthetic tsunamis are first computed with the LLW model, and their phase spectrum are corrected as their dispersion relation fits that of a target tsunami model. Watada *et al.* [2014] successfully incorporate the speed reductions the elasticity of the solid Earth, compressibility of seawater, and gravitational potential change, as well as the tsunami dispersion. Ho *et al.* [2017] improved the method by including the effects of seawater density stratification and water depth on the bending ray paths to succeed to compute tsunamis based on the sPREM model. However, the previous methods stood on an assumption that a target tsunami model has similar phase speeds to those of the reference model. As shown in Fig-A1.1, the phase speeds of the sPREM model is significantly deviated from the LLW model in short-period ranges  $< \sim 1000$  s, which makes the methods inapplicable directly to short-period tsunamis.

To overcome the problem, I propose a new phase correction method to implement short-period tsunami computations with the sPREM model. In the new method, phase corrections are performed on phase spectrum of synthetic waveforms computed with the LBW model, instead of the LLW model. By using the LBW model with more accurate dispersion curves, the assumption of small speed differences between the reference and target sPREM model is satisfied even in short-period ranges.

In addition to the incorporations of the speed reduction effects, the method is advantageous in that the computational errors caused by the Boussinesq approximation of the dispersion relation. As discussed in A1.2.1, the LBW model breaks out in the shortest-period ranges, which causes computational errors in short-period components. By correcting the phase spectrum of synthetic tsunamis of the LBW model to the sPREM, it is possible to correct the computational errors due to the Boussinesq approximation of the dispersion relation.

For the practical application of the new method, I here conduct a case study with a short-period tsunami event caused by the 2015 Torishima volcanic tsunami earthquakes [Sandarbata *et al.*, 2018; Fukao *et al.*, 2018; Wang *et al.*, 2019]. The earthquake had an intermediate magnitude  $M_w$  5.7 [GCMT] but generated large-amplitude tsunamis, which was attributed to an abnormally large uplift (over one meter) of a submarine volcanic caldera with about 8-km diameter, Smith Caldera by Fukao *et al.* [2018] (see Chapter 2). Due to its large seafloor uplift with a small source size, the tsunami had dominant short-period energy ranging from 100 to 500 s [Sandarbata *et al.*, 2018]. The tsunami was recorded by different networks of deep ocean bottom pressure gauges in a broad region: a temporal array [Fukao *et al.*, 2018], the DONET system, the Deep Sea Floor Observatory (DSFO) off Muroto Cape, and the DART system (Fig. 3.1). Because epicentral distances of the stations ranges from 90 km to 1,430 km, the earthquake is a good example to examine how the speed deviations and the approximation error of the Boussinesq approximation influence synthetic waveforms after different traveling distances. Among of the stations, I

focused on for stations, A05 from the array (105 km), KMB08 from the DONET (377 km), PG02 from the DSFO (551 km), and 52402 from the DART system (1,430 km) (Fig. 3.1). It is noted that I do not aim for waveform fitting of synthetic and observed waves, but for examination of the effects on tsunami waveforms.

#### A1.3.1. Numerical simulation of the LBW model

I first numerically computed tsunami propagations from the axially symmetrical tsunami source model of the 2015 Torishima earthquake (Eq. 2.5; Fig. 2.6b). The model consists of a central major uplift (1.5 m at maximum) and peripheral minor depression (~15 cm) covering the submarine caldera, Smith Caldera (Fig. 2.6b). The computation was performed with the JAGURS code [Baba *et al.*, 2015] employing the standard Boussinesq equations (Eqs. 2.6–2.8). The bathymetry is composed of 30-arcsec spacing JTOPO30 data covering the broad region and high-resolution 10-arcsec data from M7000 series around Smith Caldera and Aogashima Island (Fig. 3.1). The computation time step was 0.25 s as it satisfies the CFL condition of the finite difference numerical scheme, while spatial sea-surface wavefields were outputted every 5.0 s.

To compare sea-surface height of tsunami with the ocean bottom pressure records, attenuations of pressure perturbation at deep water need to be considered [Chikasada, 2019]. Following the method proposed by Chikasada [2019], I performed the Kaiura's filter ( $1/\cosh kD$ ) [Kajiura, 1963] on the outputted wavefields around stations, and then obtained synthetic waveforms of pressure changes at ocean bottom depth, which were comparable to the observed pressure records.

#### A1.3.2. Phase correction for short-period tsunamis

Next, I corrected the phase spectrum of the synesthetic waveforms at the four stations. Following the Watada *et al.* [2014] method, tsunami waveform  $u(x, y)$  observed at location  $(x, y)$  and time  $t$  is expressed in the frequency domain by

$$u(x, y, t) = \frac{1}{\pi} \int_0^{\infty} \hat{u}(x, y, \omega) \cos(\Psi(x, y, \omega)) d\omega, \quad \text{Eq-A1. 11}$$

where  $\hat{u}(x, y, \omega)$  is the amplitude spectrum, and  $\Psi(x, y, \omega)$  is the phase spectra, which is expressed by

$$\Psi(x, y, \omega) = \omega t + \Psi_0(\omega) - \frac{(\mathbf{e}\cdot\mathbf{r})\omega}{c(\omega, D(x, y))}, \quad \text{Eq-A1. 12}$$

where  $c(\omega, D(x, y))$  and  $e$  are the phase speed and the unit vector along the wavenumber vector at location  $\mathbf{r} = (x, y)$  over an ocean of depth  $D(x, y)$  with angular frequency  $\omega$ , respectively, and  $\Psi_0$  is the initial phase. If ray paths of tsunamis of the sPREM and LBW models are similar, the phase difference  $\Delta\Psi(x, y, \omega)$  of the two models at a station located at  $(x, y)$  is expressed as

$$\Delta\Psi(x, y, \omega) = \Psi_{LBW}(x, y, \omega) - \Psi_{sPREM}(x, y, \omega), \quad \text{Eq-A1. 13}$$

where  $\Psi_{LBW}(x, y, \omega)$  and  $\Psi_{SPREM}(x, y, \omega)$  are the phase spectrum of tsunami waveforms a station located at  $(x, y)$ . The phase difference accumulating during a propagation over small distance  $d\mathbf{s} = \sqrt{dx^2 + dy^2}$  is written by

$$\Delta\Psi(dx, dy, \omega) = \frac{c_{SPREM}(D(x, y), \omega) - c_{LBW}(D(x, y), \omega)}{c_{SPREM}(D(x, y), \omega) \times c_{LBW}(D(x, y), \omega)} \omega d\mathbf{s} \quad \text{Eq-A1. 14}$$

$$= \frac{\Delta c(D(x, y), \omega)}{c_{SPREM}(D(x, y), \omega) \times c_{LBW}(D(x, y), \omega)} \omega d\mathbf{s}. \quad \text{Eq-A1. 15}$$

The phase difference defined by the previous methods [Watada *et al.*, 2014; Ho *et al.*, 2017] was simpler than Eq-A1. 15, because the phase speed difference  $\Delta c$  between the LLW and PREM speed is small enough for simplification (Eq. 14 in Watada *et al.* [2014]). However, because  $|\Delta c/c_{SPREM}| = |(c_{SPREM} - c_{LBW})/c_{SPREM}|$  is large in shorter-period ranges, the approximation is not valid any more, which leaves the equation complicated.

Finally, the phase correction term  $\Delta\Psi(x, y, \omega)$  accumulating during the propagation from a source to a station is expressed as

$$\Delta\Psi(dx, dy, \omega) = \int_{path} \Delta\Psi(dx, dy, \omega) = \int_{path} \frac{\Delta c(D(x, y), \omega)}{c_{SPREM}(D(x, y), \omega) \cdot c_{LBW}(D(x, y), \omega)} \omega d\mathbf{s}. \quad \text{Eq-A1. 16}$$

By correcting the phase spectrum of synthetic tsunami waveforms of the LBW model, tsunami waveforms of the sPREM model, including the speed reduction effects and eliminating the computational errors due to the Boussinesq approximation are obtained.

To obtain ray paths at different frequencies, I traced ray paths of tsunamis with periods of 100, 200, 300, 500, 1000 and 2000 s propagating at a speed of  $c_{LGW}$  by using the ray tracing method of dispersive tsunamis [Sandarbata *et al.*, 2018]. First, I transformed the bathymetry data smoothed by a 250-km Gaussian spatial filter to the speed field of LGW model by the iterative method. Instead of the shooting method used by the previous study, I took a similar approach suggested by Ho *et al.* [2017] to trace ray paths. I first computed spatial fields of tsunami travel-times of dispersive waves with different periods from the source to a station ( $t_a$ ), and from a station to the source ( $t_b$ ) by the fast-marching method [Rickett and Fomel, 1999; Alkhalifah, 1998]. The shortest travel-time path was found by tracing with points a minimum value of  $t_a + t_b$ . A moving filter averaging five data was used twice along the ray path to smooth zig-zag paths. I assumed a point source at the center of Smith Caldera (31.485°N, 140.048°E).

The phase correction term (Eq-A1. 16) were evaluated in the frequency domain along the ray path with a closest period among 100, 200, 300, 500, 1000 and 2000 s at each period. At every point of ray paths from a source to stations, the phase shift was computed with  $c_{SPREM}(D(x, y), \omega)$  and  $c_{LBW}(D(x, y), \omega)$ .  $c_{SPREM}$  was computed by interpolating the dispersion curve of sPREM model at water

depth of 0.1, 1.0, 2.0, 4.0, 6.0, 8.0 and 10 km with fitting a spline curve, while  $c_{LBW}$  was computed by the iterative method [Sandarbata *et al.*, 2018].

#### A1.4. Results and discussion

As a result, I obtained synthetic tsunami waveforms of the sPREM model at the four stations, which is compared with waveforms of the LBW model in Fig-A1.4. As stations are further from the source, leading waves of the sPREM model is more delayed than those of the LBW model, which can be attributed to the speed reductions caused by the self-gravitating elastic Earth with density stratified oceanic layers. As expected by 1-D test, the speed reduction effects clearly affect short-period tsunamis even in propagation distance around 1,000 km, while waveform changes of long-period tsunamis caused by the 2011 Tohoku-Oki earthquake were observed stations further than ~3,000 km [Ho *et al.*, 2017]. This indicates that the speed reductions are required to be incorporated when short-period tsunamis propagate in distance around 1,000 km.

On the other hand, following waves of the sPREM model show earlier arrivals of shorter-period energy at A05, KMB08, and PG02 stations, compared to the LBW model. These waveform changes are caused by corrections of computational errors due to the Boussinesq approximation. Because the phase correction method corrects the underestimated phase speed of the LBW model in short-period ranges, the following waves also computed more accurately.

To confirm the validity of the corrected waveforms, I conducted the spectrogram analysis on the synthetic waveforms of the sPREM and LBW models, and the observed waveforms. The spectral amplitude at successive time window with 1,000-s data length are obtained for 0-1,0000 s after the earthquake origin time. I also predicted arrival times of the group speeds of the sPREM, LGW and LBW tsunami models by

$$T_g(x, y, \omega) = \int_{path} \frac{ds}{c_g^m(D(x,y), \omega)}, \quad \text{Eq-A1. 17}$$

where  $c_g$  is the group speed with a superscript  $m$  indicating tsunami models (sPREM, LGW, or LBW), which were computed in the same way for the ray tracing (see A1.3.2). The arrival time of the group speed is equivalent to arrival times energy with different periods, which enables to validate dispersion properties of synthetic tsunamis from the predictions.

Figure A1.5 compare the spectrograms of the observed and synthetic waveforms at KMB08 station with the predicted arrival times of the group speeds. The spectrogram of the observed waves shows energy peak consistent with the predicted curve of the sPREM and LGW models at every wave period. It is reasonable because they are more accurate model. On the other hand, the spectrogram of the synthetic waveform of the LBW model show that the energy in short-period range are significantly delayed compared to arrival times of the observed energy. This demonstrates that the synthetic waveforms of the LBW model are inaccurate in the later phases due to the approximation error.

The spectrogram of the sPREM model was obtained from that of the LBW model with the phase correction (Fig-A1.5c). The delayed energy arrival seen in the LBW model is significantly improved and fits well to the observations and predicted arrival times. The arrival time shift of the high-frequency energy results in the waveform change found in the waveform (Fig-A1.4c). Therefore, it is confirmed that the phase correction method improved the accuracy of tsunami computations of short-period tsunamis.

However, the spectrogram implies a limitation of the phase correction method based on the synthetic waveforms of the LBW model. Because the LBW model have greatly underestimated speed at shortest periods, the wave energy does not propagate to stations. In such cases, it is impossible to correct the waveforms in the period range. In addition, the nearly-zero speed of the LBW model at shortest period can cause divergence of the phase correction term (Eq-A1. 16), which result in overestimation of travel time shift as seen in the spectrogram of the sPREM model at  $\sim 100$  s (Fig-A1.5). Therefore, it is appropriate to filter out energy in shortest period ranges with the nearly-zero speed. As seen in Fig-A1.1, the period range with nearly-zero speed is wider at deeper water. Therefore, to compare the phase corrected waveforms with the observed waveforms, it is appropriate to remove the nearly-zero speed range of the LBW model measured at the maximum depth along a ray path.

### A1.5. Conclusions

In this Appendix, by focusing on short-period tsunamis, I demonstrated that the speed reductions due to the self-gravitating elastic Earth with density stratified oceanic layers influence waveforms and arrival times of short-period tsunamis ( $< \sim 1000$  s) more largely than it was expected before. I also pointed out the Boussinesq approximation employed in the classical formulations of tsunami propagations, the linear Boussinesq equations, cause large computational errors particularly in the following shortest-period energy.

In order to incorporate the speed reduction effects and to correct the

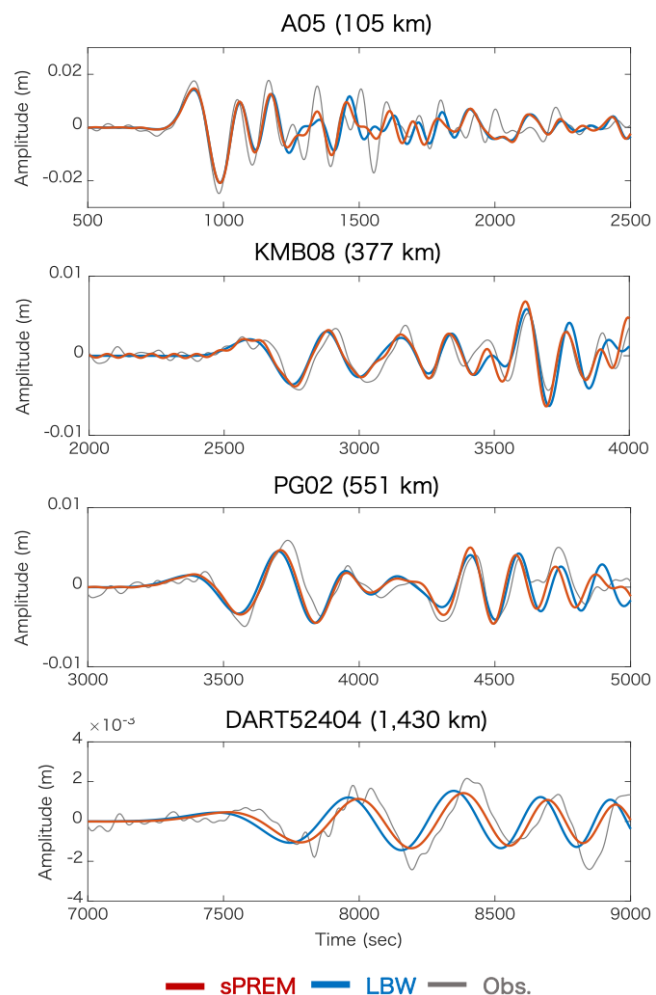


**Fig-A1.4 Comparison of synthetic waveforms with and without the phase correction**

Synthetic waveforms of the sPREM model (red) and the LBW model (blue). Gray line represents observed waveforms.

computational errors, I developed a new phase correction method. In the method, the phase spectrum of synthetic waveforms computed with the linear Boussinesq equations is corrected, instead of those computed by the linear long-wave equations in the previous methods. The new method successfully predicted travel-time delays of leading waves due to the speed reduction effects. In addition, travel-time delays of the short-period energy due to the errors of the Boussinesq approximations can be corrected, whose validities was confirmed by the spectrogram analysis comparing the observed waveforms. Such nonnegligible effects of the speed reductions and the errors inherent in the classical formulations need to be taken into account carefully. The new method enables us to improve tsunami predictions and conduct more accurate and reliable source analysis of short-period tsunamis, such as submarine landslide, or small-scaled earthquakes.

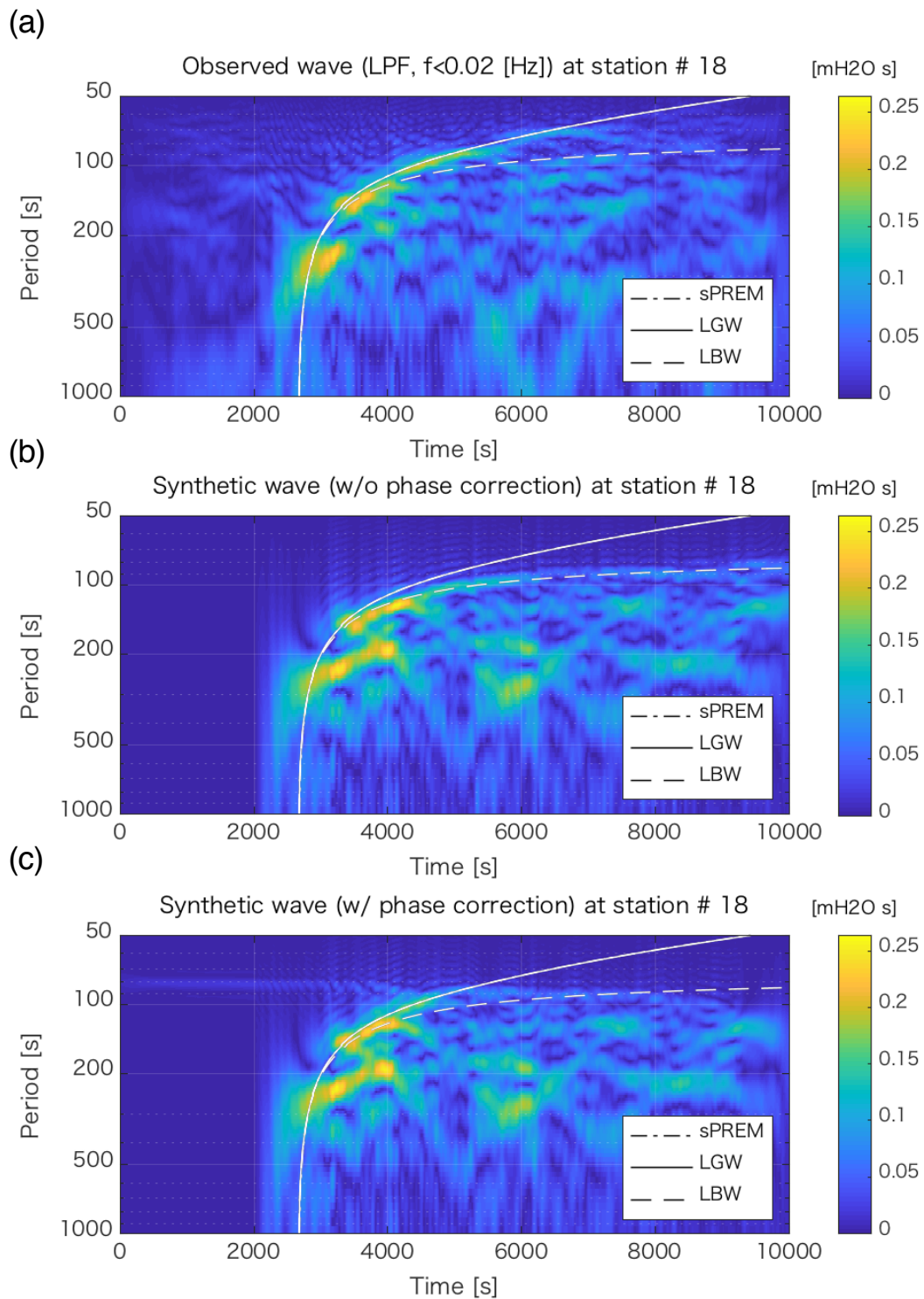


**Fig-A1.5 Spectrogram analysis at KMB08 station**

Spectrogram of (top) observed waveforms, (b) synthetic waveforms of the LBW model and (c) the sPREM model. White lines show predicted arrival times of the group speeds of the sPREM, LGW and LBW models. Note that the curve of the sPREM and LGW models are almost overlapped.

## References

- [1] Ablowitz, M. J. (2011). *Nonlinear Dispersive Waves: Asymptotic Analysis and Solitons*, Cambridge Univ. Press, Cambridge, U. K.
- [2] Alkhalifah, T. (1998). The fast marching method in spherical coordinates: Seg/eage salt-dome model. *Stanford Exploration Project*, SEP-97, pages 251–264.
- [3] Allgeyer, S., and Cummins, P. (2014). Numerical tsunami simulation including elastic loading and seawater density stratification. *Geophys. Res. Let.*, 41, 2368–2375.  
<https://doi.org/10.1002/2014GL059348>.
- [4] Baba, T., Takahashi, N., Kaneda, Y., Ando, K., Matsuoka, D., and Kato, T. (2015). Parallel implementation of dispersive tsunami wave modeling with a nesting algorithm for the 2011 Tohoku tsunami. *Pure and Applied Geophysics*, 172(12), 3455–3472. <https://doi.org/10.1007/s00024-015-1049-2>.
- [5] Chikasada, N. Y. (2019). Short-Wavelength Tsunami Observation Using Deep Ocean Bottom Pressure Gauges, International Society of Offshore and Polar Engineers, <https://www.onepetro.org/conference-paper/ISOPE-I-19-707>.
- [6] Dingemans, M. W. (1997). *Water wave propagation over uneven bottoms, part 1, linear wave propagation* (vol. 13). Advanced series on ocean engineering. River Edge: World Science Publishing.
- [7] Fukao, Y., Sandanbata, O., Sugioka, H., Ito, A., Shiobara, H., Watada, S., and Satake, K. (2018). Mechanism of the 2015 volcanic tsunami earthquake near Torishima, Japan. *Science Advances*, 4(4), eaa0219.
- [8] Glimsdal, S., Pedersen, G., Harbitz, C., and Løvholt, F. (2013). Dispersion of tsunamis: Does it really matter? *Natural Hazards and Earth Systems Sciences*, 13, 1507–1526.
- [9] Ho, T.-C., Satake, K., and Watada, S. (2017). Improved phase corrections for transoceanic tsunami data in spatial and temporal source estimation: Application to the 2011 Tohoku earthquake. *Journal of Geophysical Research: Solid Earth*, 122, 10,155–10,175. <https://doi.org/10.1002/2017JB015070>
- [10] Ho, T.-C., Satake, K., Watada, S., and Fujii, Y. (2019). Source estimate for the 1960 Chile earthquake from joint inversion of geodetic and transoceanic tsunami data. *Journal of Geophysical Research: Solid Earth*, 124. <https://doi.org/10.1029/2018JB016996>.
- [11] Kajiura, K. (1963). The leading wave of a tsunami, *Bull. Earthquake Res. Institute*, 41, 545–571.
- [12] Kirby, J., Shi, F., Tehranirad, B., Harris, J., and Grilli, S. T. (2013). Dispersive tsunami waves in the ocean: Model equations and sensitivity to dispersion and Coriolis effects, *Ocean Model.*, 62, 39–55.
- [13] Lamb, H. (1932). *Hydrodynamics* (6th ed.). Cambridge: Cambridge University Press.
- [14] Nwogu, O.: Alternative Form of Boussinesq Equations for Nearshore Wave Propagation, *J. Waterw. Port Coast. Ocean Eng.*, 119, 618–638, 1993.
- [15] Pedersen, G. and Løvholt, F. (2008). Documentation of a global Boussinesq solver, Preprint Series in Applied Mathematics 1, Dept. of Mathematics, University of Oslo, Norway, available at: <http://urn.nb.no/URN:NBN:no-27775>.

- [16] Peregrine, H. (1972). Equations for water waves and the approximations behind them, edited by R. E. Meyer, pp. 95–121, *Waves on Beaches and Resulting Sediment Transport*, Academic Press, New York.
- [17] Rickett, J., Fomel, S. A. (1999). Second-order fast marching eikonal solver, Stanford Exploration Project SEP100, Report SERGEY, Stanford University, Stanford, CA. 509-514.
- [18] Saito, T., and T. Furumura (2009). Three-dimensional simulation of tsunami generation and propagation: Application to intraplate events, *J. Geophys. Res. Oceans*, 114, B02307, doi:10.1029/2007JB005523.
- [19] Saito, T., Satake, K., and Furumura, T. (2010). Tsunami waveform inversion including dispersive waves: The 2004 earthquake off Kii Peninsula, Japan. *Journal of Geophysical Research*, 115, B06303. <https://doi.org/10.1029/2009JB006884>.
- [20] Sandanbata, O., S. Watada, K. Satake, Y. Fukao, H. Sugioka, A. Ito, and H. Shiobara (2018). Ray tracing for dispersive tsunamis and source amplitude estimation based on Green's law: Application to the 2015 volcanic tsunami earthquake near Torishima, south of Japan, *Pure Appl. Geophys.*, 175 4, DOI: 10.1007/s00024-017-1746-0, 1371-1385.
- [21] Tsai, V. C., Ampuero, J. P., Kanamori, H., and Stevenson, D. J. (2013). Estimating the effect of Earth elasticity and variable water density on tsunami speeds. *Geophysical Research Letters*, 40, 492–496. <https://doi.org/10.1002/grl.50147>
- [22] Watada, S., Kusumoto, S., and Satake, K. (2014). Traveltime delay and initial phase reversal of distant tsunamis coupled with the self-gravitating elastic Earth. *Journal of Geophysical Research: Solid Earth*, 119, 4287–4310. <https://doi.org/10.1002/2013JB010841>.

## ***Appendix 2. Moment tensor inversion using W-phases of seismic waves***

In this Appendix, model performances of the moment-tensor inversion using W-phase of seismic waves of the 2015 Torishima and 2017 Curtis volcanic tsunami earthquakes are shown. Only the data used for the MT inversion are shown here.

### **A2.1. The 2015 Torishima volcanic tsunami earthquake**

See Chapter 5.2.2 for the detail of the MT inversion including the method and results. The moment tensor solution is shown in Fig. 5.7.

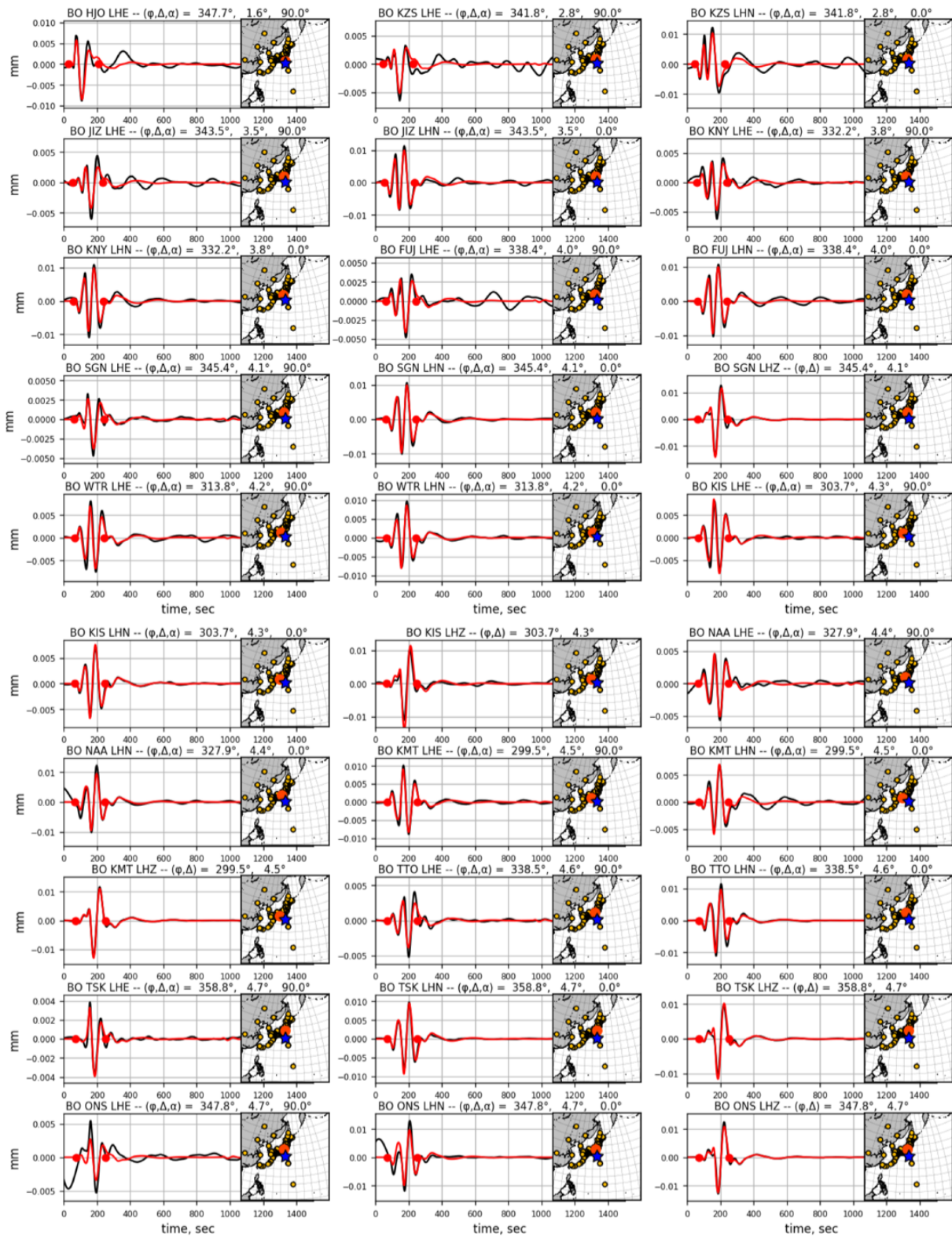


**Fig-A2.1 Model performances of the MT inversion for the 2015 Torishima volcanic tsunami earthquake (1/6)**

W-phase time windows indicated by red circles are used for the inversion. Only waveforms used for the MT inversion are shown. Red and black lines represent synthetic and observed waveforms, respectively. Blue star and big orange circle represent locations of the epicenter (Smith Caldera) and a station, in inset figures.

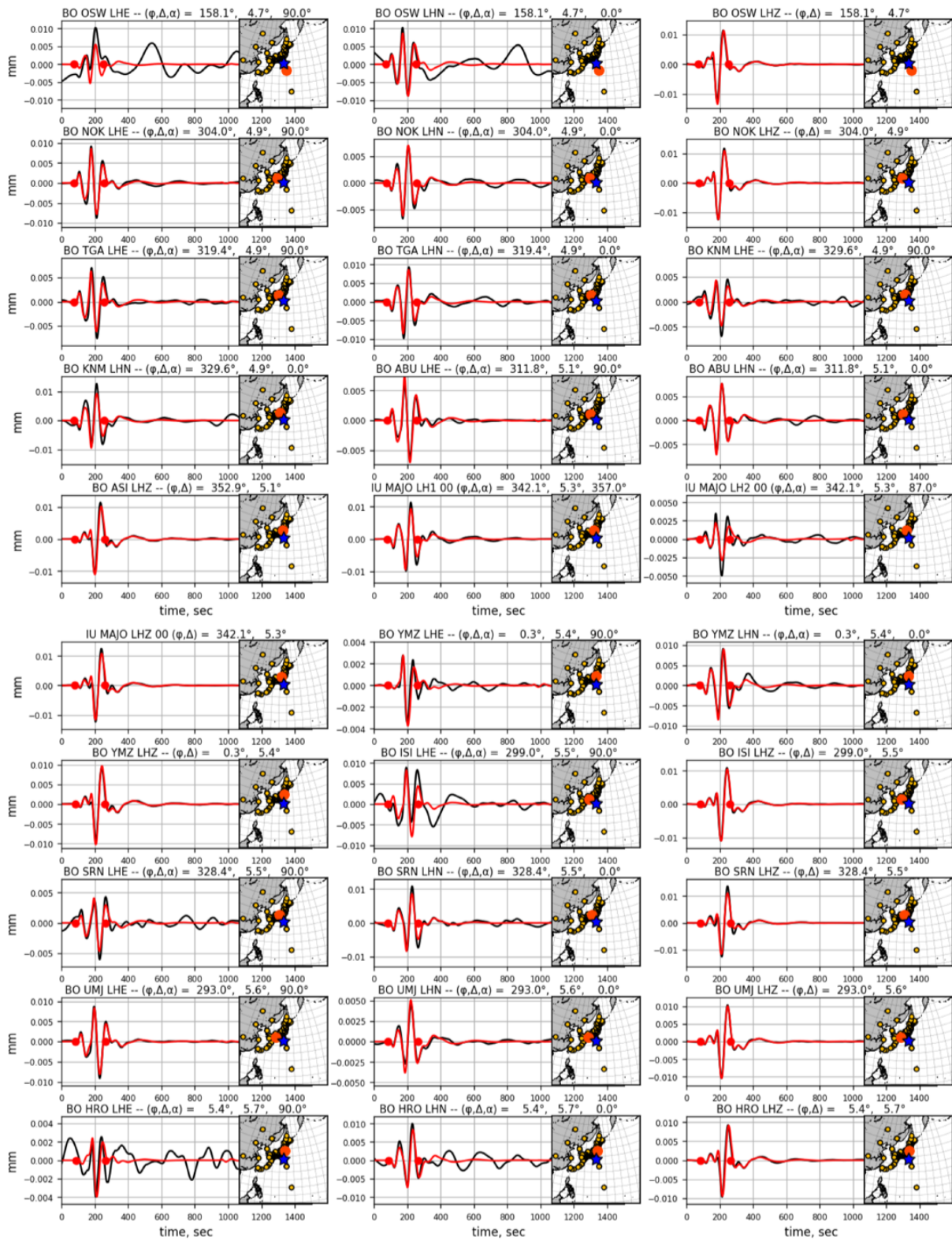


Fig-A2.1 (Continued: 2/6)

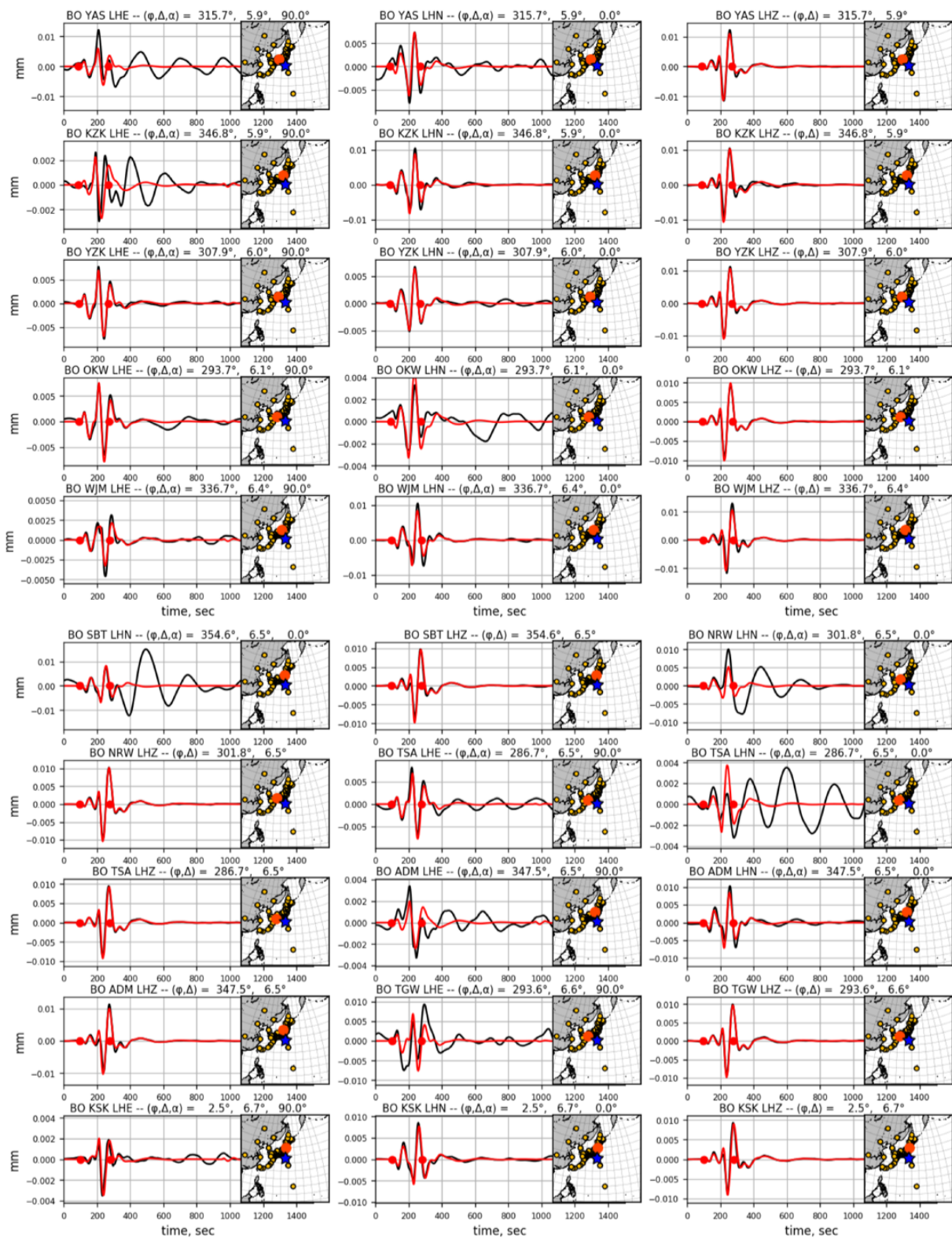


Fig-A2.1 (Continued: 3/6)

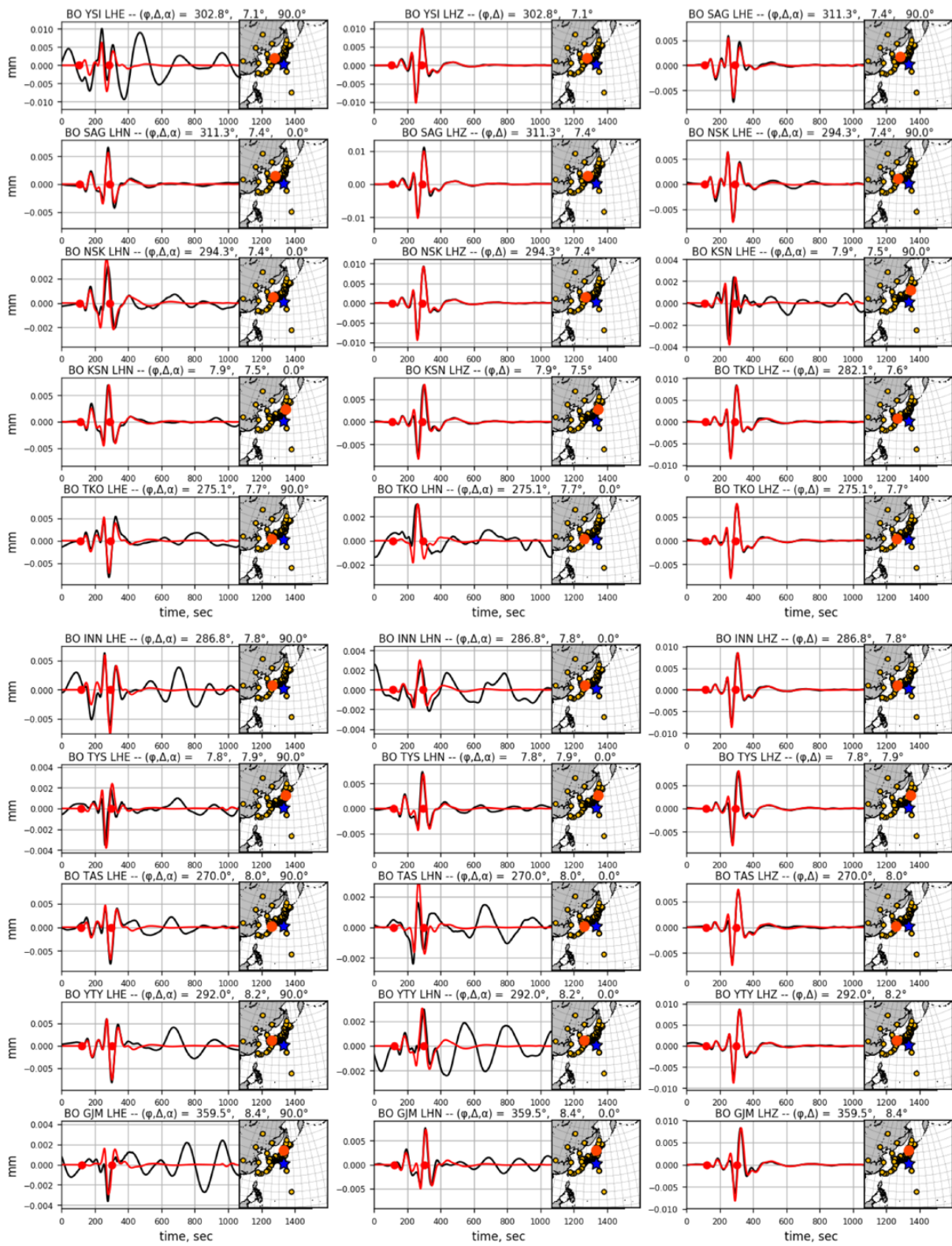


Fig-A2.1 (Continued: 4/6)

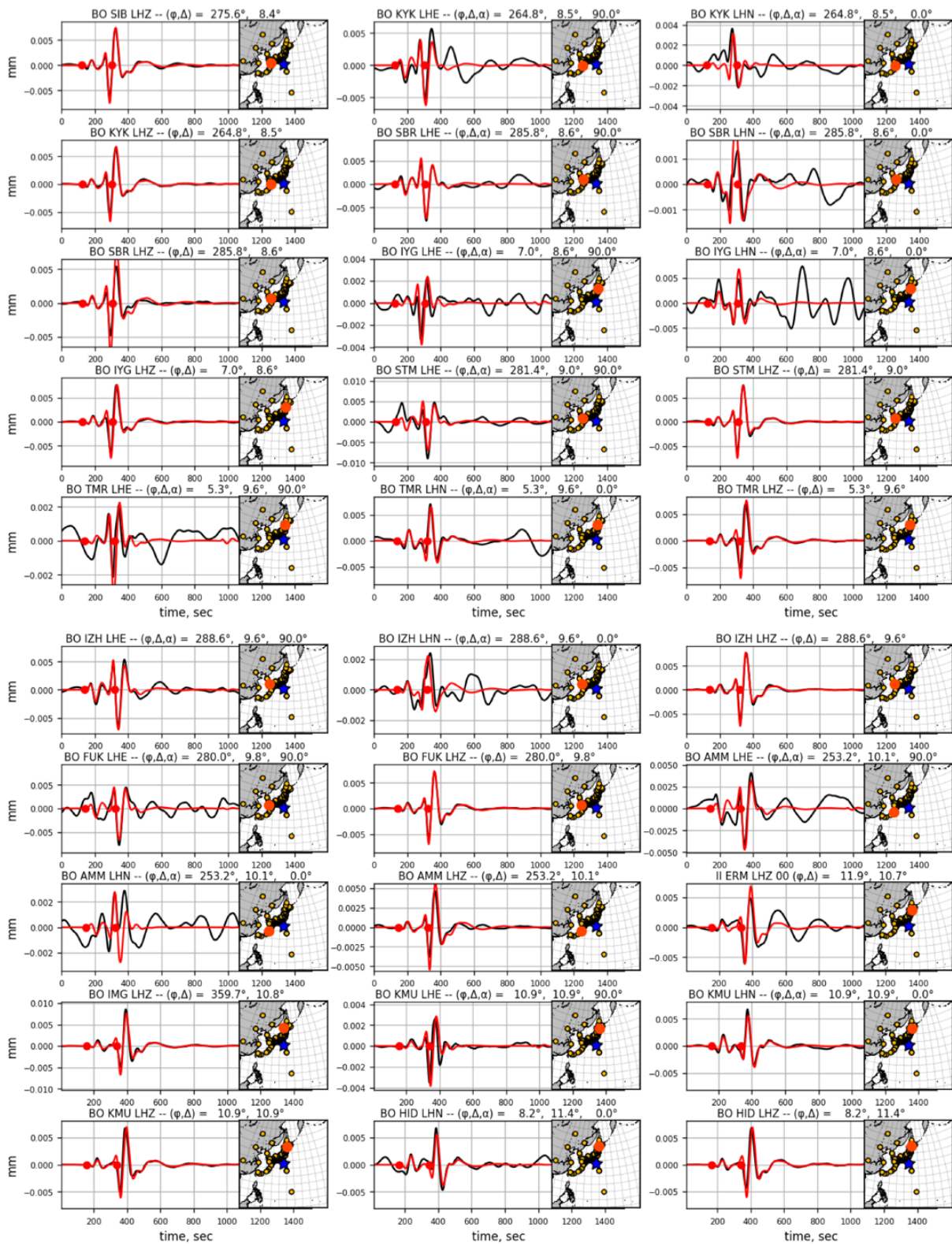


Fig-A2.1 (Continued: 5/6)

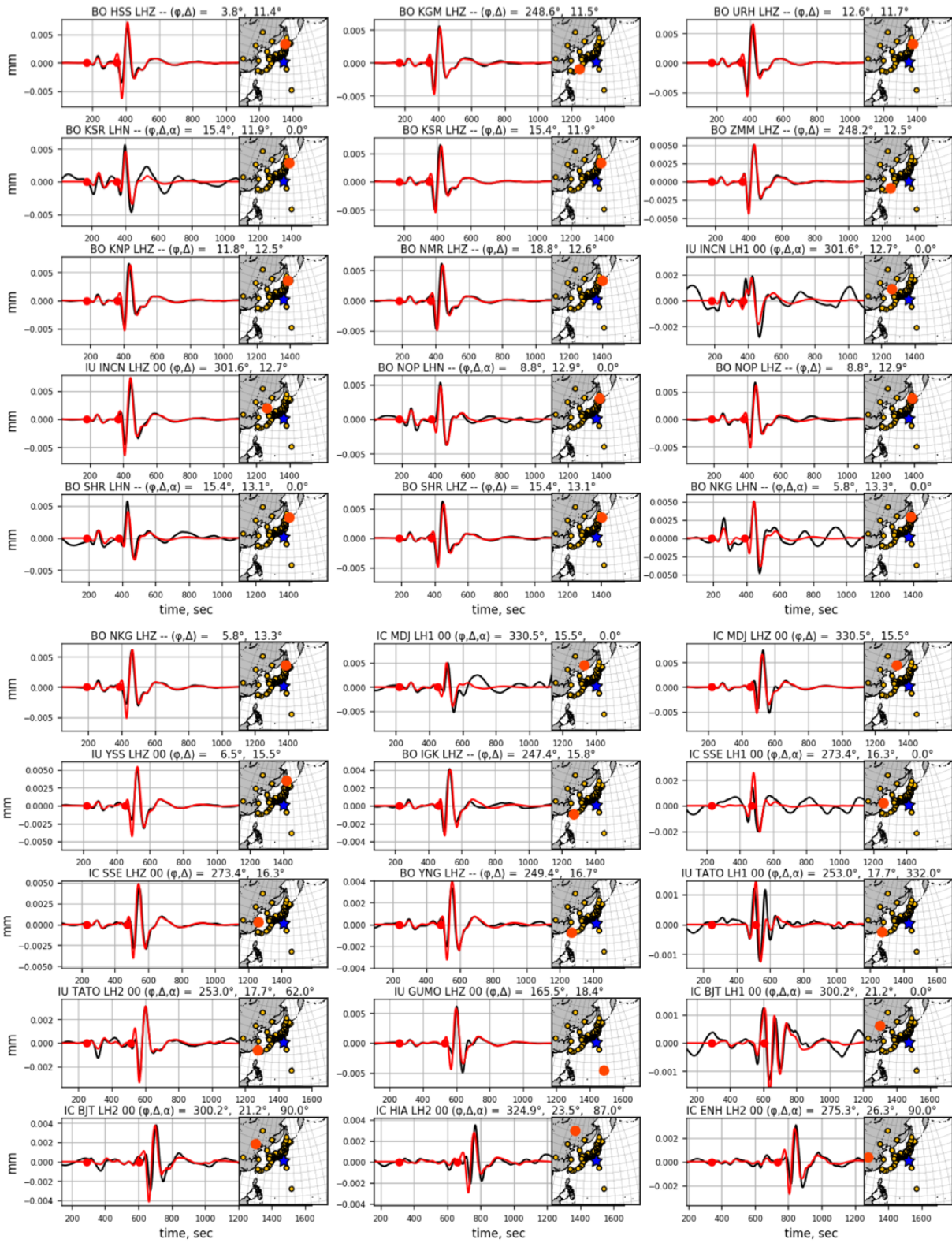
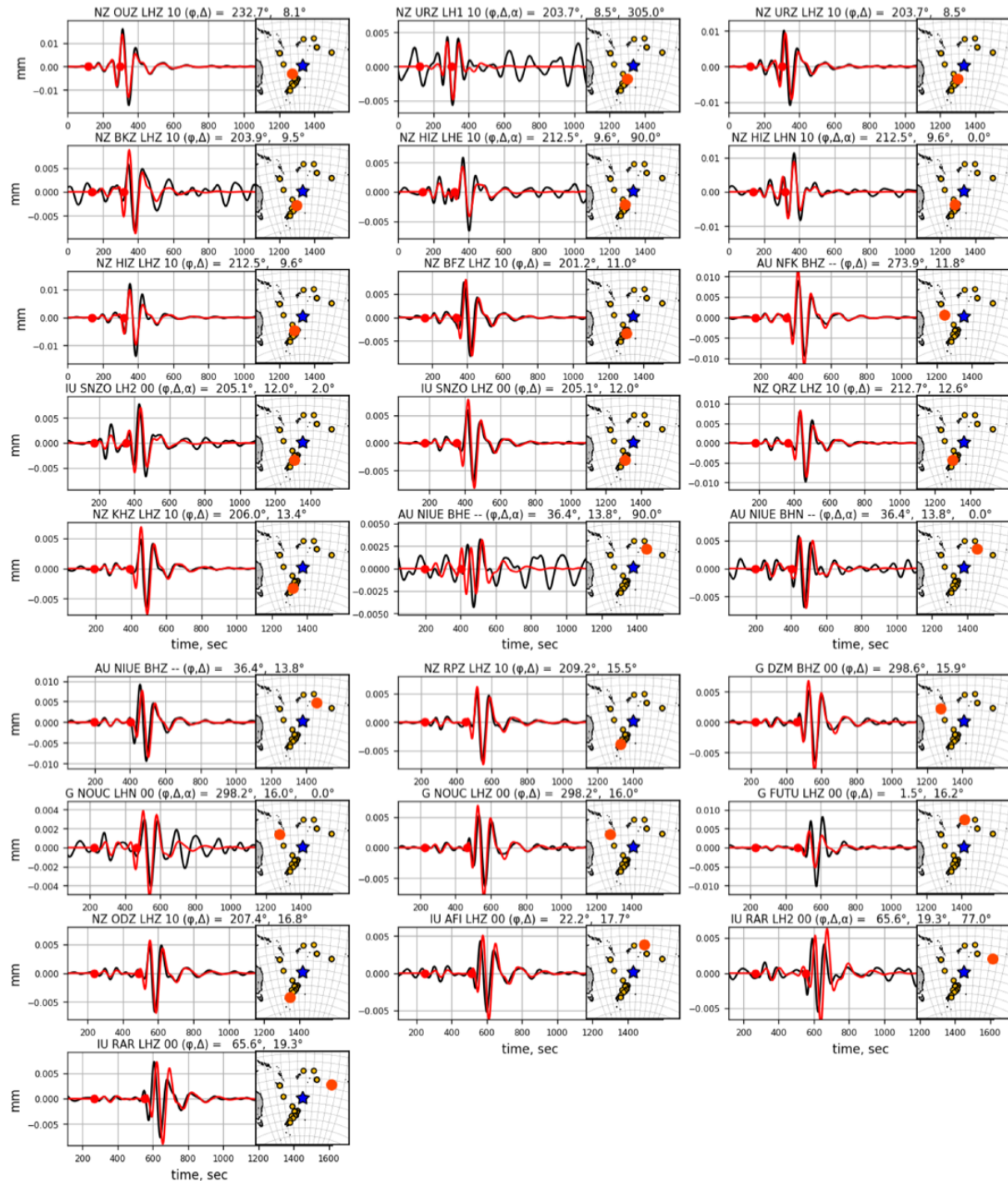


Fig-A2.1 (Continued: 6/6)

## A2.2. The 2017 Curtis volcanic tsunami earthquake

See Chapter 5.2.2 for the detail of the MT inversion including the method and results. The moment tensor solution is shown in Fig. 5.8.



**Fig-A2.2 Model performances of the MT inversion for the 2017 Curtis volcanic tsunami earthquakes**

See caption of Fig-A2.1. Blue star and big orange circle represent locations of the epicenter (Curtis Caldera) and a station, in inset figures.

